A Measurement of the B_s^0 Lifetime at CDF Run II

Sinéad M. Farrington

UNIVERSITY
of
GLASGOW

Department of Physics and Astronomy

August 2004

A thesis submitted to the Physical Science Graduate School

for the degree of Doctor of Philosophy.

Abstract

This thesis describes a measurement of the proper lifetime of the B_s^0 mesons produced in proton-antiproton collisions at a centre of mass energy of 1.96TeV, collected by the CDF experiment at Fermilab. The B_s^0 meson lifetime is measured in its semileptonic decay mode, $B_s^0 \to \ell^+ \nu_\ell D_s^-$. The D_s^- meson candidates are reconstructed in the decay mode $D_s^- \to \phi\pi$, with $\phi \to K^+K^-$, in a trigger sample which requires a muon or an electron and another track which has a large impact parameter. The large impact parameter track is required by the silicon vertex trigger which is an innovative triggering device which has not previously been used in lifetime measurements. A total of 905 ± 42 B_s^0 candidates are reconstructed in a sample which has an integrated luminosity of $140 pb^{-1}$ using data gathered between February 2002 and August 2003.

The pseudo-proper lifetime distribution of these candidates is fitted with an unbinned maximum likelihood fit. This fit takes into account the missing momentum carried by the neutrino and the bias caused by requiring a track with large impact parameter by modelling these effects in simulations. The fit yields the result for the B_s^0 proper lifetime:

$$c\tau(B_s^0) = 419 \pm 28\,^{+16}_{-13}\ \mu m$$

$$\tau(B_s^0) = 1.397 \pm 0.093\,^{+0.053}_{-0.043}\ ps$$

where the first error is statistical and the second is systematic.

Acknowledgements

I thank PPARC for their financial support to study for a PhD and to spend time at Fermilab. I also thank the Liverpool group for their support and advice during the final stages of this thesis.

There are several members of the Glasgow group to thank. I thank my supervisor, Rick St Denis, for his support and comments on the thesis. I also thank my second supervisor Peter Bussey. Thanks to Saverio D'Auria for his help over the years from the early days at SiDet to his advice on the analysis and in particular the generation of simulation samples. Thanks to Stan Thompson for his help in my first year at Glasgow, not only with the physics but also for introducing me to the delights of real ale.

My first task at CDF was to help with the assembly and installation of the silicon detector and I thank the silicon group for their guidance in the various tasks.

I am grateful to Alessandro Cerri for his invaluable sustained advice and guidance at the crucial stages of the analysis. Marjorie Shapiro suggested the topic for this thesis and was most encouraging throughout, both of the analysis and of my career. I also thank Christoph Paus for his support and comments.

I thank the members of the Semileptonic B group for many helpful discussions. In addition, Stefano Giagu was most helpful with practical advice for the coding and Andreas Korn advised on aspects of the parametric simulation and furthermore his instigation of occasional afternoon CDF "koffein-time" was both fun and productive.

My friends at Fermilab made my two years there enjoyable and midwestern suburbia was a less sober place for their company. Among this number are my partners in crime Simon and Bryan, other students past and present: Lucio, Aidan, Thilo, Helen, Anant, Martin T; and c-quark Harry.

Chicago is a great city and I feel someone ought to be thanked for that - maybe the architects?... and my car for getting me there almost unfailingly!

I owe tremendous thanks to Ian for always being there, no mean feat at 3712 miles,

and for always encouraging me. I also thank him for his comments on the theoretical aspects of this work.

Finally I wish to thank my parents, John and Bernadette, and my brother, Conor, for their constant support, humour and encouragement which have underpinned all of my efforts.

Declaration

No portion of the author's work described in this thesis has been submitted in support of an application for another degree or qualification in this, or any other, institute of learning.

Contents

List of Figures

List of Tables

Chapter 1

Theoretical Background

This thesis describes a measurement of the B_s^0 meson lifetime. In this chapter, the theoretical framework of particle physics is introduced and its application to the B_s^0 system is discussed in detail.

This chapter begins with a brief introduction to the Standard Model of electromagnetic, weak and strong interactions in section 1.1. The motivation for the B_s^0 lifetime measurement and the history of the B_s^0 are given in sections 1.2 and 1.3. Particle production in the Tevatron collider environment is discussed in section 1.4 and the decays of the B_s^0 are discussed in section 1.5. The phenomenology of the B_s^0 time evolution is detailed in section 1.6 followed by the Standard Model description of this process in section 1.7. The diagram in figure 1.1 shows all of the processes which are described in this chapter. The scales and details are explained throughout this chapter. Throughout this thesis charge conjugate modes are included.

1.1 The Standard Model

The modern description of particles and their interactions, known as the Standard Model, is based on renormalisable, gauge-invariant field theories. These describe the interactions of the fundamental particles, quarks and leptons, by the exchange of gauge bosons. The

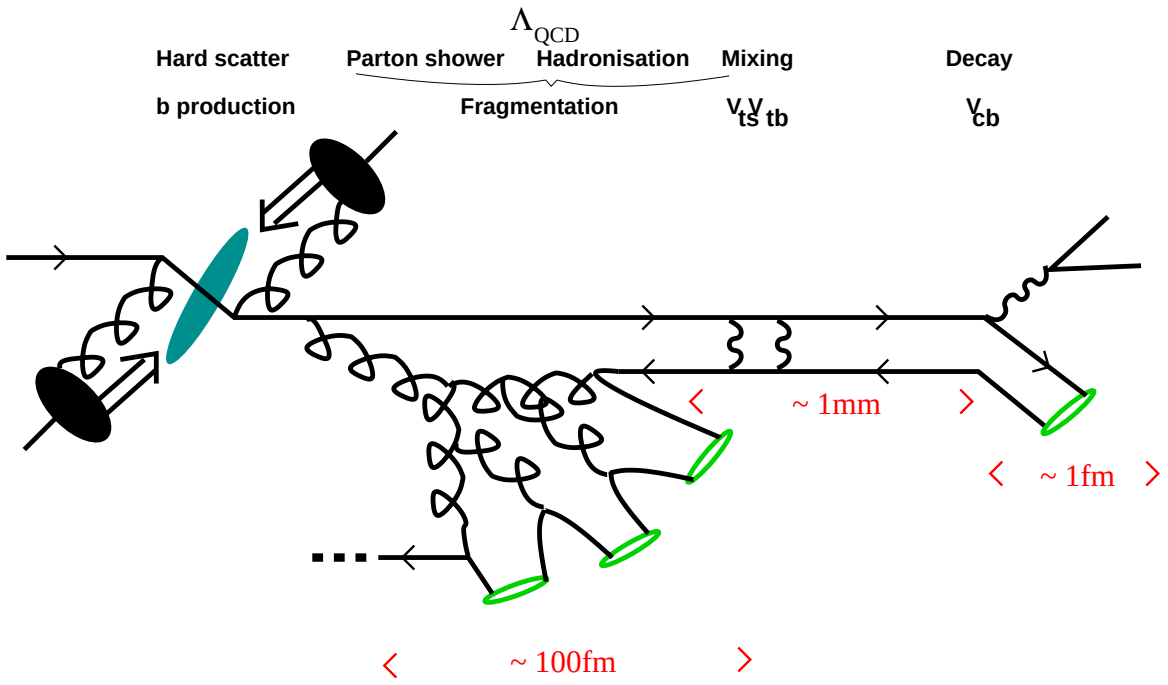

Figure 1.1: *Diagram to show the processes from production to decay of a B meson.*

quarks and leptons and the forces which act among them are listed in table 1.1. In this model, the leptons are fundamental particles and occur in pairs: electrically neutral neutrinos and charged leptons. Leptons do not feel the strong force. The fractionally charged quarks are also believed to be fundamental particles. They are either up type (charge=+2/3) or down type (charge=−1/3). Quarks are not seen in isolation but are confined in bound states known as hadrons. For each fundamental particle in table 1.1 there is a corresponding antiparticle, which has the same mass, spin and lifetime but opposite charges. The strong force is described by an SU(3) invariant gauge theory, known as Quantum Chromodynamics, and is mediated by gluons. Quantum Chromodynamics (QCD) has two regimes which are demarcated by the scale of $\Lambda_{QCD} \sim 200$MeV which is the confinement scale of a hadron. In cases where the momentum transfer in an interaction is much smaller than Λ_{QCD}, the force is very strong and not well understood. For large momentum transfer scales, much higher than Λ_{QCD}, the coupling decreases and per-

	leptons		quarks			strong	e-m	weak
	ν_e	e^-	u	d	neutrinos			•
generation	ν_μ	μ^-	c	s	charged leptons		•	•
	ν_τ	τ^-	t	b	quarks	•	•	•

Table 1.1: *The fundamental particles and the forces which act among them.*

turbation theory can be deployed. This running of the coupling is known as asymptotic freedom and allows the quarks to be treated as almost free particles at high momentum transfer.

A unified description of the electromagnetic and weak forces is provided by a chiral $SU(2)_L \times U(1)_Y$ invariant gauge theory. This symmetry is broken, leaving a U(1) invariant description of electromagnetism which is mediated by massless photons and a description of the weak force mediated by massive Z^0 and $W^\pm$ bosons. The photons couple only to $\ell\ell$ and qq and these are flavour diagonal processes. Exchange of the Z^0 gives rise to non-flavour-changing neutral current processes in which the Z^0 coupling is to $\nu\overline{\nu}$, $\ell\overline{\ell}$ and $q\overline{q}$. Exchange of the $W^\pm$ gives rise to charged current processes which are responsible for particle decays. In the lepton sector, the W coupling is simply to $\ell\overline{\nu}_\ell$. In the quark sector, the W couplings are more complicated as inter-generational transitions are allowed: $u\bar{d}$ and also $u\bar{s}$, $u\bar{b}$ etc. These couplings have weights V_{ud}, V_{us}, V_{ub} etc. which are known as Cabibbo-Kobayashi-Maskawa (CKM) matrix elements. These are discussed in detail in section 1.7.

1.2 Physics Motivation

A B_s^0 meson consists of a bottom antiquark and a strange quark. Its antiparticle, the $\overline{B}_s^0$, consists of a bottom quark and a strange antiquark. The B_s^0 system provides an excellent laboratory for studying many of the profound consequences of the Standard Model, particularly in the weak force sector, but also in the QCD part. The lifetime of

the B_s^0 meson is a fundamental observable which can be expressed in terms of parameters of the Standard Model. Furthermore, the lifetime and related parameters of the B_s^0 system are sensitive to physics beyond the Standard Model.

Theoretical calculations predict the following hierarchy of the lifetimes of b hadrons [1]:

$$\tau(B^+) \geq \tau(B_d^0) \approx \tau(B_s^0) > \tau(\Lambda_b^0) \gg \tau(B_c^-)$$

which agrees with experimental measurements, shown in figure 1.2, except for the Λ_b^0 baryon which has a shorter measured lifetime than theory predicts. One of the prime motivations for measuring the B_s^0 lifetime is to refine the tests of the theoretical predictions of the pattern of b hadron lifetimes.

The B_s^0 system is also interesting since the B_s^0 and $\overline{B}_s^0$ may oscillate into one another in a process known as mixing. In the Standard Model, this process is described by second order weak interactions which result in a time evolution whereby the propagating meson states are superpositions of flavour eigenstates, or equivalently CP eigenstates, which have different masses (m_H and m_L) and lifetimes (τ_H and τ_L), equivalent to widths: $\Gamma = \hbar/\tau$. Semileptonic decays of the B_s^0 meson, $B_s^0 \to \ell^+ \nu_\ell D_s^-$, occur in a roughly equal admixture of the two physical states and so allow a measurement of the (weighted) average lifetime. By selecting other decay modes carefully, the balance of the two states is altered and so the heavy and light components can be measured separately. At CDF the most promising channel is the decay $B_s^0 \to J/\Psi\phi$. In this channel, the decay modes $J/\Psi \to \mu^+\mu^-$ and $\phi \to K^+K^-$ can be cleanly reconstructed. The angular distribution of the μ^+, μ^-, K^+ and K^- allow the CP eigenstates to be separated using the distribution of events in the so-called transversity angle [2, 3, 4]. By analysing these distributions, particular physical B_s^0 states are selected and hence their individual lifetimes are accessible.

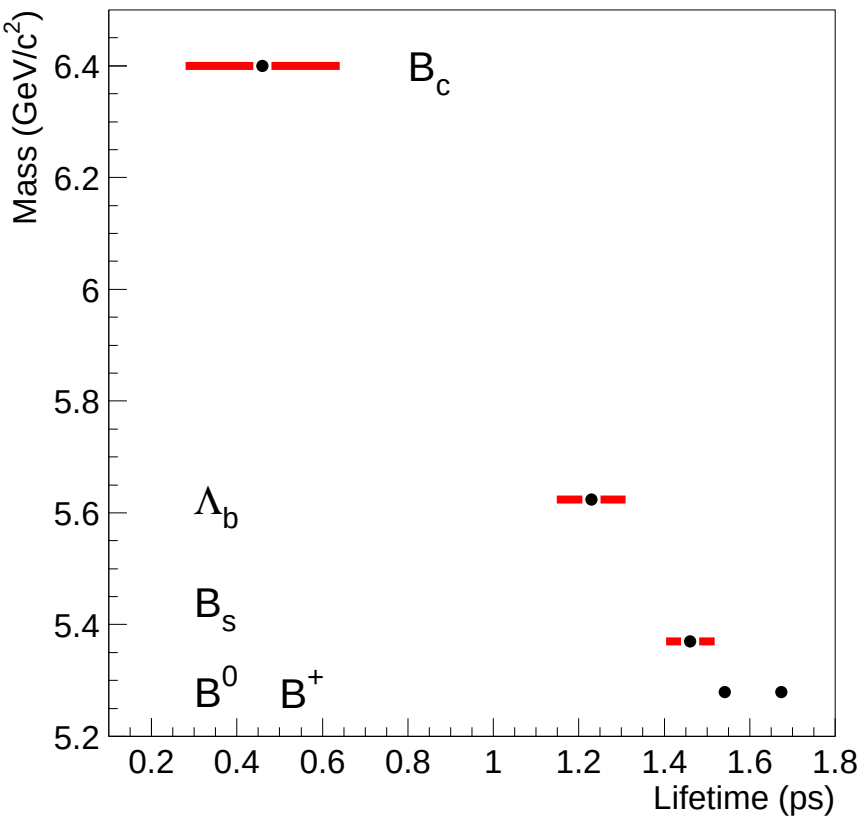

Figure 1.2: *B meson lifetimes as a function of mass.*

1.3 History of the B_s^0 Meson

Evidence for the B_s^0 meson was first published by the LEP experiments ALEPH [5], DELPHI [6] and OPAL [7], in 1992. It was detected via its semileptonic decay $B_s^0 \to \ell^+ \nu_\ell D_s^-$ (BR=7.9±2.4%), a quark line diagram of which is shown in figure 1.3. This channel is distinctive since it features a lepton carrying large momentum and choosing the decay $D_s^- \to \phi\pi^-$ (BR=3.6±0.9%) utilises the very narrow ϕ mass peak to eliminate combinatorial background. It was also in this channel that the first lifetime measurements were made by the same experiments. The OPAL collaboration published their result in

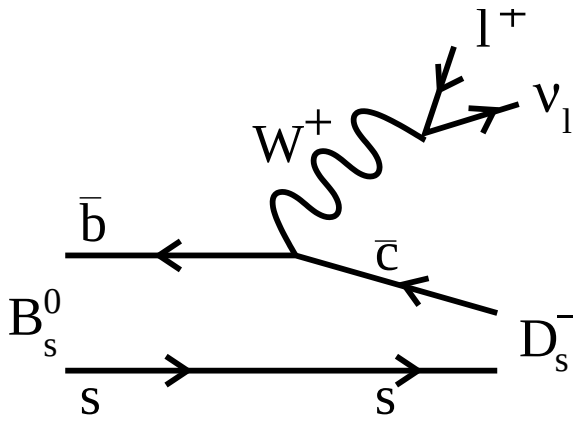

Figure 1.3: *Quark line diagram of the semileptonic decay of the* B_s^0 *meson,* $B_s^0 \to \ell^+ \nu_\ell D_s^-$.

1993 [8]; ALEPH [9] and DELPHI [10] one year later. However this channel is not useful for determining the B_s^0 mass since it is not fully reconstructed, owing to the missing momentum carried by the neutrino. A suitable channel for this purpose is the fully reconstructed $B_s^0 \to J/\psi\phi$ decay (BR=$(9.3\pm3.3)\times10^{-4}$) in which mass measurements were made in 1993 by ALEPH [11] and subsequently by DELPHI [12] and OPAL [13]. Figure 1.4 shows the history of B_s^0 lifetime measurements as listed in the PDG [1] from the LEP experiments and CDF.

The CDF collaboration has the world's best measurements to date for the mass [14], using the $J/\psi\phi$ decay, and lifetime [15], using the $\ell^+ \nu_\ell D_s^-$ decay, of the B_s^0 meson.

1.4 b Production

In this section, hadron-hadron scattering and the theoretical treatment of the processes by which partons interact to produce the particles observed in the laboratory are described. The special case of heavy flavour hadron production is examined in further detail.

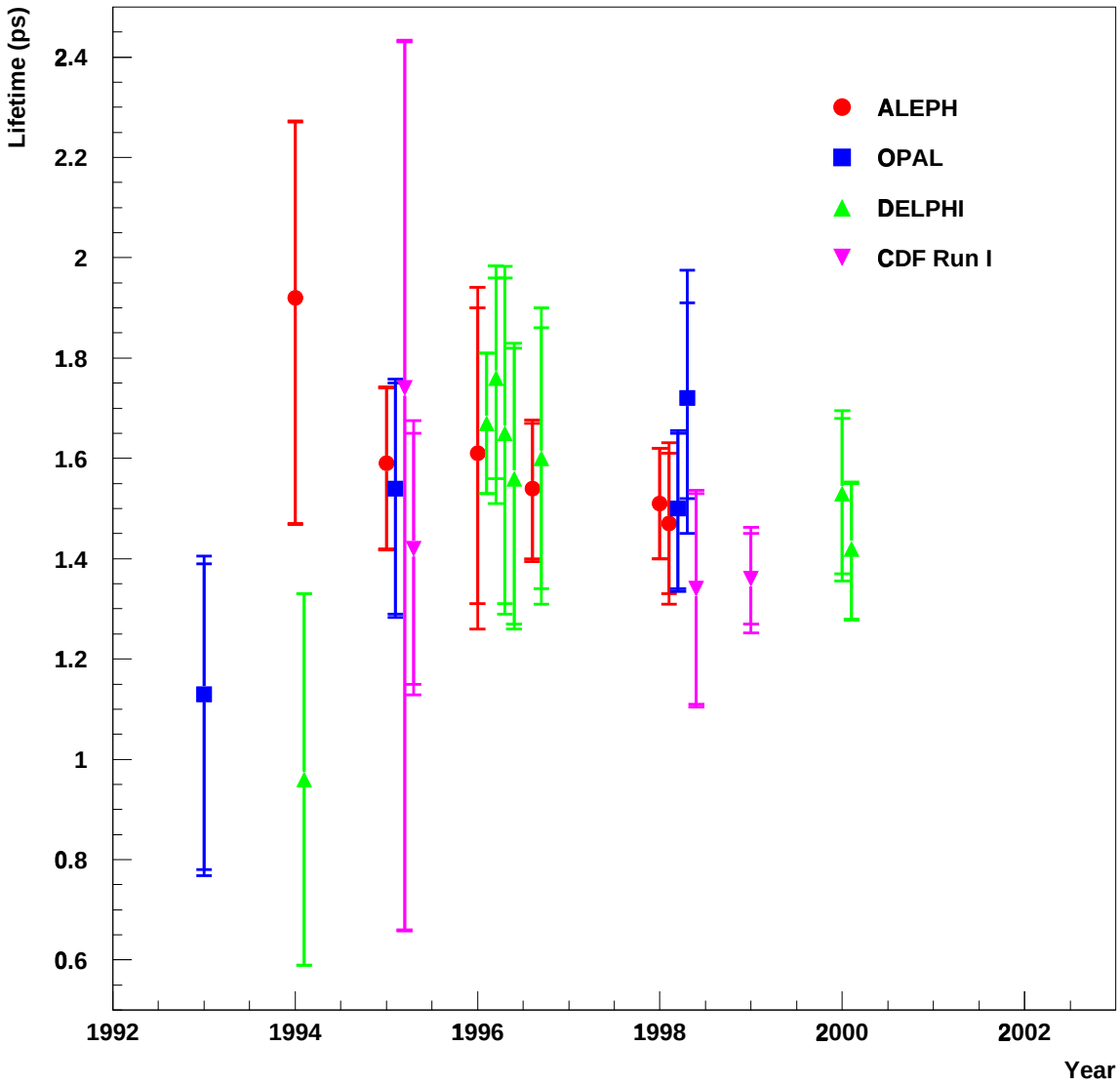

Figure 1.4: *History of* B_s^0 *meson lifetime measurements. The smaller error bars are statistical only and the larger also include systematic errors. Measurements published in the same year are shown slightly offset for clarity.*

1.4.1 Hadron-Hadron Scattering

Hadron-hadron collisions result in a large variety of outcomes which are divided into two types. These are soft interactions in which only small momenta are transferred and hard interactions which contain a large momentum transfer, compared with the characteristic scale of QCD, $\Lambda_{\rm QCD}$, and are thus amenable to perturbative calculations. Examples of hard interactions include jet production, high mass lepton pair production and heavy quark production which is the subject of interest here and will be discussed further in this section. For a full discussion of hadron-hadron scattering and heavy quark production see [16] or [17].

The total cross section in $\mathrm{p\overline{p}}$ collisions has been measured in Tevatron collisions at a centre of mass energy of 1.8 TeV to be 75mb [18, 19, 20]. In this regime, the cross section increases slowly with centre of mass energy, as can be seen in figure 1.5, and at a centre of mass energy of 2 TeV it is predicted to rise to 80mb. The simplest component contributing to this cross section is that due to *elastic* collisions in which the proton and antiproton are deflected but remain intact and have no excitations of internal degrees of freedom. This component accounts for $\approx$ 20mb [18, 21, 22] and the cross section also grows slowly with centre of mass energy, again see figure 1.5. The next simplest component consists of *diffractive* events, in which one or both of the incident hadrons dissociates into a small cluster of particles. The diffractive cross section is expected to be $\approx$10mb at 2 TeV [23]. These components are characterised by very forward peaked differential cross sections and a lack of central activity. Therefore they require specialised far forward detectors to measure them. Such "Roman pot" devices are installed at CDF and are described in [23]. The remaining events are dominated by soft inelastic collisions which appear to be glancing collisions in which the leading fragments leave behind an intervening trail of particles which are uniformly distributed in rapidity, y, and have limited transverse momenta

$$\frac{\mathrm{d}^2\sigma}{\mathrm{d}y\mathrm{d}p_{\mathrm{T}}} \sim e^{-p_{\mathrm{T}}^2/\sigma^2} \quad \text{where } y = \frac{1}{2}\ln\left(\frac{E+p_z}{E-p_z}\right) \tag{1.1}$$

Events involving a large momentum transfer, leading to significant central activity, are

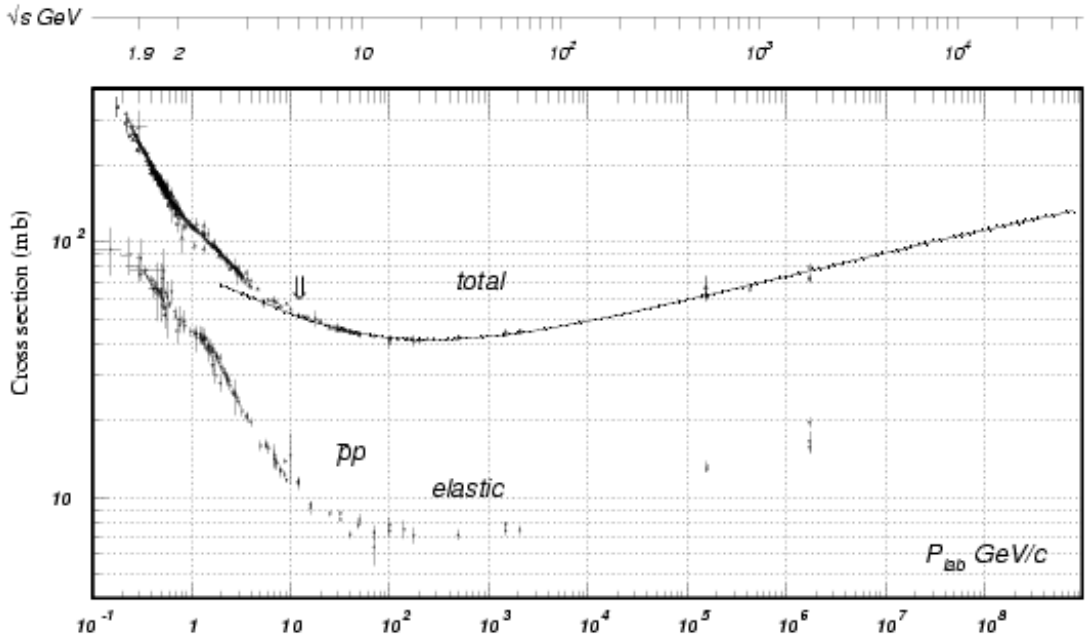

Figure 1.5: *Total and elastic cross sections for* $\mathrm{p\overline{p}}$ *collisions as a function of laboratory beam momentum and total centre of mass energy. [1]*

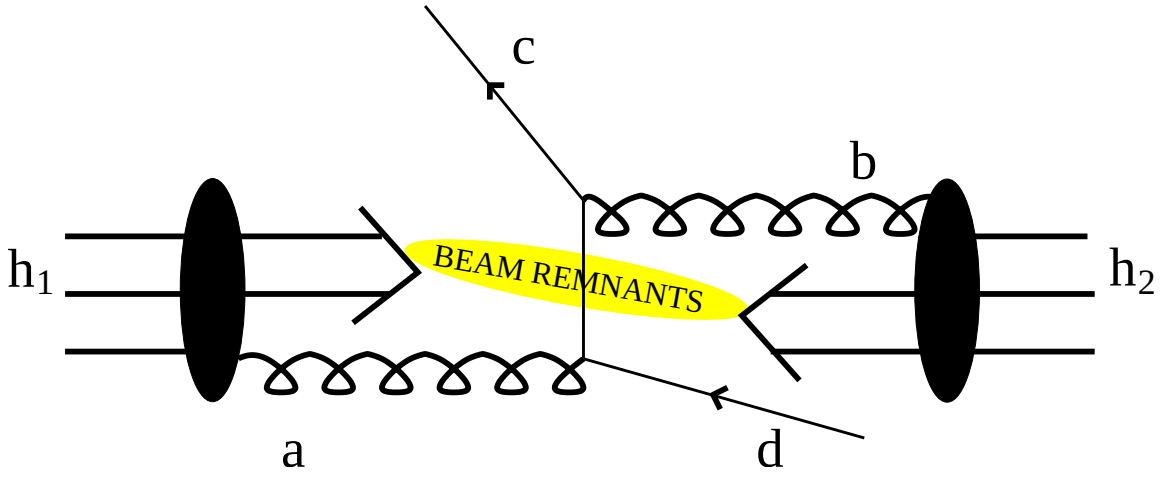

Figure 1.6: *Schematic diagram of the production of final state particles, c and d, in a hard collision of hadrons, h_1 and h_2.*

relatively rare. For example, the total cross section for b quark production at the Tevatron is predicted, from current data, to be $\mathcal{O}(10\mu\mathrm{b})$ [24].

The treatment of a hard process is illustrated for the case of a general two to two body process. Specific cases will then be discussed. The short distance scales involved in a hard process suggest working in a framework of quarks and gluons rather than hadrons. The production process is then depicted by a diagram such as that shown in figure 1.6. At tree level, the cross section formula for a proton and antiproton to collide and produce partons c and d is given by

$$\mathrm{d}\sigma(\mathrm{p\overline{p}} \to cd) = \int_0^1 \mathrm{d}x_\mathrm{p}\mathrm{d}x_{\overline{\mathrm{p}}} \sum_{a,b} f_a^\mathrm{p}(x_\mathrm{p}, \mu_F^2) f_b^{\overline{\mathrm{p}}}(x_{\overline{\mathrm{p}}}, \mu_F^2) \mathrm{d}\hat{\sigma}^{ab\to cd}(Q^2, \mu_F^2) \qquad (1.2)$$

Here x_p and $x_{\bar{\mathrm{p}}}$ are the momentum fractions carried by partons in the proton and antiproton respectively. The probability of finding parton a inside the hadron p carrying a momentum fraction in the range $[x, x + \mathrm{d}x]$ when the hadron is probed at the factorisation scale, μ_F^2, is given in terms of the parton density functions (p.d.f.s) by $f_a^\mathrm{p}(x_\mathrm{p}, \mu_F^2)dx$ and similarly for $f_b^{\overline{\mathrm{p}}}$. The hadronic cross section is given as a sum over the contributing

partonic cross sections: $a, b = \{q, \overline{q}, g\}$ and the partonic cross section is given by

$$\mathrm{d}\hat{\sigma}(ab \to cd) = \frac{1}{2\hat{s}} \overline{\sum} \left| \mathcal{M}(ab \to cd) \right|^2 d\Phi_2 \tag{1.3}$$

where $d\Phi_2$ is the two body phase space of the final state particles. In equation 1.2 the p.d.f.s and $\hat{\sigma}$ depend on the factorisation scale, μ_F, and the factorisation scheme used. In higher orders there is also a dependence on the renormalisation scale and scheme. Often these scales are set equal to a characteristic scale for convenience. In all orders of calculation there is no dependence on either of these scales, though residual dependences arise at finite order.

The leading order processes which contribute to the matrix element are $q\overline{q} \to Q\overline{Q}$ and $gg \to Q\overline{Q}$ which are shown in figure 1.7. The propagating particles in the leading order diagrams all have a virtuality greater than the transverse mass $\mathrm{m_T^2 = M_Q^2 + {p_T}^2}$ which is much larger than Λ_{QCD} and so b production can be treated using perturbative QCD. This also suggests using $\mathrm{m_T}$ as the characteristic scale for the processes. The matrix elements of these processes are given by [16]

$$\begin{aligned} \overline{\sum} \left| \mathcal{M}(q\overline{q} \to Q\overline{Q}) \right|^2 &= g_s^4 \frac{4}{9} \left(\tau_1^2 + \tau_2^2 + \frac{\rho}{2} \right) \\ \overline{\sum} \left| \mathcal{M}(gg \to Q\overline{Q}) \right|^2 &= g_s^4 \left(\frac{1}{6\tau_1\tau_2} - \frac{3}{8} \right) \left(\tau_1^2 + \tau_2^2 + \rho - \frac{\rho^2}{4\tau_1\tau_2} \right) \end{aligned} \tag{1.4}$$

where g_s is the strength of the strong coupling, $g_s^2 = 4\pi\alpha_s$ and

$$\tau_1 = \frac{2p_a \cdot p_c}{\hat{s}}, \quad \tau_2 = \frac{2p_b \cdot p_c}{\hat{s}}, \quad \rho = \frac{4M_Q^2}{\hat{s}}, \quad \hat{s} = (p_a + p_b)^2 \tag{1.5}$$

The momenta of the partons are given by $p_a = x_{\mathrm{p}} p_{\mathrm{p}}$ and $p_b = x_{\bar{\mathrm{p}}} p_{\bar{\mathrm{p}}}$ where in general $x_{\mathrm{p}} \neq x_{\bar{\mathrm{p}}}$ and so the resulting hard subprocess is generally boosted along the beamline. This is useful for measuring quantities such as the lifetime of a hadron where its decay length is exaggerated by the boost and this is exploited in this analysis of the $\mathrm{B_s^0}$ lifetime measurement.

The hadronic cross section in terms of the rapidities and equal and opposite transverse

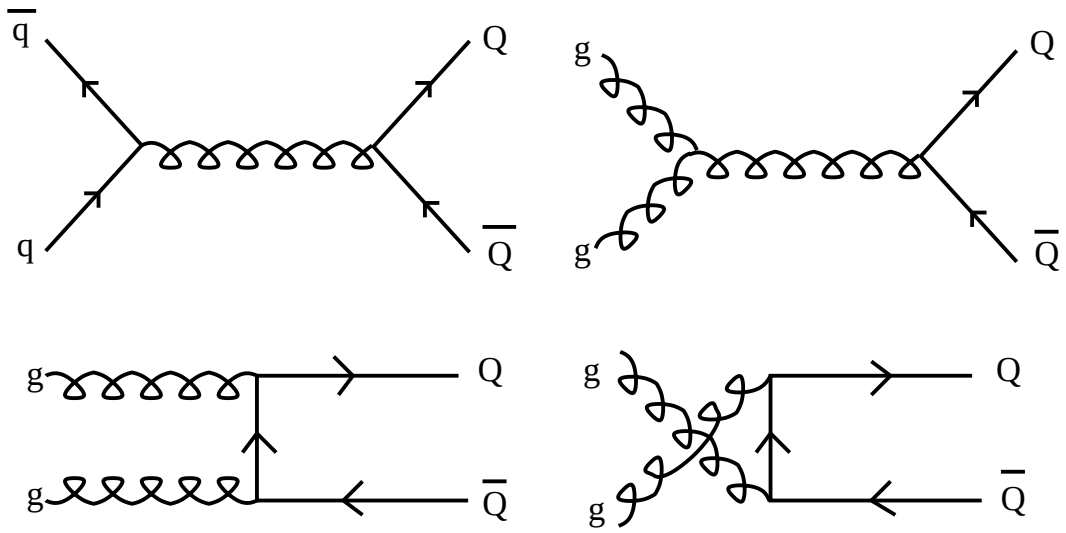

Figure 1.7: *Heavy quark production Feynman diagrams at leading order.*

momenta of the outgoing heavy quarks is

$$\frac{\mathrm{d}^3\sigma}{\mathrm{d}y\mathrm{d}\bar{y}\mathrm{d}p_T^2} = \frac{\pi}{4m_{\mathrm{T}}^4}\frac{1}{[1+\cosh(y-\bar{y})]^2}\frac{1}{(4\pi)^2}\sum_{a,b} x_{\mathrm{p}} f_a^{\mathrm{p}}(x_{\mathrm{p}}) x_{\bar{\mathrm{p}}} f_a^{\mathrm{p}}(x_{\bar{\mathrm{p}}}) \overline{\sum}\left|\mathcal{M}(ab\to \mathrm{Q}\overline{\mathrm{Q}})\right|^2 \tag{1.6}$$

where

$$\begin{aligned} x_{\mathrm{p},\bar{\mathrm{p}}} &= \tfrac{m_{\mathrm{T}}}{\sqrt{S}}(e^{\pm y}+e^{\pm\bar{y}}) \quad & \hat{s} &= 2m_{\mathrm{T}}^2[1+\cosh(y-\bar{y})] \\ \tau_{1,2}\hat{s} &= m_{\mathrm{T}}\sqrt{S}e^{\mp y} & S &= (p_{\mathrm{p}}+p_{\bar{\mathrm{p}}})^2 \end{aligned} \tag{1.7}$$

The first piece of equation 1.6 is the flux factor which favours the Q and $\overline{\mathrm{Q}}$ being produced close together in rapidity, $y \sim \overline{y}$. The factor $1/m_{\mathrm{T}}^4$ ensures that the cross section falls quickly with increasing p_{T}. Figures 1.8 and 1.9 show the b quark production cross section as a function of rapidity and p_{T}.

Higher order terms must be added to the lowest order contributions in a series expansion in the running coupling, α_s. A full calculation at next to leading order (NLO) involves real and virtual corrections, as shown in figure 1.10. The loop diagram is divergent for large values of momentum in the loop. This is known as an ultraviolet divergence and requires renormalisation to remove it. This involves the choice of a particular renormalisation scheme and the introduction of a renormalisation scale, μ_R^2. After renormalisation,

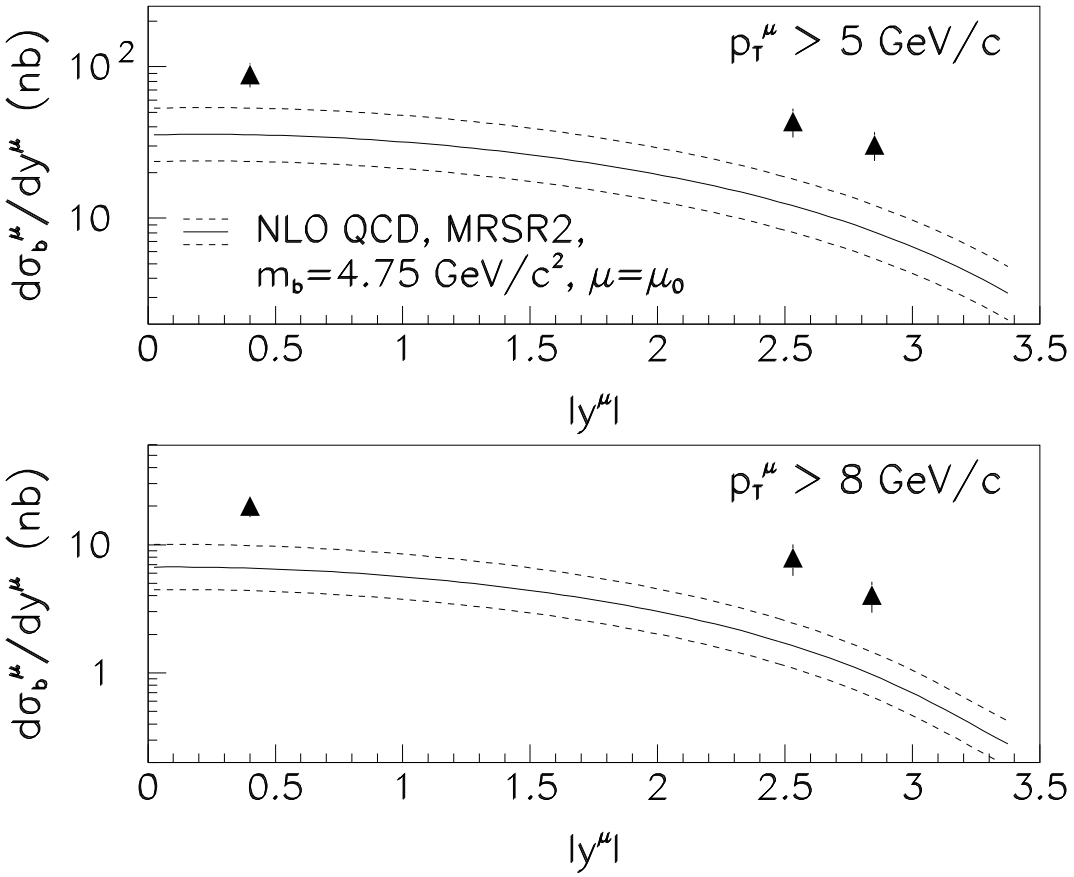

Figure 1.8: *b quark production cross section as a function of rapidity for two p_{T} regions [25].*

the coupling constant and quark masses are functions of μ_R^2. At leading order the μ_R^2 dependence of the strong coupling is given by

$$\alpha_s(\mu_R^2) \equiv \frac{g_s^2}{4\pi} = \frac{1}{\beta_0 \ln(\mu_R^2/\Lambda_{\mathrm{QCD}}^2)} \qquad \beta_0 = \frac{33 - 2n_f}{12\pi^2} \tag{1.8}$$

where n_f is the number of active flavours. The coupling decreases as the scale increases. Physical quantities, such as a cross section, do not depend on the arbitrary renormalization scale. This constrains their form

$$\sigma(\mu_R^2) = \alpha_s^2(\mu_R^2)A_0 + \alpha_s^3(\mu_R^2)\left[A_1 + 2\beta_0 \ln\left(\frac{\mu_R^2}{Q^2}\right) A_0\right] + \mathcal{O}(\alpha_s^4) \tag{1.9}$$

Here A_0 and A_1 are independent of μ_R^2 whilst Q is the momentum scale characterising the

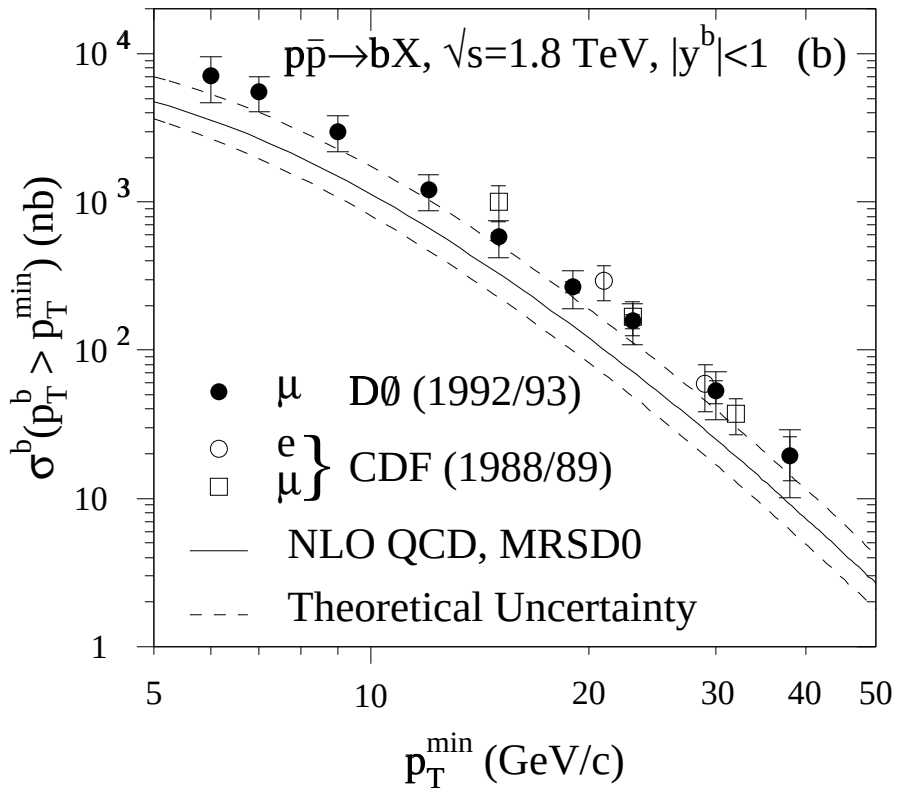

Figure 1.9: *b quark production cross section as a function of* p_{T} *[25].*

cross section. This form ensures that σ is independent of μ_R^2 to leading order, $\mathcal{O}(\alpha_{\mathrm{s}}^2)$. In practice a choice is still required for μ_R^2. This chosen scale depends on the process involved, and should be commensurate with the magnitude of Q^2 in order to maintain the basis that the orders (LO, NLO...) contribute successively less to the overall sum. For heavy quark production above a minimum p_{T}, a typical choice would be $\mu_R^2 \simeq Q^2 = M_Q^2 + {p_{\mathrm{T}}}^2_{\mathrm{min}}$.

In addition to the ultraviolet divergences, both the tree and loop diagrams contain infrared divergences; these occur whenever the radiated gluon or on-mass-shell, internal gluon has vanishing energy or becomes collinear to an external particle. When dealing with an infrared safe experimental quantity -which is insensitive to either soft or near collinear gluons - then the divergences cancel between the real and virtual processes. However, the cancellation does not occur for an initial state radiation gluon which is almost collinear with an incoming quark or gluon. In this case, factorisation is invoked. This requires the

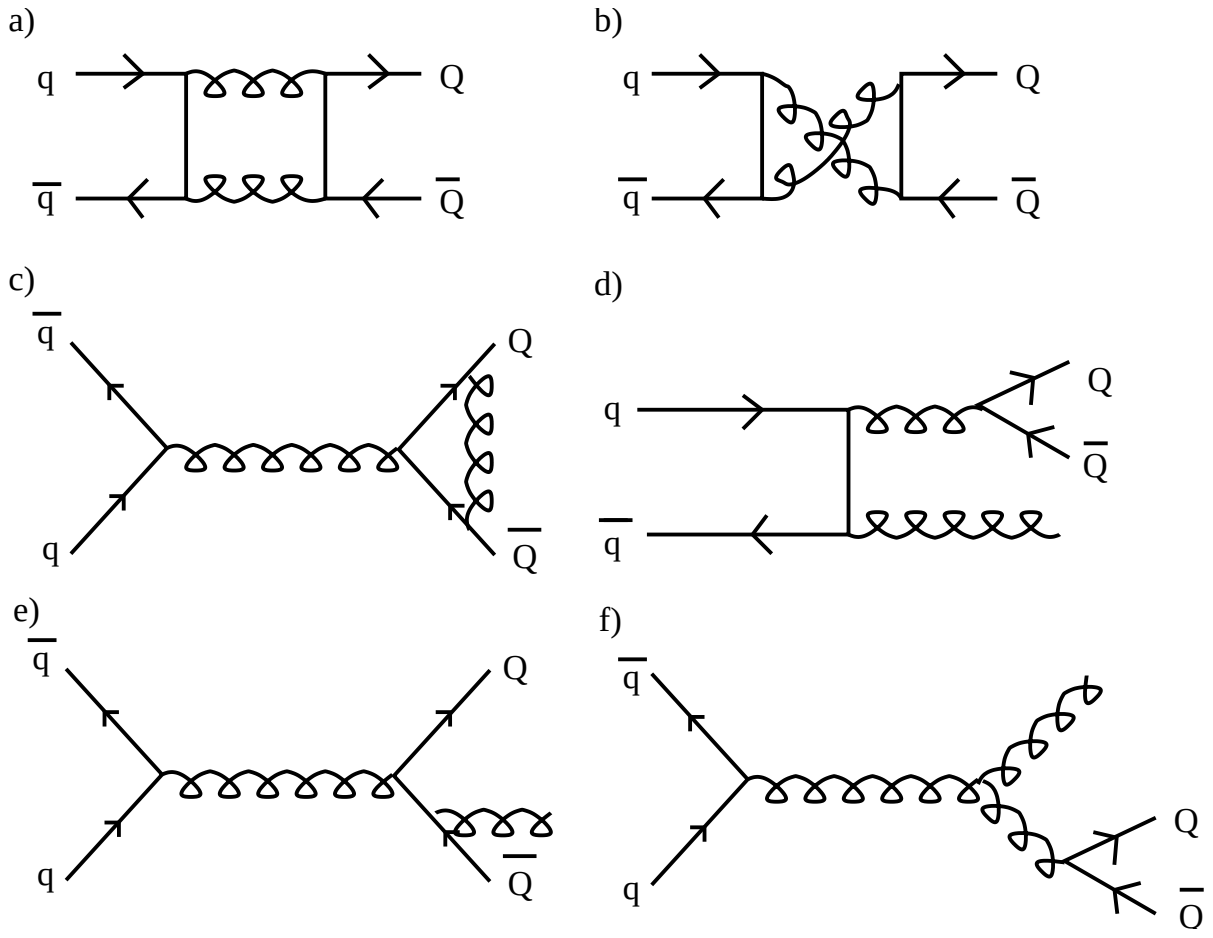

Figure 1.10: *Heavy quark production Feynman diagrams at next-to-leading order. Figures a)-c) are examples of virtual corrections; figures d)-f) are examples of real corrections.*

choice of a factorisation scheme and the introduction of a factorisation scale, μ_F^2. This scale separates the calculation into two parts: a soft, long-distance, non-perturbative component which is incorporated into hadron-specific p.d.f.s and a short-distance component which may be treated perturbatively and independently of the incoming hadrons. After factorisation, the p.d.f.s are dependent on μ_F^2 and this dependence is described by the DGLAP equations [26]. They are extracted within some chosen scheme from simultaneous fits to large data sets [27]. The leading dependences on μ_F^2 and μ_R^2 disappear in a NLO calculation but a NLO dependence remains.

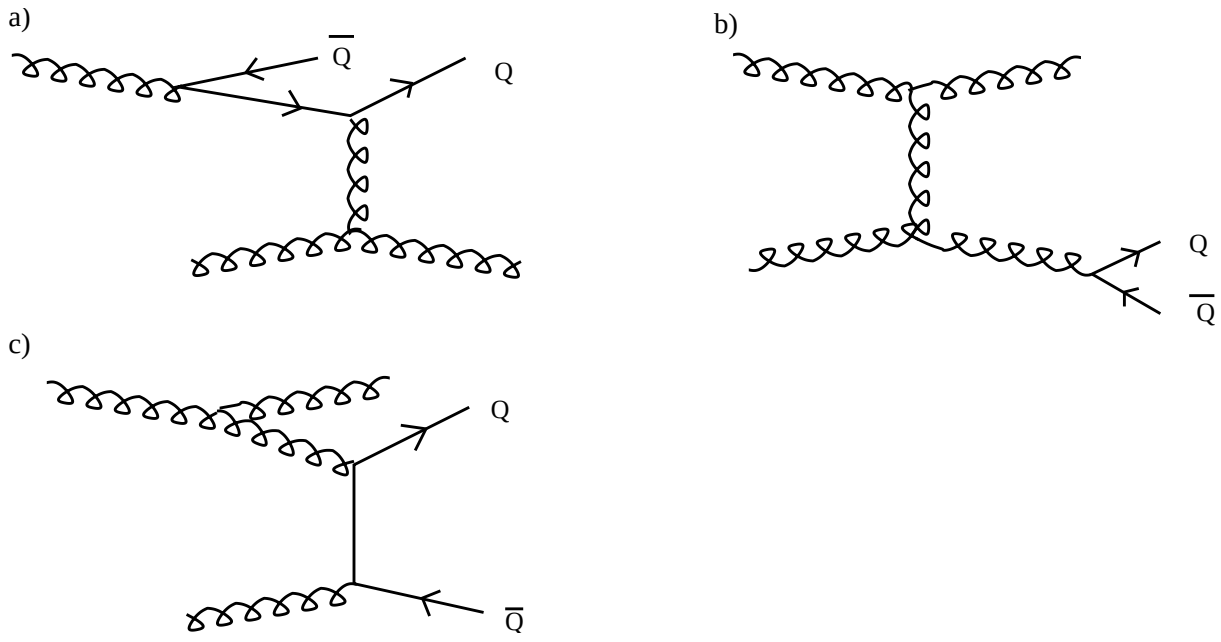

Figure 1.11: *Schematic diagrams of NLO processes which are particularly enhanced. Figure a) shows flavour excitation, figure b) shows gluon splitting and figure c) shows the small-x gluon process.*

In the NLO calculation, there are three regions of phase space where the cross section is particularly enhanced [28]. In these regions the matrix elements squared simplify in such a way that these leading contibutions can be identified and summed for all orders in α_s, a process known as resummation. The resulting three enhanced processes are colloquially called flavour excitation, gluon splitting and small-x gluons. These are shown schematically in figure 1.11. Since these regions are dominant, Monte Carlo packages focus on reproducing them well. The regions are of further interest to experimentalists since they are topologically distinct and may be distinguished from one another [29]. Each region is now discussed in turn:

Flavour Excitation is shown in figure 1.11a. In this case, the heavy flavour component of one hadron (for a proton this comes from a prior g$\rightarrow$ Q$\overline{\text{Q}}$ branching) scatters against a parton from the other hadron and is forced on mass shell in the process

Qg→Qg or Qq→Qq. In this process, one heavy quark, Q is assumed to be collinear with the parent hadron and is lost as it travels in the beam direction.

Gluon Splitting is shown in figure 1.11b. In this case, only gluons and light flavours are involved in the hard scattering subprocess. Subsequently an outgoing gluon branches resulting in a pair of heavy quarks, g→ $Q\overline{Q}$, which are close together in the detector.

Small-x is shown in figure 1.11c. This process appears similar to the leading order gg→ $Q\overline{Q}$ process. It is enhanced when a prior branching leaves one of the incoming gluons nearly on mass shell and with a small fraction of the parent proton's momentum.

1.4.2 b Fragmentation

The production of heavy quarks is described in section 1.4.1 and it is shown that the matrix elements for production of b quarks are calculable. However, in the laboratory, collimated jets of hadrons are observed rather than quarks. The transition from quark to jet is known as fragmentation. Uncertainties in the fragmentation process result in a systematic error in the lifetime analysis which is discussed further in chapter 6.

Once the b quark has been formed, it propagates, showering gluons, which may in turn split into further gluons or $q\overline{q}$ pairs, to form a parton shower and losing energy as it does so [16, 17]. While the partons are sufficiently virtual, the evolution is described by perturbative calculations. However, non-perturbative effects become important when the virtualities fall below a cut-off scale. This coincides with the binding together of the b quark with a lighter quark (u, d or s) or diquark into a colour neutral hadron and likewise for the other partons in the shower. CDF has measured the fractions $f_{\mathrm{u}}, f_{\mathrm{d}}, f_{\mathrm{s}}$, and f_{baryon} of produced b quarks which hadronise with a light quark to yield $\mathrm{B}^-, \overline{\mathrm{B}}^0_{\mathrm{d}}, \overline{\mathrm{B}}^0_{\mathrm{s}}$ and Λ^0_{b} hadrons [30]. These are found to be $f_{\mathrm{u}} = f_{\mathrm{d}} = 0.375 \pm 0.023$, $f_{\mathrm{s}} = 0.160 \pm 0.044$ and $f_{\mathrm{baryon}} = 0.090 \pm 0.029$. The process of showering and hadronisation is described by the fragmentation function, $D(x) = d_{PT} \otimes d_{NP}$, which is the probability distribution

of the fraction, x, of the b quark momentum or energy which is retained by the hadron and, as described, has perturbative and non-perturbative components. Calculations at NLO predict a sharply forward peaked distribution for the perturbative component. The non-perturbative component is described by theoretically inspired forms which match the available data. One such form is the Peterson et al. fragmentation function [31]:

$$d_{NP}(x) = \frac{N}{x}\left(1 - \frac{1}{x} - \frac{\epsilon_Q}{1-x}\right)^{-2} \tag{1.10}$$

where N is a normalisation factor and ϵ_Q is the so-called Peterson-epsilon parameter which is tuned according to the hadron type under consideration. Theory suggests that $\epsilon_{\rm Q} \sim (\Lambda_{\rm QCD}/M_{\rm Q})^2$. The non-perturbative fragmentation function is hard: $\langle x \rangle = 1 - \sqrt{\epsilon_{\rm Q}}$. Some descriptions of the data use the Peterson fragmentation function to describe the entire fragmentation process and neglect the perturbative component. Therefore the ϵ_Q becomes energy dependent. A more comprehensive description of the non-perturbative hadronic process presently relies on models, the most popular of which are the String Model, as used by the PYTHIA Monte Carlo [32] and the Cluster Model, as used in the HERWIG Monte Carlo [33]. The Monte Carlo models provide a full list of all of the particles produced in a collision and their properties, such as momenta and decay vertices. This enables studies, for example, of correlations between the B meson flavour and other properties of the event as a means of tagging the B flavour at production. This is useful for reasons which will be discussed in section 1.6.

1.5 B Decays

The b hadrons decay into many different final states. Semileptonic final states are amongst the most common. These consist of a charged lepton - neutrino pair and hadrons. An example is depicted in figure 1.3. In these decays, the b quark predominantly decays to a c quark or, at a rate suppressed by the ratio of CKM elements $|V_{\rm ub}|^2/|V_{\rm cb}|^2$, to a u quark, by emitting a virtual W^- boson which subsequently decays to $\ell^-\overline{\nu}_\ell$. In the case of a semileptonic decay, the decay amplitude is amenable to theoretical treatment using

invariant form factors to quantify the effects of the strong interaction. These form factors depend only on the type of hadron produced in the final state and the momentum carried by the W. The decay of interest in this thesis is $\mathrm{B_s^0} \to \ell^+\nu_\ell \mathrm{D_s^{(\star)-}}$. The formalism for treating a semileptonic B decay is now discussed [34].

In a semileptonic decay, the amplitude has two components: a leptonic current, at the $W^+ \to \ell^+\nu_\ell$ vertex and a hadronic current at the $\bar{\mathrm{b}} \to \bar{\mathrm{q}}W^+$ (q=c or u) vertex:

$$\mathcal{L}_{\mathrm{eff}} = -2\sqrt{2}G_F V_{\mathrm{qb}} \left[J_{\mathrm{had}} \cdot J^\dagger_{\mathrm{lept}} + J_{\mathrm{lept}} \cdot J^\dagger_{\mathrm{had}} \right] \tag{1.11}$$

where V_{qb} is a CKM matrix element. The leptonic current in the Standard Model, $J^\mu_{\mathrm{lept}} = \bar{u}(\ell^-)\gamma^\mu(1-\gamma_5)v(\bar{\nu}_\ell)$, is calculable. However, the hadronic current, J_{had}, is complicated by strong interaction corrections and must be parameterised by form factors which contain all information on the decay. For a pseudoscalar B meson to pseudoscalar D meson decay:

$$J^\mu_{\mathrm{had}} \equiv \langle \mathrm{D}(p')|\bar{\mathrm{c}}\gamma^\mu(1-\gamma_5)\mathrm{b}\big|\overline{\mathrm{B}}(p)\big\rangle = f_+(Q^2)(p+p')^\mu + f_-(Q^2)(p-p')^\mu \tag{1.12}$$

where the Lorentz scalar form factors, $f_\pm$, have a kinematic dependence through the square of the momentum transfer, $Q^2 = (p-p')^2$. $f_\pm(Q^2)$ describe the probabilities for the final state quarks to form the D meson. For a pseudoscalar to vector decay, such as $\mathrm{B} \to \mathrm{D}^\star$, the $\mathrm{D}^\star$ may be polarised and has contributions from vector and axial currents:

$$\begin{aligned} J^\mu_{\mathrm{had}} &\equiv \langle \mathrm{D}^\star(p',\epsilon)|\bar{\mathrm{c}}\gamma^\mu(1-\gamma^5)\mathrm{b}\big|\overline{\mathrm{B}}(p)\big\rangle & (1.13)\\ &= -i\epsilon^{\mu\nu\sigma\tau}\epsilon^\star_\nu p_\sigma p'_\tau \frac{2V(Q^2)}{(M_{\mathrm{B}}+M_{\mathrm{D}^\star})} + (M_{\mathrm{B}}+M_{\mathrm{D}^\star})A_1(Q^2)\epsilon^{\star\mu} \\ &\quad - \frac{p\cdot\epsilon^\star}{(M_{\mathrm{B}}+M_{\mathrm{D}^\star})}A_2(Q^2)(p+p')^\mu + 2\frac{M_{\mathrm{D}^\star}(p\cdot\epsilon^\star)}{Q^2}A(Q^2)(p-p')^\mu & (1.14)\end{aligned}$$

The first term describes the vector, γ^μ, interaction and the remaining three terms describe the axial, $\gamma^\mu\gamma_5$, interaction. The differential cross-section may be calculated in terms of the unknown, non-perturbative, dimensionless, form factors, using these currents. The fully differential decay rate for $\mathrm{B} \to \ell\nu_\ell\mathrm{D}$ written in terms of Q^2 and the invariant mass of the lepton-D system, $M_{\mathrm{D}\ell}$, is

$$\frac{\mathrm{d}^2\Gamma}{\mathrm{d}Q^2\mathrm{d}M^2_{\mathrm{D}\ell}} = \frac{G_{\mathrm{F}}^2|V_{\mathrm{cb}}|^2}{32\pi^3 M_{\mathrm{B}}^3}|f_+(Q^2)|^2\left[(M^2_{\mathrm{D}\ell}-M^2_{\mathrm{D}})(M^2_{\mathrm{B}}-M^2_{\mathrm{D}\ell}) - Q^2M^2_{\mathrm{D}\ell}\right] \tag{1.15}$$

Integrating over $M_{\mathrm{D}\ell}$ gives

$$\frac{\mathrm{d}\Gamma}{\mathrm{d}Q^2} = \frac{G_F^2|V_{\mathrm{cb}}|^2}{24\pi^3} p_{\mathrm{D}}^3 |f_+(Q^2)|^2 \tag{1.16}$$

Here, p_D is the magnitude of the D meson's three momentum in the B meson rest frame, given by

$$p_D^2 = \frac{1}{4M_{\mathrm{B}}^2}\left[(M_{\mathrm{B}} - M_{\mathrm{D}})^2 - Q^2\right]\left[(M_{\mathrm{B}} + M_{\mathrm{D}})^2 - Q^2\right] \tag{1.17}$$

In equations 1.15 and 1.16 the terms proportional to $p - p'$ are vanishing for electrons and muons since $(p - p') \cdot J_{\mathrm{lept}} \propto m_\ell$ and the leptons are very light. In the case of a tau lepton, terms containing f_- should be included. Similar expressions to 1.15 and 1.16 can be given for the decay $\mathrm{B} \to \ell\nu_\ell \mathrm{D}^\star$ in terms of the form factors $V,\ A_1,\ A_2$ and A.

The form factors cannot be predicted by theory directly, but the development of a Heavy Quark Effective Theory (HQET) [35] has allowed predictions which match data well. In this effective theory, the approximation that $m_Q \to \infty$ corresponds to the limit where the quark is heavy enough for the non-perturbative physics of the light quarks to be independent of the heavy quark's mass and spin. Therefore the heavy quarks can be treated in isolation from the light quarks. This general formalism was developed by Isgur and Wise [36]. Its most important feature is to reduce all of the form factors in this limit to a single universal form factor $\xi(w)$, known as the Isgur-Wise function, where $w = v \cdot v'$ and v and v' are the four-velocities of the initial and final state heavy mesons: $p = m_{\mathrm{B}} v$ and $p' = m_{\mathrm{D}} v'$. The momentum transfer, Q^2 and w are related via $Q^2 = (p - p')^2 = M_{\mathrm{B}}^2 + M_{\mathrm{D}}^2 - 2M_{\mathrm{B}}M_{\mathrm{D}}w$. The HQET relations between each form factor and $\xi(w)$ are:

$$f_\pm(Q^2) = \frac{(M_{\mathrm{D}} \pm M_{\mathrm{B}})}{2\sqrt{M_{\mathrm{D}} M_{\mathrm{B}}}}\xi(w) \tag{1.18}$$

$$V(Q^2) = \frac{(M_{\mathrm{D}^\star} + M_{\mathrm{B}})}{2\sqrt{M_{\mathrm{D}^\star} M_{\mathrm{B}}}}\xi(w) = A_2(Q^2) \tag{1.19}$$

$$A(Q^2) = \frac{Q^2}{M_{\mathrm{B}}\sqrt{M_{\mathrm{D}^\star} M_{\mathrm{B}}}}\xi(w) \tag{1.20}$$

$$A_1(Q^2) = \frac{[(M_{\mathrm{B}} + M_{\mathrm{D}^\star})^2 - Q^2]}{2(M_{\mathrm{B}} + M_{\mathrm{D}^\star})\sqrt{M_{\mathrm{D}^\star} M_{\mathrm{B}}}}\xi(w) \tag{1.21}$$

Thus, in HQET the differential semileptonic decay rate for $B \to \ell\nu D$ is

$$\frac{d\Gamma}{dw} = \frac{G_F^2}{48\pi^3} M_D^3 (M_B + M_D)^2 \left(w^2 - 1\right)^{3/2} |V_{cb}|^2 |\xi(w)|^2 \tag{1.22}$$

An important property of $\xi(w)$ is that in the zero-recoil limit ($w = 1$), where the D meson is produced at rest in the B rest frame, $\xi(1) = 1$ [45]. There is a similar expression for $B \to \ell\nu D^\star$ in terms of $\xi(w)$. Higher order corrections in the HQET are available [44].

The authors of [37] provide a model for calculating form factors using quark wave-functions for the mesons. This "ISGW" method is applicable to semileptonic decays and enables the calculation of branching ratios such as those used in this analysis for $B_s^0 \to \ell^+ \nu_\ell D_s^-$, $B_s^0 \to \ell^+ \nu_\ell D_s^{-\star}$ and $B_s^0 \to \ell^+ \nu_\ell D_s^{-\star\star}$ where $D_s^{-\star\star}$ stands for the four P-wave mesons. In practice, the ISGW functions are used for semileptonic B and D decays in Monte Carlo decay packages which will be discussed in chapter 4. In the channel of interest in this analysis, $B_s^0 \to \ell^+ \nu_\ell D_s^-, D_s^- \to \phi\pi, \phi \to K^+K^-$ the ISGW form factors from [37] are used. The subsequent D_s^- decay is modelled by the pseudoscalar to vector pseudoscalar model and the ϕ decay is modelled by the vector to pseudoscalar pseudoscalar model. The amplitude for the decay in these models is $p.\epsilon$, where p is the four-momentum of the daughter particle and ϵ is the polarisation vector of the ϕ meson.

1.6 Mixing Formalism

The aim of this thesis is to measure the lifetime of the B_s^0 meson in the flavour specific decay $B_s^0 \to \ell^+ \nu_\ell D_s^- / \overline{B}_s^0 \to \ell^- \overline{\nu}_\ell D_s^+$. It is not theoretically straightforward to interpret the B_s^0 lifetime in terms of a single parameter. The existence of common decay modes allows particle-antiparticle transitions via second order weak interactions. The Standard Model explanation for this is shown in figure 1.12. These processes cause the B_s^0 to change into a $\overline{B}_s^0$ and vice versa. This process is known as mixing and results in two physical states which are superpositions of the B_s^0 and $\overline{B}_s^0$. Each of these two states has its own mass and lifetime. These parameters can be probed at CDF Run II. A general formalism for

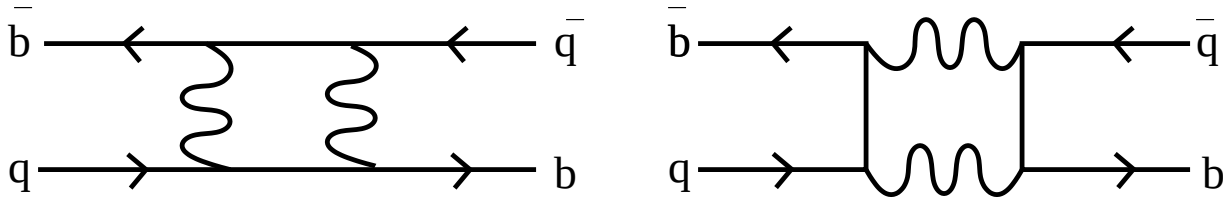

Figure 1.12: *Diagrams, known as box diagrams, which describe mixing between* B_q^0 *and* $\overline{\mathrm{B}}_q^0$.

mixing is now discussed which is applicable not only to the B_s^0 meson system but also for the $\mathrm{K}^0, \mathrm{D}^0$ and B_d^0 systems [40, 41].

Through the process of mixing, an initial B^0 evolves as a time dependent superposition of the flavour eigenstates B^0 and $\overline{\mathrm{B}}^0$. Defining $B^0(t)$ and $\overline{B}^0(t)$ as the probability amplitudes for there being a B^0 or $\overline{\mathrm{B}}^0$ at time t, the mixed state can be written as

$$|\mathrm{B}^0(t)\rangle = B^0(t)|\mathrm{B}^0\rangle + \overline{B}^0(t)|\overline{\mathrm{B}}^0\rangle \tag{1.23}$$

with the initial condition

$$|\mathrm{B}^0(0)\rangle = |\mathrm{B}^0\rangle \tag{1.24}$$

Here, all possible decay states are neglected. A similar relation holds for an initial $\overline{\mathrm{B}}^0$ state.

Invoking the Wigner-Weisskopf approximation [38], the time dependences of the probability amplitudes are governed by the Schrödinger equation:

$$i\hbar\frac{d}{dt}\begin{pmatrix} B^0(t) \\ \overline{B}^0(t) \end{pmatrix} = \begin{pmatrix} H_{11} & H_{12} \\ H_{21} & H_{22} \end{pmatrix}\begin{pmatrix} B^0(t) \\ \overline{B}^0(t) \end{pmatrix} \tag{1.25}$$

The Wigner-Weisskopf approximation assumes that only $B^0(t)$ and $\overline{B}^0(t)$ are to be calculated, neglects amplitudes for other possible decay states, assumes that they are non-zero at t=0 and that times shorter than the strong interaction time scale are neglected. In the expression, $H_{OI} = \langle \mathrm{O}|\hat{\mathrm{H}}|\mathrm{I}\rangle$ is the matrix element of the Hamiltonian for a transition from

$|I\rangle$ to $|O\rangle$ with 1 representing a B^0 flavour meson and 2 representing a $\overline{\mathrm{B}}^0$ flavour meson. Since other possible transition states are neglected, the matrix H is non-Hermitian ($H \neq H^\dagger$). The CPT invariance of the Hamiltonian gives the equality $H_{11} = H_{22}$. Furthermore, if the Hamiltonian is also CP invariant, then $H_{12} = H_{21}$. The CP transformation interchanges the states $|\mathrm{B}^0\rangle$ and $|\overline{\mathrm{B}}^0\rangle$, modulo a phase:

$$CP|\mathrm{B}^0\rangle = e^{+i\xi}|\overline{\mathrm{B}}^0\rangle \qquad CP|\overline{\mathrm{B}}^0\rangle = e^{-i\xi}|\mathrm{B}^0\rangle \tag{1.26}$$

The transition $\overline{\mathrm{B}}^0 \to \mathrm{B}^0$ is described by the matrix element $H_{12} = \langle \mathrm{B}^0|\hat{\mathrm{H}}|\overline{\mathrm{B}}^0\rangle$. If the Hamiltonian is invariant under a CP transformation, $(CP)\hat{\mathrm{H}}(CP)^\dagger = \hat{\mathrm{H}}$, then

$$\begin{aligned} H_{12} &= \langle \mathrm{B}^0|(CP)^\dagger(CP)\hat{\mathrm{H}}(CP)^\dagger(CP)|\overline{\mathrm{B}}^0\rangle & (1.27)\\ &= e^{-2i\xi}H_{21} & (1.28)\\ \Longrightarrow\ |H_{12}| &= |H_{21}| & (1.29) \end{aligned}$$

In the Standard Model, the Hamiltonian is in general the sum of strong, electromagnetic and weak interactions:

$$\hat{\mathrm{H}} = \hat{\mathrm{H}}_{\mathrm{ST}} + \hat{\mathrm{H}}_{\mathrm{EM}} + \hat{\mathrm{H}}_{\mathrm{WK}}$$

Since the strong and electromagnetic forces cannot give rise to flavour changing interactions, they may be neglected for the discussion of mixing and $\hat{\mathrm{H}}$ will stand for the weak interaction only. In the Standard Model, the weak interaction is not CP conserving, but the level of CP violation is small [39].

The matrix H may be diagonalised, yielding complex eigenvalues of $\lambda_\pm = H_{11} \pm \sqrt{H_{12}H_{21}}$. The normalised eigenvectors are then

$$|\mathrm{B}_\pm\rangle = \frac{1}{\sqrt{|p|^2 + |q|^2}} \begin{pmatrix} p \\ \pm q \end{pmatrix} \tag{1.30}$$

with time dependences:

$$e^{-\left(H_{11} \pm \sqrt{H_{12}H_{21}}\right)\frac{it}{\hbar}} \tag{1.31}$$

respectively. The values of p and q may not be determined separately but their ratio is determined up to a sign:

$$\frac{p}{q} = \sqrt{\frac{H_{12}}{H_{21}}} \tag{1.32}$$

Furthermore, if CP is conserved then

$$\frac{p}{q} = e^{-i\xi} = 1 \tag{1.33}$$

The states B_+ and B_- are the physical, propagating states. A common alternative to this +/- notation is "heavy" and "light". By convention, and to lend some physical meaning to these expressions, it is usual to make the following definitions:

$$H_{11} \pm \sqrt{H_{12}H_{21}} \equiv M_\pm - i\frac{\Gamma_\pm}{2} \tag{1.34}$$

Using this convention, the time dependence of a state evolving via $\hat{H}$ is $|\psi(t)\rangle = e^{-i\frac{M}{\hbar}t - \frac{\Gamma}{2\hbar}t}$ $|\psi(0)\rangle$. This gives the physical interpretation of M, which equals E in the rest frame, as the mass of the state. The normalisation of the state is $\left||\psi\rangle\right|^2 \sim e^{-\Gamma t/\hbar}$ giving the physical interpretation of Γ as the width of the state, equivalent to its lifetime via $\Gamma = \hbar/\tau$. It is useful to introduce the mass and width differences, together with the average width of the physical eigenstates:

$$\Delta\mathrm{m} \equiv M_+ - M_- \tag{1.35}$$

$$\Delta\Gamma \equiv \Gamma_+ - \Gamma_- \tag{1.36}$$

$$\Gamma \equiv \frac{\Gamma_+ + \Gamma_-}{2} \tag{1.37}$$

These quantities are fundamental parameters which describe the time evolution of the B_s^0 system and techniques for accessing these will be discussed a little later.

At CDF the B mesons are produced via strong interactions which are flavour conserving. Therefore at production, $t = 0$, a B meson is either pure B^0 or $\overline{B}^0$. These flavour eigenstates can be expressed as linear combinations of the propagating states $|B_\pm\rangle$ whose time dependences are known. For example, a state of pure B^0 at time 0 may be

decomposed as:

$$|\mathrm{B}^0(0)\rangle = \begin{pmatrix} 1 \\ 0 \end{pmatrix} = \frac{\sqrt{|\mathrm{p}|^2+|\mathrm{q}|^2}}{2\mathrm{p}}\Big(|\mathrm{B}_+\rangle + |\mathrm{B}_-\rangle\Big) \tag{1.38}$$

A similar expression holds for $\overline{\mathrm{B}}^0$. Inserting the time dependences of $|\mathrm{B}_\pm\rangle$ and inverting the change of basis states the result is:

$$|\mathrm{B}^0(t)\rangle = f_+(t)|\mathrm{B}^0\rangle + \frac{q}{p}f_-(t)|\overline{\mathrm{B}}^0\rangle \tag{1.39}$$

$$|\overline{\mathrm{B}}^0(t)\rangle = \frac{p}{q}f_-(t)|\mathrm{B}^0\rangle + f_+(t)|\overline{\mathrm{B}}^0\rangle \tag{1.40}$$

where

$$f_\pm(t) = \frac{1}{2}\left(e^{-i(M_+ - i\Gamma_+/2)t} \pm e^{-i(M_- - i\Gamma_-/2)t}\right) \tag{1.41}$$

In this equation and from now on, natural units are used; $\hbar = 1 = c$. In a semileptonic decay of a B^0 meson $\mathrm{B}^0 \to \ell^+\nu_\ell X$, the charge of the lepton indicates the flavour of the B^0 meson at the time of decay: ℓ^+ indicates a B^0 meson, ℓ^- indicates a $\overline{\mathrm{B}}^0$ meson. Using such a flavour specific decay and the time evolution given in equations 1.39 and 1.40, it is possible to calculate, for a given initial flavour, the probability for a B^0 or $\overline{\mathrm{B}}^0$ final state:

$$\mathcal{P}\left(\mathrm{B}^0(t) = \mathrm{B}^0\right) = \left|\langle \mathrm{B}^0|\mathrm{B}^0(t)\rangle\right|^2 = |f_+(t)|^2 \tag{1.42}$$

Similar relations hold for all of the permutations of initial and final states with

$$\begin{aligned} \left|\langle \mathrm{B}^0|\mathrm{B}^0(t)\rangle\right|^2 &= \frac{e^{-\Gamma t}}{2}\left[\cosh\left(\frac{\Delta\Gamma}{2}t\right) + \cos(\Delta m t)\right] = \left|\langle \overline{\mathrm{B}}^0|\overline{\mathrm{B}}^0(t)\rangle\right|^2 \\ \left|\frac{p}{q}\right|^2\left|\langle \overline{\mathrm{B}}^0|\mathrm{B}^0(t)\rangle\right|^2 &= \frac{e^{-\Gamma t}}{2}\left[\cosh\left(\frac{\Delta\Gamma}{2}t\right) - \cos(\Delta m t)\right] = \left|\frac{q}{p}\right|^2\left|\langle \mathrm{B}^0|\overline{\mathrm{B}}^0(t)\rangle\right|^2 \end{aligned} \tag{1.43}$$

In the first expression, the equality $\langle \mathrm{B}^0|\mathrm{B}^0(t)\rangle = \langle \overline{\mathrm{B}}^0|\overline{\mathrm{B}}^0(t)\rangle$ is expected due to CPT invariance. In the second expression, the amount of indirect CP violation in the mixing determines the difference in the rates $\mathrm{B} \to \overline{\mathrm{B}}$ and $\overline{\mathrm{B}} \to \mathrm{B}$. If there is indirect CP violation, then $|p/q| \neq 1$.

The principle of flavour conservation requires that in the strong interactions which give rise to production of B mesons, an equal number of B and $\overline{\mathrm{B}}$ mesons are produced.

In the analysis presented in this thesis, techniques have not been used to tag the flavour of the initial state, and therefore the sample of B_s^0 mesons contains an equal mixture of B_s^0 and $\overline{B}_s^0$ at production. The lifetime distributions of the flavour specific decays are given by:

$$\sum_{I=B,\overline{B}} \left|\langle l^+\nu_\ell D_s^- | I(t)\rangle\right|^2 = \frac{e^{-\Gamma/t}}{2}\left[\left(1+\left|\frac{p}{q}\right|^2\right)\cosh\left(\frac{\Delta\Gamma}{2}t\right)+\left(1-\left|\frac{p}{q}\right|^2\right)\cos(\Delta m t)\right] \times \left|\langle l^+\nu_\ell D_s^- | B_s^0\rangle\right|^2 \quad (1.44)$$

$$\sum_{I=B,\overline{B}} \left|\langle l^-\nu_\ell D_s^+ | I(t)\rangle\right|^2 = \frac{e^{-\Gamma/t}}{2}\left[\left(1+\left|\frac{q}{p}\right|^2\right)\cosh\left(\frac{\Delta\Gamma}{2}t\right)+\left(1-\left|\frac{q}{p}\right|^2\right)\cos(\Delta m t)\right] \times \left|\langle l^-\nu_\ell D_s^+ | \overline{B}_s^0\rangle\right|^2 \quad (1.45)$$

CP conservation implies that $|p/q| = 1$ which is expected to be a good approximation for the B_s^0 system in the Standard Model [39]. Under this assumption, these expressions simplify to

$$\overset{|p/q|=1}{\approx} e^{-\Gamma t}\cosh\left(\frac{\Delta\Gamma}{2}t\right) = \frac{1}{2}\left(e^{-\Gamma_+ t}+e^{-\Gamma_- t}\right) \quad (1.46)$$

Furthermore, for the B_s^0 sytem, $\Delta\Gamma$ is expected to be relatively small in the Standard Model. This means that the expression for the lifetime in the semileptonic channel simplifies further to $e^{-\Gamma t}$. This is implemented in the lifetime fitter for this analysis, as described in chapter 5. It should be noted that the terms in the sum of the exponentials in equation 1.46 are weighted by their widths, Γ_+ and Γ_-.

Studying the lifetime distribution of B^0 mesons leads to measurements of Γ and $\Delta\Gamma$. The difference in masses of the two physical states, Δm, controls the rate of mixing between the states, as indicated in equation 1.43. In order to evaluate Δm experimentally, asymmetries in the rate of mixing are studied. One such asymmetry is the time-dependent difference between the number of unmixed B^0s decaying as B^0s and the number which

mix and decay as $\overline{\mathrm{B}}^0$s:

$$A(t) = \frac{N\Big(\mathrm{B}^0 \to \mathrm{B}^0(t)\Big) - N\Big(\mathrm{B}^0 \to \overline{\mathrm{B}}^0(t)\Big)}{N\Big(\mathrm{B}^0 \to \mathrm{B}^0(t)\Big) + N\Big(\mathrm{B}^0 \to \overline{\mathrm{B}}^0(t)\Big)} \tag{1.47}$$

$$= \frac{\cos(\Delta m t) + R\cosh\left(\frac{\Delta\Gamma}{2}t\right)}{\cosh\left(\frac{\Delta\Gamma}{2}t\right) + R\cos(\Delta m t)} \tag{1.48}$$

where

$$R = \frac{\left(|p/q|^2 - 1\right)}{\left(|p/q|^2 + 1\right)} \overset{|p/q|=1}{\approx} 0$$

Assuming CP conservation in the mixing and further assuming that $\Delta\Gamma$ is small, the asymmetry simplifies to

$$A(t) = \frac{\cos\Delta m t}{\cosh\left(\frac{\Delta\Gamma}{2}t\right)} \approx \cos\Delta m t \tag{1.49}$$

In this way, measuring A(t) should give a cosine form with frequency Δm [42].

The calculation of the mixing parameters $\Delta\Gamma$ and Δm is discussed in section 1.7.1.

1.7 Mixing in the Standard Model

As indicated earlier, the Standard Model describes the weak and electromagnetic interactions of fermions (quarks and leptons) via the exchange of gauge bosons. The theory is based on the symmetry group, $SU(2)_L \otimes U(1)_Y$. In the pure form of the theory, the gauge symmetry forbids gauge boson mass terms and the chiral asymmetry forbids fermion mass terms. This is because fermion mass terms in the Lagrangian have the structure $m(\overline{\Psi}_L\psi_R + \overline{\psi}_R\Psi_L)$ and left handed fields transform as members of a doublet whereas right handed fields transform as singlets and so this term is not gauge invariant.

Experiments have determined that the $\mathrm{W}^\pm$ and Z^0 gauge bosons are both massive, as are the charged leptons and quarks. To accommodate this, a Higgs field is introduced and the mechanism of spontaneous symmetry breaking is invoked. This breaks the original $SU(2)_L \otimes U(1)_Y$ symmetry giving masses to the $\mathrm{W}^\pm$ and Z^0 bosons and leaves a residual $U(1)_{EM}$ symmetry. The introduction of the doublet Higgs field also allows the possibility

of Yukawa interactions, of the form $\overline{\Psi}_L \Phi \psi_R$, in which left and right chirality fermions couple to the Higgs field. After spontaneous symmetry breaking, this gives rise to fermion mass terms and Higgs-fermion couplings.

In the quark sector, the situation is complicated since the flavour, or interaction, eigenstates are not the same as the physical, or mass, eigenstates and the matrix which describes the transformation between these two bases is not in general diagonal. This means that, for example, as well as mass terms of the form $\bar{\mathrm{u}}\mathrm{u}$ and $\bar{\mathrm{c}}\mathrm{c}$ there are also terms of the form $\bar{\mathrm{u}}\mathrm{c}$. In contrast, the interaction of the charged W with quarks is simple: the W couples to a pair of u and d quarks, or pair of c and s quarks, but not, for example, to a pair of u and s quarks. In terms of these interaction basis quark states the Lagrangian for the couplings of the W to quarks and the quark mass terms takes the form:

$$-\mathcal{L} = \frac{g}{\sqrt{2}} \delta_{ij} \overline{u}^I_{Li} \not{W}^+ d^I_{Lj} + \frac{v}{\sqrt{2}} Y^u_{ij} \overline{u}^I_{Li} u^I_{Rj} + \frac{v}{\sqrt{2}} Y^d_{ij} \overline{d}^I_{Li} d^I_{Rj} + h.c. \tag{1.50}$$

Here the indices i and j label the quark generations, g is the gauge coupling of the $SU(2)_L$ interaction and v is the vacuum expectation value of the Higgs field. The label I denotes the interaction basis quark states. To obtain physical quark states, it is necessary to diagonalise the Yukawa matrices, Y^u and Y^d. This is achieved by unitary rotations of the up and down type quark fields of left and right chirality, such as $u^I_{Li} = L^u_{ij} u_{Lj}$. The Lagrangian for the couplings of the W to quarks and quark mass terms then becomes

$$-\mathcal{L} = \frac{g}{\sqrt{2}} \overline{u}_{Li} \left(L^{u\dagger} L^d \right)_{ij} \not{W}^+ d_{Lj} - M^u_{ij} \overline{u}_{Li} u_{Rj} + M^d_{ij} \overline{d}_{Li} d_{Rj} + h.c. \tag{1.51}$$

where, in terms of the physical quark fields, the mass matrices are now diagonal: $M^d = \mathrm{diag}(m_{\mathrm{d}}, m_{\mathrm{s}}, ...)$ and $M^u = \mathrm{diag}(m_{\mathrm{u}}, m_{\mathrm{c}}, ...)$. As a consequence of this diagonalisation, the W interactions are less straightforward (all other fermion interactions are unaffected by the change of basis)

$$-\frac{g}{\sqrt{2}} \left(V_{ij} \overline{u}_{Li} \not{W}^+ d_{Lj} + V^\star_{ij} \overline{d}_{Lj} \not{W}^- u_{Li} \right) \tag{1.52}$$

Here the combination $V = L^{u\dagger} L^d$ is known as the Cabibbo-Kobayashi-Maskawa (CKM) matrix which describes the mixing between quark flavours. For three quark generations

it is written as

$$V_{CKM} = \begin{pmatrix} V_{\rm ud} & V_{\rm us} & V_{\rm ub} \\ V_{\rm cd} & V_{\rm cs} & V_{\rm cb} \\ V_{\rm td} & V_{\rm ts} & V_{\rm tb} \end{pmatrix} \tag{1.53}$$

It can be seen quickly that the CKM matrix is unitary since $V^\dagger V = L^{d\dagger} L^u L^{u\dagger} L^d = \mathbb{1} = V V^\dagger$. A general $N \times N$ complex matrix has $2N^2$ free parameters. The unitarity condition imposes N^2 conditions. To parameterise a real $N \times N$ orthogonal matrix requires $N(N-1)/2$ Euler angles. This leaves $N(N+1)/2$ additional phases in a unitary matrix. Furthermore, in the diagonalisation of the Yukawa matrices, described above, there is a freedom to rephase the up and down type quark fields, retaining the same results for the quark masses, but altering the CKM matrix by

$$V_{\rm ud} \to e^{i(\phi_{\rm d} - \phi_{\rm u})} V_{\rm ud} \quad etc. \tag{1.54}$$

Allowing for these $2N-1$ relative phases leaves $(N-1)(N-2)/2$ physical phases. Kobayashi and Maskawa used this result to demonstrate that, while for one or two generations there are no physical phases, for three (or more) generations there is a remaining phase in the quark mixing matrix. Experiments have given evidence for three generations of quarks, while the LEP experiments showed that there are only three generations of light neutrinos [43]. The remaining phase in the CKM matrix is the source of CP violation in the Standard Model. This can be seen by taking the CP conjugate of the terms in equation 1.52 which gives

$$-\frac{g}{\sqrt{2}} \left(V_{ij} \overline{d}_{Lj} \not{W}^- u_{Li} + V_{ij}^\star \overline{u}_{Li} \not{W}^+ d_{Lj} \right) \tag{1.55}$$

This equation is the same as 1.52 with the terms swapped, provided that $V_{ij} = V_{ij}^\star$. Since there may be a phase somewhere in the CKM matrix, this may not be the case and so the CP symmetry would be violated.

There is one remaining choice in the CKM matrix, which is to specify a permutation of the quark fields. The conventional choice is to order, separately, the up and down type quarks by their mass: {u, c, t} and {d, s, b}. This gives the pairs of quarks in

the generations: {u, d}, {c, s} and {t, b}. With this choice, the CKM matrix shown in equation 1.53 is almost diagonal with small inter-generational transitions.

The CKM matrix is usually parameterised in such a way as to incorporate the constraints of its unitarity. The Particle Data Group adopt the exact parameterisation of Chau and Keung which uses three Euler angles and a phase:

$$V_{CKM} = \begin{pmatrix} 1 & 0 & 0 \\ 0 & c_{23} & s_{23} \\ 0 & -s_{23} & c_{23} \end{pmatrix} \begin{pmatrix} c_{13} & 0 & s_{13}e^{-i\delta_{13}} \\ 0 & 1 & 0 \\ -s_{13}e^{i\delta_{13}} & 0 & c_{13} \end{pmatrix} \begin{pmatrix} c_{12} & s_{12} & 0 \\ -s_{12} & c_{12} & 0 \\ 0 & 0 & 1 \end{pmatrix} \quad (1.56)$$

$$= \begin{pmatrix} c_{12}c_{13} & s_{12}c_{13} & s_{13}e^{-i\delta_{13}} \\ -s_{12}c_{23} - c_{12}s_{23}s_{13}e^{i\delta_{13}} & c_{12}c_{23} - s_{12}s_{23}s_{13}e^{i\delta_{13}} & s_{23}c_{13} \\ s_{12}s_{23} - c_{12}c_{23}s_{13}e^{i\delta_{13}} & -c_{12}s_{23} - s_{12}c_{23}s_{13}e^{i\delta_{13}} & c_{23}c_{13} \end{pmatrix} \quad (1.57)$$

Here $c_{ij} = \cos\theta_{ij}$ and $s_{ij} = \sin\theta_{ij}$ where θ_{12}(=Cabibbo angle), θ_{13} and θ_{23} are the Euler angles, which lie in the range [0,$\pi/2$], and δ_{13}, in the range [0,2π], is the phase which gives rise to CP violation. The experimental observation that this matrix is almost diagonal implies that the angles θ_{ij} are all small. The angles can be extracted from the off-diagonal matrix elements using

$$s_{12} \approx |V_{\rm us}| = \mathcal{O}(10^{-1}) \quad (1.58)$$

$$s_{23} \approx |V_{\rm cb}| = \mathcal{O}(10^{-2}) \quad (1.59)$$

$$s_{13} = |V_{\rm ub}| = \mathcal{O}(10^{-3}) \quad (1.60)$$

The phase, δ_{13}, can be extracted from CP violating processes which involve three generations such as loop diagrams like that shown in figure 1.12. The Standard Model CP violation can be seen to be small in this formulation since the CP phase always appears in the combination $s_{13}e^{-i\delta_{13}}$ and s_{13} is known to be small.

Another useful parameterisation is that of Wolfenstein, which highlights the hierarchy

of the CKM matrix elements. Introducing the parameters,

$$s_{12} = \lambda \tag{1.61}$$

$$s_{23} = A\lambda^2 \tag{1.62}$$

$$s_{13}e^{-i\delta} = A\lambda^3(\rho - i\eta) \tag{1.63}$$

the CKM matrix is then expanded in terms of powers of λ^2 leading to

$$V_{CKM} = \begin{pmatrix} 1-\lambda^2/2 & \lambda & A\lambda^3(\rho - i\eta) \\ -\lambda & 1-\lambda^2/2 & A\lambda^2 \\ A\lambda^3(1-\rho-i\eta) & -A\lambda^2 & 1 \end{pmatrix} + \mathcal{O}(\lambda^4) \tag{1.64}$$

1.7.1 Calculations of Mixing Parameters

The time evolution in the B_s^0 system is controlled by Γ, Δm and $\Delta\Gamma$.

The lifetime of the B_s^0 meson is calculated using the Operator Product Expansion, which is an expansion in powers of $1/m_b$. The decay rate is given by [47]

$$\Gamma = \frac{m_Q^5 G_F^2}{64\pi^3}\left[c^{(0)}\langle Q\overline{Q}\rangle + \frac{1}{m_Q^2}c^{(2)}\langle \overline{Q}\sigma^{\mu\nu}G_{\mu\nu}Q\rangle + \frac{1}{m_Q^3}16\pi^2\sum_i c^{(3)}\left(\overline{q}_i\Gamma_i q_i\right)\langle \overline{Q}\Gamma_i' Q\rangle\right] \tag{1.65}$$

The coefficients $c^{(n)}$ are calculable perturbatively. There is no $1/m_Q$ correction. The first of these terms is the spectator model approximation [48]. In this model the weak decay of the b quark into a c (or u) quark is considered in isolation from the spectator quark which, in the case of the B_s^0 meson is a strange quark. Thus, the spectator model prediction is for all b hadrons to have equal lifetimes. The exception is the B_c^- meson in which the charm quark can also decay and so the B_c^- is expected to decay faster. The second term in the effective Lagrangian is also independent of the spectator quark and takes account of the gluons in the meson. The third term takes into account the effects of the spectator quark. The factor of $16\pi^2$ arises from phase space and means that the contribution from spectator effects is not negligible.

Due to uncertainties in the dynamics of quarks inside hadrons, it is usual for predictions to be given as ratios of lifetimes rather than absolute values, following the hierarchy noted in 1.2. The ratio of $\Gamma(B_d^0)/\Gamma(B_s^0) = 1.00 \pm 0.01$.

In the Standard Model Δm and $\Delta\Gamma$ can be calculated using the box diagrams shown in figure 1.12. Rather than calculating the transition matrix directly it is usual to divide it into two Hermitian matrices

$$H = M - \frac{i}{2}\Gamma \tag{1.66}$$

The absorptive part, M, is given by virtual intermediate states in the loop and the dispersive part, Γ, by real intermediate states in the loop. The difference in mass and lifetime between the two eigenstates of the matrix, Δm and $\Delta\Gamma$ are given by

$$\{\Delta m, \Delta\Gamma\} = \{2\mathcal{R}e, -4\mathcal{I}m\}\left[\sqrt{H_{12}H_{21}}\right] \tag{1.67}$$

$$= \{2\mathcal{R}e, -4\mathcal{I}m\}\left[\sqrt{(M_{12} - \frac{i}{2}\Gamma_{12})(M_{12}^{\star} - \frac{i}{2}\Gamma_{12}^{\star})}\right] \tag{1.68}$$

In the box diagram, the two internal quark legs are any of the up type quarks, thus giving nine contributions. The loop amplitude is proportional to the heaviest quark mass, m_{q}, and to $V_{\mathrm{qb}}^{\star}V_{\mathrm{qs}}V_{\mathrm{q'b}}^{\star}V_{\mathrm{q's}}$. The top quark therefore dominates the absorptive part of the loop since $m_{\mathrm{t}} \gg m_{\mathrm{c}}, m_{\mathrm{u}}$. Thus [50],

$$M_{12} \propto m_{\mathrm{t}}^2 |V_{\mathrm{tb}}^{\star}V_{\mathrm{ts}}|^2 \tag{1.69}$$

However, the top quark cannot contribute to the dispersive amplitude since $m_{\mathrm{t}} \gg M_{\mathrm{B}}$ and so only charm and up quarks contribute. Of these, the charm quark dominates since $|V_{\mathrm{cb}}| \gg |V_{\mathrm{ub}}|$. Thus [50],

$$\Gamma_{12} \propto m_{\mathrm{c}}^2 |V_{\mathrm{cb}}^{\star}V_{\mathrm{cs}}|^2 \tag{1.70}$$

and as a consequence $|\Gamma_{12}| \ll |M_{12}|$. Therefore equations 1.68 simplify leading to

$$\Delta m = 2|M_{12}| \qquad \Delta\Gamma = 2|\Gamma_{12}|\cos\phi, \quad \phi = \mathrm{Arg}\left(\frac{\Gamma_{12}}{M_{12}}\right) \tag{1.71}$$

CP conservation in mixing, which is a good approximation in the $\mathrm{B_s^0}$ system, is equivalent to $\phi = 0$. Contributions to the loop from new physics would be unlikely to affect Γ_{12} since they would have to give real intermediate states. Instead, new physics could affect the relative phase, ϕ. As a consequence, new physics can only reduce $\Delta\Gamma$.

The dispersive part of the effective Hamiltonian for $b\bar{s} \leftrightarrow \bar{b}s$ transitions is

$$\hat{\mathrm{H}}_{eff} = \frac{G_{\mathrm{F}}^2}{\pi^2}|V_{\mathrm{tb}}^* V_{\mathrm{ts}}|^2 m_{\mathrm{t}}^2 S\left(\frac{m_{\mathrm{t}}^2}{M_{\mathrm{W}}^2}\right)\hat{\mathcal{O}}_0 \tag{1.72}$$

where $\hat{\mathcal{O}}_0$ is the four-quark operator

$$\hat{\mathcal{O}}_0 = (\overline{s}_L\gamma_\mu b_L)(\overline{s}_L\gamma^\mu b_L)$$

The function S arises from the integration over the W and top quark loop.

$$S(x) = \frac{1}{4} + \frac{9}{4(1-x)} - \frac{3}{2(1-x)^2} - \frac{3x^2\ln x}{2(1-x)^3} \tag{1.73}$$

The difference in mass between the two physical eigenstates, Δm, is given by the matrix element for the effective Hamiltonian between $\mathrm{B_s^0}$ and $\overline{\mathrm{B}}_{\mathrm{s}}^0$:

$$\Delta m = \frac{1}{2m_{\mathrm{B_s^0}}}\langle \mathrm{B_s^0}|\hat{\mathrm{H}}_{eff}|\overline{\mathrm{B}}_{\mathrm{s}}^0\rangle \tag{1.74}$$

$$= \frac{G_{\mathrm{F}}^2}{6\pi^2}|V_{\mathrm{tb}}^* V_{\mathrm{ts}}|^2 M_{\mathrm{W}}^2 S\left(\frac{m_{\mathrm{t}}^2}{M_{\mathrm{W}}^2}\right)\eta_{QCD}(\mu) f_{\mathrm{B_s^0}}^2 B(\mu) M_{\mathrm{B_s^0}} \tag{1.75}$$

where the last line follows from the parameterisation

$$\langle \mathrm{B_s^0}|\hat{\mathcal{O}}_0|\overline{\mathrm{B}}_{\mathrm{s}}^0\rangle = \frac{2}{3} f_{\mathrm{B_s^0}}^2 M_{\mathrm{B_s^0}}^2 B(\mu) \tag{1.76}$$

and η_{QCD} represents the short distance contribution of QCD corrections from perturbation theory. The normalisation of this equation is such that the bag parameter, $B(\mu)$, is of order unity. $B(\mu)$ and the decay constant, $f_{\mathrm{B_s^0}}$ represent the long distance contributions to the corrections and are presently calculated using lattice QCD techniques at scales where $\mu \approx M_{\mathrm{B_s^0}}$ and HQET may be used.

A similar expression can be derived for the difference in widths:

$$\Delta\Gamma = -\frac{G_{\mathrm{F}}^2 m_{\mathrm{b}}^2}{12\pi}|V_{\mathrm{cb}}V_{\mathrm{cs}}^\star|^2 f_{\mathrm{B_s^0}}^2 M_{\mathrm{B_s^0}}\left[\frac{2}{3}\mathcal{F}\left(\frac{m_{\mathrm{c}}^2}{m_{\mathrm{b}}^2}\right)B(\mu) - \frac{5}{12}\frac{M_{\mathrm{B_s^0}}}{(m_{\mathrm{b}}+m_{\mathrm{s}})^2}\mathcal{F}_S\left(\frac{m_{\mathrm{c}}^2}{m_{\mathrm{b}}^2}\right)B_S(\mu)\right] \tag{1.77}$$

Here $\mathcal{F}$ and $\mathcal{F}_S$ are known functions and $B_s = \mathcal{O}(1)$ is a second bag parameter:

$$\langle \mathrm{B_s^0}|\hat{\mathcal{O}}_S|\overline{\mathrm{B}}_{\mathrm{s}}^0\rangle = -\frac{5}{12} f_{\mathrm{B_s^0}}^2 M_{\mathrm{B_s^0}}^2 \frac{M_{\mathrm{B_s^0}}^2}{(m_{\mathrm{b}}+m_{\mathrm{s}})^2} B_S(\mu) \qquad \text{where} \quad \hat{\mathcal{O}}_S = (\bar{b}_L s_L)(\bar{b}_L s_L) \tag{1.78}$$

Dividing equation 1.77 by 1.75 relates $\Delta\Gamma$ to Δm and eliminates the dependence on the decay constant f_{B_S}. Using the resulting relation, an experimental determination of either quantity serves as an indirect measurement of the other. The sensitivity of $\Delta\Gamma$ to $V_{\rm cb}$ can be eliminated by normalising to the total decay width, Γ, which can be calculated in terms of the measured semileptonic brancing ratio of the $\rm B_s^0$:

$$\Gamma = \frac{\Gamma(\rm B_s^0 \to X e \nu_e)}{\rm B.R.(B_s^0 \to X e \nu_e)} = \frac{G_F^2 m_{\rm b}^5}{192\pi^3}|V_{\rm cb}|^2 \phi(z)\tilde{\eta}_{QCD}\frac{1}{B.R.(\rm B_s^0 \to X e \nu_e)} \tag{1.79}$$

where $\phi(z)$ is a phase space factor depending on $z = m_{\rm c}^2/m_{\rm b}^2$. This leads to an expression for the ratio:

$$\frac{\Delta\Gamma}{\Gamma} = -16\pi^2 \frac{M_{\rm B_s^0}^2 f_{\rm B_s^0}^2}{m_{\rm b}^3}|V_{\rm cs}|^2 \frac{B.R.(\rm B_s^0 \to X e \nu_e)}{\phi(z)\tilde{\eta}_{QCD}} \left[\frac{2}{3}\mathcal{F}(z)B + \frac{5}{12}\frac{M_{\rm B_s^0}^2}{(m_{\rm b}+m_{\rm s})^2}\mathcal{F}_S(z)B_S\right] \tag{1.80}$$

The present evaluations of the parameters are [46]

$$\begin{aligned} \eta_{QCD} &= 0.55 \\ f_{\rm B_s^0} &= 240 \pm 35 MeV \\ B &= 1.31 \pm 0.10 \end{aligned}$$

Including all known corrections, this leads to

$$\Delta m_{\rm s} = 18.8 {\rm ps}^{-1} \left(\frac{|V_{\rm ts}|}{0.04}\frac{f_{\rm B_s^0}}{240{\rm MeV}}\right)^2 \frac{B}{1.31} \tag{1.81}$$

and [50]

$$\frac{\Delta\Gamma_{\rm s}}{\Gamma_{\rm s}} = \left(\frac{f_{\rm B_s^0}}{240{\rm MeV}}\right)^2 \left[0.006\left(\frac{B}{1.31}\right) + 0.165\left(\frac{B_S}{0.8}\right) - 0.078\right] = 10.4\% \tag{1.82}$$

where the last term accounts for $1/m_{\rm b}$ corrections in the calculation of $\Delta\Gamma_{\rm s}$. The top quark mass used is that of the $\overline{\rm MS}$ scheme [49].

1.7.2 Experimental Determination of CKM Matrix Elements

All but two of the Cabibbo-Kobayashi-Maskawa matrix elements can be directly determined experimentally. The remaining two, $V_{\rm td}$ and $V_{\rm ts}$, are determined indirectly. Each

matrix element and its determination is now discussed briefly. Values quoted for CKM matrix elements are the PDG averages [1]. For details and further references for all these measurements see the PDG review on the CKM quark-mixing matrix.

$\mathbf{V_{ud}}$ is measured in nuclear beta decays. Three methods are used: super-allowed nuclear beta decays ($0^+ \to 0^+$), beta decays of polarised neutrons ($\mathrm{n} \to \mathrm{pe}^-\bar{\nu}_\mathrm{e}$) and beta decay of the charged pion ($\pi^+ \to \pi^0\mathrm{e}^+\nu_\mathrm{e}$). The present value is:

$$|V_{\mathrm{ud}}| = 0.9734 \pm 0.0008$$

$\mathbf{V_{us}}$ is measured in semi-leptonic Kaon decays, for example $\mathrm{K}^+ \to \pi^0\mathrm{e}^+\nu_\mathrm{e}$ and $\mathrm{K}^0{}_L \to \pi^-\mathrm{e}^+\nu_\mathrm{e}$; hyperon decays, for example $\Lambda \to \mathrm{pe}^-\bar{\nu}_\mathrm{e}$; and from tau decays, for example $\tau^- \to \overline{\mathrm{K}}^0\pi^-\nu_\tau$. The present value is

$$|V_{\mathrm{us}}| = 0.2196 \pm 0.0026$$

$\mathbf{V_{cd}}$ is measured in collisions of neutrinos on nuclei. This gives rise to charm production from valence d quarks which results in a distinctive final state containing dimuon pairs. This is understood to occur by the interaction $\nu_\mu + \mathrm{N} \to \mu^- + \mathrm{c} + X$ followed by $\mathrm{c} \to \mathrm{s} + \mu^+ + \mu_\nu$. The cross section for this interaction is related to V_{cd} and gives the present value of

$$|V_{\mathrm{cd}}| = 0.224 \pm 0.016$$

$\mathbf{V_{cs}}$ has for a long time been measured by the semi-leptonic decays of D mesons, $\mathrm{D}^+ \to \overline{\mathrm{K}}^0\ell^+\nu_\ell$ and $\mathrm{D}^0 \to \mathrm{K}^-\ell^+\nu_\ell$, which are limited by a theoretical uncertainty of over 10%. In recent years [51] the measurement has been much improved by direct measurements in charm-tagged W decays, $\mathrm{W}^+ \to \mathrm{c\bar{s}} \to \mathrm{DK} + X$. The average result is now

$$|V_{\mathrm{cs}}| = 0.996 \pm 0.013$$

It is interesting at this point to note that if one were living in the belief that there are only two families, the data from the four matrix elements discussed so far would do nothing

to disprove that belief. A unitarity check of the 2×2 matrix is satisfactory, the largest discrepancy from the unitarity condition being that of $|V_{ud}|^2 + |V_{us}|^2$ at 1.8σ from 1. Therefore the existence of a third family could not be inferred from this data alone.

A fit to the 2×2 matrix gives a value for the Wolfenstein parameter, λ:

$$\lambda = 0.2235 \pm 0.0033$$

V_{cb} is measured in exclusive and inclusive semileptonic B decays. Heavy Quark Effective Theory provides a nearly model independent framework for relating the width of the exclusive decay $B^+ \to D^{*0}\ell^+\nu_\ell$ to $|V_{cb}|^2$ and the width of the inclusive semileptonic decays $B \to \ell\nu_\ell X$ to a weighted sum of $|V_{cb}|^2$ and $|V_{ub}|^2$. This analysis relies on the assumption of quark-hadron duality to relate the V-A b quark decay to that of the hadron. The resulting measurement is:

$$|V_{cb}| = 0.0412 \pm 0.0020$$

This matrix element is equal to $A\lambda^2$. A is then also known, $A = 0.1876 \pm 0.0500$, since $V_{us} = \lambda^2$.

V_{ub} is extracted from inclusive, $b \to \ell^-\overline{\nu}_\ell u$, and exclusive semileptonic B decays into charmless final states, for example $B^+ \to \ell^+\nu_\ell\rho^0$ or $B^0 \to \ell^+\nu_\ell\pi^-$. In the inclusive case, the decays selected are those for which the lepton energy is higher than the endpoint of the $b \to \ell^-\overline{\nu}_\ell c$ lepton energy spectrum. The main obstacle is the background from $B \to \ell^+\nu_\ell D$ and theoretical uncertainties are large because the theory for heavy to light ($b \to u$) is not as well understood as that for heavy to heavy ($b \to c$) transitions. The current value is

$$|V_{ub}| = 0.0036 \pm 0.0007$$

For the following two matrix elements, V_{td} and V_{ts}, direct measurements are not available. These parameters are accessed by virtual one-loop effects in which it is assumed for these purposes that there are no contributions from new physics.

$\mathbf{V_{td}}$ is accessible through B^0_d mixing since $\Delta m_d \propto |V^\star_{tb} V_{td}|^2$. The constant of proportionality is a set of constants: $G_F^2 M_W^2 M_{B^0_d} f^2_{B^0_d} B \eta_{QCD}/6\pi^2$ where the largest uncertainty is that of the bag parameter coming from Lattice QCD. The world average for the rate of oscillation of B^0_d is 0.502 ± 0.007 ps^{-1}. This gives a measurement of V_{td} relative to V_{tb}:

$$|V_{td}| = \frac{(9.2 \pm 1.4 \pm 0.5) \times 10^{-3}}{|V_{tb}|} \tag{1.83}$$

$\mathbf{V_{ts}}$ could be similarly accessed through B^0_s oscillations. However, Δm_s has not yet been measured and so it can only be used to set a limit of $|V_{ts}| > 0.033/|V_{tb}|$. When Δm_s is measured, it will also provide a constraint on the ratio V_{ts}/V_{td} since (see equation 1.75)

$$\frac{\Delta m_s}{\Delta m_d} = \frac{m_s}{m_d} \frac{B_s f_s^2}{B_d f_d^2} \frac{|V_{ts}|^2}{|V_{td}|^2} \tag{1.84}$$

Alternatively, the ratio of "penguin" to "tree" contributions in B meson decays to hadrons can give access to V_{ts}. These are related by

$$\left| \frac{P_{\pi\pi}}{T_{\pi\pi}} \right| \simeq \left| \frac{V_{td}}{V_{ts}} \right| \sqrt{\frac{B.R.(B^0_d \to K^+\pi^-)}{B.R.(B^0_d \to \pi^+\pi^-)}}$$

$\mathbf{V_{tb}}$ is determined relative to V_{td} and V_{ts} by semileptonic decays of the top quark. The $t \to b\ell^+\nu_\ell$ semileptonic decays were among the decays of the top quark which gave evidence for its existence at the Tevatron in 1994 [52]. Subsequently, CDF measured the fraction of such semileptonic decays as distinct from semileptonic decays to s or d quarks. This ratio is

$$R = \frac{|V_{tb}|^2}{|V_{td}|^2 + |V_{ts}|^2 + |V_{tb}|^2} = 0.94^{+0.31}_{-0.24}$$

where it is assumed that the top quark decays to non-W final states are negligible. Furthermore, if the three generation CKM matrix is unitary then the denominator is equal to 1 and so $|V_{tb}| = 0.97^{+0.16}_{-0.12}$.

The final three elements may also be determined by assuming unitarity of the CKM matrix. Thus

$$|V_{tb}|^2 = 1 - |V_{cb}|^2 - |V_{ub}|^2 \Longrightarrow |V_{tb}| = 0.99913 \pm 0.00009 \tag{1.85}$$

This, together with equation 1.83, gives that $|V_{\rm td}| = (9.2 \pm 1.4 \pm 0.5) \times 10^{-3}$. This can be used in the following unitarity requirement to give:

$$|V_{\rm ts}|^2 = |V_{\rm cb}|^2 + |V_{\rm ub}|^2 - |V_{\rm td}|^2 \Longrightarrow |V_{\rm ts}| = 0.0406 \pm 0.0023 \tag{1.86}$$

$V_{\rm ub}$ and $V_{\rm td}$ determine $A\lambda^3\sqrt{\rho^2+\eta^2} = 0.0038 \pm 0.0004$, an error of $\pm 10\%$.

A conventional pictorial device for the CKM matrix is a triangle; in fact there are six such triangles. These come from the unitarity constraint of the CKM matrix, so that for example the following relation holds

$$V_{\rm ub}V_{\rm ud}^\star + V_{\rm cb}V_{\rm cd}^\star + V_{\rm tb}V_{\rm td}^\star = 0 \tag{1.87}$$

In the complex plane, this relation can be represented by a triangle. In this example, the triangle which has sides $V_{\rm ub}^\star V_{\rm ud}/V_{\rm cb}^\star V_{\rm cd} = (\overline{\rho} + i\overline{\eta})$, 1 and $V_{\rm tb}^\star V_{\rm td}/V_{\rm cb}^\star V_{\rm cd}$ is useful for studying the $\rm B_d^0$ system. Here, $\bar{\rho} = \rho(1 - \lambda^2/2)$ and $\bar{\eta} = \eta(1 - \lambda^2/2)$. The angles of the triangle are given by

$$\alpha = {\rm Arg}\left(-\frac{V_{\rm td}V_{\rm tb}^\star}{V_{\rm ud}V_{\rm ub}^\star}\right), \quad \beta = {\rm Arg}\left(-\frac{V_{\rm cd}V_{\rm cb}^\star}{V_{\rm td}V_{\rm tb}^\star}\right), \quad \gamma = {\rm Arg}\left(-\frac{V_{\rm ud}V_{\rm ub}^\star}{V_{\rm cd}V_{\rm cb}^\star}\right)$$

Since ρ and η are not accurately determined, it is usual to plot the experimental constraints on these Wolfenstein parameters in the $\bar{\rho} - \bar{\eta}$ plane. Figure 1.13 shows the most recent evaluation of the constraints by the Heavy Flavour Averaging group [53]. Constraints are given by measurements of the $\rm B_d^0$ and $\rm B_s^0$ mixing frequencies, the ratio $|V_{\rm ub}/V_{\rm cb}|$, the angle $\sin 2\beta$ and the measurement of indirect CP violation in the K meson system, ϵ_K, defined by $q/p = (1 - \epsilon_K)/(1 + \epsilon_K)$ (see the discussion of mixing in section 1.6). The remaining allowed region is delimited in red.

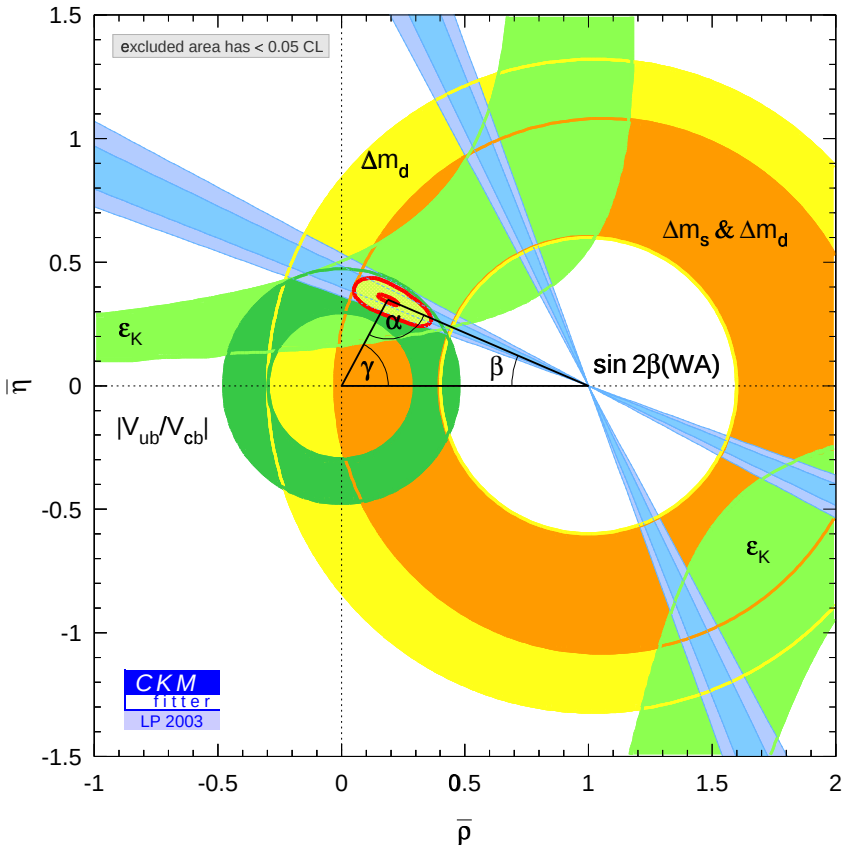

Figure 1.13: *Current experimental bounds on the unitarity triangle.*

Chapter 2

The Tevatron and CDF

The first $p\overline{p}$ collisions at the Collider Detector at Fermilab, CDF, took place in October 1985 with a centre of mass energy of 1.8TeV. Since then, the Tevatron accelerator and CDF experiment have improved their performance and taken increasingly large datasets. The first major data taking period was CDF Run I which gathered $110pb^{-1}$ between 1992 and 1996. Between 1996 and 2001 the Tevatron was shut down for upgrades of the detectors and accelerator. The CDF detector was upgraded by the replacement and addition of several detector components. It is hoped that with the increased luminosity from the upgraded Tevatron accelerator, and the improved CDF detector, CDF Run II will accumulate 2000 pb^{-1} of data by 2006.

This chapter discusses the accelerator complex at Fermilab and each of the components of the CDF detector facility.

2.1 The Accelerator Complex

The Tevatron is a proton-antiproton colliding beam accelerator at Fermilab near Chicago in the United States. It has a circumference of $2\pi(=6.28)$km and, since the upgrade, collides protons and antiprotons with a centre of mass energy of 2.0TeV. In order to attain this energy, a chain of accelerators is deployed, depicted in figure 2.1. Each component

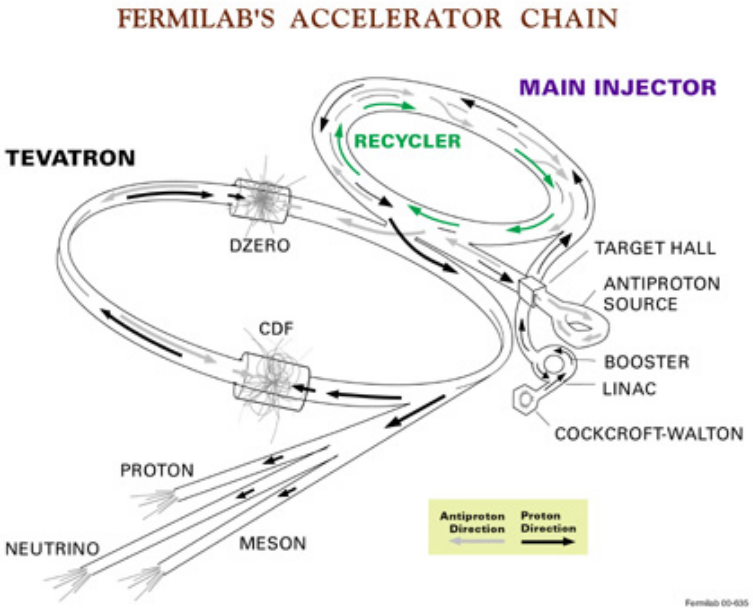

Figure 2.1: *Schematic of the Tevatron and accompanying suite of accelerators.*

in this chain of accelerators is now discussed in turn:

The Cockcroft-Walton Pre-Accelerator ionises Hydrogen gas using an electric field to strip away the electrons. The remaining protons then drift towards a Caesium surface and, due to its low work function, collect electrons to form negative ions, H^-. The H^- are accelerated across a series of voltage gaps to an energy of 750keV.

The Linac (linear accelerator) accelerates the H^- along a straight 145m long line of radio frequency cavities to 400MeV. The radio frequency cavities are made up of drift tubes separated by gaps, contained within a vacuum. While in the drift tubes, the ions are shielded from the electric field and so drift at constant velocity: while in the gaps, the H^- accelerate towards the next drift tube. The length of the drift tubes and gaps increases as the particles travel faster. In this way, the time spent in a drift tube is constant, and matched to the radio frequency. At the end of the Linac, the ions are passed through a Carbon foil, stripping them of their electrons, and in this way protons are passed onto the next stage.

The Booster is a synchrotron which accelerates the protons to an energy of 8GeV in a ring of circumference 475m. The protons are held in a circular orbit by dipole magnets. Each time the protons circulate they are accelerated by radio frequency cavities, which change frequency with the momentum of the protons. The booster also performs bunching of protons. Stable regions, known as buckets, inside the booster allow protons of the same energy to be collected. Between 6 and 8 bunches are provided to the main injector in each store. A store is the entire process from producing p and $\overline{\mathrm{p}}$ to delivering them to the experiments, CDF and D0.

The Main Injector was completed in 1999 as part of the upgrade to the Tevatron for the current phase of running, Run II [54]. It was designed to replace the Main Ring in order to achieve several goals. Firstly, the cycling rate and beam current were increased which leads directly to an increase in luminosity and energy of the Tevatron. This in turn increases physics cross-sections. Secondly, the Main Injector can fulfil several roles. It accelerates 8GeV protons to 150GeV for injection into the Tevatron. It also allows a focused beam of 120GeV protons to be extracted for use in fixed target experiments. For example, this is used to produce secondary neutrinos for the MINOS experiment [55]. In addition, the 120GeV protons also act as the first stage in the production of antiprotons in the **antiproton source**. The protons and antiprotons are then transferred in bunches to the Tevatron. As an additional upgrade, an **Antiproton Recycler** has been added to the main injector ring to recycle antiprotons remaining after a store which are recovered from the Tevatron. This provides more antiprotons to the Tevatron, thus increasing the luminosity.

The Antiproton Source comprises the debuncher and accumulator rings and the $\overline{\mathrm{p}}$ injection line. The 120GeV protons are focused onto a small Nickel target with which they collide, creating, among other secondary particles, antiprotons. Antiprotons of approximately 8GeV are selected by magnets and are then focused by a lithium lens into the antiproton injection line which passes them into a **debuncher ring**.

The purpose of the debuncher is to reduce the spread of antiproton energies through stochastic cooling. The antiprotons are then circulated in the **Accumulator ring** until there is a sufficient number and they are then sent to the main injector. The main injector then accelerates the antiprotons to 150GeV.

The Tevatron accelerates the protons and antiprotons from energies of 150GeV to 980GeV using superconducting magnets with a field strength of 4T. Since protons and antiprotons have opposite charge, they circulate in the same ring under the influence of the same magnetic fields in opposite directions. The protons and antiprotons are grouped into 36 bunches, which are formed into four trains each of nine bunches. The radio frequency of the Tevatron is 53MHz and so selecting every 21st bucket in a train means that there is a bunch crossing every 396.2ns at each of the two collision points on the Tevatron ring: one at the D0 detector and the other at the CDF detector (point B0). Run I of the Tevatron which ran from 1992 to 1996 also had a bunch crossing of $\simeq$ 396ns. The Run II Tevatron can also be run with a bunch crossing of 132.1ns and so this design requirement was included for the CDF Run II detector design. On either side of the two detectors, the beams of protons and antiprotons are focused by quadrupole magnets. This leads to beams with small transverse size and Gaussian profiles of widths σ_x and σ_y, of approximately 25μm [56]. Table 2.1 contains details of the run II Tevatron beam parameters. This means that for a detector with sufficient resolution, it is possible to trigger on displaced vertices found in events containing b hadrons. The bunch length is parameterised by the Gaussian width, $\sigma_z \simeq$ 30cm. Thus the collision region is approximately 60cm long, and this sets the scale for the CDF Run II tracking detectors, the innermost of which is 128cm long. Assuming that there is a head-on collision of two Gaussian distributions with equal parameters, the instantaneous luminosity of the Tevatron is given by

$$\mathcal{L} = \frac{N_{\mathrm{p}} N_{\bar{\mathrm{p}}}}{4\pi\sigma_x\sigma_y} \cdot f N_B \tag{2.1}$$

Here, $N_{\rm p}$ and $N_{\bar{\rm p}}$ are the number of protons and antiprotons in the bunches; σ denotes the width of the proton or antiproton bunch in direction x or y; f denotes the revolution frequency and N_B is the number of bunches circulating. The number of events occuring per second in CDF's interaction region is given by

$$\text{Number events / s} = \mathcal{L} \cdot \sigma \tag{2.2}$$

where σ is the cross-section of the process under consideration. Also of interest is the number of events which occur for every bunch crossing. If this rate is too high, it can lead to high occupancy in the detector, and so must be a consideration in design of both the accelerator and detector:

$$\begin{aligned} \text{Number events / crossing} &= \frac{\mathcal{L}}{f N_B} \cdot \sigma \\ &= \frac{\mathcal{L}}{1.72 \times 10^6} \cdot \sigma \end{aligned} \tag{2.3}$$

Centre of mass energy	1.96TeV
Proton/antiproton Bunches: N_B	36
Bunch crossing time	396ns
Beam size: σ_x	$25.7\pm 1.9\mu$m
Beam size: σ_y	$25.8\pm1.7\mu$m
Beam size: σ_z	30cm
Peak Instantaneous Luminosity: $\mathcal{L}_0$	$2 \times 10^{32}\text{cm}^{-2}\text{s}^{-1}$
Run IIa Integrated Luminosity	2fb^{-1}

Table 2.1: *Design parameters of the Tevatron collider.*

The instantaneous luminosity in fact peaks at the start of each run, when new bunches are accelerated in the Tevatron, after which there are losses due to particles

interacting in bunches and also losses to beam gas. The loss is exponential and so the luminosity has the form

$$\mathcal{L} = \mathcal{L}(t) = \mathcal{L}_0 e^{-t/t_0} \tag{2.4}$$

This progressively reduces the event rate until a new run is started; runs usually last 7-15 hours.

All of the Run II design parameters of the Tevatron are summarised in table 2.1.

As well as the detectors situated directly on the Tevatron ring, the accelerator complex serves several fixed target experiments by taking protons from the main injector. These may be used directly, or collided with targets to produce beams of secondary particles [57].

2.2 The Collider Detector Facility

The Collider Detector Facility, CDF, has the standard structure of a colliding beams experiment. It is a solenoidal detector with cylindrical symmetry and is designed to combine precision tracking inside a 1.4T magnetic field with fast projective 4π calorimetry and muon detection. The experiment has been designed with a broad physics programme in mind. A full description of the detector is given in its Technical Design Report [58] and a more brief description is given here.

The detector is shown in figure 2.2. Figure 2.3 shows a detailed cutaway view of the detector. The tracking systems are contained within the 1.4T superconducting solenoid magnet of radius 1.5m and length 4.8m and comprise silicon detectors and a drift chamber. Outside the solenoid there are electromagnetic and hadronic calorimeters and muon chambers. The signatures of typical leptons and hadrons is shown in figure 2.4.

In the coordinate system used by CDF, the polar angle, θ, is measured from the direction of the p beam. This is equivalent to the pseudorapidity defined by $\eta = -\ln(\tan(\theta/2))$. The azimuthal angle, ϕ, is measured anticlockwise from the plane of the Tevatron, about the direction of the proton beam.

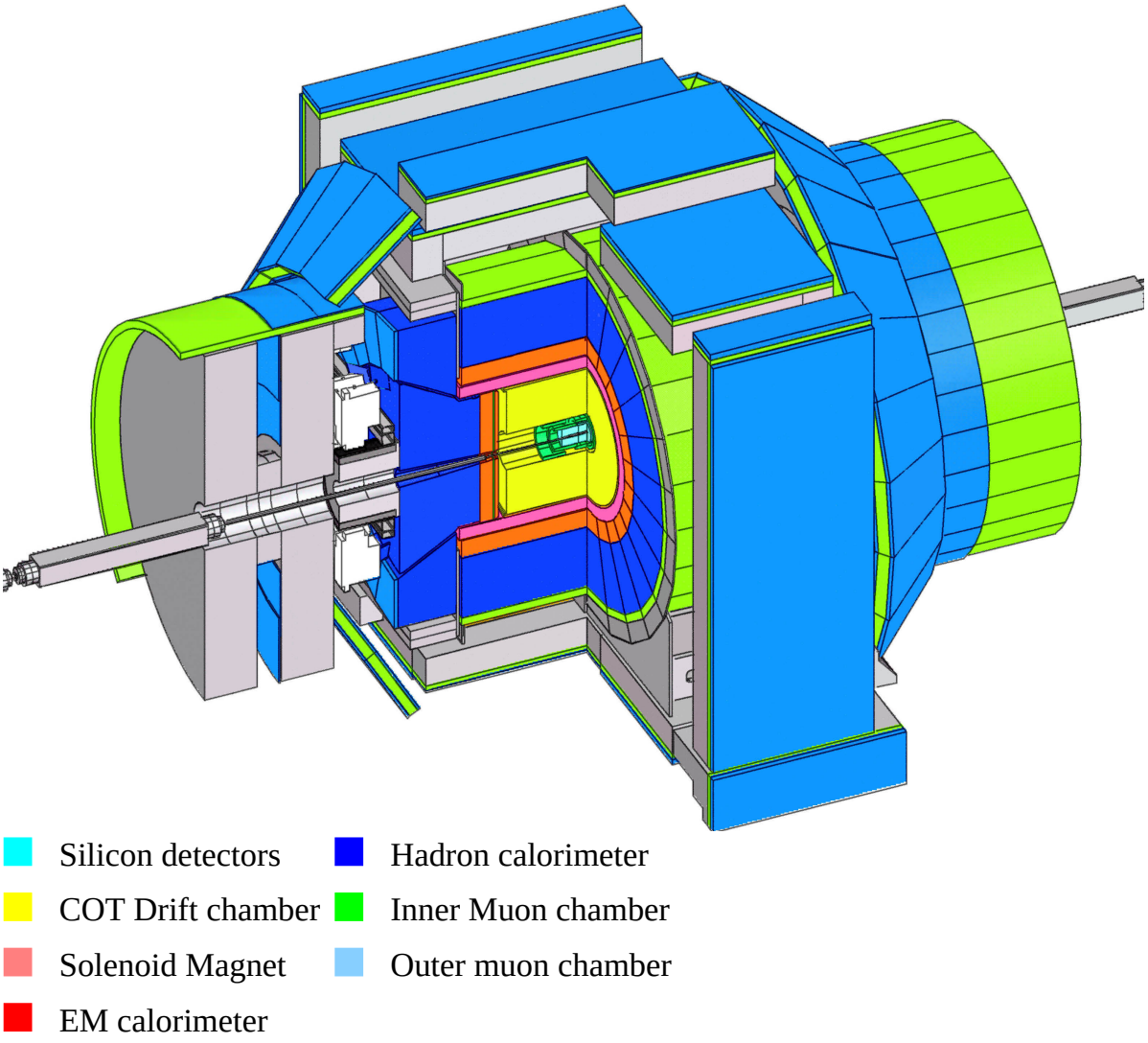

Figure 2.2: *The 5000ton CDF detector.*

2.2.1 Tracking Devices

Charged particle trajectories are reconstructed using the tracking detectors which occupy the region between the beam pipe at a radius of 1.25cm and the solenoid magnet at a radius of 1.5m. The solenoid magnet causes charged particles produced in an interaction to travel in trajectories in which the radius of curvature is proportional to their transverse momentum. The inner part of the tracking system comprises three sets of silicon

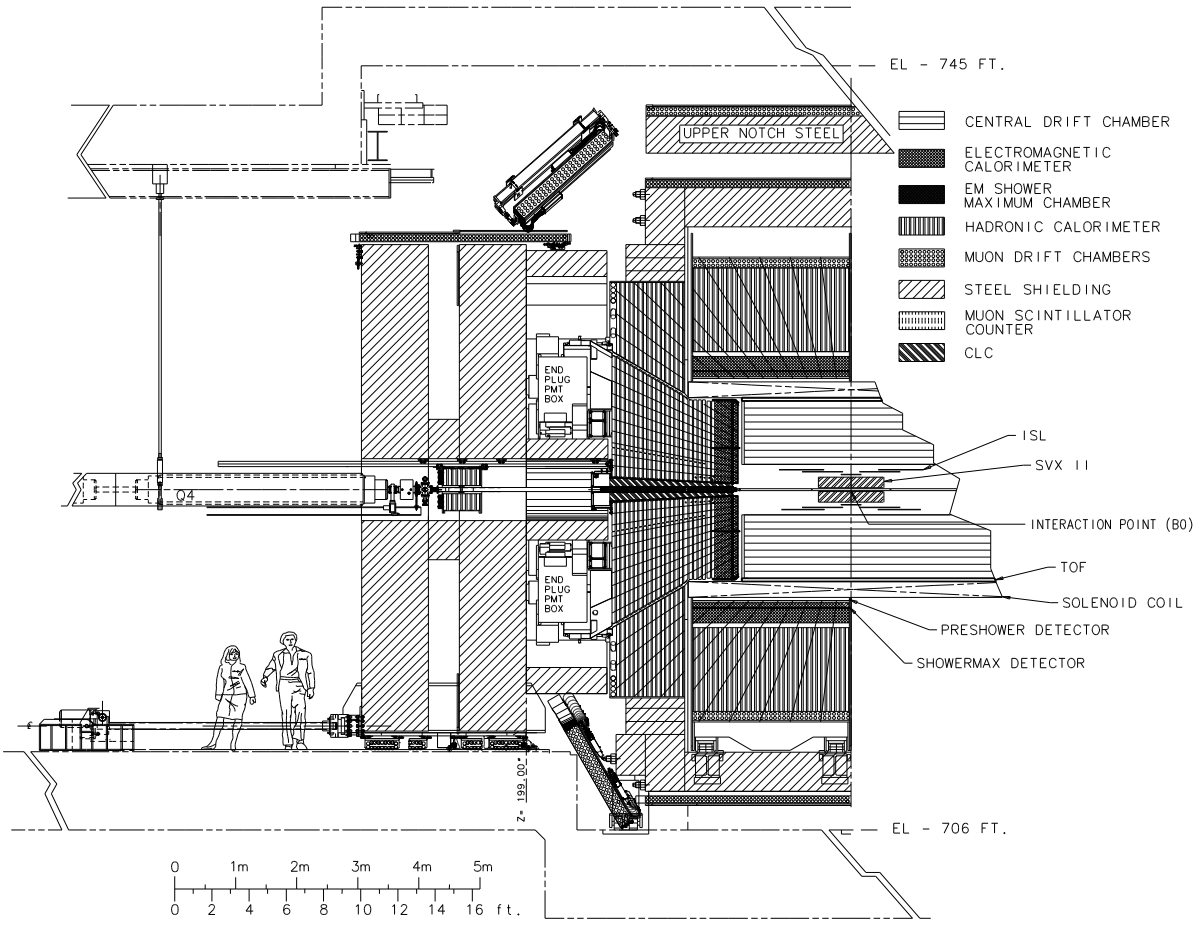

Figure 2.3: *One half of the CDF detector in cut away view. The Layer 00 detector is not shown in this diagram.*

microstrip detectors: Layer 00 (L00), the Silicon Vertex detector (SVXII) and the Intermediate Silicon Layers (ISL), which are detailed below. These silicon detectors give accurate track reconstruction allowing vertex detection and momentum measurement. SVXII is the largest of the three silicon detectors and it operates at sufficiently high speed and accuracy that it may be used for triggering on tracks with large impact parameters thus providing datasets rich in the long-lived decays of B mesons. In a typical $b\bar{b}$ event, five vertices are to be expected: the primary vertex where the $b\bar{b}$ are produced, one vertex for the decay of each b hadron which typically produces a c hadron, resulting in two further

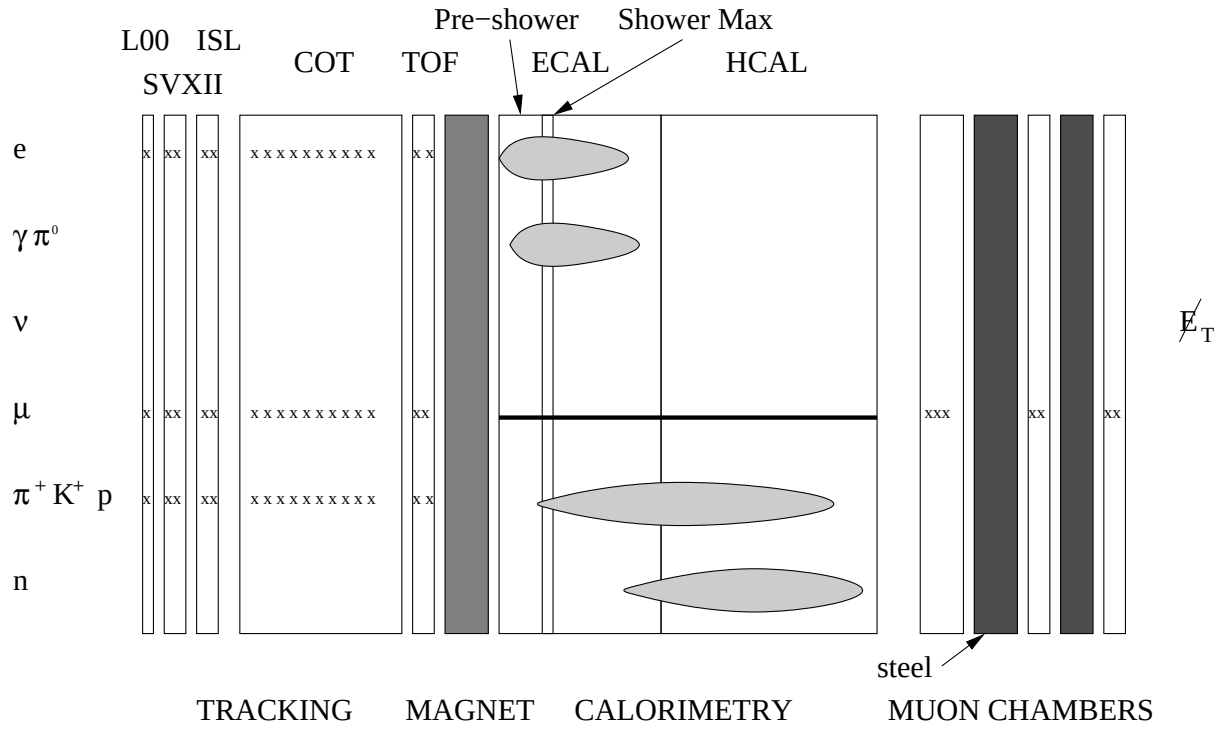

Figure 2.4: *Diagram to show the interaction of leptons and hadrons with the CDF detector components.*

vertices. The triggers are detailed in section 2.2.4. The remaining tracking volume is occupied by the Central Outer Tracker COT which is an open cell drift chamber which supplies good momentum resolution for the tracks which are extended from the silicon detectors into the COT.

Silicon Detectors

The system of silicon tracking detectors [59] extends from a radius of 1.25cm to 29cm and has coverage to $|\eta| < 2$. It comprises three concentric detectors, L00, SVXII and ISL, as shown in figure 2.5. The principal component of the silicon detectors is the SVXII. This replaced the CDF Run I SVX′ [60] detector in order to meet the challenges of higher luminosity and potentially more rapid bunch crossing, and also to provide precise 3D track impact parameters over a wider acceptance range, to support the broad physics

programmes in top production, supersymmetry, Higgs searches and b physics. SVXII was designed to meet these goals and provides coverage of the luminous region which, due to the $p\overline{p}$ bunch length, is a Gaussian of width $\sigma = 30$cm. The coverage of SVXII along the z axis is approximately 2.9σ and gives almost 100% geometrical acceptance for b-tagging.

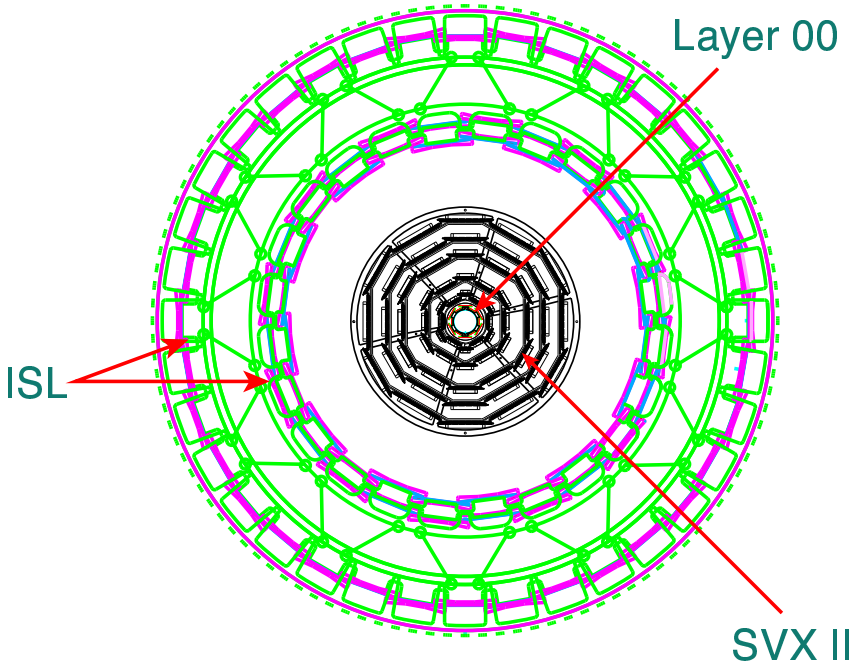

Figure 2.5: *Schematic drawing of the silicon tracking system comprising Layer 00, SVXII and ISL.*

As a particle passes through a layer of Silicon, it produces electron-hole pairs in the material by the process of ionisation. By applying a potential across the silicon detector, the region surrounding the silicon and the doped implants within it is depleted of charge carriers and thus an electric field is established. The electron-hole pairs thus drift towards electrodes which are etched on the Silicon surface where they deposit charge and produce an electrical signal.

The SVXII detector comprises three cylindrical barrels placed end-to-end, each 29cm in length. Each barrel provides the support frame for five layers of double sided silicon

microstrip detectors between a radius of 2.4cm and 10.6cm. Each layer is divided in azimuthal angle into twelve wedges. Three of the five layers provide a measurement in r-ϕ on one side and a 90° stereo measurement on the other. The other two layers provide r-ϕ on one side and a small angle (1.2°) stereo measurement on the other. The pitches and other design parameters for these detectors are shown in table 2.2. SVXII provides standalone track information in the pseudo-rapidity range of $|\eta| < 2$ and 3D vertex reconstruction capability. SVXII also has a precise impact parameter resolution of better than 50μm allowing CDF, for the first time in the world, to trigger on displaced vertices.

Number of layers	5
Number of ϕ wedges	12
Number of barrels	3
Barrel length	29cm
Ladder length	20.9cm
Radius: Layer 0	2.44cm
Radius: Layer 4	10.6cm
Stereo angle	90, 90, 1.2, 90, 1.2°
r-ϕ pitch	60, 62, 60, 60, 65μm
r-z pitch	141, 125.5, 60, 141, 65μm

Table 2.2: *Design parameters of the SVXII detector.*

In addition to the SVXII there are silicon detectors both at smaller and at larger radii. Layer 00 was added to the design at a radius of just 1.25cm and is mounted directly onto the beampipe. It is interesting to note that most b hadrons decay inside the beampipe, since they travel approximately 1mm before decaying. The addition of this detector improves the impact parameter, d_0, resolution as a function of p_T (measured in GeV/c) from

$$\sigma(d_0) = 9 \oplus \frac{34}{p_T} \longrightarrow 6 \oplus \frac{22}{p_T}\ \mu\text{m}$$

for tracks which do not pass through SVXII readout boards and from

$$\sigma(\mathrm{d}_0) = 9 \oplus \frac{66}{\mathrm{p_T}} \longrightarrow 6 \oplus \frac{27}{\mathrm{p_T}}\ \mu\mathrm{m}$$

for tracks which do pass through SVXII readout boards. Improved impact parameter resolution is important to the physics programme at CDF and contributes to the physics analyses listed above. An improvement in the impact parameter resolution enables the $\mathrm{B_s^0}$ decay vertex to be determined more accurately and hence its lifetime is determined with a smaller error.

The ISL detector is a large silicon detector located concentrically outside the SVXII. In the central region, $|\eta| < 1$, the ISL has one layer of silicon, placed at a radius of 22cm. In the region $1 < |\eta| < 2$ there are two layers of silicon at radii of 20cm and 28cm. The additional coverage provided by the ISL provides hits which aid in linking SVXII hits to COT tracks, in the region where the COT provides coverage ($|\eta| < 1$). In addition, in the forward regions where there is little COT coverage, the combination of ISL and SVXII information provides a standalone tracking in 3D. The additional space required for the ISL system was gained by the removal of a CDF Run I gas track detector which had been used to determine the position of the primary interactions. Since the SVXII is able to provide this capability, the gas detector was removed.

The design of the ISL and the SVXII is identical with respect to the data acquisition, cooling mechanism and power supplies, but differs in significant ways due to the large surface area of ISL and its increased distance from the beampipe and consequently reduced radiation. Longer silicon strips with a wider readout pitch are used. Alternate strips are read out but all contribute to the resolution through charge sharing. The silicon is double sided. One side has axial strips with a pitch of 55μm, the other has small angle stereo (1.2°) strips at a pitch of 73μm.

Central Outer Tracker

The Central Outer Tracker, COT, is a drift chamber which enables tracking in the region $|\eta| < 1$. The principle of the drift chamber is to detect the ionisation electrons which occur

when a particle passes through a gas. Measurement of their drift time and location allow a measurement of the momentum and position of particles. Tracks formed in the COT may be matched with tracks from the silicon detector providing an overall momentum resolution of $\sigma(p_T)/p_T^2 < 0.1\%/\mathrm{GeV/c}$ and a hit position resolution of 180μm. The COT is the successor to CDF Run I's Central Tracking Chamber which would suffer from serious occupancy problems at high luminosity ($>1\mathrm{x}10^{32}\mathrm{cm}^{-2}\mathrm{s}^{-1}$). The COT is a cylindrically symmetric open cell drift chamber occupying the region between 43.4cm and 132.3cm in radius and is 310cm in length along the beam direction. The limiting factor for the drift time is the bunch crossing of 396ns in Run IIa and later 132ns in the proposed Run IIb upgrades. The factors controlling the drift time are the maximum drift distance and the gas type. The challenge is met at CDF by having a maximum drift distance of 0.88cm and filling the COT with a fast gas mixture of Argon, Ethane and Carbon tetrafluoride giving a maximum drift time of about 100ns.

The COT comprises 96 layers of sense wires which are grouped into 8 concentric "super layers" as shown in figure 2.6. Alternate superlayers have wires running parallel to the beam which enable measurements of r-ϕ. The wires of the other superlayers are angled at 3° to the beamline and enable measurement of the particles' z coordinates.

A segment of a super layer in ϕ is known as a "super cell", depicted in figure 2.7. The number of super cells in a super layer varies with radius so that the maximum drift distance is approximately the same for each super layer. To compensate for the Lorentz angle of electrons drifting in the magnetic field, super cells are tilted with respect to the radial direction. A super cell is made up of a wire plane which contains 12 sense wires alternated with 12 potential wires with a field sheet to either side. This configuration causes electrons produced by ionisation to drift towards the sense wires. The use of a field sheet rather than field wires allows operation at higher electric fields and gives increased uniformity to the drift trajectories near to the cell boundary, marked by the field sheet. The sheets also comprise less material which helps to reduce scattering in the tracking region. The sense and potential wires are 20μm radius Gold plated Tungsten.

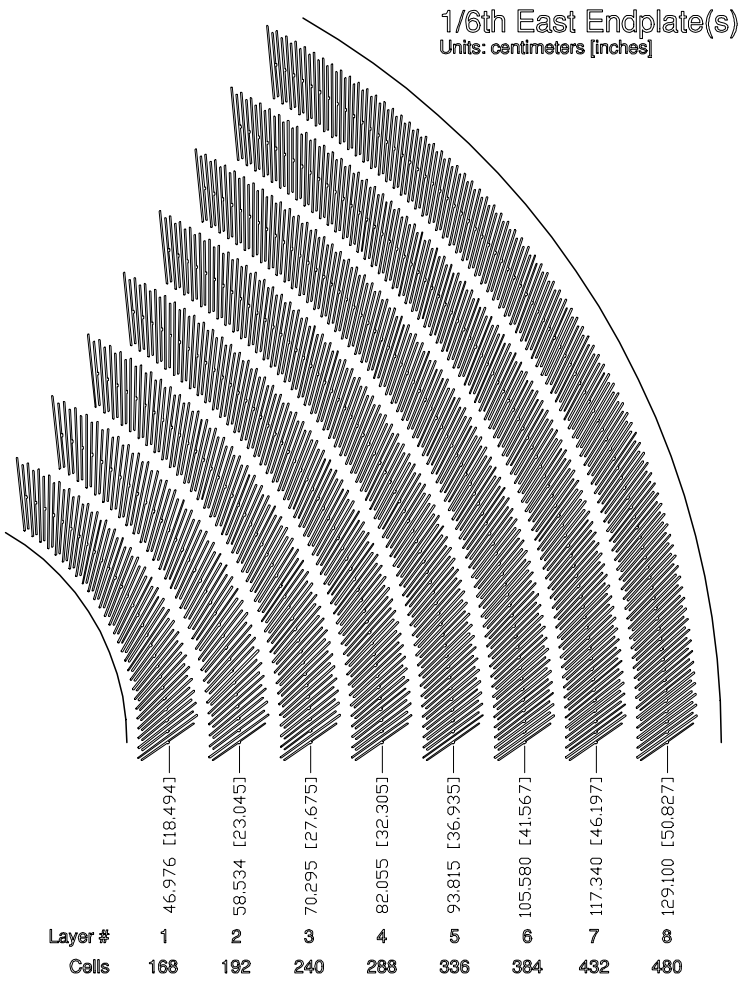

Figure 2.6: *The COT east endplate layout. The 8 superlayers can be seen. In each of these there are slots, the longer slots being for field sheets and the shorter (with a notch added in the diagram for clarity) for shaper panels and sense wires.*

The field sheet is a 6.35μm thick Mylar plate coated in Gold on both sides. In addition to the field sheets, placed to either side of the set of 12 sense and potential wires, the cell is enclosed at the inner and outer radial sides by Mylar shaper panels. The wires and field planes are suspended between two Aluminium endplates. In total, the COT comprises 2520 super cells and therefore 30240 readout channels. At the chamber face a single chip per two super cells carries out the pulse amplification, shaping and discrimination. These

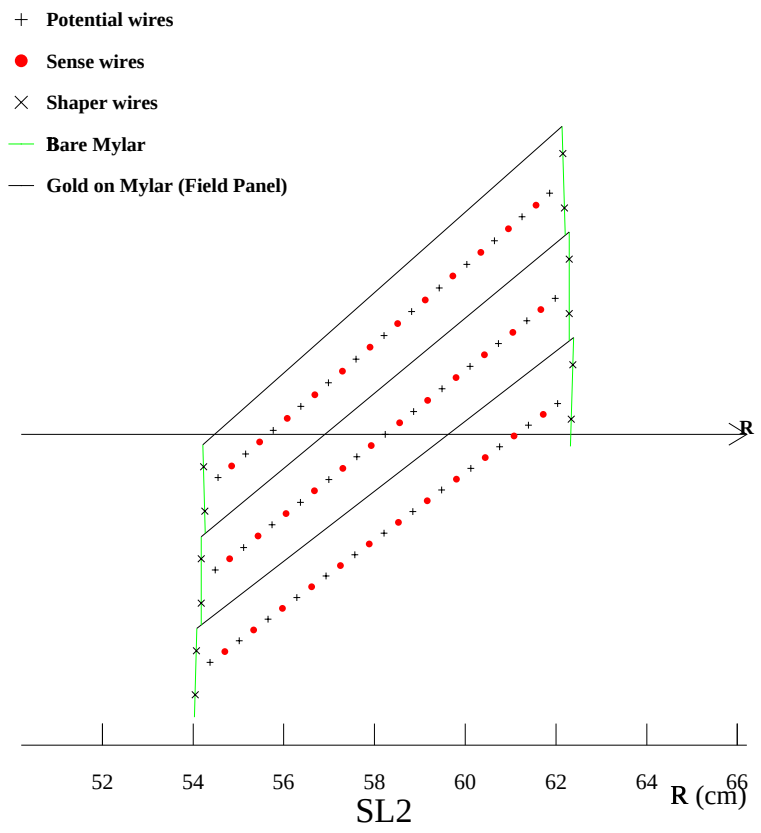

Figure 2.7: *A close-up of the superlayer super cell geometry. Shown here are three super cells in superlayer 2, which is centred on a radius of 58.53cm.*

signals are then transmitted to the CDF hall end-walls by a coaxial cable. Time to digital conversion is performed by TDCs which contain trigger level 1 and 2 event buffering. The hits in the COT are used to form tracks at Level 1 for the eXtremely Fast Tracker which is discussed further in section 2.2.4.

The COT also has particle identification capabilities through the measurement of a particle's energy loss per unit length in the gas, dE/dx. When a charged particle traverses the drift chamber it leaves an ionisation trail. The amount of ionisation is proportional to the energy loss which is described by the Bethe-Bloch formula. This formula shows that

the dE/dx depends only on the particle's velocity. Combining the dE/dx measurement with the COT momentum measurement one can infer the mass of the particle and hence its type, subject to the momentum range and type of the particle. In fact the dE/dx information is utilised to give a probability for a particle type: it gives a one sigma K/π separation for tracks with momenta above 2 GeV/c.

Time of Flight Detector

A Time of Flight detector (TOF) was added to the CDF design as part of the Run II upgrade [61]. Its primary physics motivation is to enhance the particle identification power given by the dE/dx information obtained in the COT. The COT gives separation for K/π above 2GeV/c and below 0.6GeV/c but does not provide separation between 0.6 and 2GeV/c since the dE/dx is similar for K and π in this range. The design time of flight resolution is 100ps which enables the separation of charged kaons from pions at a level of two sigma for tracks of p_T <1.6 GeV/c^2. This can play a crucial role in, among other analyses, the b-flavour tagging technique of "same-side" tagging thus improving measurements of CP violation parameters and B_s^0 mixing.

The time taken for a particle to travel from the interaction point to the TOF detector is characteristic of its particle type since the flight time, t, depends on the particle mass, m:

$$\frac{d}{ct} = \frac{p}{\sqrt{m^2 + p^2}}$$

where d is the path length travelled by the particle and p is its momentum.

The TOF resides at a radius of 138cm from the beampipe and is installed between the outer wall of the COT and the inner wall of the solenoid magnet. In CDF Run I this space was occupied by the Central Drift Tube (CDT) detector which was designed to measure a track's z position accurately but in CDF Run II this capability is provided by the COT. Therefore, the CDT was removed leaving a radial gap of 4.8cm to be occupied by the TOF. The TOF consists of 216 scintillator (Bicron BC-408) bars each measuring 4cm×4cm×279cm. Incidentally, 69 of the bars come from the CLEO detector. At both

ends of each scintillator bar there is a photomultiplier tube (PMT) which connects via a leading edge discriminator to a preamplifier card for readout. Since the TOF detector is within the solenoid magnet, the choice of PMT is limited to those which can operate in a magnetic field. Due to cost, the chosen PMTs are fine-mesh dynode. This in turn limits the types of scintillator which are suitable. The TOF is a long device, of its type, and so the material must have a long attenuation length. Also, the decay time must be short so that bunch crossings can be resolved. The signal is used in conjunction with a precision $p\overline{p}$ bunch crossing time signal to measure the time of flight. The pulse height is also measured to provide information for corrections due to a pulse height dependence in the firing of the discriminator.

The time of a hit in the TOF is then given in terms of the times of arrival of the left and right signals, t_L and t_R, by

$$\mathrm{t_{hit}} = \frac{1}{2}\left(\mathrm{t_L} + \mathrm{t_R} - \frac{\mathrm{L}}{\mathrm{v_{scint}}}\right) \tag{2.5}$$

where L is the length of the scintillator and $\mathrm{v_{scint}}$ is the light propagation speed in the scintillator material. The z position of a track can also be measured by the TOF by

$$\mathrm{z} = \frac{1}{2}\Big(\mathrm{L} + \mathrm{v_{scint}}(\mathrm{t_L} - \mathrm{t_R})\Big) \tag{2.6}$$

Hits in the TOF are matched to tracks by projecting the track trajectory from the COT into the TOF and requiring that the ϕ and z positions measured by the two devices match.

2.2.2 Calorimeters

Calorimeters are deployed to measure the energy deposits of electrons, photons and hadrons as they are absorbed by material. The interactions of electrons and photons are dominated by the processes of bremsstrahlung and pair production and through these processes a single electron or photon can result in a collimated high multiplicity shower of electrons, positrons and photons. There are numerous processes by which a hadron interacts and the resulting showers are somewhat different from the electromagnetic case. The

most important processes in this case are secondary hadron ionisation, electromagnetic cascades from π^0's ($\pi^0 \rightarrow \gamma\gamma$) produced in nuclear reactions, and the loss of energy due to breaking up nuclei and producing neutrinos. Due to the differing processes involved in electromagnetic and hadronic showers they are characterised by differing amounts of energy deposited and times taken for the showers to develop. As a result, separate calorimetry is used for electromagnetic and hadronic shower detection.

CDF has electromagnetic and hadronic calorimetry in the central ($|\eta| <1$) and forward ($1.1< |\eta| <3.6$) regions [62]. The central calorimetry deployed in Run II is mostly retained from Run I, except for new readout systems. The forward, so-called "plug", calorimeters are new and replace the gas calorimeters of Run I whose response time would be too slow for the proposed reduced bunch crossing interval in the upgraded Tevatron environment. The design parameters of the calorimetry are given in table 2.3. The central and plug calorimeters are now discussed in turn.

Central Calorimeter

The central calorimeter is segmented into projective towers of 15° in ϕ by 0.11 in η which point to the interaction region. (The largest tower measures 24.1cm in the z direction and 46.2cm in the $r - \phi$ plane.) Each of these towers comprises a Lead scintillator electromagnetic section followed by a Steel scintillator hadronic calorimeter.

The central electromagnetic calorimeter (CEM) is a Lead-scintillator sandwich sampling calorimeter made of alternating Lead (4.5mm thick) and scintillator (4mm thick) layers. Lead is chosen since it is a dense material which enhances bremsstrahlung and pair production. The charged particles in the shower produce light in the scintillator. The light from the scintillators passes through wavelength shifter sheets at the sides of the towers and is then directed to PMTs by light guides. The light is thereby converted into electrical signals and read out. There are 31 unit layers in a tower giving a total depth of 19 radiation lengths (X_0), related to the probability of occurrence of bremsstrahlung or pair production. Figure 2.8 shows one wedge of the CEM which comprises 10 towers.

	CEM	CHA&WHA	PEM	PHA
Segmentation ($\Delta\eta \times \Delta\phi$)	$0.1 \times 15^\circ$	$0.1 \times 7.5^\circ$	$0.16 \rightarrow 0.64 \times 7.5^\circ$	$0.2 \rightarrow 0.6 \times 15^\circ$
Thickness	$19\mathrm{X}_0$, $1\lambda_0$	$4.5\lambda_0$	$21\mathrm{X}_0$, $1\lambda_0$	$7\lambda_0$
Scintillator thickness	4mm	6mm	4mm	6mm
Passive layer thickness	4.5mm Pb	50.8mm Fe	4.5mm Pb	50.8mm Fe
Resolution	$14\%/\sqrt{E}\oplus 1.5\%$	$75\%/\sqrt{E}\oplus 5\%$	$16\%/\sqrt{E}\oplus 1\%$	$80\%/\sqrt{E}\oplus 5\%$

Table 2.3: *Design parameters of the calorimetry.*

The energy resolution of the CEM is

$$\frac{\sigma(E)}{E} = \frac{13.5\%}{\sqrt{E_T(\mathrm{GeV})}} \oplus 1.5\% \tag{2.7}$$

where the first term is due to shower and PMT fluctuations and the second term is due to the statistical limitation of the calibration sample. The first layer of the CEM is occupied by a pre-shower wire chamber detector (CPR) to aid with the separation of electrons and photons.

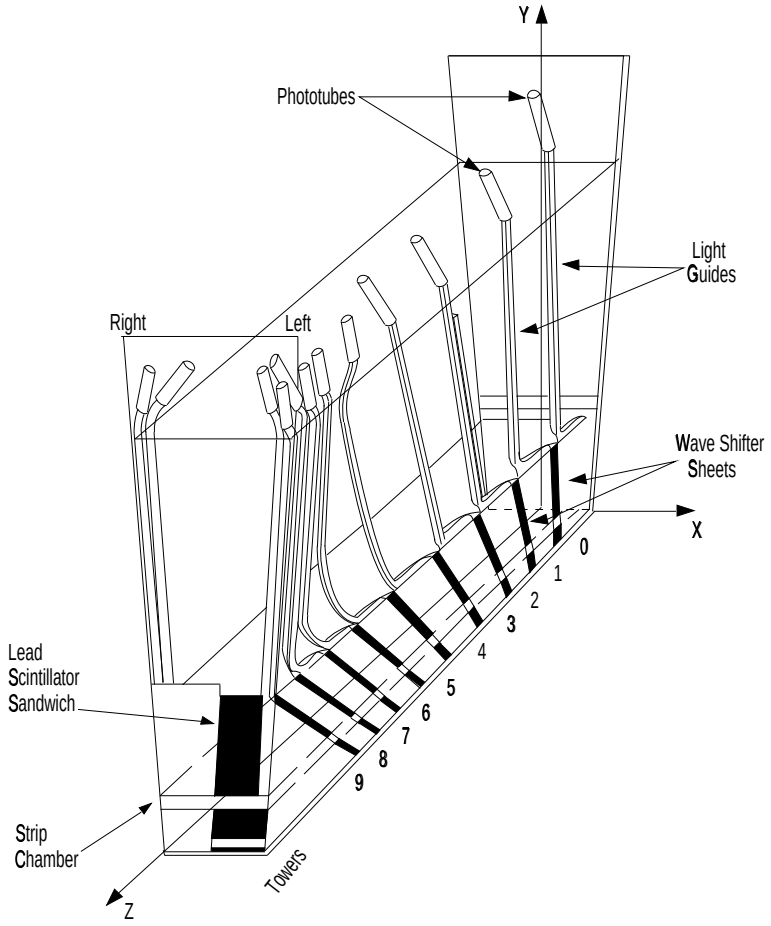

Figure 2.8: *Diagram of one wedge of the Central ElectroMagnetic Calorimeter.*

The transverse shower shape is measured by the central strip chamber (CES) which is placed at a depth of 5.9 radiation lengths, corresponding to the shower maximum. Its

purpose is to measure the position of $e^{\pm}$ and γ showers for matching with tracks and to separate $e^{\pm}$s and γs from π^0s. The neutral pions rapidly decay to $\gamma\gamma$ and can give rise to overlapping showers in the EM calorimeter. The CES is a multiwire proportional chamber which has a position resolution of $\pm$2mm [62]. It has fine segmentation of 1.4-2cm allowing an electron or photon shower to span several CES channels.

The longitudinal development of hadronic showers scales with the *interaction length* of the material, λ_0. The depth of the CEM is one interaction length and so hadrons pass through the electromagnetic calorimetry depositing only a fraction of their energy. A hadronic shower takes longer to form than an electromagnetic one and so a deeper calorimeter is needed. Since Iron is cheaper and also self-supporting, it is used as the absorbing material in the hadronic calorimetry at CDF [63]. The central hadron calorimeter (CHA) comprises 23 layers of iron and scintillator corresponding to 4.5 interaction lengths. A unit layer is made up of 50.8mm of iron and 6mm of scintillator. The CHA is segmented into towers of the same dimensions as the CEM and they also point towards the interaction region. There is an additional piece of hadron calorimetry in the central region known as the endwall (WHA) which fills the region between the central ($40^\circ \rightarrow 140^\circ$) and plug hadronic calorimeters ($3^\circ \rightarrow 37^\circ$ and $143^\circ \rightarrow 177^\circ$). This covers polar angles from 30° to 45° and 135° to 150° and has the same design as the CHA.

Plug Calorimeters

The plug calorimeters cover the region 3° to 37° corresponding to $1.1 < |\eta| < 3.6$ [64]. A schematic of the plug calorimetry is shown in figure 2.9. This calorimetry is a new addition for Run II and replaces the older system to allow for the faster bunch crossing. The plug calorimeter has an electromagnetic component with shower maximum position detection and a hadronic component at larger distance from the interaction point. Both components have the same basic tower segmentation. This was optimised for $e^{\pm}$ identification in b quark jets. This channel is chosen for tuning since the electron shower is similar to a hadronic jet. Similarly to the CEM, the plug EM calorimeter is a $21X_0$ lead and scintillator

sampling device. The dimensions are detailed in table 2.3. The hadron calorimeter is a 7 interaction length Iron and scintillator sampling device with the same design as the CHA and WHA between 10° and 37°. Between 3° and 10°, stainless steel disks are alternated with scintillator. The dimensions are also given in table 2.3.

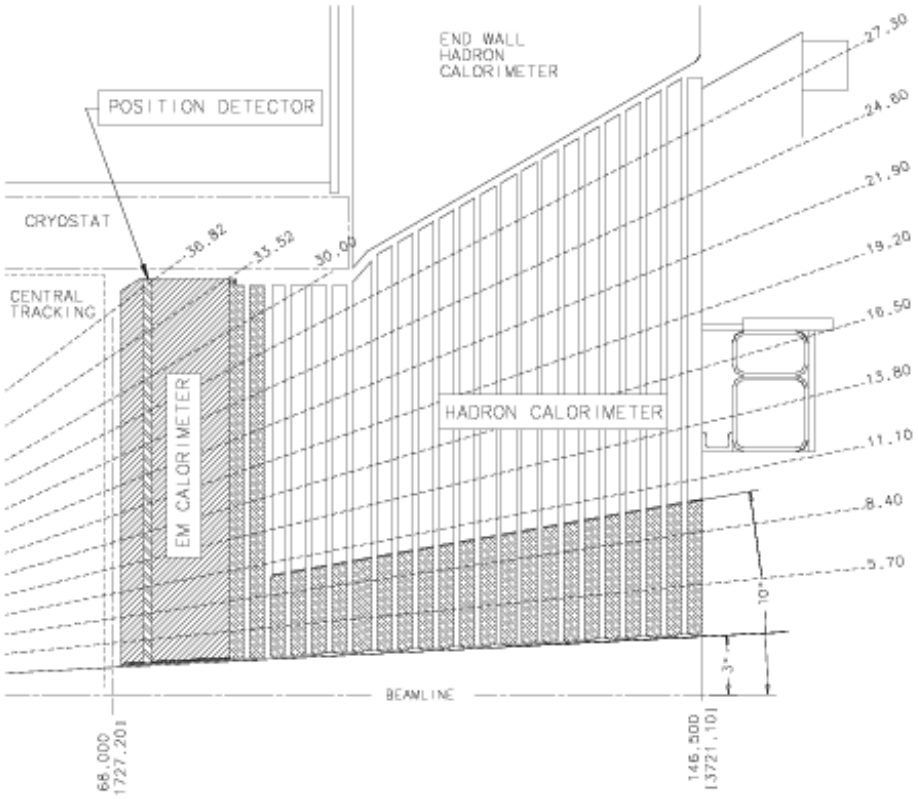

Figure 2.9: *Diagram of the plug electromagnetic and hadronic calorimeters. The plug hadronic calorimeter is Iron-scintillator between 10° and 37° and is stainless steel - scintillator between 3° and 10°, shown by the darker shading in that region.*

2.2.3 Muon Chambers

Gathering events containing muons is central to several important physics programs. Top quarks decay via b quarks and W bosons, which are both often identified via their decay to muons. Muons have a relatively clean signature in the detector and so for B physics the

$J/\psi \rightarrow \mu^+\mu^-$ sample is an important benchmark for many lifetime and mixing studies. In addition, samples of semileptonic decays of B mesons are also important for the study of lifetimes and mixings, as described in the analysis presented in this thesis. Many new physics signatures also involve one or more leptons. Thus muon detectors are vital to many analyses.

A muon's momentum, as for other tracks, is measured by its curvature in the tracking detectors. Muons are identified by their ability to penetrate materials which is unique among charged particles. Following the tracking detectors, they pass through the magnet and calorimetry with minimal energy loss. On the outside of the detector there are four systems of scintillators and wire chambers which are used to detect muons in the pseudo-rapidity range $|\eta| \leq 2$. The muons ionise gas in the wire chambers as they pass through, and the resulting electrons are gathered by a single wire per chamber. Scintillators are used in three of the subsystems for triggering and for associating muon candidates with the bunch crossing which gave rise to them. A schematic diagram showing the coverage of the four regions is shown in figure 2.10 and detailed parameters of the muon subsystems are given in table 2.4. The four systems, CMX, CMP, CMU and IMU, will now be discussed in turn.

The Central MUon detector, CMU, covers the region $|\eta| \leq 0.6$ [65]. This comprises 144 modules each containing 16 wire chambers which measure $2.68 \times 6.35 \times 226$cm and have a 50μm stainless steel wire at their centre, running along the beam direction. The absorbing material for this detector is the magnet, CEM, and CHA which corresponds to 5.5 pion interaction lengths. The cells are mounted 4 deep in radius, but with an offset in ϕ between the first and third, and second and fourth layers. The readout is ganged in the same way so that the muon's location is measured in ϕ by the wire chambers containing hits, and in z by measuring the difference in charge at the two ends of the wire, (the principle of charge division).

The muon detection was enhanced in the central region by the Central Muon uPgrade, CMP, in order to cut down the number of hadrons which are not fully contained in

	CMU	CMP	CMX	IMU
η range	$\leq$0.6	$\leq$0.6	0.6$\rightarrow$1.0	1.0$\rightarrow$ 1.5
Drift tube cross-section (cm)	2.68$\times$ 6.35	2.5$\times$15	2.5 $\times$15	2.5 $\times$ 8.4
Drift tube length (cm)	226	640	180	363
Max drift time (ns)	800	1400	1400	800
Total drift tubes	2304	1076	2208	1728
Scintillation counter dimensions (cm)	-	2.5$\times$30$\times$320	1.5$\times$30-40$\times$180	2.5$\times$17$\times$180
Total number scintillation counters	-	269	324	864
Pion interaction lengths	5.5	7.8	6.2	6.2-20
Minimum detectable muon p_T (GeV/c)	1.4	2.2	1.4	1.4-2.0
Multiple scattering resolution	12cm/p(GeV/c)	15cm/p(GeV/c)	13cm/p(GeV/c)	13-25cm/p(GeV/c)

Table 2.4: *Design parameters of the muon chambers.*

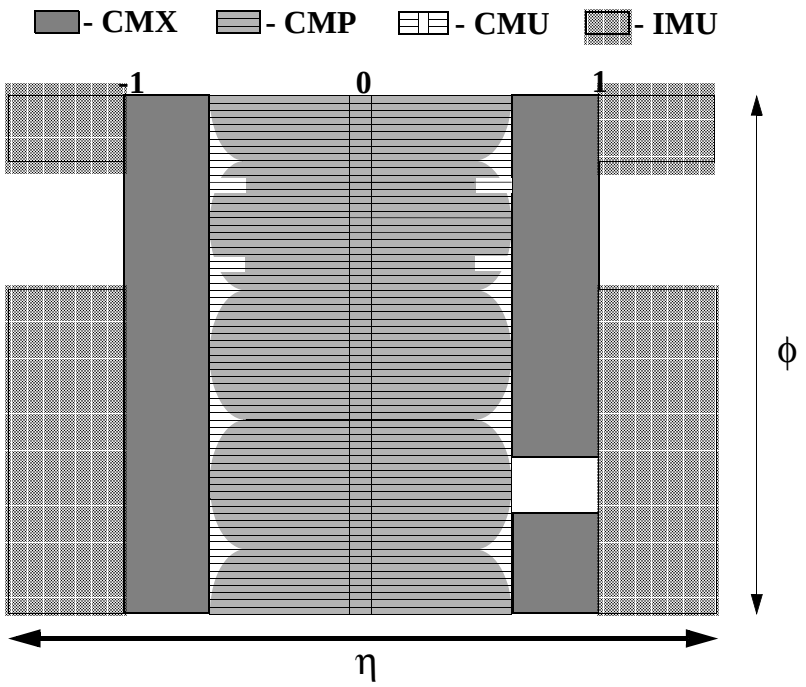

Figure 2.10: *Schematic diagram of the muon chamber coverage in pseudorapidity and azimuth.*

the CHA and hence "punch through" to the muon chambers. The CMP was partly implemented in Run I and partly in the Run II upgrades [66]. The CMP is set at larger radius than the CMU behind an additional 60cm layer of steel and again consists of wire chambers. The coverage given by the CMP varies in pseudorapidity since it forms a box shape around the CMU, and is approximately $|\eta| \leq 0.6$. Rectangular scintillation counters are mounted on the outside of the CMP and provide timing and triggering capability.

The Central Muon eXtension, CMX, gives muon chamber coverage in $0.65 \leq |\eta| \leq 1$. As figure 2.10 shows, the CMX comprises two broken rings at the ends of the central muon chambers. The rings have gaps in ϕ at the top of the detector for the CDF magnet cryogenic cooling system and at the bottom of the detector where there is a gap for the floor of the collision hall. However this gap in coverage is filled by the so-called "mini-skirt" arrangement of a fan of muon chambers located in a slot in the floor. The rings are

composed of conical sections of drift tubes which are shorter but otherwise identical to those in the CMU, and scintillation counters at 15° intervals which are used for triggering.

The Intermediate MUon detector, IMU, gives additional coverage allowing triggering on muons at $|\eta|$ <1.5 and identification of muons to $|\eta|$ <2. The detector consists of two barrels of chambers, similar to those in the CMP, and scintillation counters mounted next to the plug and outside the CMX detector. In addition, there is extra scintillator on the endwall and between the toroids which is used for triggering.

2.2.4 Event Triggers

The upgraded Tevatron luminosity and proposed reduction in the proton and antiproton bunch spacing present a trigger and data recording challenge. Furthermore, the total hadronic cross section at CDF is 80mb. This figure includes contributions from elastic ($\simeq$18mb) collisions. For example, by comparision the cross section for $b\overline{b}$ production is 0.1mb, a small percentage of the total cross section. Therefore, b physics occurs in 1 out of every 800 events. This, coupled with the limitations of tape writing speed and data storage capactity, requires that only a subset of the events in $p\overline{p}$ collisions at CDF can be selected to be written to tape. CDF does this by using three tiers of triggers to select the interesting events. Each level provides a reduction in rate which is sufficient to allow an event to be processed at the next level with a minimum deadtime in the experiment. The trigger decision has to occur very quickly since events can occur every 132ns in Run II. Ideally, a trigger should be designed to keep the events of interest, i.e. have a high efficiency, and to reject those deemed to be of no interest, i.e. have high purity. In the first trigger level it is possible make requirements on quantities which indicate, for example, the presence of one 10GeV electron or two 2GeV muons using only low level detector information. At Level 2, there are fewer events to process and therefore there is more time available for simple event reconstruction using programmable processors and at Level 3 complete detector information and resolutions are available for a full reconstruction of events. In all, the rate must be reduced from a bunch crossing rate of

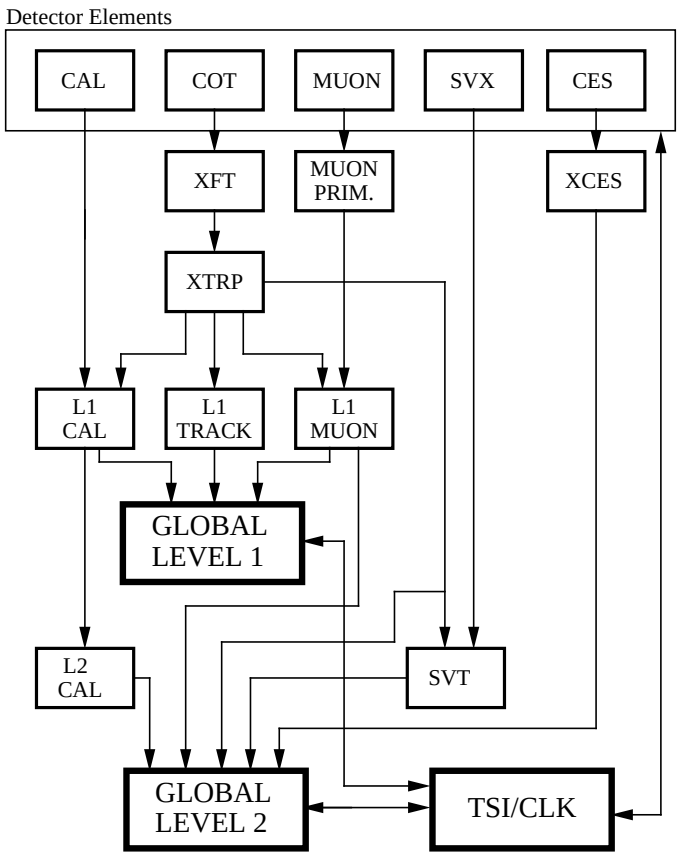

Figure 2.11: *Block diagram of the Level 1 and 2 trigger systems.*

7.6MHz, corresponding to 132ns, to 50Hz, corresponding to 20ms, at Level 3, a factor of 150 thousand.

The Level 1 and 2 triggers are hardware triggers using VME boards and the Level 3 trigger is run in a farm of processors.

The trigger levels are now discussed in turn. A flowchart representation of the Level 1 and 2 system is shown in figure 2.11.

Level One

The level one trigger has 5.5μs (equivalent to 42×132ns bunch crossings) to make its accept or reject decision. To allow for this latency period, each detector component buffers 42 events. Since the accelerator is operating at present with a bunch crossing of 396ns the two intermediate clock cycles are ignored. The Level 1 accept rate is 40kHz (=25μs), a reduction of a factor of 190.

Three parallel, synchronous processing streams are run in Level 1 to find tracks, calorimeter objects and muons. Tracking at Level 1 is a new development for CDF Run II and offers not only better electron and muon identification but also track-only triggers. In total, 64 different triggers are formed at Level 1 using ANDs and ORs of objects from the three streams.

Tracking has been made possible at Level 1 by the eXtremely Fast Tracker (XFT). This is a parallelised device which gathers information from the COT and provides results quickly enough to be used at Level 1. There are two processes in the track finding, the "Finder" and the "Linker". The Finder looks for high p_T track segments in each of the four outermost superlayers of the COT. The Linker searches in a 1.25° wedge in ϕ for track segments which are consistent in each of the four layers with one high p_T track. The highest p_T track per 1.25° is then reported. The minimum track p_T is 1.5GeV/c and the momentum resolution is $\Delta p_T/p_T^2 < 2\%/\text{GeV/c}$. Once XFT tracks are formed, they are passed onward to Level 1 and Level 2 trigger subsystems by the eXTRaPolation unit (XTRP). Tracks are either passed directly on to Level 2, sometimes for use with the Silicon Vertex Trigger (SVT), or they are passed to L1CAL, L1TRACK and L1MUON. The operation of L1CAL and L1MUON will now be described.

The L1CAL is intended to trigger on electrons, photons, jets, total event transverse energy (ΣE_T) and missing transverse energy ($\not\!\!E_T$). Triggers may require thresholds in one or more individual electromagnetic calorimeter towers or in a sum of tower

deposits. Triggers may also reject events based on hadronic calorimeter deposits. Jet triggers require deposits in hadronic calorimetry in addition to the electromagnetic calorimeter. The tower activity may be matched to tracks passed from the XTRP: L1CAL receives track information corresponding to separate momentum thresholds, for each 15°ϕ wedge. The tracks are extrapolated using look up tables. The various combinations of e, γ, jets, ΣE_T and $\not\!\!E_T$ information are passed to the Level 1 decision card, known as "FRED".

L1MUON Muons are identified at Level 1 by single hits or coincidences of hits in the scintillator components of the muon system and by patterns of hits in the wire chambers. These groupings form muon "stubs" which may be matched with XFT tracks. Tracks are extrapolated to the CMU and CMX muon chambers by look up tables. Information is given in 2.5° segmentation in ϕ on the p_T and amount of multiple scattering. The signals are transmitted to the FRED.

Level Two

Once an event has been accepted by Level 1 it is shunted to one of four Level 2 event buffers. Level 2 has an accept rate of 300Hz (=3.38ms) and so the combined Level 1 and 2 rejection rate is 20000:1. The time taken to reach an accept or reject decision at Level 2 is approximately 20μs, which results in less than 10% deadtime due to the Level 2 processing time. In total around 100 Level 2 triggers are in use. The Level 2 trigger subsystems include the shower maximum detector (CES), discussed in section 2.2.2, higher level calorimeter information such as the presence of tower clusters, and a displaced vertex trigger, the Silicon Vertex Trigger (SVT). The SVT is the first operational trigger of its kind allowing highly efficient collection of b (and c) physics events. The analysis presented in this thesis uses samples collected by this trigger combined with calorimeter or muon chamber triggers. The displaced vertex trigger works by identifying tracks with large impact parameters. These are calculated at Level 2 by reading out the entire SVXII detector after each Level 1 trigger. Hit finders firstly remove bad channels from the hit

finding process, by consulting a database. The pedestals, which are the mean output voltages of each silicon detector when there is no beam, are subtracted from the signal and then the remaining hits are grouped into "clusters" by cluster-finding algorithms. The centre of each cluster is output as it is the most likely point of intersection of the track and the silicon layer. This information is combined with the Level 1 XFT tracks and gives an impact parameter resolution comparable with that found in the offline reconstruction.

The Level 1 and 2 triggers are managed by a trigger supervisor, TSI/CLK which clocks at the rate of the bunch crossings. The trigger master clock is locked to the radio frequency signal from the Tevatron, at a rate of 53MHz.

Level Three

Events which pass Level 2 then move to Level 3 at a rate of 300Hz. At Level 3 the events are processed for recording to tape or disk storage, which has a writeable rate of 30-40Hz. The size of one event is approximately 250Kb and so the rate of writing to storage is approximately 7.5-10Mb/s. The estimates are that in one year, 80Tb of raw data will be recorded. An Event Building Network comprising a farm of UNIX CPU's takes the events from Level 2 and passes them to the Level 3 trigger subsystem. Level 3 then processes events, assembling them into data structures which are suitable for analysis. At level 3, full detector information and improved resolutions are available, including online track reconstruction and matching requirements of tracks to muon stubs and calorimeter deposits. An event which passes Level 3 is passed to storage by the Data Logging subsystem.

Chapter 3

B_S^0 Event Selection

The analysis presented here is a measurement of the lifetime of the B_s^0 meson reconstructed via its semileptonic decay, $B_s^0 \to \ell^+ \nu_\ell D_s^-$. Here ℓ refers to either an electron or a muon. In this channel, the B_s^0 meson cannot be fully reconstructed owing to the neutrino carrying missing four-momentum and so the B_s^0 is only partially reconstructed by identifying lepton and D_s^- meson candidates. In this analysis, the $D_s^- \to \phi\pi^-$ decay is used, since the narrowness of the ϕ resonance suppresses background. The decay vertex of the B_s^0 is established by finding the intersection point of the lepton and candidate D_s^- meson trajectories. The decay length is given by the distance between the primary vertex and the B_s^0 decay vertex. The proper *pseudo-lifetime* of each B_s^0 candidate is then calculated from its transverse decay length and the $\ell^+ D_s^-$ momentum taking into account a correction for the missing neutrino four-momentum. A maximum likelihood fit to the pseudo-lifetime distribution is performed, as described in chapter 5, which yields the B_s^0 average lifetime of the flavour eigenstates as discussed in chapter 1. This chapter presents an overview of the analysis method and describes the triggers which collect the data samples and the reconstruction techniques and cuts used to select B_s^0 candidate events.

3.1 Analysis Overview

The CDF Run I semileptonic analysis of the B_s^0 lifetime is the most accurate to date, with a value of $1.36 \pm 0.09^{+0.06}_{-0.05}$ ps. The CDF Run I methodology is largely followed for the analysis of CDF Run II data presented here:

- The D_s^- meson candidates are reconstructed in proximity to lepton candidates.
- The proper lifetime is calculated from the decay distance in the x-y plane which is measured by finding the vertex of the lepton and D_s^- candidate:

$$c\tau = \frac{m(B_s^0)}{p_T(B_s^0)} L_{xy} \tag{3.1}$$

  where the factor $m(B_s^0)/p_T(B_s^0)$ takes into account the velocity and time dilation of the B_s^0 meson due to its Lorentz boost. Figure 3.1 shows the $c\tau$ defined in three dimensions versus the $c\tau$ defined in two dimensions. This shows that no bias is introduced by working in two dimensions, using L_{xy} and p_T.

- since $p_T(B_s^0)$ is not measurable, owing to the missing four-momentum carried by the neutrino and possibly particles from higher state charm mesons, a pseudo-proper lifetime is defined:

$$c\tau^\star = \frac{m(B_s^0)}{p_T(\ell^+ D_s^-)} L_{xy} K, \qquad \text{where} \qquad K = \frac{p_T(\ell^+ D_s^-)}{p_T(B_s^0)} \tag{3.2}$$

  The distribution of the K factor, $p_T(\ell^+ D_s^-)/p_T(B_s^0)$, is extracted from Monte Carlo.

In CDF Run II there is one further significant complication to this measurement, namely the lifetime bias from the displaced vertex trigger which requires a 4 GeV lepton and a 2 GeV track with impact parameter cuts: 0.12mm$< |d_0| <$1.00mm. Therefore another step is added to the analysis procedure compared with that of Run I:

- Emulate the trigger bias using a full or parametric trigger simulation in order to evaluate the lifetime bias and factor it into the lifetime fit function.

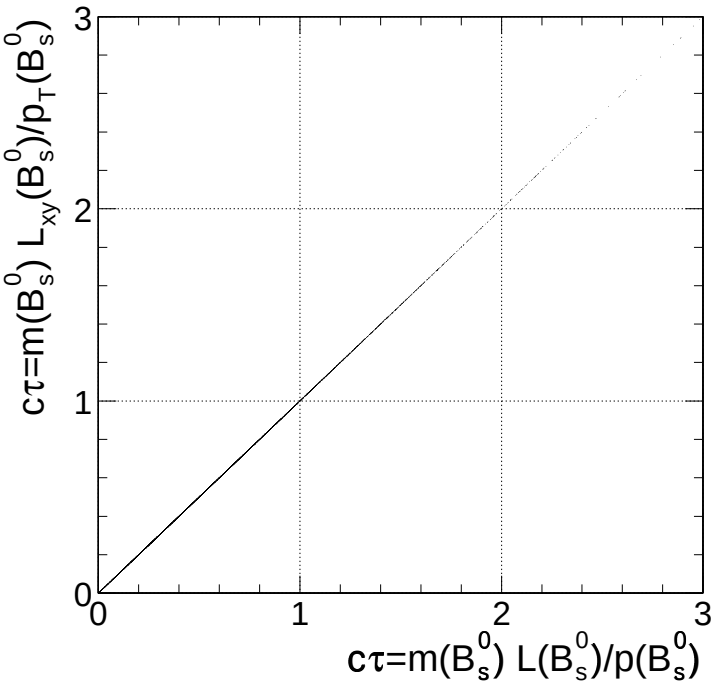

Figure 3.1: *The $c\tau$ defined in three dimensions, using the three dimensional decay distance and momentum, versus the $c\tau$ defined in two dimensions, using the decay distance and momentum projected into the x-y plane. These values are obtained from truth level simulation. This shows that there is no bias due to the use of two dimensions only. A grid is superimposed to guide the eye.*

3.2 Trigger and Data Sets

In CDF Run II, triggers were specifically designed for the collection of b-hadron decays [67]. There are two triggers for semileptonic decays, one for the electron and another for the muon channel. These use the standard technique of seeking a high transverse momentum lepton in conjunction with the innovative Silicon Vertex Trigger, SVT, which allows triggering on a track's impact parameter in the Level 2 trigger [68]. The SVT is discussed in more detail in section 2.2.4. The samples used in this analysis come from triggers which are optimised for the collection of semileptonic b hadron decays, such as

$B_s^0 \to \ell^+ \nu_\ell D_s^-$. The triggers require a lepton, e or μ, and another track in the event with large impact parameter. The exact requirements of these triggers are discussed in sections 3.2.1 and 3.2.2 and the full CDF trigger path names are given in appendix B. The optimisation of these triggers is described in [69].

The total integrated luminosity in each of these triggers is approximately $140 pb^{-1}$ gathered between February 2002 and August 2003 corresponding to the run range 138425 to 168000. These datasets are produced with cdfsoft2 version 4.8.4.

3.2.1 Trigger Lepton Requirements

Several variables are used to identify the candidate leptons, e or μ. There are then two samples: electron plus displaced track and muon plus displaced track. The trigger lepton cuts are now discussed in turn and are summarised in tables 3.1 and 3.2.

Trigger Electrons

To identify an electron, cluster finding algorithms combine energy deposits in the central electromagnetic and hadronic calorimeters and the resulting clusters are matched to tracks by proximity and pointing requirements [70]. CDF's calorimetry is composed of electromagnetic calorimeters arranged in projective towers in pseudorapidity and azimuth, behind which are the hadronic calorimeters which have identical projection. The calorimeters are discussed in depth in section 2.2.2. The Cluster finding algorithm for the CEM begins by iterating over all calorimeter towers, selecting those with greater than 2 GeV of electromagnetic transverse energy, E_T^{EM}, and ordering them in decreasing E_T^{EM}: these are known as seed towers. These are the candidates for the central tower in a cluster which, by definition is the tower with highest energy in a cluster. The towers adjacent in pseudorapidity to the seed tower form a cluster with it if they have non-zero electromagnetic or hadronic energy: these are known as shoulder towers. This means that it is possible for a tower with no electromagnetic energy to be included in a cluster. This aids in the rejection of hadrons since a cut is also applied on the ratio of hadronic to

electromagnetic energy of the cluster, described below. To ensure there are no overlapping clusters, any towers which are allocated to clusters are removed from further cluster finding so that they cannot be included in other clusters. The maximum size of a cluster is three towers in pseudorapidity, corresponding to 0.33 in η ($\approx 19^\circ$ at $\eta = 0$) and one tower in azimuth corresponding to 15° in ϕ. Clusters are not permitted to be formed over different EM calorimeter regions so that, for example, a seed tower at the edge of the CEM cannot be clustered with a tower in the plug EM calorimeter. This can lead to two-tower clusters. Only the electromagnetic energy deposits are used to determine the centroid of the cluster and its total energy. The iterative process continues until the list of seed towers has been exhausted.

In addition to the energy deposits measured in towers, the electromagnetic calorimeter also measures shower position using the central electromagnetic strip chamber, CES, positioned between the eighth and ninth lead-scintillator layers. In order to match a track to an electromagnetic cluster, each track in the event is extrapolated, assuming helical motion in the solenoidal magnetic field, to the plane of the CES. Multiple scattering corrections are not applied. The track is required to be within 25cm in x-ϕ of the shower position at the CES. Here x is a direction perpendicular to the beam pipe, running through the centre of the EM seed tower . This corresponds to approximately three η towers, the maximum cluster size. The track is also required to be within 38cm in z of the centre of the EM tower which seeded the cluster, which is approximately 2cm to either side of the boundary of the shoulder towers. To be considered as a matching track, it must also traverse a CEM tower in the wedge under consideration. If several tracks fulfil these requirements, then the one with highest p_{T} is chosen. This eliminates the cases where the highest p_{T} track is not the electron and the electron has lower p_{T}. In this case, the electron's energy would not be well measured since it is not isolated and it is therefore desirable that such electron candidates fail. This is accomplished by applying cuts to reject hadrons, such as the Had/EM cut, described below [71]. The combined track and cluster information, along with CES hit information, form an electron candidate. Specific

requirements are demanded of the electron candidate to attempt to eliminate background from neutral (for example $\pi^0 \to \gamma\gamma$, BR=98.798±0.032% and $\eta \to \gamma\gamma$, BR=39.43±0.26%, or $\eta \to \pi^0\pi^0\pi^0$, BR=32.51±0.29%) and charged hadrons.

For the electron plus displaced track trigger, candidate electrons are selected by imposing specific selection cuts. The cuts are summarised in table 3.1 [82, 72] followed by a discussion of the cut variables.

Variable		Cut
p_T	$>$	4 GeV/c
E_T	$>$	4 GeV
$E_{\rm had}/E_{\rm em}$	$<$	0.15
L_{shr}	$<$	0.2
Δx	$<$	5cm
Δz	$<$	3cm
χ^2_{strip}	$<$	10
χ^2_{wire}	$<$	15

Table 3.1: *Trigger selection cuts for electrons.*

Each of the electron identification cut variables is now discussed in turn:

p_T is the transverse momentum of the track associated with the calorimeter cluster. This is required to be greater than 4 GeV/c. Since the cross-section for b production decreases as p_T increases, the ideal choice to capture more b events is a low p_T cut, but this is limited by the Level 1 and 2 trigger bandwidth. See [69] for details.

E_T is the transverse energy, defined by $E_{em} \sin\theta$ where E_{em} is the cluster energy measured in the EM calorimeter and θ is the polar angle of the track which is matched to the EM cluster. This is required to be greater than 4GeV.

E_{had}/E_{em} is the ratio of the energy deposited in the hadronic calorimeter to that in

the electromagnetic calorimeter for the towers included in the EM cluster. The EM calorimeter depth is designed to be such that an electromagnetic shower is contained within the calorimeter whereas hadrons are expected to deposit some energy in the electromagnetic calorimeter and most of their energy in the hadronic calorimeter where they are stopped. This ratio is required to be less than 0.15 to reject hadronic background.

L_{shr} is the lateral shower profile, defined by

$$L_{shr} = 0.14 \frac{\sum_i (M_i - P_i)}{\sqrt{\left(0.14\sqrt{E_{em}}\right)^2 + \sum_i (\Delta P_i)^2}}$$

where the sum variable, i, runs over the shoulder towers adjacent to the seed tower; M_i is the measured energy in tower i; $P_i \pm \Delta P_i$ is the predicted energy in tower i, calculated using a parameterisation of test beam data and E_{em} is the total electromagnetic energy in the cluster. The predicted energy sharing comes from an extrapolated trajectory between the primary vertex and the z position given by the CES. The L_{shr} variable is designed to reject the wider clusters formed by multiple particles [74]. In the trigger used here, L_{shr} is required to be less than 0.2 [75].

$\Delta x, \Delta z$ are the distances between the x and z coordinates of the track extrapolated to the CES and the x and z coordinates as measured in the CES itself. These distances measure how well the position of the track which is matched to the electron candidate, matches to the shower position in the CES which is embedded in the CEM. This is expected to distinguish from backgrounds by rejecting energy deposit from neutral particles, which have no matching track, and background from neutrals which occur in loose proximity to charged hadrons. Δx is required to be less than 5cm and Δz is required to be less than 3cm.

$\chi^2_{strip}, \chi^2_{wire}$ measure how well a candidate electron matches electron test beam measurements of the pulse height shape in the CES. In the strip (z) view, $\chi^2 < 10$ and in the wire $(r - \phi)$ view, $\chi^2 < 15$.

Trigger Muons

Muons are identified by seeking patterns of hits, known as stubs, in the muon chambers and associating these with tracks. This process and the values of the cuts used are discussed in detail in [76]. The muon chambers used in the muon plus displaced vertex trigger are the Central MUon chamber, CMU, and the Central Muon uPgrade, CMP, as described in chapter 2. Stub finding algorithms iterate over all wedges in the CMU and all regions (north, south, top and bottom) in the CMP requiring the number of hits to be greater than two, and furthermore that the number of layers with hits should be greater than two. All pairs of hits in layers 0 and 2 within a certain distance of each other are examined (7.5cm in the CMU and 12cm in the CMP). The line between the two hits is evaluated at the layer 1 and 3 radii to give a prediction for the location of hits in those layers, on the assumption that the layer 0 and 2 hits were the basis of a muon trajectory. The predictions are then tested against the locations of real hits and if one or two hits are found in those layers within 0.5cm for the CMU and 1.5cm for the CMP of the predicted position then a muon stub is formed. Stubs can be made up of either 3 or 4 hits. This procedure is repeated, beginning with layers 1 and 3 and this time testing the hit predictions for layers 0 and 2.

Hits of the ionisation particles on the CMU and CMP wires give their drift times which are converted to drift distances using the known drift velocity in the gas. A drift model can then be applied to the stubs to determine the muon trajectory more accurately than the linear assumption used so far. Using the drift model, the expected drift distance is calculated and a fit is performed to obtain the stub parameters. For each hit, the expected drift distance is compared to the measured distance and the parameters are adjusted to obtain the best match. This is an iterative process. The result is a set of stubs which are then ranked according to the number of hits and the χ^2 from the drift model fit. Duplicates, defined as stubs containing two or more hits in common, are eliminated by discarding the lower ranking stub. Track matches are then sought for the muon stubs. Each track is extrapolated to the radius of the CMU or CMP with energy loss and multiple

scattering effects being included. A χ^2-like quality variable, q, is evaluated for each track-stub pair and the combinations are ranked in order of quality. For each stub, the track with lowest q is chosen to be the matched track.

For the muon plus displaced track trigger, candidate muons are selected by imposing specific selection cuts. The cuts are summarised in table 3.2 and a more detailed discussion of cut variables follows here. Each of the muon identification cut variables is now discussed

Variable		Cut
p_T	$>$	4 GeV/c
Muon system		CMUP
Δx_{CMU}	$<$	15cm
Δx_{CMP}	$<$	20cm

Table 3.2: *Trigger selection cuts for muons.*

in turn:

p_T is the transverse momentum of the track which matches the muon candidate stub. This is required to be greater than 4 GeV/c. This value is chosen to gather the most b physics, subject to trigger bandwidth restrictions, as in the electron case [69].

Muon system Only the CMU and CMP muon chambers are used for identifying muons in the muon plus displaced track trigger. By requiring the muons to pass through both of these chambers, the configuration of which is shown in figure 2.10, and the 60cm layer of steel between them, the rate of fake muons arising from punch through from the hadronic calorimeter is cut down considerably and so the fake rate is very low. This has been studied [77] in the decay chain $D^{\star+} \rightarrow D^0\pi^+$ with $D^0 \rightarrow K^-\pi^+$ which gives a clean sample of D^0 mesons and hence clean sets of K's and π's, identified by their charge. The percentage of these K or π mesons with p_T greater than 4 GeV/c and less than 11 GeV/c which pass the muon identification requirements is $0.602\pm0.063\%$. The number of tracks in proximity to the D_s^- candidate which could

fake a muon in this way is on average 0.14. Assuming that these are Kaons, which have the higher fake probability, results in a contribution to the B_s^0 semileptonic sample of only 1 fake muon candidate.

$\Delta x_{CMU}, \Delta x_{CMP}$ are the distances, in the $x(r-\phi)$ plane, between the track and the muon stubs in the CMU and CMP detectors. For the CMU detector, this distance is required to be less than 15cm and in the CMP detector the cut is less stringent at less than 20cm, to allow for scattering in the intervening detector material and steel layer.

3.2.2 Displaced Track Requirements

In addition to requiring a lepton fulfilling the above requirements for either an electron or a muon, the trigger utilises the Silicon Vertex Trigger (SVT) to identify the presence of a track with sufficiently large momentum and impact parameter. In the D_s^- meson reconstruction, which will be discussed in section 3.5, one of the decay tracks of the candidate D_s^- will be required to have triggered the SVT. Since the D_s^- meson sought is expected to come from the decay of a B_s^0 meson, the impact parameter is expected to be large and, since the B is heavy, the decay products are expected to carry significant transverse momentum. The p_T is therefore required to be greater than 2GeV/c and the impact parameter, $|d_0|$, between 0.12mm and 1.00mm. The value of $|d_0|$ >0.12mm was chosen, using trigger studies [69], to maximise the B decay content of the sample whilst minimising the trigger cross-section. The upper cut of $|d_0|$ <1mm eliminates badly measured tracks and those coming from multiple $p\overline{p}$ interactions. It also eliminates background from Kaon decays [24].

The SVT track and lepton track are required, by the Level 3 trigger, to be different tracks. This is enforced in the Level 3 trigger by requiring that the tracks formed in Level 3 for the lepton and SVT track are not identified as the same track. Furthermore, there is an angular cut of $\geq 2^\circ$ between the lepton and SVT tracks to eliminate cases where the

Variable	Cut
track p_T	> 2 GeV/c
track $\|d_0\|$	$>120\mu$m and <1mm
$\Delta\phi(\ell, SVT)$	$\geq 2^\circ$ and $<90^\circ$
$M(\ell, SVT)$	<5 GeV/c^2

Table 3.3: *Trigger selection cuts for SVT (displaced) track and pairwise cuts between the SVT track and lepton.*

lepton and SVT tracks may originate from the same track but do not have the same track identity. In addition, an upper cut of 90° is imposed to try to ensure that the lepton and SVT track come from the same B meson [69]. As an aside, a displaced lepton trigger was also considered for CDF Run II and would indeed give enhanced B yields compared with a lepton which is not displaced. However, Monte Carlo studies showed that the lepton plus displaced track should be favoured since it yields more B decays [69]. Furthermore, the fraction of B decays is enhanced at Level 3 by requiring that the invariant mass of the lepton and SVT track is < 5 GeV/c^2. Since the trigger is designed to collect the semileptonic decays of b hadrons, the mass of two of its decay products cannot exceed any b hadron mass, which ranges from 5.2790 ± 0.0005 GeV/c^2 for the B^- to 6.40 ± 0.41 GeV/c^2 for the B_c^- . The cut therefore eliminates combinatorial background. All cuts on the SVT track, and the Level 3 "pairwise" cuts are summarised in table 3.3.

3.3 Preselection Cuts

The samples gathered by the muon and electron plus SVT trigger, described above, are passed through further filters before being used for reconstruction.

3.3.1 Event Filters

At present, before any analysis takes place the entire set of tracks is refit. There are several reasons for this. Firstly, the Layer 00 and ISL silicon hits are to be removed from the tracks. Both of these silicon tracking detectors require further study before being approved for physics analyses. The Layer 00 pedestals are not currently well understood, and furthermore, the alignments for both detector components are preliminary. Secondly, after dropping the Layer 00 and ISL hits, the tracks are to be refit accounting for energy loss and multiple scattering using different mass hypotheses. In the production software, the energy loss and multiple scattering is calculated using the pion mass as a default. In refitting, it is possible to choose several mass hypotheses: in this analysis the K, π, μ and e masses are used, providing four sets of refit tracks. A GEANT [78] material map of the CDF detector is used to calculate the amount of material through which a track has passed and hence the amount of energy loss and multiple scattering it is likely to have undergone. Thirdly, it is observed that the errors on COT track parameters are underestimated and so a scaling must be applied to the COT track error matrix [79]. Fourthly, the magnetic field of CDF's solenoid is corrected and an additional layer of material is added to the GEANT map of CDF. These corrections were established by scaling the magnetic field and thickness of the additional material layer in order to obtain the correct mass for the J/ψ meson [80, 81].

The trigger cuts are then re-imposed on the sample, using the refit quantities, using the SemileptonicB package [82]. This serves two purposes. The trigger lepton, which is not otherwise flagged, is identified and the SVT track is matched with an offline track reconstructed in the SVX. In addition, a small number of offline variables differ slightly from the Level 3 versions and so differences may arise. For example, the L_{shr} definition differs between offline and online since a faster algorithm is used in the trigger.

The electron sample at this stage contains conversion electrons, which are produced by the interaction of photons with detector material causing them to convert to e^+e^- pairs. Two variables are used to eliminate the conversion electrons. Firstly the angle between

conversion electrons is expected to be small and so electron candidates are excluded which have a nearby track such that $|\cot\theta_e - \cot\theta_{trk}| < 0.03$, where θ is the polar angle. Secondly, the separation between conversion electrons in the $r-\phi$ plane at the point where they are tangent, is expected to be small since the two conversion electrons originate from the same point. Therefore electron candidates are excluded which have another track within a distance of 0.2cm in the $r-\phi$ plane [83].

3.3.2 Track Filters

Each track is required to pass track quality cuts to ensure that all of the tracks used in the reconstruction are well measured. These are a minimum track p_T and minimum numbers of hits in the COT and SVXII to cut down on the number of tracks formed from random hits. These cuts are shown in table 3.4.

Variable	Cut
track p_T	> 0.5 GeV/c
number of COT axial hits	≥ 20
number of COT stereo hits	≥ 20
number of SVX hits	≥ 3

Table 3.4: *Track quality cuts required on all tracks, including the leptons, used in the reconstruction.*

3.4 Primary Vertex Reconstruction

It is necessary to have precise knowledge of the primary $p\bar{p}$ vertex in order to measure the B_s^0 decay length, since it is defined as the distance between the primary vertex and the secondary B_s^0 decay vertex.

In an event containing a B hadron, most of the observed tracks are from the decay

of the B itself. The other tracks to be found in such an event are typically from the soft underlying event and are typically low momentum tracks which curve tightly under the influence of the magnetic field and travel along the beamline. Tracks emanating from a B decay are displaced from the primary vertex. Therefore, determining the primary vertex position in a B event is difficult and is likely to be biased. The solution employed here is based on the run averaged beamline in a generic sample. This is calculated offline for each data acquisition run.

In order to obtain a run averaged beamline, a primary vertex finding algorithm is applied to each event in samples of generic jets with $E_T \geq$8 GeV. Through an iterative process, sets of tracks which are consistent with coming from a primary vertex are found. The first step is to fit a vertex for all tracks which pass some basic track quality cuts. Then, in a loop over all tracks, the χ^2 of each track with respect to the vertex is calculated. Tracks which have individual χ^2 exceeding a maximum value are removed and a new fit is performed. This iterative procedure is repeated until all remaining tracks have individual χ^2 values below the maximum, or until a minimum number of tracks has survived the cut. At this point, the vertex fit to the remaining tracks (in Run II the mean number of tracks remaining is $\sim$16) is the primary vertex. Multiple interactions in the $p\overline{p}$ bunch crossing can give rise to several vertices in an event and these are found by repeating the primary vertex finding procedure on tracks which were removed from the primary vertex fit. The beamline is the straight line which is fit through all primary vertices found during the run. The beamline is found to be offset from the centre of the detector, in x and y. At $z = 0$, a typical value of x_0 is -0.22cm and of y_0 is 0.44cm. It is also sloping in x and y as a function of z by approximately $x_{slope} = 0.6$mrad and $y_{slope} = -0.1$mrad [84]. The beam position has resolutions of σ_x=25.7$\pm$1.9μm and σ_y=25.8$\pm$1.7μm [56]. The primary vertex, for the purposes of this analysis, is found by first averaging the z_0 values of the lepton and D decay tracks, where z_0 is the z coordinate evaluated at the beamline. This gives a resolution in the z direction of $\sigma_z = 45\mu$m. The x and y positions are then located

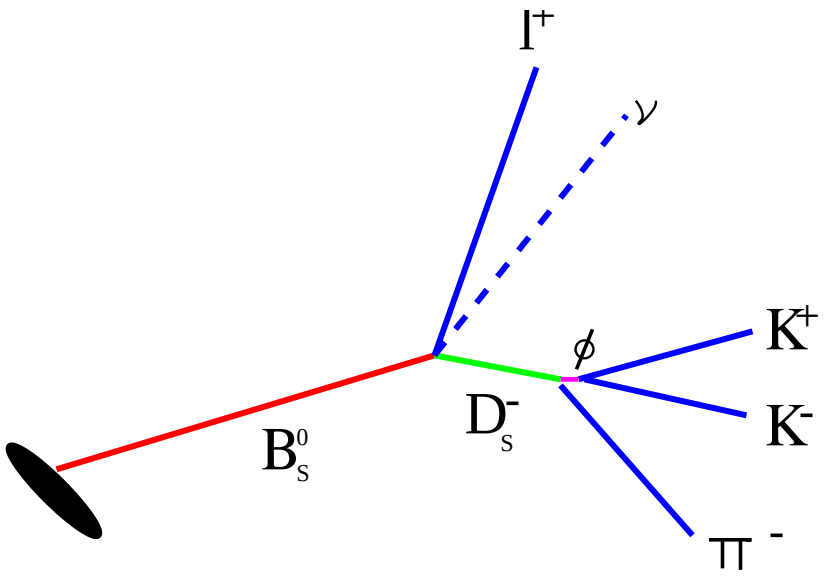

Figure 3.2: *Schematic of the B_s^0 semileptonic decay. The ϕ meson does not have any lifetime but is shown here to give a representation of the decay chain.*

by using the beamline equations:

$$x = x_{slope} \times z + x_0 \qquad\qquad y = y_{slope} \times z + y_0 \tag{3.3}$$

3.5 Signal Reconstruction

In the decay of interest, the B_s^0 meson decays to $\ell^+\nu_\ell D_s^-$, where the D_s^- is reconstructed through its decay to $D_s^- \to \phi\pi^-$ and $\phi \to K^+K^-$. A schematic view of the decay is shown in figure 3.2.

3.5.1 Partial B_s^0 Reconstruction

The optimisation of the selection cuts which are used in the partial B_s^0 reconstruction is detailed in [85].

The trigger lepton is identified by reapplying the trigger selection cuts, as described above. A cone around the lepton of size $\Delta R = \sqrt{(\Delta\eta)^2 + (\Delta\phi)^2} \leq 1.2$ is searched for

candidate pairs of oppositely charged tracks, each assigned the $K^{\pm}$ mass, which are used to reconstruct the ϕ meson. Simulation samples show that the cut at $\Delta R \leq 1.2$ does not eliminate signal. The ϕ resonance is very narrow and so a tight mass constraint can be applied, contributing to a large signal to background ratio. If the invariant mass of the pair of tracks lies within the ϕ mass window, each remaining track which passes the track cuts defined in section 3.3.2 and further cuts discussed below is added and assigned the π^- mass. One of the candidate D_s^- decay products must be an SVT track. A loose cut is applied to the D_s^- candidate mass, requiring it to be in the window $1.8 \rightarrow 2.05$ GeV/c^2. This is to allow signal and sideband regions to be defined in the D_s^- mass for use in the lifetime fitting procedure which is described in chapter 5. The D_s^- decay position is reconstructed by vertexing together its decay products, $K^+K^-\pi^-$, using VertexFit, a vertexing package which varies the track parameters within their errors and performs a χ^2 minimisation to determine where the tracks meet and gives a quantified probability [86]. To determine the B_s^0 decay vertex the D_s^- candidate trajectory is intersected with that of the lepton and their intersection point gives the B_s^0 decay vertex. The B_s^0 decay distance in the transverse plane, L_{xy} , is then given by the distance in the xy plane between the event's primary vertex and the B_s^0 decay vertex. Similarly, the D_s^- decay distance is that between the B_s^0 and D_s^- decay vertices. The proper lifetime is given by the ratio of this length to the meson's p_T multiplied by its mass: $c\tau = L_{xy}m/p_T$. Further discussion of this is to be found in chapter 5.

The detailed requirements for a D_s^- candidate are as follows [85]:

- At least one of the three tracks, K^+, K^- or π^-, should be the SVT matched track
- $p_T(K) > 0.8$ GeV/c
- $p_T(\pi) > 0.35$ GeV/c
- $Q(\ell)=-Q(\pi)$ In a decay where the D_s^- and ℓ^+ come from the same B_s^0 the π and ℓ must, by simple charge conservation, have opposite charge.

- $\Delta R(\text{track}, \ell) \leq 1.2$ for each of the decay products of the D_s^- , K^+, K^- and π^-.

- $|\cos\psi| > 0.4$, where ψ is the helicity angle between the K^+ and D_s^- in the rest frame of the ϕ meson, as shown in figure 3.3. This is a useful variable since the D_s^- and π^- are spin 0 particles and the ϕ meson has spin 1 and so information on the D_s^- is preserved. The angle ψ is thus expected to have a $\cos^2\psi$ distribution in D_s^- events and to be flat in combinatorial background events, as shown in figure 3.4.

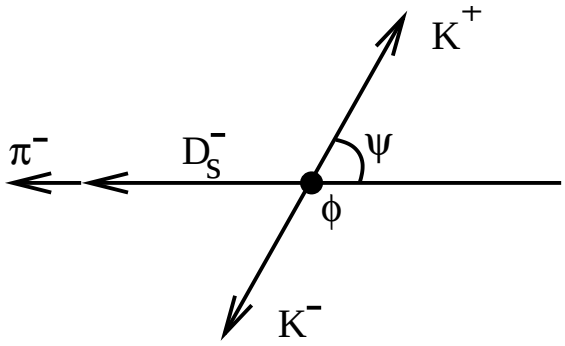

Figure 3.3: *The helicity angle is defined as the angle between the* K^+ *and* D_s^- *in the rest frame of the* ϕ *meson.*

- $|m(K^+K^-) - 1.0195| < 0.01$ GeV/c^2. This range is based on the PDG [1] values for the ϕ mass, 1.0195$\pm$0.00002 GeV/c^2, and width, $\Gamma_\phi = 4.26 \pm 0.05$MeV/c^2. The narrowness of the resonance contributes to the cleanliness of the resulting D_s^- mass peak (S/B=3.5). The invariant mass of the ϕ candidates is shown in figure 3.5.

- $3.0 < m(\ell^+ D_s^-) < 5.0$ GeV/c^2 to exclude combinatorial backgrounds. The upper limit of 5 GeV/c^2 excludes combinatorial background since the mass of the B_s^0 is not fully reconstructed.

- $L_{xy}(D_s^{PV}) > 400\mu m$, where $L_{xy}(D_s^{PV})$ is the distance between the D_s^- decay vertex and the primary vertex in the transverse x-y plane. Since D_s^- mesons are long-lived ($\tau_{D_s^-} = 0.49 \pm 0.01$ps), this cut reduces combinatoric background to the D_s^- .

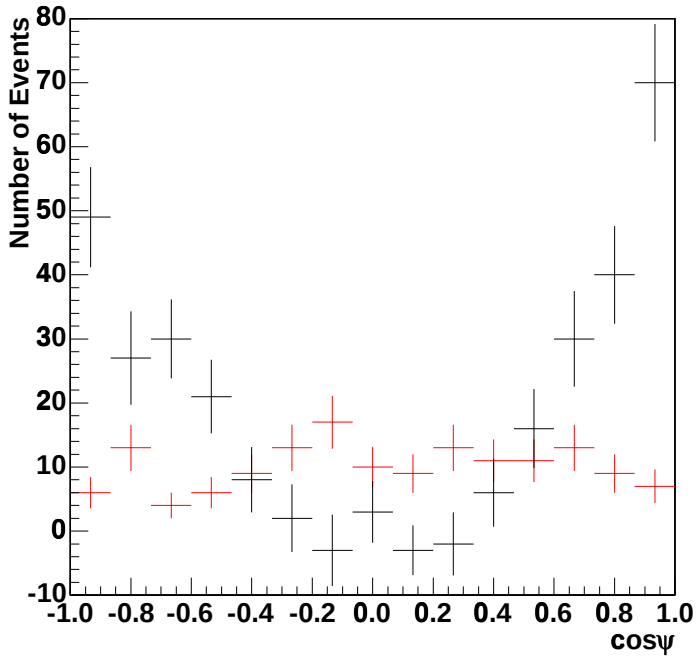

Figure 3.4: *The distribution of the cosine of the helicity angle, ψ, for signal (black) and background (red) events. To obtain the signal events, the distribution in the sideband regions defined in section 4.5 is subtracted from the distribution in the signal region.*

- $\sigma(L_{xy}(\mathrm{B_s^0}) * m(\mathrm{B_s^0})/p_{\mathrm{T}}(\mathrm{B_s^0}) < 400\mu m$ This cut removes events with large errors on the $\mathrm{B_s^0}$ decay distance.
- $\mathrm{Prob}(\chi^2_{\mathrm{r}\phi}) > 10^{-4}$ for the $\mathrm{B_s^0}$ vertex. The vertexing procedure of the $\mathrm{D_s^-}$ meson with the lepton returns a probability that a χ^2 function has a value greater than the actual χ^2 of the fit. Hence smaller χ^2 values give larger probabilities.
- $\chi^2_{\mathrm{r}\phi} < 40$ for the $\mathrm{D_s^-}$ vertex.
- $-0.01 < c\tau(\mathrm{D_s^-}) < 0.10\mathrm{cm}$ is required in order to eliminate combinatorial background since the $\mathrm{D_s^-}$ is long-lived.

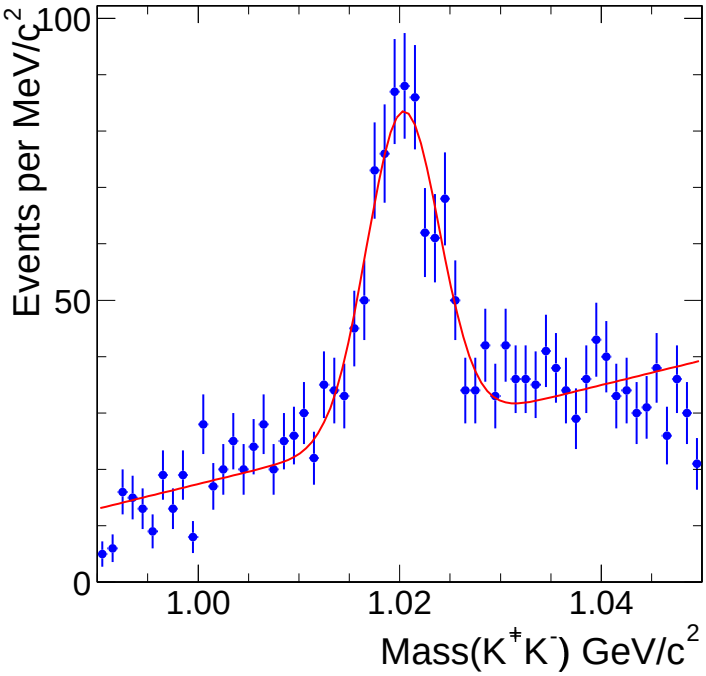

Figure 3.5: *The invariant mass of the ϕ meson candidates.*

3.5.2 Determination of D_s^- Mass

The invariant mass distribution of the D_s^- candidates which pass the cuts detailed in this chapter is shown in figures 3.6 and 3.7 for the electron+SVT and muon+SVT samples respectively. The figures show the invariant mass distribution for "right sign", $Q(\ell)=-Q(\pi)$, and "wrong sign", $Q(\ell)=+Q(\pi)$, combinations. A signal in the wrong sign combination would be an indication that there are D_s^- meson candidates forming B_s^0 candidates with a lepton which does not come from the same B_s^0 decay. Figures 3.6 and 3.7 show no evidence for a signal in the wrong sign distribution. There are 364 ± 19 D_s^- candidates found in the D_s^- mass peak in the right sign e+SVT sample and 541 ± 33 in the μ+SVT sample. Overlaid is the result of a fit which comprises a Gaussian distribution to describe the signal and a first-order polynomial to describe the combinatoric background. In addition, a further Gaussian distribution is added to fit the Cabibbo-suppressed decay $D^- \to \phi\pi^-$

which is the lower visible peak centred around 1.869 GeV/c^2. There are 96 ± 13 D^- candidates in the e+SVT sample and 154±20 in the μ+SVT sample. Note that the ratio of the number of events in these peaks is not expected to equal the ratio at production since the D^- meson has a shorter lifetime than the D_s^- and is suppressed by the cut on the $c\tau$ of the D_s^- candidate. The muon and electron samples are combined to give the invariant mass distribution shown in figure 3.8.

The resulting values for the D_s^- mass are shown in table 3.5. These agree quite well with the PDG value [1] of 1.9683± 0.0005 GeV/c^2. The combined result differs from the expected value by 2.7 standard deviations but this measurement does not include systematic errors.

Sample	D_s^- Mass (GeV/c^2)	D_s^- Gaussian Width (MeV/c^2)
Muon	1.9661±0.0005	8.3±0.4
Electron	1.9674±0.0006	8.2±0.6
Combined	1.9666±0.0004	8.4±0.3

Table 3.5: *D_s^- mass determined from fits to the data shown in figures 3.6 to 3.8. Errors are statistical only.*

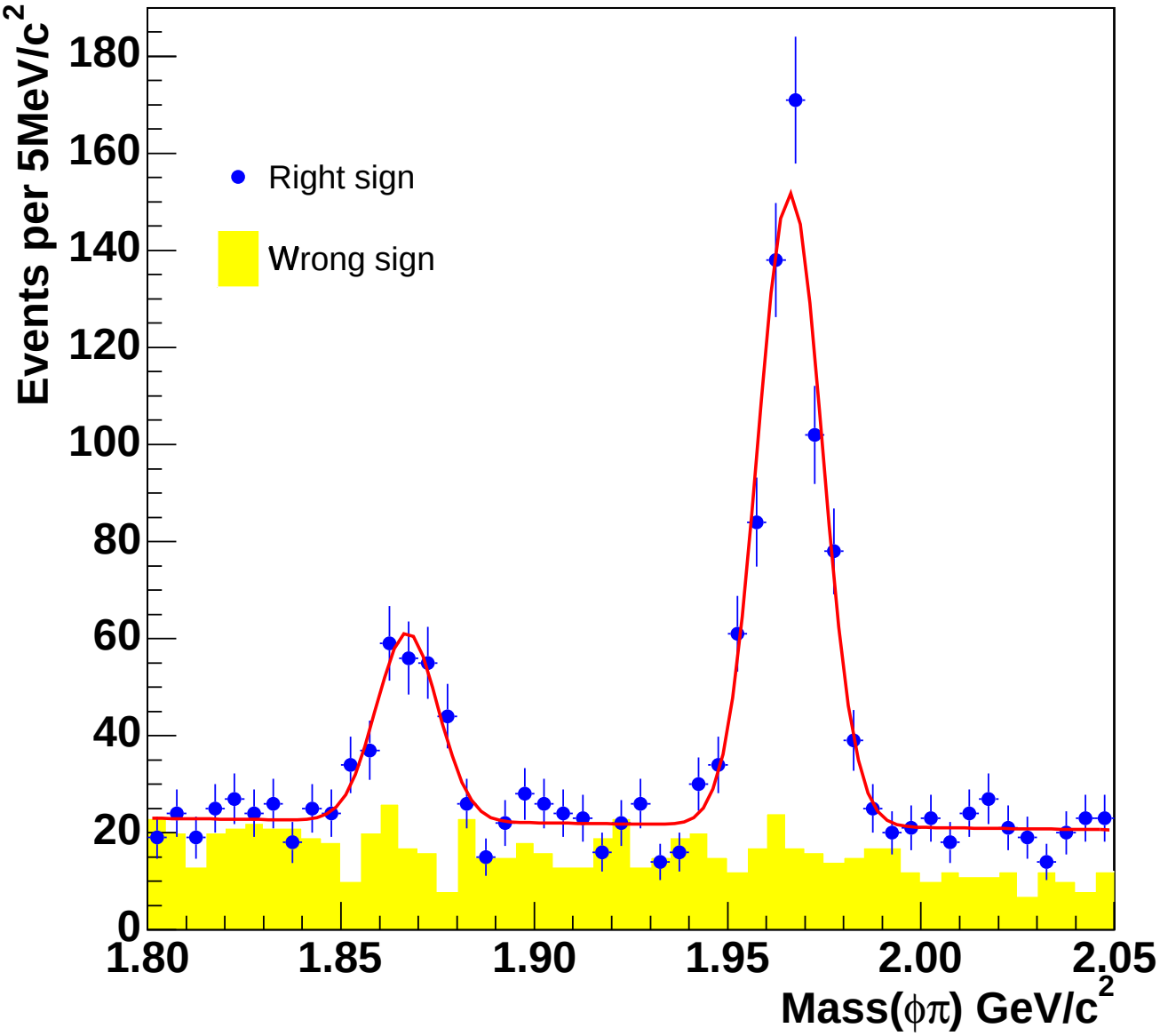

Figure 3.6: D_s^- *candidate mass from the muon sample. There are* 541 ± 33 *events in the* D_s^- *peak, centred around* $1.9661 \pm 0.0005\,GeV/c^2$ *. The lower peak is from* $D^- \to \phi\pi^-$ *decays.*

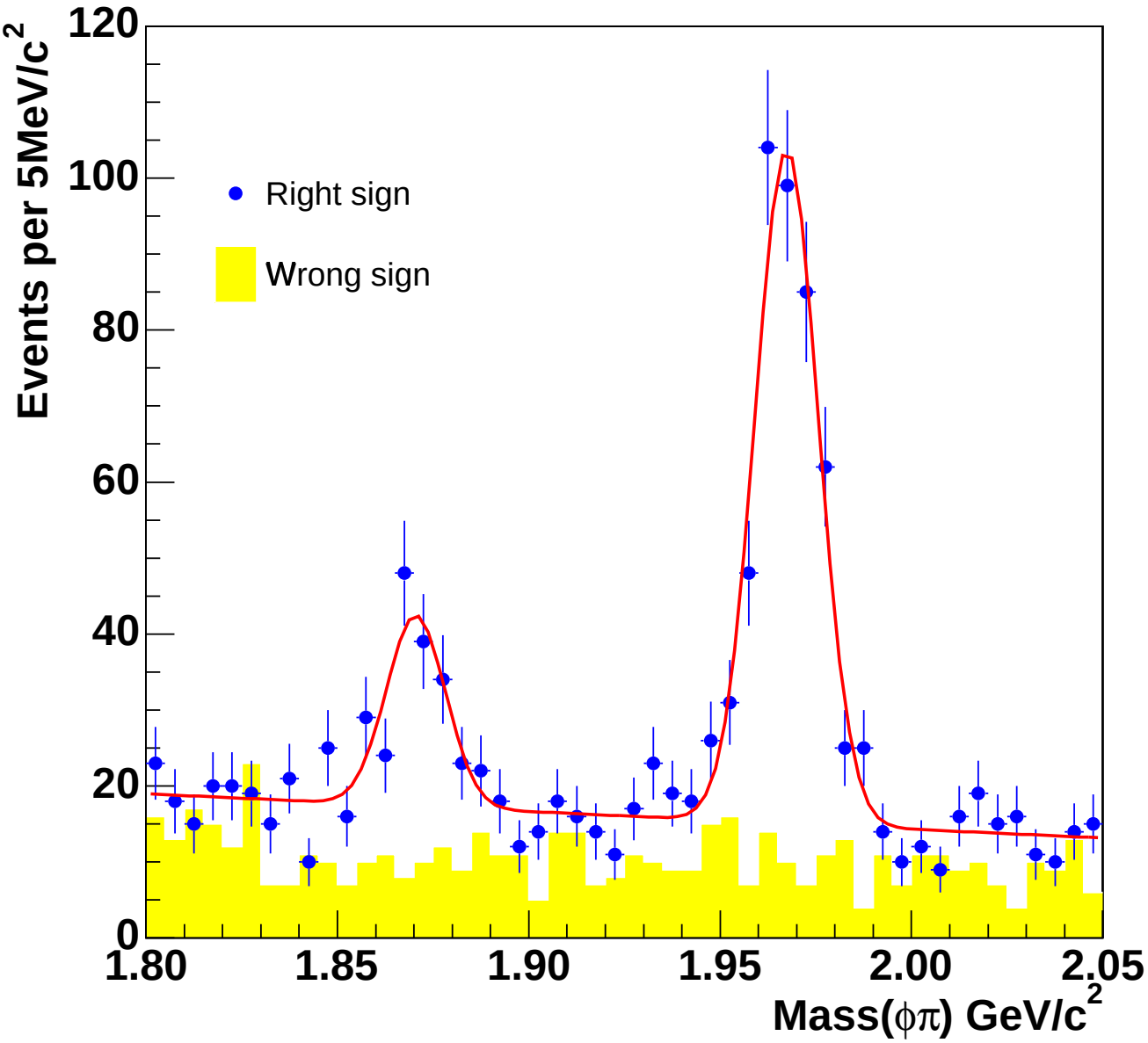

Figure 3.7: *D_s^- candidate mass from the electron sample. There are 364 ± 19 events in the D_s^- peak, centred around $1.9674 \pm 0.0006 GeV/c^2$. The lower peak is from $D^- \to \phi\pi^-$ decays.*

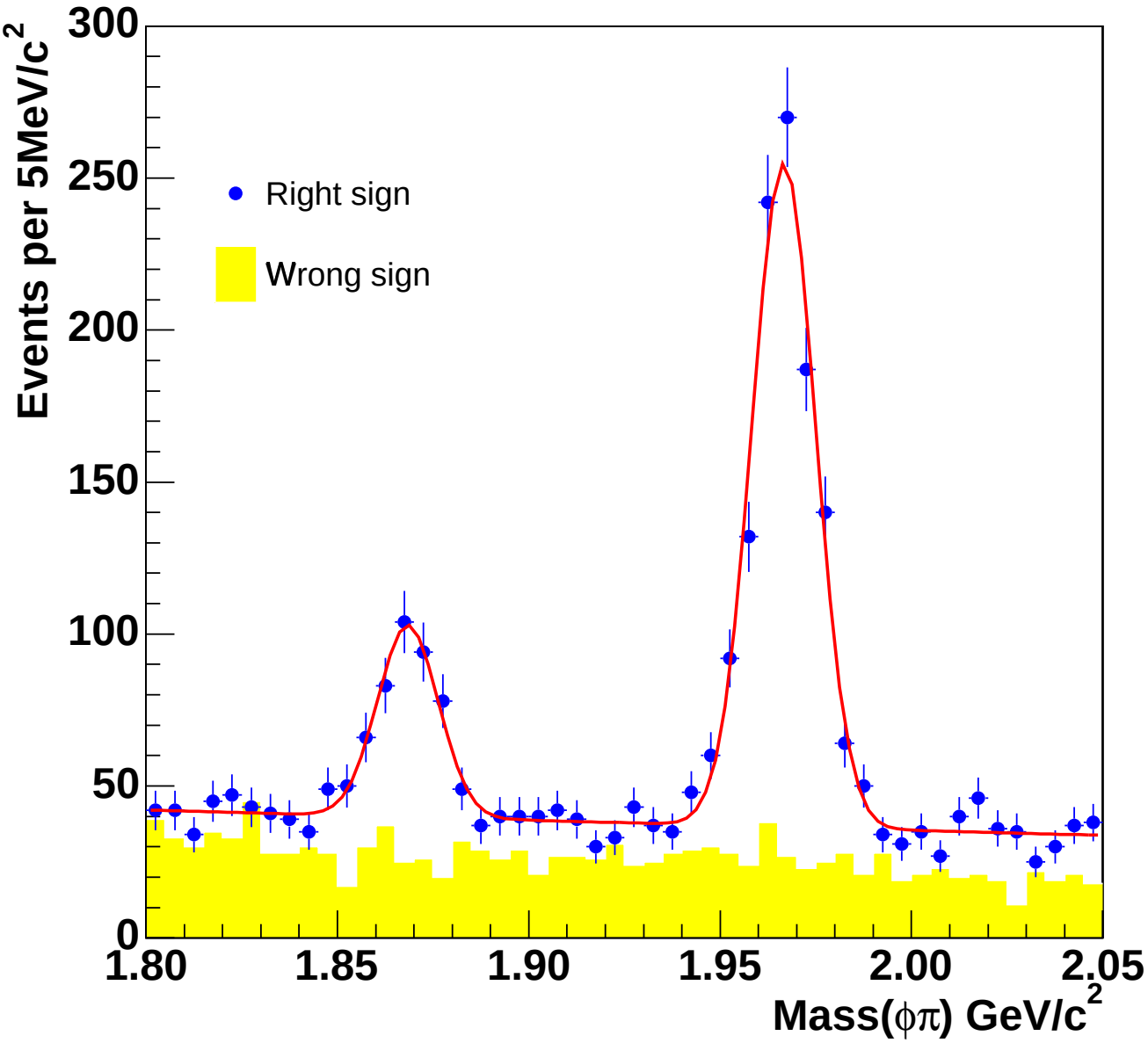

Figure 3.8: D_s^- *candidate mass from the combined electron and muon samples. There are* 905 ± 42 *events in the* D_s^- *peak, centred around* $1.9666 \pm 0.0004 GeV/c^2$. *The lower peak is from* $D^- \to \phi\pi^-$ *decays.*

Chapter 4

Event Simulations

The use of simulated event samples is an important component of the B_s^0 semileptonic lifetime measurement. The fit to the pseudo-proper lifetime distribution of B_s^0 candidates requires two inputs from the event simulations, which can not be established using data samples alone. Simulations are used to model the production of particles in $p\bar{p}$ collisions and their decay chains. By using simulations, the production and decay of particles are completely controlled.

The first Monte Carlo input to the lifetime fit is a correction factor for the missing neutrino in the B_s^0 meson reconstruction. A B_s^0 semileptonic decay, $B_s^0 \to \ell^+ \nu_\ell D_s^-$, is partially reconstructed, as described in section 3.5, by first reconstructing a D_s^- candidate and then intersecting its trajectory with that of a trigger lepton. The neutrino from the B_s^0 decay is, in practice, undetectable and so its momentum is lost. Comparisons between data and simulation distributions, described in section 4.5, show that the kinematics derived from the calculated B momentum spectrum and ISGW model [36], described in section 1.5, are sufficiently well-modelled to be relied upon to extract a correction factor, K. This is defined in equation 3.2. The K factor distribution is described in detail in section 5.2.

The second Monte Carlo input is a lifetime weighting distribution. The trigger, described in section 3.2, which is used to collect the sample under consideration requires

the presence of a track with an impact parameter which is in the range 0.12 to 1.00 mm. This introduces a selection bias which excludes B_s^0 mesons which travel short distances and B_s^0 mesons which travel very far. This results in an interesting bias and sculpting of the distribution of $c\tau$ values. In Monte Carlo, the usage of trigger simulations enables the effect of the bias to be understood and it is quantified by extracting the trigger efficiency as a function of B_s^0 meson lifetime. This is described in further detail in section 5.3.

This chapter describes the simulation techniques and samples which are used in the subsequent chapters of this thesis.

4.1 Simulation Chain

A flowchart of the simulation chain is shown in figure 4.1. The Monte Carlo event generation is performed by `Bgenerator` [87], which is a parametric generator of b (and c) quarks developed by the CDF collaboration. The generation is discussed in section 4.2. The decay model for the B_s^0 and D_s^- mesons is handled through either the `QQ` [90] or the `EvtGen` [91] decay package, described in section 4.2.

For the detector and trigger simulation, two complementary approaches are used. In the first approach, the generator level track parameters are smeared according to the average resolutions which are observed in data. This is a very simple model which contains a small set of tunable parameters, each of which is measurable in data. Due to its simplicity, this model is not CPU intensive and therefore has the advantage of facilitating, with relative speed and ease, the study of many alternative settings. In the second, more CPU intensive, approach, detector effects are modelled more accurately by GEANT4 [78] and samples produced in this way enable studies of higher order effects including detector coverage and beam and luminosity dependent conditions. The first of these simulations is henceforth referred to as *parametric*, while the second is called *full* simulation. These are described in sections 4.3 and 4.4.

Apart from the simulation of B_s^0 events with simulation settings which are as close as

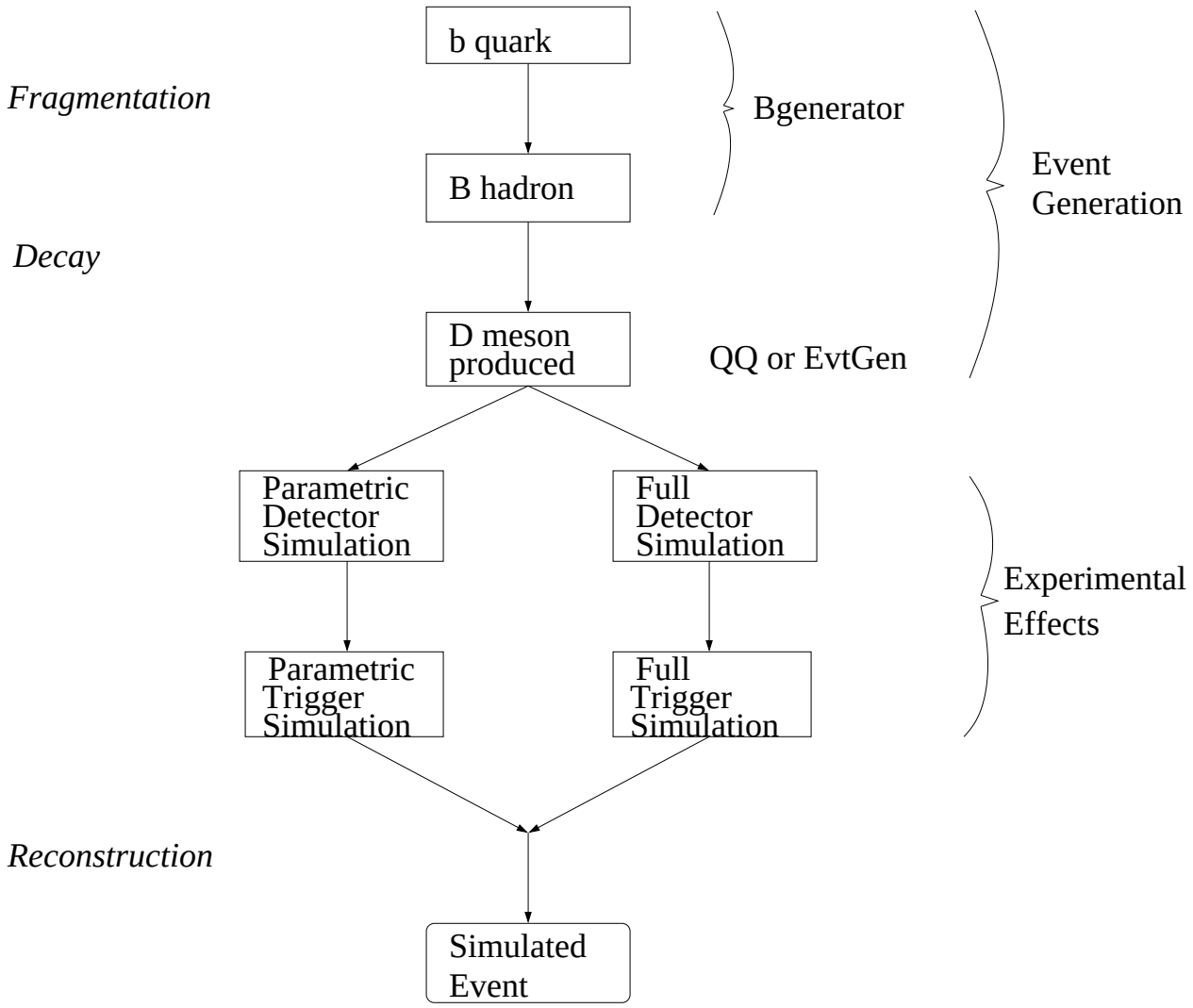

Figure 4.1: *Simulation chain for the generation, decay and experimental simulation of events containing B mesons.*

possible to the known theoretically and experimentally determined values, several other samples are generated where the decay, trigger or detector conditions are varied in order to evaluate systematic effects. These samples rely on the two types of detector and trigger simulation described in this chapter and on the physics models mentioned above, and will be described in chapter 6 which is devoted to the discussion of systematic effects.

In order to have confidence in the simulation for the purpose of extracting the dis-

tribution of K factor values and the trigger bias function, the simulation samples are required to be validated by comparisons with data. Section 4.5 describes the comparisons made between sets of variables including basic kinematic observables, impact parameter distributions and correlations. These quantities are compared among the three samples; data, parametric and full simulations, after applying the reconstruction cuts described in section 3.5.

4.2 Event Generation and B Decays

The Monte Carlo events are generated using the `Bgenerator` package. This gives the choice of producing either one or two b (or c) quarks using the NLO matrix element from [88] or [89]. For this analysis, only one quark, b or $\bar{\mathrm{b}}$, is generated, for simplicity. Two quarks are required only for studies involving two B mesons, such as mixing studies. The b or $\bar{\mathrm{b}}$ quark is generated according to calculated transverse momentum (p_{T}) and pseudorapidity (η) spectra and is required to have a minimum p_{T} of 4.5 GeV/c and a maximum $|\eta|$ of 1.3. `Bgenerator` also handles the fragmentation of the quark into a specific b hadron, in this case a $\mathrm{B_s^0}$ meson. The Peterson function (see equation 1.10) is used to calculate the fraction of the quark's momentum which is retained by the hadron. `EvtGen` is then used as the default decay package. There are two reasons for this choice. Firstly, `EvtGen` is more accurate in modelling the Dalitz phase space structure of the decays whereas in the `QQ` package, the resonant and non-resonant branching fractions are scaled so that their contributions to the inclusive rate equals its PDG value [90] but interference between identical final states is not included. Secondly, `EvtGen` uses a more recent and accurate version of the ISGW decay model [37] for handling the semileptonic decays of the $\mathrm{B_s^0}$ meson as described in section 1.5. The decays included in this analysis are

$$
\begin{aligned}
\mathrm{B_s^0} &\rightarrow \ell^+\nu_\ell \mathrm{D_s^-} \\
\mathrm{B_s^0} &\rightarrow \ell^+\nu_\ell \mathrm{D_s^{\star -}} \\
&\qquad\qquad \hookrightarrow \mathrm{D_s^-}\gamma \\
\text{with} \quad \mathrm{D_s^-} &\rightarrow \phi\pi^- \\
&\qquad\quad \hookrightarrow K^+K^-
\end{aligned}
$$

The branching ratios come from experimental measurements, where available [1], and theoretical predictions taken from the ISGW model [37]. It is assumed that the semileptonic branching ratios for the $\mathrm{B_s^0}$ are the same as for the $\mathrm{B_d^0}$. The total semileptonic branching ratio for the $\mathrm{B_d^0}$ is 10.5±0.8% [1]. Of this, 2.14±0.20% is accounted for by $\mathrm{B_d^0} \rightarrow \ell^+\nu_\ell \mathrm{D}^-$ decays and 5.53±0.23% by $\mathrm{B_d^0} \rightarrow \ell^+\nu_\ell \mathrm{D}^{\star -}$ decays. In the latter decay, the $\mathrm{D}^{\star -}$ further decays to a D^- meson and γ (BR=94.2±2.5%) or π^0 (BR=5.8±2.5%). The remaining decays are attributed to $\mathrm{B_d^0} \rightarrow \ell^+\nu_\ell \mathrm{D}^{\star\star -}$. The $\mathrm{D}^{\star\star -}$ mesons are the orbitally excited, P-wave D mesons[1]: $\mathrm{D_1^-(L)}$, $\mathrm{D_0^{\star -}}$, $\mathrm{D_1^-(H)}$, $\mathrm{D_2^{\star -}}$. The relative branching fractions for the individual $\mathrm{D}^{\star\star -}$ mesons are not well understood for the $\mathrm{D_s^-}$ system. The $\mathrm{D}^{\star\star -}$ mesons undergo a strong decay which is governed by isospin. This predicts that one third of decays are to charged D mesons and the remaining two thirds of decays are to neutral D mesons and so approximately only 10% of the $\mathrm{D_s^{\star\star -}}$ decays result in a $\mathrm{D_s^-}$ meson. These states are poorly understood and so are not taken into account here. In summary, the branching fractions of the $\mathrm{B_s^0}$ which are used here are:

$$\mathrm{BR}(\mathrm{B_s^0} \rightarrow \ell^+\nu_\ell \mathrm{D_s^-}) = 2.14\%$$

$$\mathrm{BR}(\mathrm{B_s^0} \rightarrow \ell^+\nu_\ell \mathrm{D_s^{\star -}}) = 5.53\%$$

[1]The two $\mathrm{D_1^-}$ states, $^1\mathrm{P_1}$ and $^3\mathrm{P_1}$, have the same quantum numbers and therefore they mix. The two physical states are distinguished by their masses, $\mathrm{D_1^-(L)}$ and $\mathrm{D_1^-(H)}$.

4.3 Parametric Detector and Trigger Simulation

Detector and trigger simulation are the next steps in the simulation chain. The parametric simulation is performed by the `GenTrig` [92, 93] detector and trigger simulation. `GenTrig` is a set of modules which takes the events generated by `Bgenerator` and applies a simple detector model, including the tracking and muon chambers, together with the smearing of variables. The primary vertex location is smeared according to Gaussian distributions of widths 25 μm in the x and y directions. All stable charged particles in the generated event are formed into simple tracks, which hold the charge, vertex, η, p_{T}, $\mathrm{p_z}$, ϕ_0 and $\mathrm{d_0}$ information. The hardware and trigger simulation then operates on these simple tracks. The CDF triggers are described in 2.2.4 and in detail in [58]. The `GenTrig` simulation is now discussed.

4.3.1 Track Trigger Simulation

The following modules are used to simulate the displaced vertex trigger component of the muon plus displaced track trigger.

XFT: The eXtra Fast Tracker examines tracks with p_{T} greater than 1.5 GeV/c, in each ϕ bin of 1.25°, and retains the highest p_{T} track per bin. `GenTrig` mimics this behaviour and uses the correct p_{T} smearing, $\sigma(p_{\mathrm{T}})/\mathrm{p_T^2} = 0.015$ GeV^{-1}c, together with the discretisation of $\phi = 1.5$mrad and applies a track finding efficiency of 97%.

XTRP: The eXTRaPolator unit passes only the two outermost tracks with respect to COT superlayer 6, in each ϕ bin of 15°, which have momenta greater than 2 GeV/c to the Level 1 trigger logic simulation. `GenTrig` applies the same requirements and segmentation. For the lepton plus displaced track sample this is the only requirement placed on the track at Level 1.

SVXII and SVT: Tracks which pass the Level 1 trigger are extrapolated through a model of the Silicon VerteX detector, SVXII. This model comprises five layers

of Silicon at the correct radii and with the correct length in z. Gaps between Silicon ladders are also modelled. Hit efficiencies of the Silicon detector are taken into account by applying the efficiencies found in data per Silicon layer. Pattern recognition and overall efficiencies due to requiring hits in four layers result in a total efficiency of 87.62% per track. The Silicon Vertex Trigger, SVT, requirements are then enforced, namely 0.12mm$< d_0 <$1.00mm and p_{T}>2 GeV/c. It is important that the simulation models correctly the correlation between the impact parameters as measured by the SVT and SVXII. This is because the track which triggers the SVT is matched with an offline reconstructed track using SVXII information. The tracks are matched by examining their parameters, and so the SVT and SVXII impact parameters must be correlated to ensure that the correct tracks are matched. This is achieved by the smearing of the primary vertex. The correlation between the SVT and SVXII impact parameters is shown in figure 4.2 and is measured to be 0.812±0.004 in the parametric simulation. In data the correlation is 0.82 [94]. The correlation is defined by

$$\mathrm{Cor} = \frac{\mathrm{Cov}(x,y)}{\sqrt{\mathrm{Var}(x)\mathrm{Var}(y)}} \tag{4.1}$$

where

$$\mathrm{Cov}(x,y) = \frac{1}{N}\sum_i (x_i - \bar{x})(y_i - \bar{y}) \tag{4.2}$$

$$\mathrm{Var}(x) = \frac{1}{N}\sum_i (x_i - \bar{x})^2 \tag{4.3}$$

4.3.2 Muon Trigger Simulation

The following modules are used to simulate the muon component of the muon plus displaced track trigger.

XFT: For triggering on muons, no cuts are applied to the XFT tracks except that they should originate from a generator, truth level, muon. All XFT tracks are passed to the XTRP.

XTRP: The XTRP extrapolates XFT tracks to the muon chamber radius taking the magnetic field, multiple scattering and energy loss into account by using a look-up table. This indicates which muon chambers should be checked for track-stub matching.

CMU: The geometry of the Central MUon chamber is simulated by 24 towers, each subtending 15° in ϕ, and implements the gaps between towers. In this way, the tower which is hit by the extrapolated track is determined. In practice, there is a cut on the time allowed for the candidate muon to travel to the CMU radius. This corresponds to a cut on p_{T} in the absence of multiple scattering. The trigger turn-on curve efficiency resulting from this is modelled and parameterised in `GenTrig` using input parameters determined in data.

CMP: The muon track is also required to be within the acceptance region of the Central Muon uPgrade [95].

The author of this thesis contributed to the `GenTrig` package by providing an implementation of the muon plus displaced vertex trigger using the existing simulation described above.

The trigger cuts given in section 3.2.1 are applied by `GenTrig` and in section 4.5 it is demonstrated that kinematic and other quantities are modelled well by the `GenTrig` simulation.

4.4 Full Detector and Trigger Simulation

As an alternative to the parametric simulation, a full simulation of the detector and triggers is available, based on `GEANT4` [78]. The events are generated and decayed as described in 4.2 and then passed to the full simulation which is now described.

Since the full simulation is substantially more CPU intensive than the parametric simulation, loose kinematic requirements are made at generator level, prior to applying

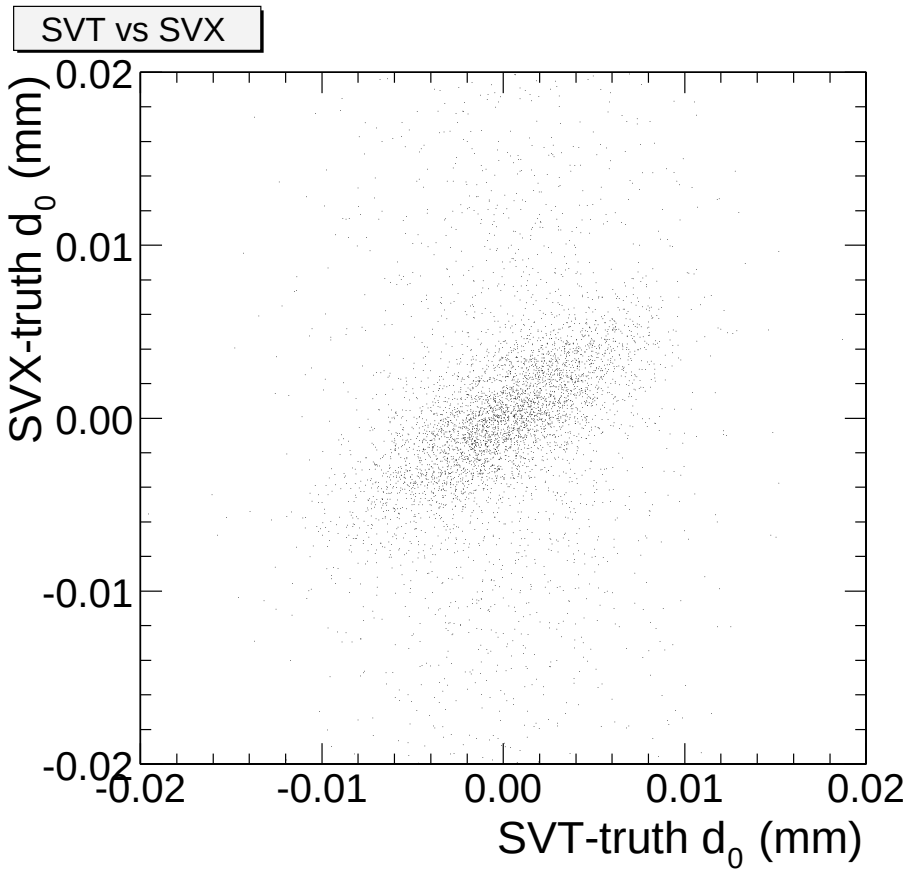

Figure 4.2: *Correlation between SVT and SVX impact parameters in the parametric simulation. The quantity shown is the difference between the true d_0 and the d_0 given by the simulation for SVX or SVT. The correlation value is 0.812±0.004.*

the full detector and trigger simulation. This relieves the burden of having to apply the CPU intensive detector simulation to all of the generated events. The preselection requires the presence of a generator, truth level, lepton (either μ or e) with Monte Carlo truth level p_{T} greater than 3.8 GeV/c and $|\eta|$ less than 1.2. No preselection is applied for a displaced track.

Events which pass these requirements are then passed to a full `GEANT4` simulation of the detector. `GEANT4` is programmed with the full detector geometry and tracks particles through the detector materials, applying models for the physics processes involved in

the interactions of particles with matter. The detectors' response to these tracks is also modelled by `GEANT4`. This simulation contains a full and accurate description of the CDF detector geometry, including misalignment effects of the Silicon detector at the level of individual ladders, and the removal of dead or hot (constantly noisy) Silicon detector channels according to the database information gathered in a dedicated calibration run which can be specified for the simulation.

The database information also provides the beamline positions and widths for a specified run number. In addition, the trigger conditions, including the SVXII and SVT configurations, can be simulated according to run number. This can have a large effect on which events are triggered since the configuration of Silicon ladders which are switched on and included in data taking varies due to intermittent problems with individual ladders. `TRGSim++` fully emulates the Level 1 and Level 2 trigger conditions [96], reconstructing the SVT banks (SVTD) according to the simulated run number, while a standalone module, `svtfilter`, applies the Level 2 trigger selection of the lepton plus displaced vertex trigger [97].

At Level 2, `TRGSim++` applies the emulation of the SVT, with the same configuration used for the actual data taking in the real detector. In addition, the actual beamlines measured by the SVT for the configuration being simulated are used to provide the beamspot used in the simulation and hence to calculate the impact parameter of the SVT trigger tracks.

The only expected difference between full detector simulation and real data is that the detector alignment which is used to position the detectors in the GEANT4 model is only as good as the current alignment knowledge and is not necessarily an exact match for the actual positions of detectors. The determination of alignments of the CDF detector is described in 6.2.1.

It is important for the SVT-SVXII track matching that the simulation models accurately the correlation between the impact parameters measured by the SVT and the SVXII detector. The correlation between these variables proves that the beamline used

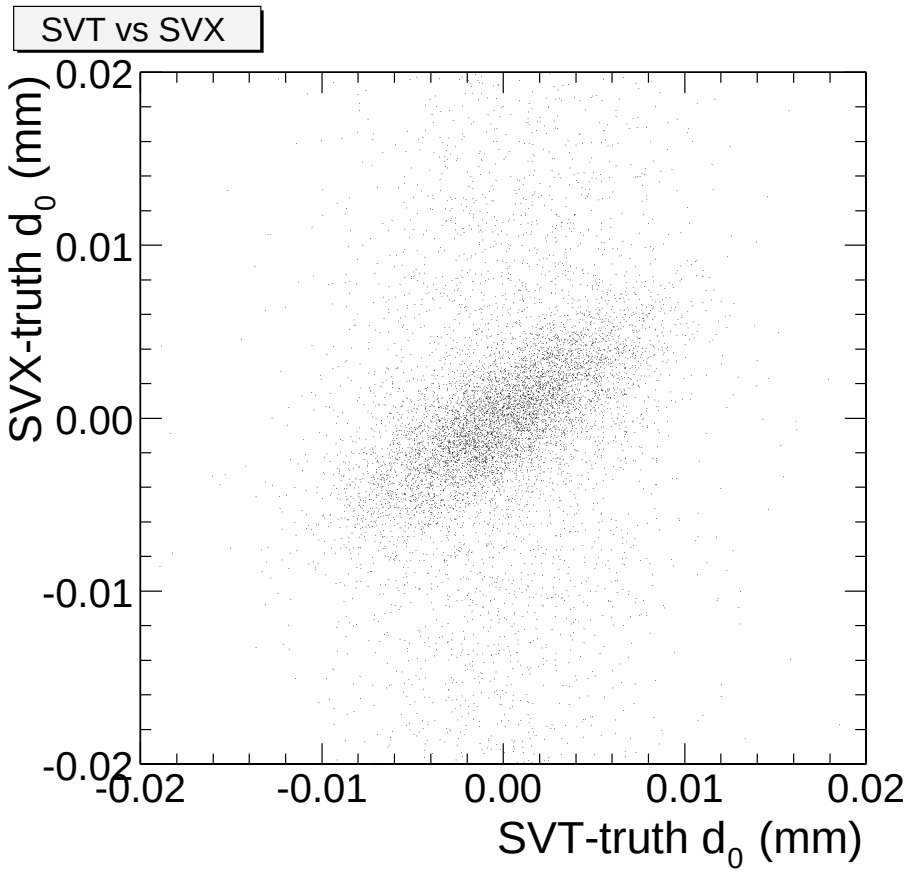

Figure 4.3: *Correlation between SVT and SVX impact parameters in the full simulation. The quantity shown is the difference between the true d_0 and the d_0 given by the simulation for SVX or SVT. The correlation value is 0.77.*

in the simulation of the SVXII and SVT devices is the same. The distribution is shown in figure 4.3.

After the trigger simulation, the standard CDF reconstruction code is applied, and the sample can be treated in the same way as real data. In particular, the same reconstruction procedure and selection cuts are applied on the full simulation sample as those used in the real data sample. A difference between this sample and the real data is that the Level 3 trigger is not applied in the simulation. Specifically, this means that the pairwise cuts (see table 3.3), are not applied. This can be overcome by the use of the offline trigger

re-confirmation as part of the reconstruction code to ensure that the Level 3 cuts are applied since these selections are equal to or stricter than those applied at Level 3.

4.5 Comparison of Simulations to Data

This B_s^0 lifetime analysis relies strongly on distributions taken from the simulations described thus far. It is therefore necessary to ensure that the simulations emulate the data very well and to quantify the agreement between them, especially for distributions directly related to the K factor and lifetime bias distributions. Therefore, comparisons are made between the parametric and full simulation samples and between each of these with the data sample for many quantities.

All of the simulations described are of the $B_s^0 \to \ell^+ \nu_\ell D_s^-$ signal only. Background studies are described in section 8.3.4. In data there is a combinatorial background contribution which is expected to contribute to the D_s^- candidates within the D_s^- mass peak. A method of extracting distributions from the data which are representative of the signal behaviour alone is sideband subtraction. The premise of this method is that the background found under the mass peak arises from the same physics as those to the sides of the mass peak. For this purpose, and for the lifetime fitting technique described in chapter 5, sideband and signal regions are defined by:

$$\begin{aligned} \text{sideband} : 1.908 &< M(D_s^-) < 1.933 \\ 2.000 &< M(D_s^-) < 2.025 \\ \text{signal} : 1.941 &< M(D_s^-) < 1.992 \end{aligned}$$

The significance of these numbers is that the signal region is $\pm 3\sigma$ around the central D_s^- fit mass value and the sidebands are 3σ in width each taken from regions separated by 1σ from the signal region. These sideband regions are expected to contain as many background events as the area underneath the D_s^- mass peak since the invariant mass distribution on both sides of the D_s^- mass peak is described by a single linear fit (see

figure 3.8). Many distributions were examined to ensure that the simulations reproduce the behaviour seen in the data. These were selected because they are deemed important for the lifetime measurement. The list of distributions examined is: p_{T} of the individual decay products $(\ell^+, \mathrm{K}^+, \mathrm{K}^-, \pi^-)$ and $\ell^+\mathrm{D}_{\mathrm{s}}^-$, d_0 of the individual decay products, cone distribution $(\Delta R = \sqrt{\Delta\phi^2 + \Delta\eta^2})$ of the individual decay products with the lepton, $c\tau(B)$, $c\tau(D)$, $\mathrm{L}_{xy}(\mathrm{PV}\rightarrow D)$, η distribution of the individual decay products and $\sigma_{L_{xy}}(B)$. The kinematical variables are important to the determination of the K factor and all lifetime distributions and decay distances should be reproduced in order to determine the trigger bias function correctly. The comparisons between the parametric simulation and data are shown in figures 4.4 to 4.8, between full simulation and data in figures 4.9 to 4.13 and between parametric and full simulation in figures 4.14 to 4.18. The comparisons are limited by the statistics in the data sample but are satisfactory in all cases.

The quality of the comparison between all sets of distributions is indicated by the Kolmogorov-Smirnov distance and probability for each pair of distributions which are compared [98]. These values are given in table 4.1. The Kolmogorov-Smirnov test gives two quantities: the distance is the maximum difference between the cumulative distribution functions of the two distributions which are being compared given by

$$Dist = max|S_{N_1}(x) - S_{N_2}(x)| \tag{4.4}$$

The probability that the distance is larger than Dist is given by

$$Prob = Q_{KS}\left(\left[\sqrt{N_e} + 0.12 + \frac{0.11}{\sqrt{N_e}}\right]\right) D \tag{4.5}$$

where $Q_{KS}(\lambda)$ is given by

$$Q_{KS}(\lambda) = 2\sum_{j=1}^{\infty}(-1)^{j-1}e^{-2j^2\lambda^2} \tag{4.6}$$

Parameter	**Parametric vs Data**		**Full vs Data**		**Parametric vs Full**	
	Dist.	Prob.	Dist.	Prob.	Dist.	Prob.
$p_{\mathrm{T}}(\mathrm{K}^+)$	0.04	0.06	0.06	0.06	0.001	0.06
$p_{\mathrm{T}}(\mathrm{K}^-)$	0.14	0.05	0.07	0.01	1×10^{-20}	0.08
$p_{\mathrm{T}}(\pi^-)$	0.49	0.04	0.06	0.06	0.002	0.03
$p_{\mathrm{T}}(\mu^-)$	0.74	0.03	0.09	0.0002	1×10^{-16}	0.07
$\mathrm{d}_0(\mathrm{K}^+)$	0.19	0.05	0.03	0.6	0.15	0.02
$\mathrm{d}_0(\mathrm{K}^-)$	0.86	0.03	0.03	0.5	0.08	0.02
$\mathrm{d}_0(\pi^-)$	0.37	0.04	0.05	0.08	0.07	0.02
$\mathrm{d}_0(\mu^-)$	0.29	0.04	0.03	0.5	0.6	0.01
$c\tau(\mathrm{D}_\mathrm{s}^-)$	3×10^{-10}	0.01	8×10^{-12}	0.01	0.77	0.01
$c\tau(\mathrm{B}_\mathrm{s}^0)$	4×10^{-7}	0.01	6×10^{-5}	0.09	0.01	0.03
$L_{xy}(PV \to \mathrm{D}_\mathrm{s}^-)$	0.15	0.05	0.02	0.8	0.001	0.03
$\sigma(\mathrm{Ł}_{xy}(\mathrm{B}_\mathrm{s}^0))$	1×10^{-19}	0.02	1×10^{-13}	0.02	1×10^{-5}	0.04
$\eta(\mathrm{K}^+)$	0.06	0.05	0.2	0.04	0.19	0.02
$\eta(\mathrm{K}^-)$	0.04	0.06	0.2	0.03	0.25	0.02
$\eta(\pi^-)$	0.14	0.05	0.5	0.03	0.01	0.03
$\eta(\mu^-)$	0.13	0.05	0.7	0.03	0.01	0.02
$\Delta R(\mathrm{K}^+)$	0.14	0.05	0.04	0.4	2×10^{-13}	0.06
$\Delta R(\mathrm{K}^-)$	0.31	0.04	0.05	0.08	4×10^{-12}	0.04
$\Delta R(\pi^-)$	0.21	0.04	0.06	0.04	6×10^{-7}	0.04

Table 4.1: *Kolmogorov Test values for comparisons of parameters between data and full and parametric simulation samples.*

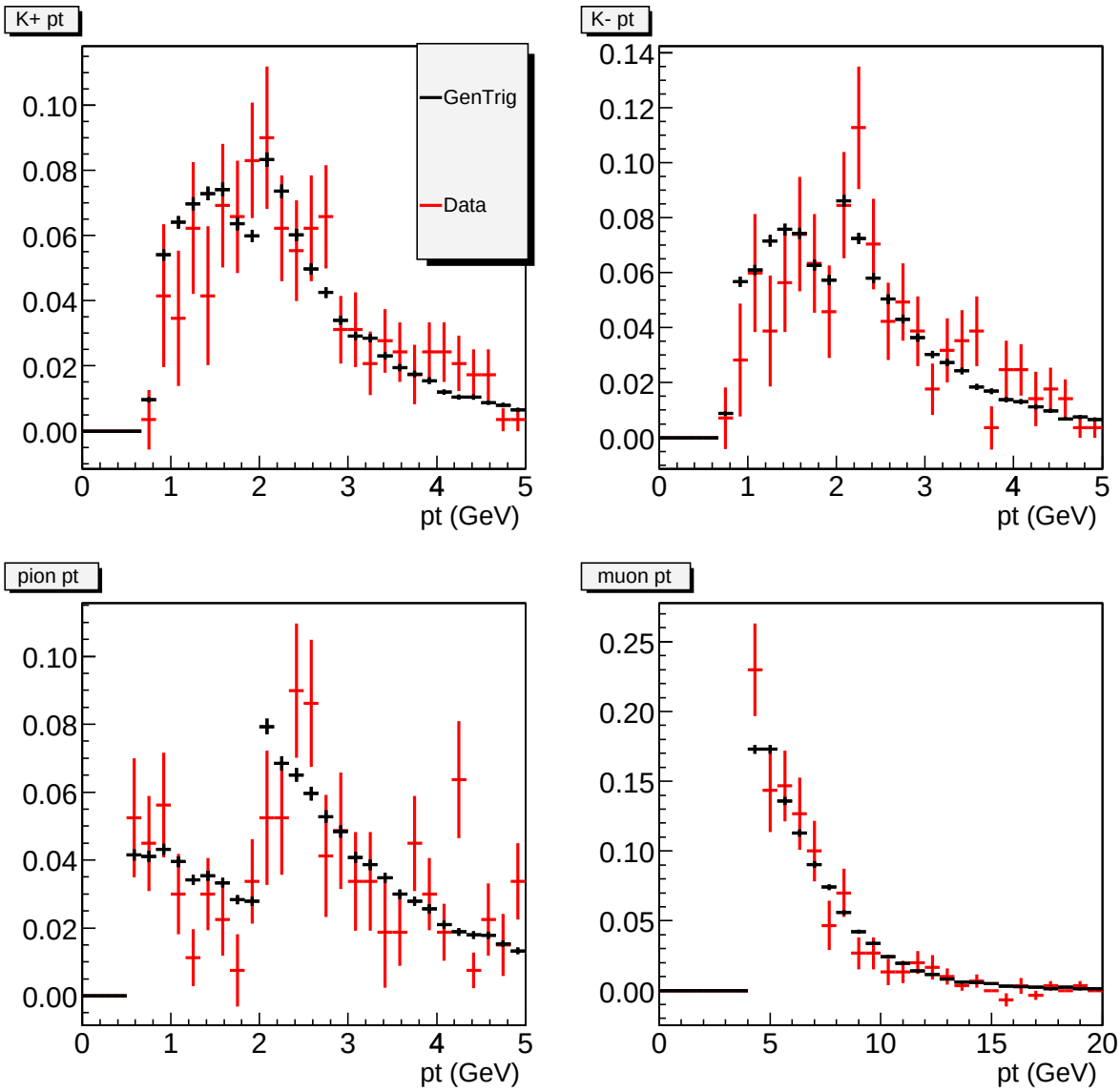

Figure 4.4: *Comparison of pt distributions in parametric (GenTrig) Monte Carlo to side-band subtracted data.*

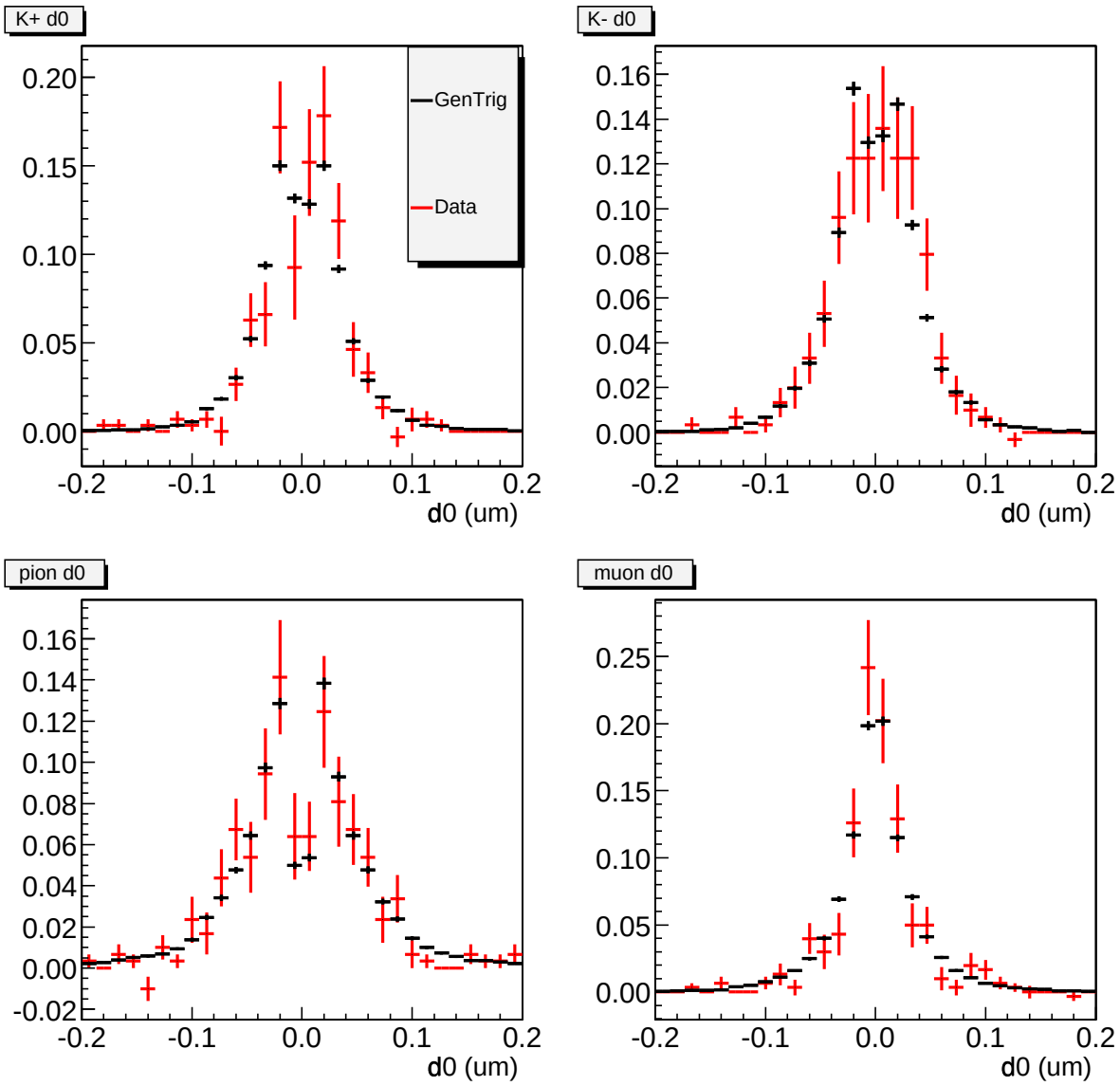

Figure 4.5: *Comparison of d0 distributions in parametric (GenTrig) Monte Carlo to side-band subtracted data.*

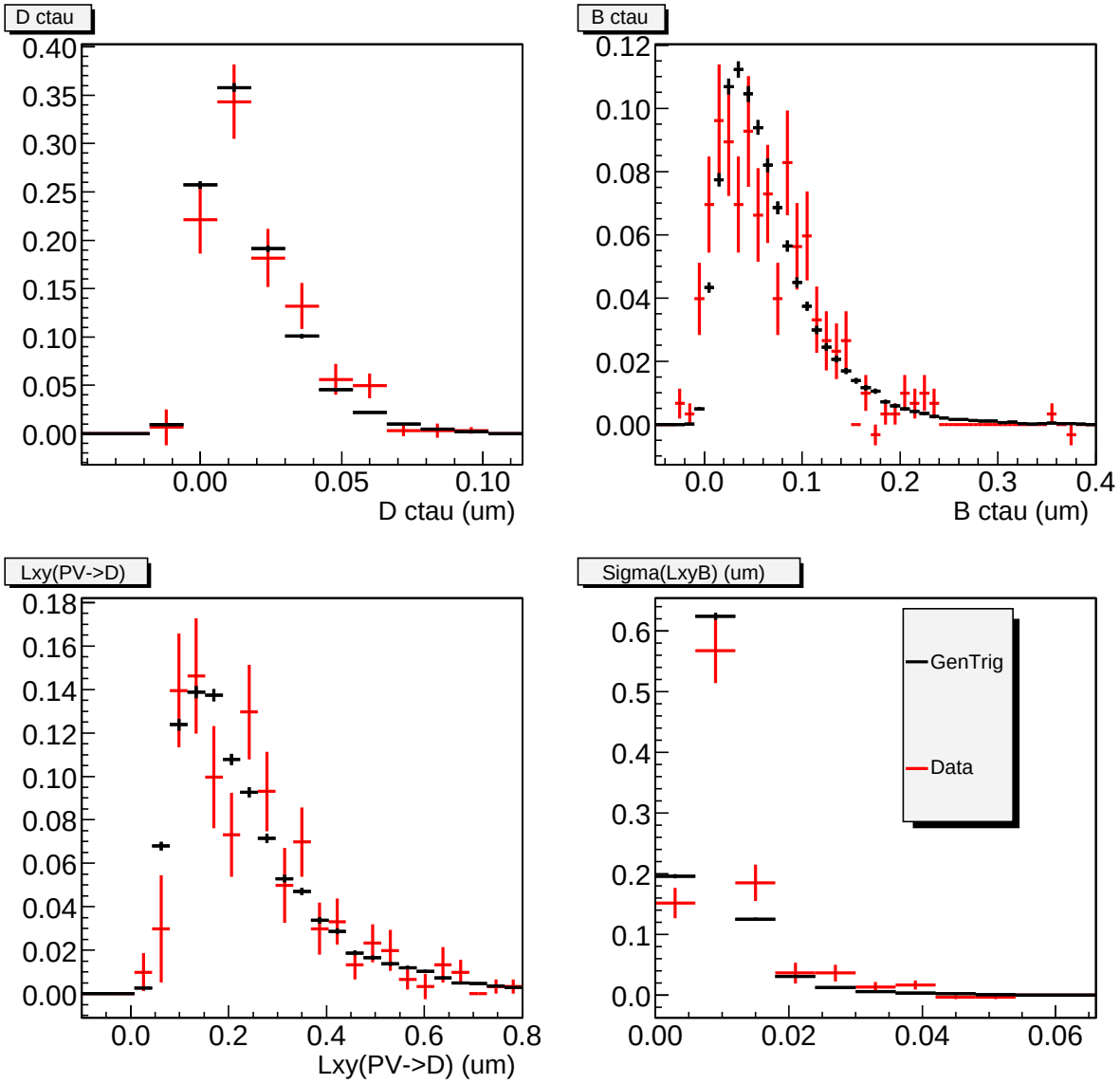

Figure 4.6: *Comparison of ctau and related distributions in parametric (GenTrig) Monte Carlo to sideband subtracted data. The distribution of sigma($L_{xy}(B)$) does not compare particularly well. This is partly because the error is not well estimated in the data and this is corrected by a scale factor, described in 5.5.3.*

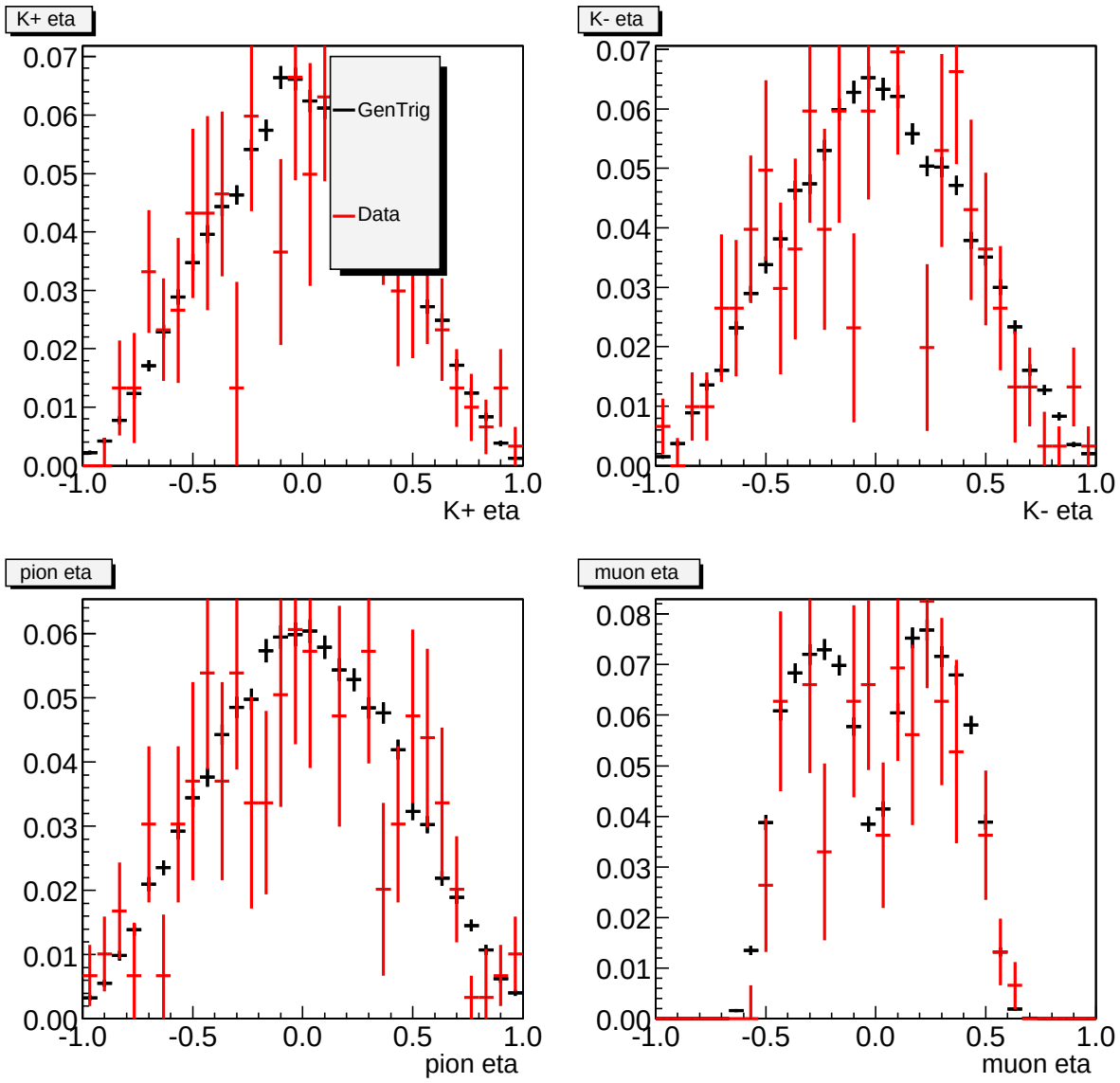

Figure 4.7: *Comparison of eta distributions in parametric (GenTrig) Monte Carlo to sideband subtracted data.*

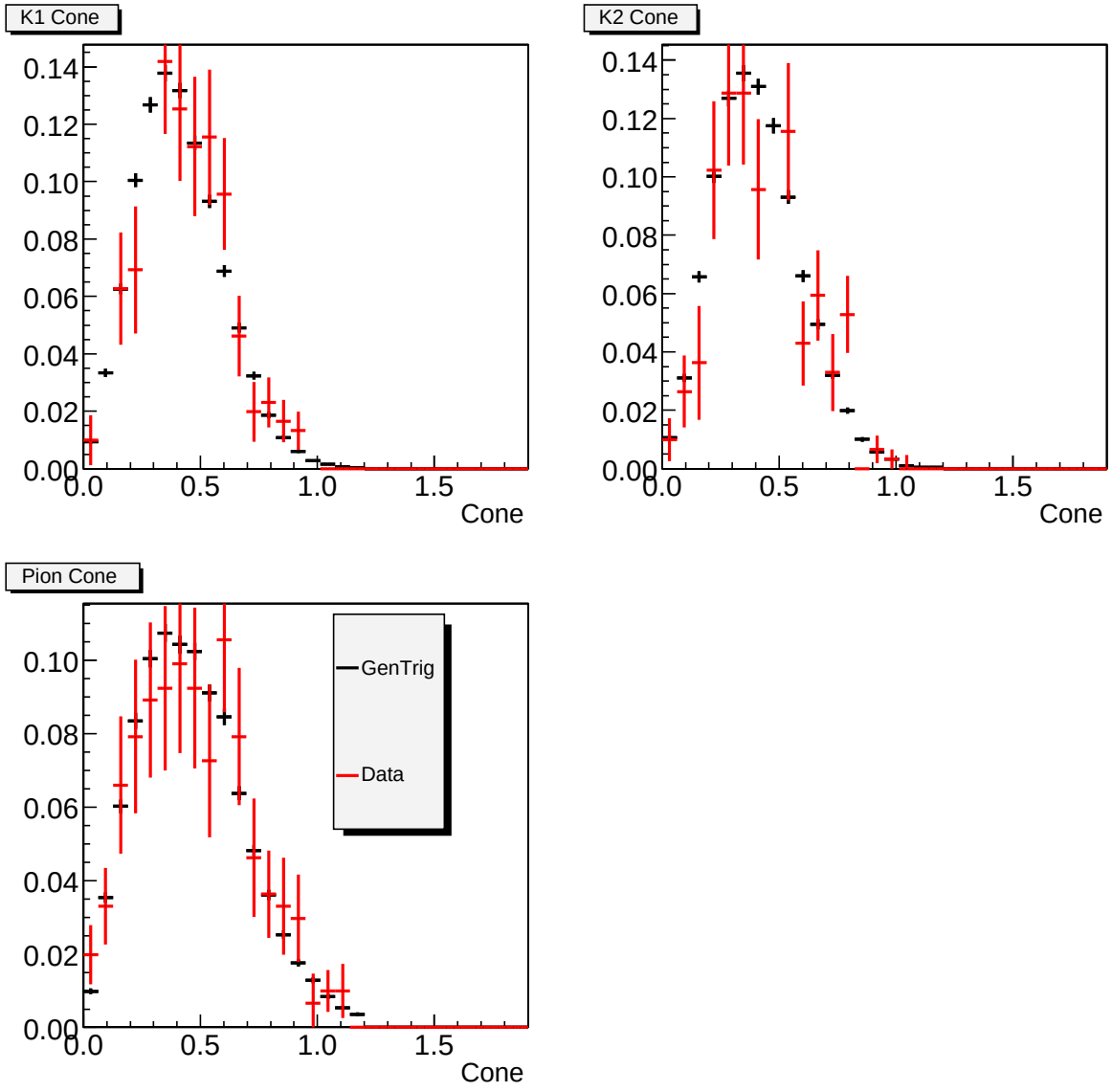

Figure 4.8: *Comparison of the cone sizes* ($\Delta R = \sqrt{\phi^2 + \eta^2}$) *of the* $D_s^{\pm}$ *decay products with respect to the muon in parametric (GenTrig) Monte Carlo and sideband subtracted data.*

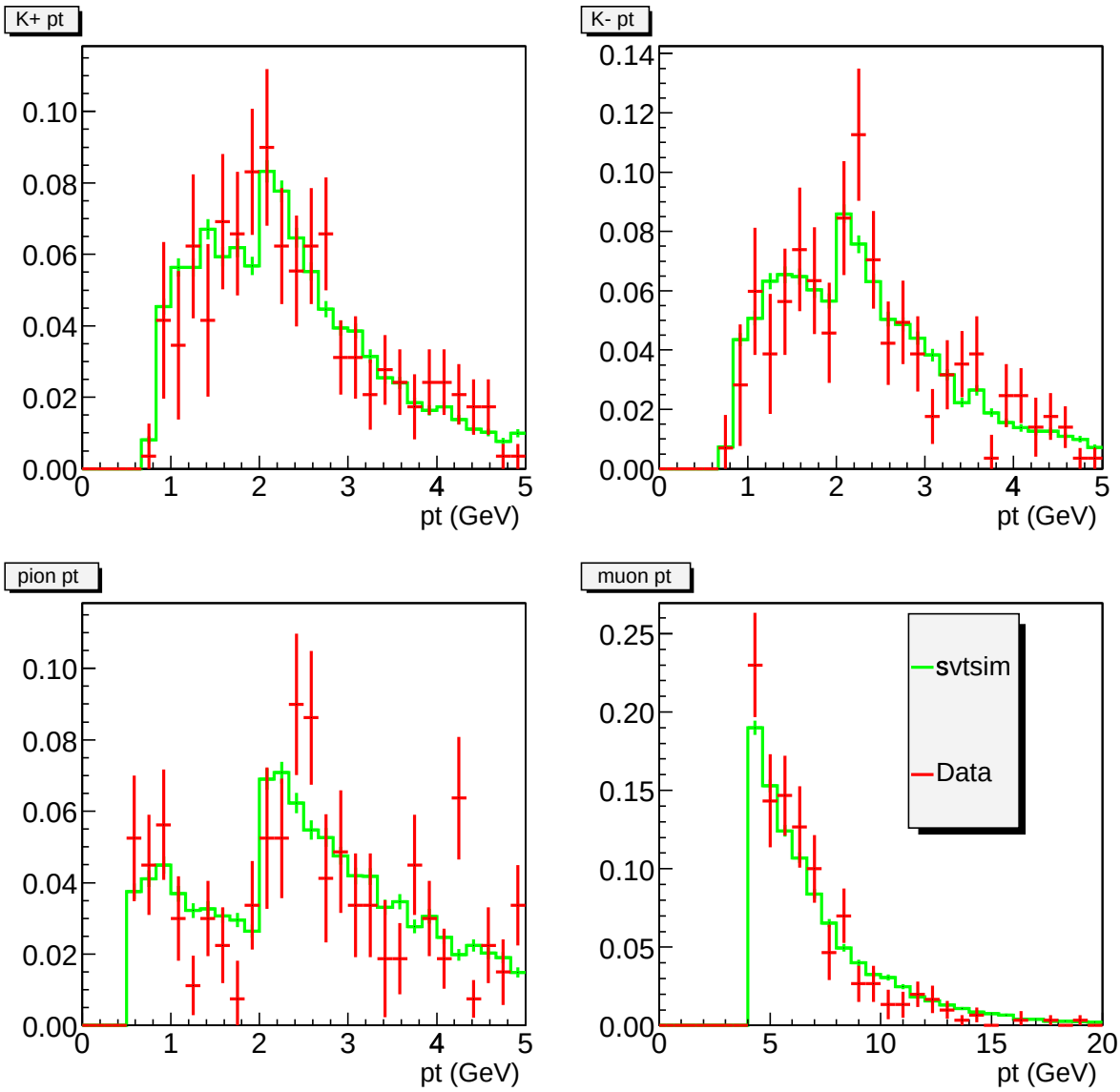

Figure 4.9: *Comparison of pt distributions in full Monte Carlo to sideband subtracted data.*

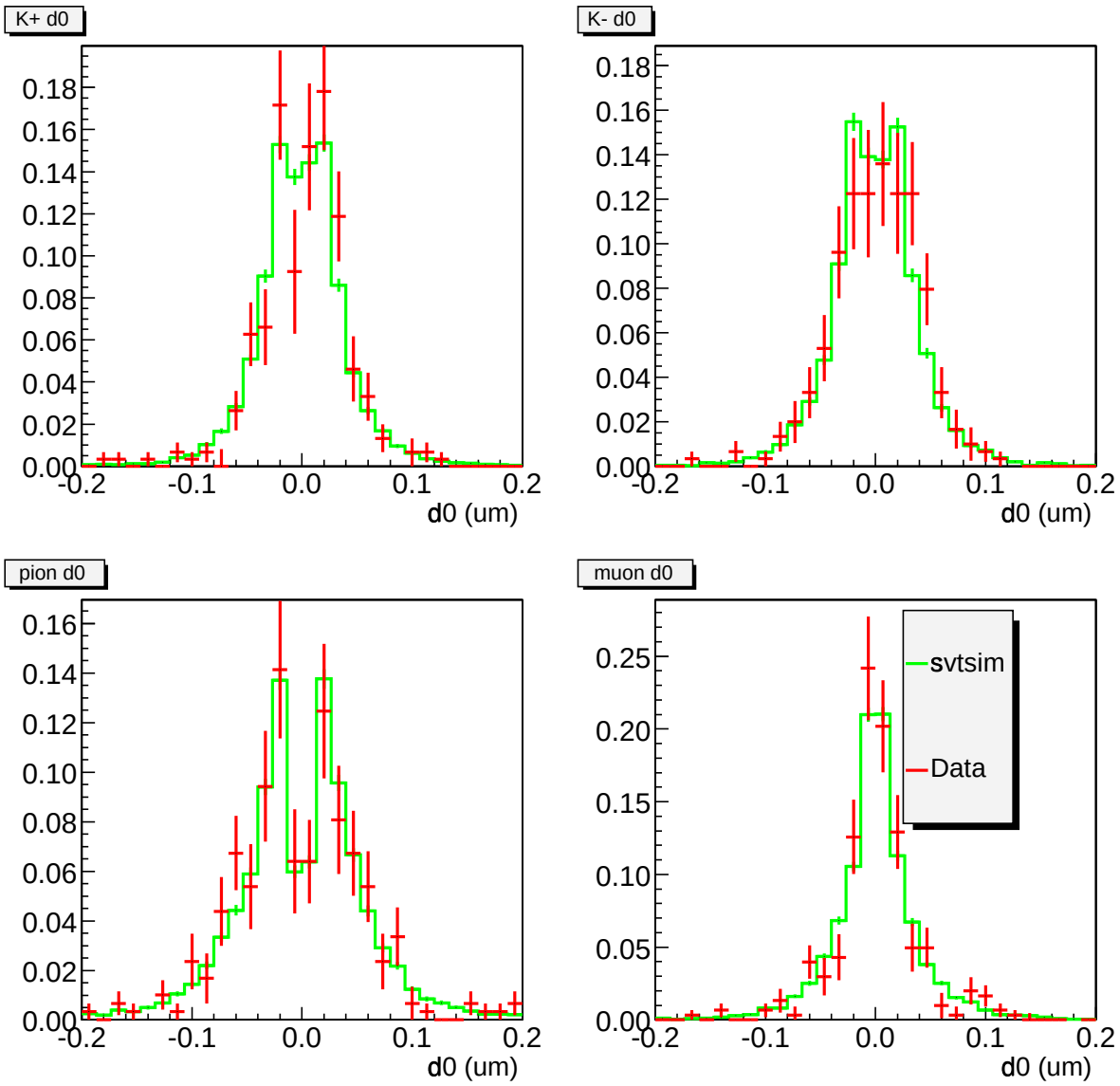

Figure 4.10: *Comparison of d0 distributions in full Monte Carlo to sideband subtracted data.*

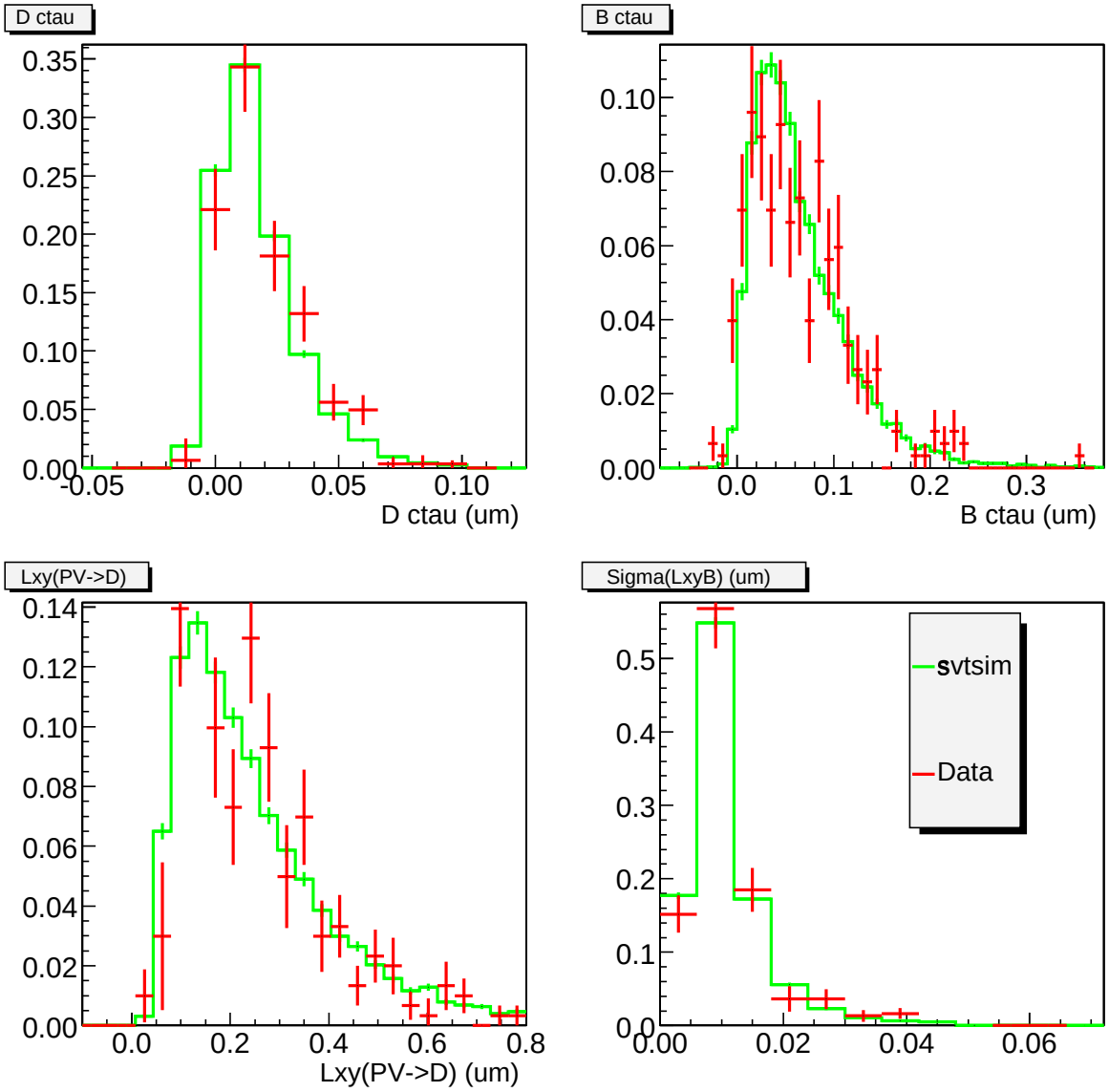

Figure 4.11: *Comparison of ctau and related distributions in full Monte Carlo to sideband subtracted data. The distribution of sigma($L_{xy}(B)$) does not compare particularly well. This is partly because the error is not well estimated in the data and this is corrected by a scale factor, described in 5.5.3.*

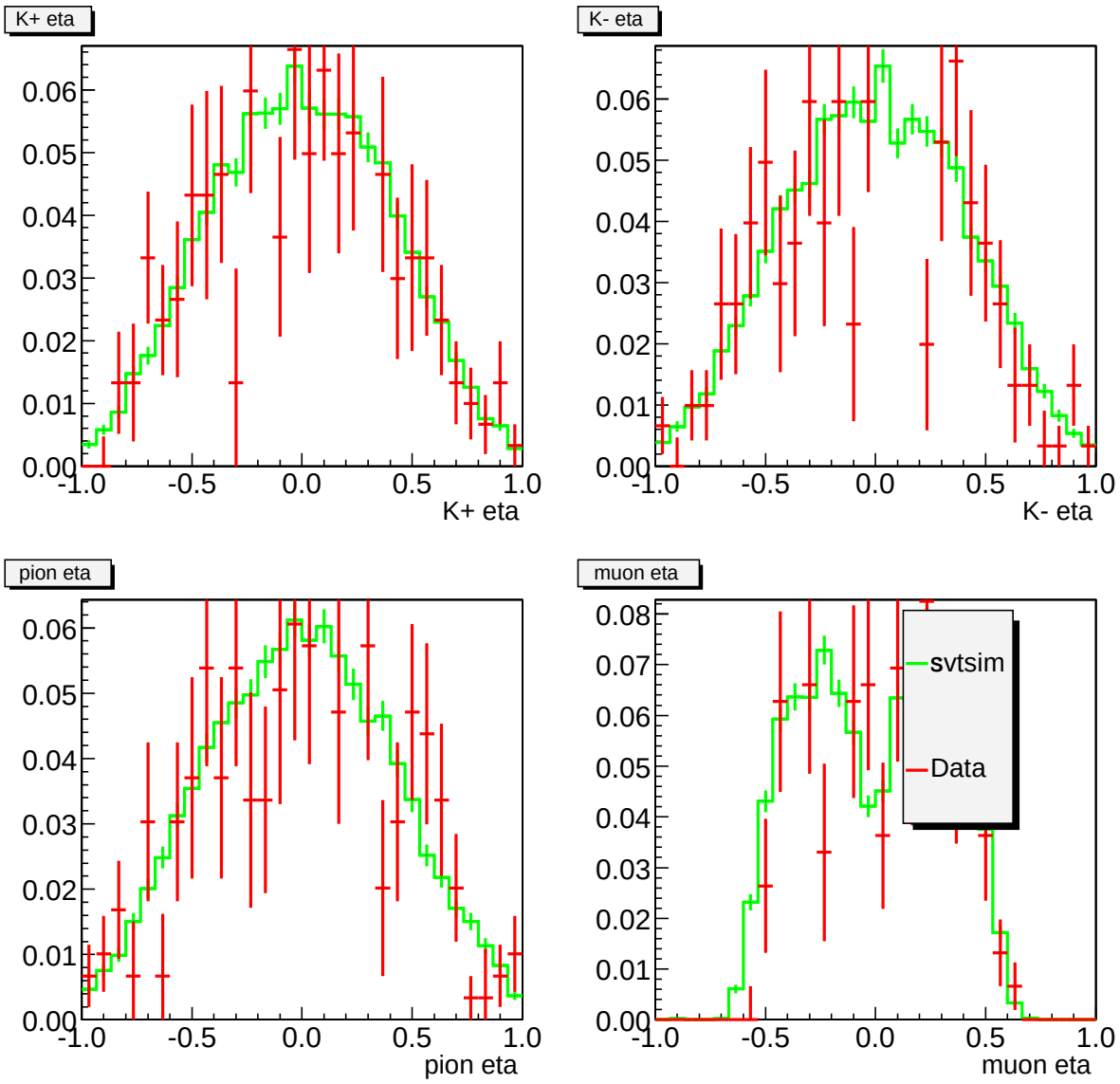

Figure 4.12: *Comparison of eta distributions in full Monte Carlo to sideband subtracted data.*

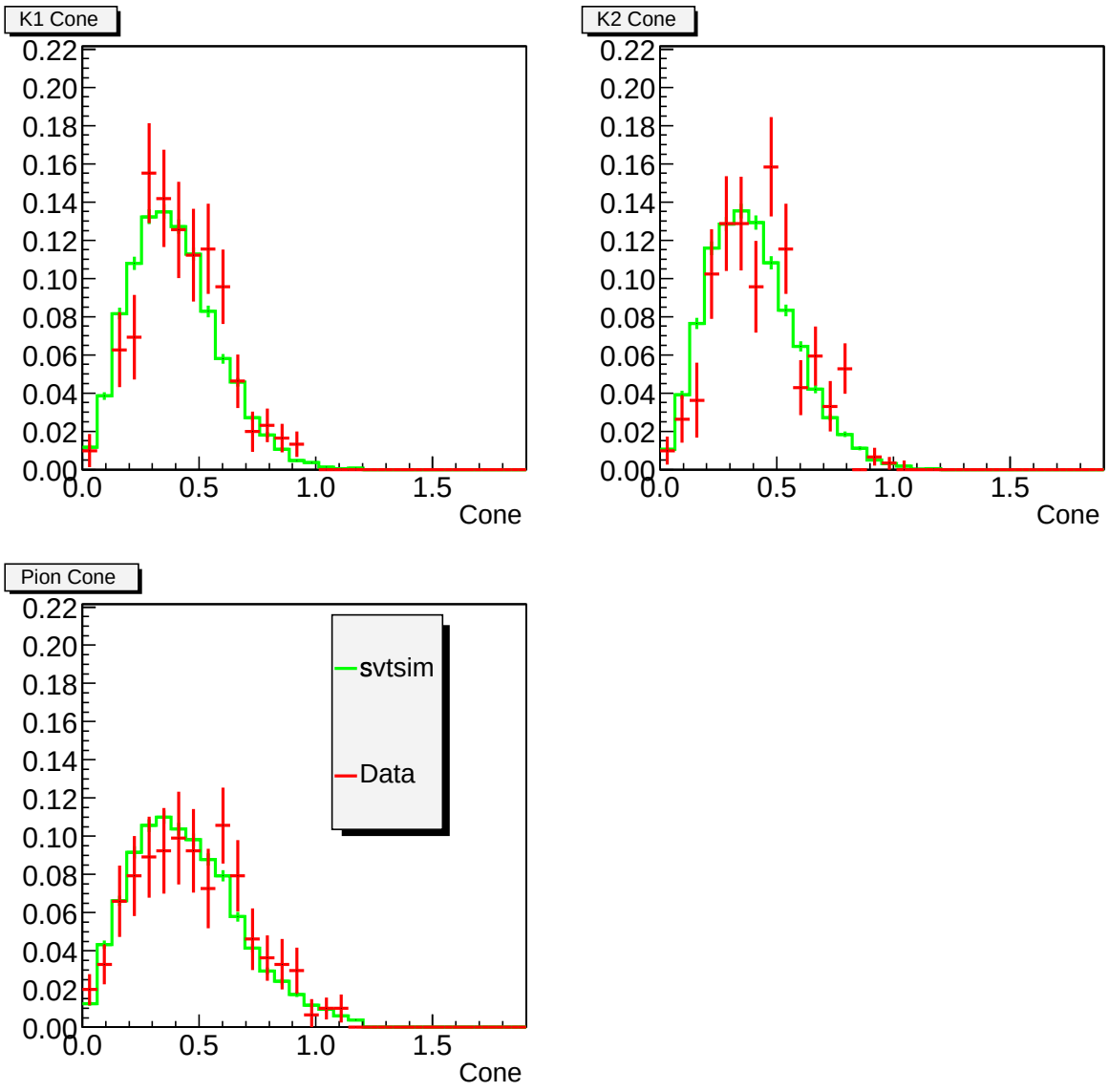

Figure 4.13: *Comparison of cone ($\Delta R = \sqrt{\phi^2 + \eta^2}$) distributions in full Monte Carlo to sideband subtracted data.*

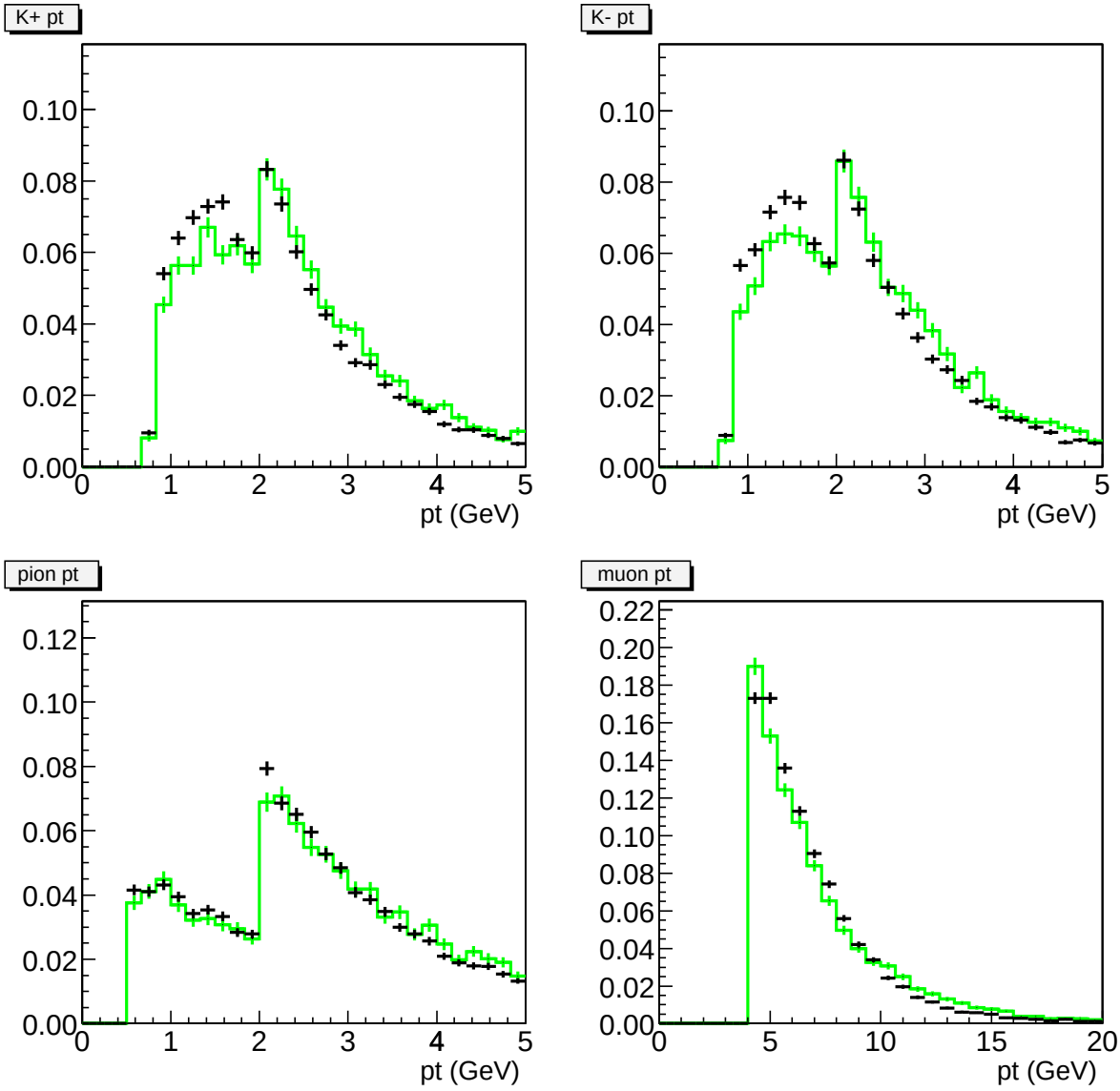

Figure 4.14: *Comparison of pt distributions in full Monte Carlo to parametric simulation. The differences visible in the Kaon pt are thought to be due to decay in flight which is not modelled in the parametric simulation. Parametric: black, Full: green*

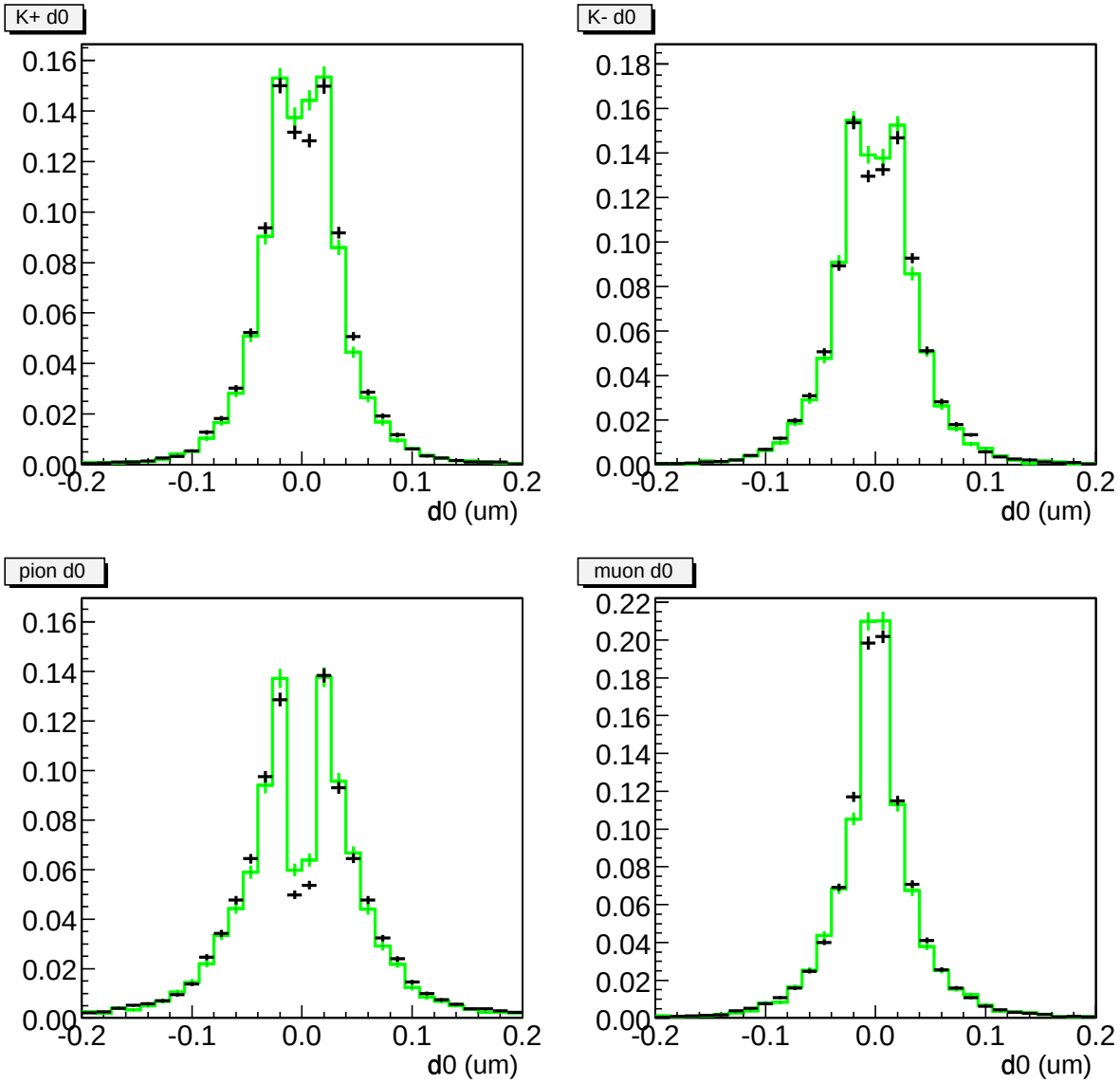

Figure 4.15: *Comparison of d0 distributions in full Monte Carlo to parametric simulation. In all cases the central bins are lower in the parametric simulation. This is thought to be due to an underestimation by the full simulation of the impact parameter resolution. Parametric: black, Full: green*

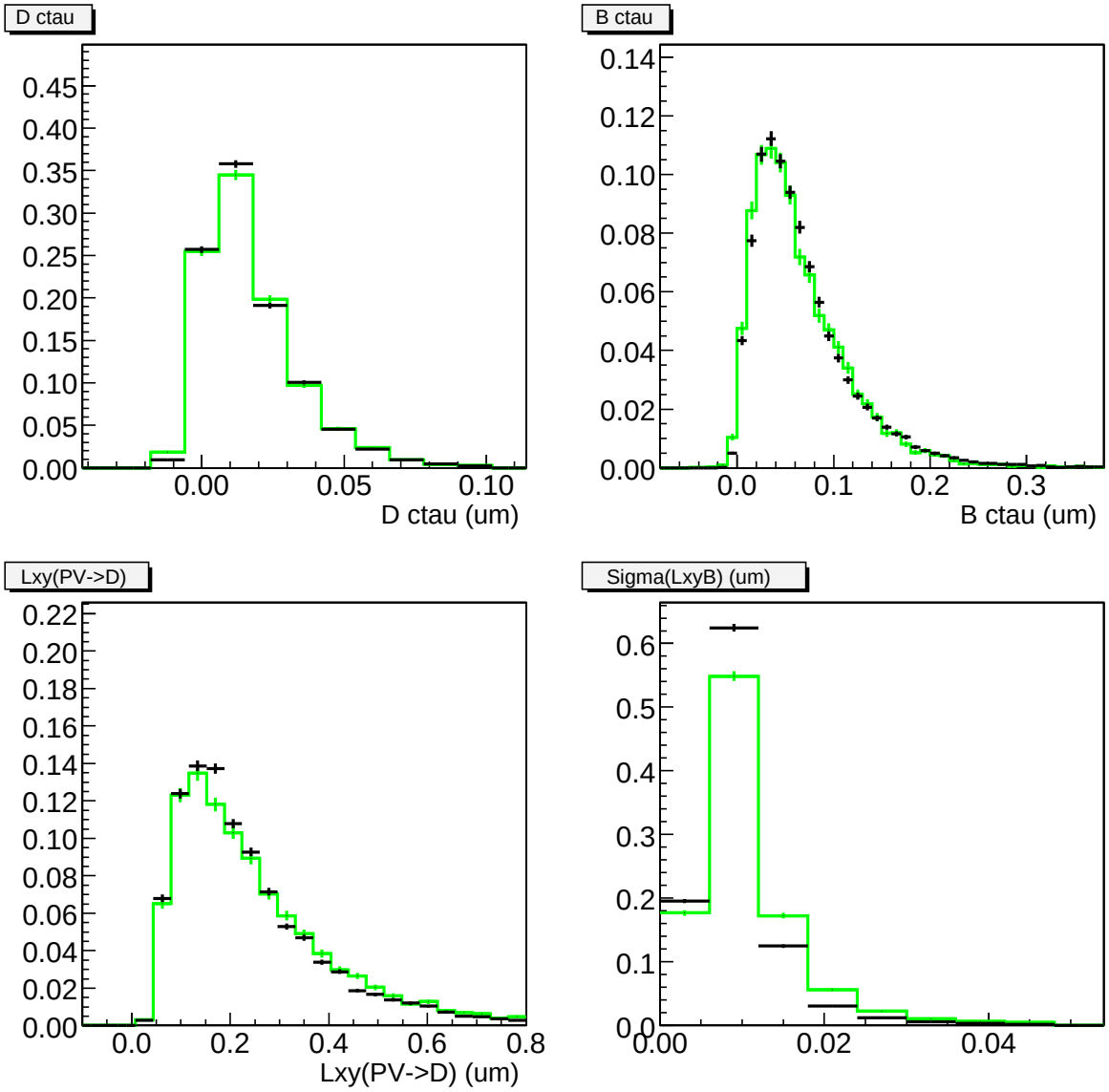

Figure 4.16: *Comparison of ctau and related distributions in full Monte Carlo to parametric simulation. The distribution of sigma($L_{xy}(B)$) does not compare particularly well. This is partly because the error is not well estimated in the data or simulation and this is corrected by a scale factor, described in 5.5.3. Parametric: black, Full: green*

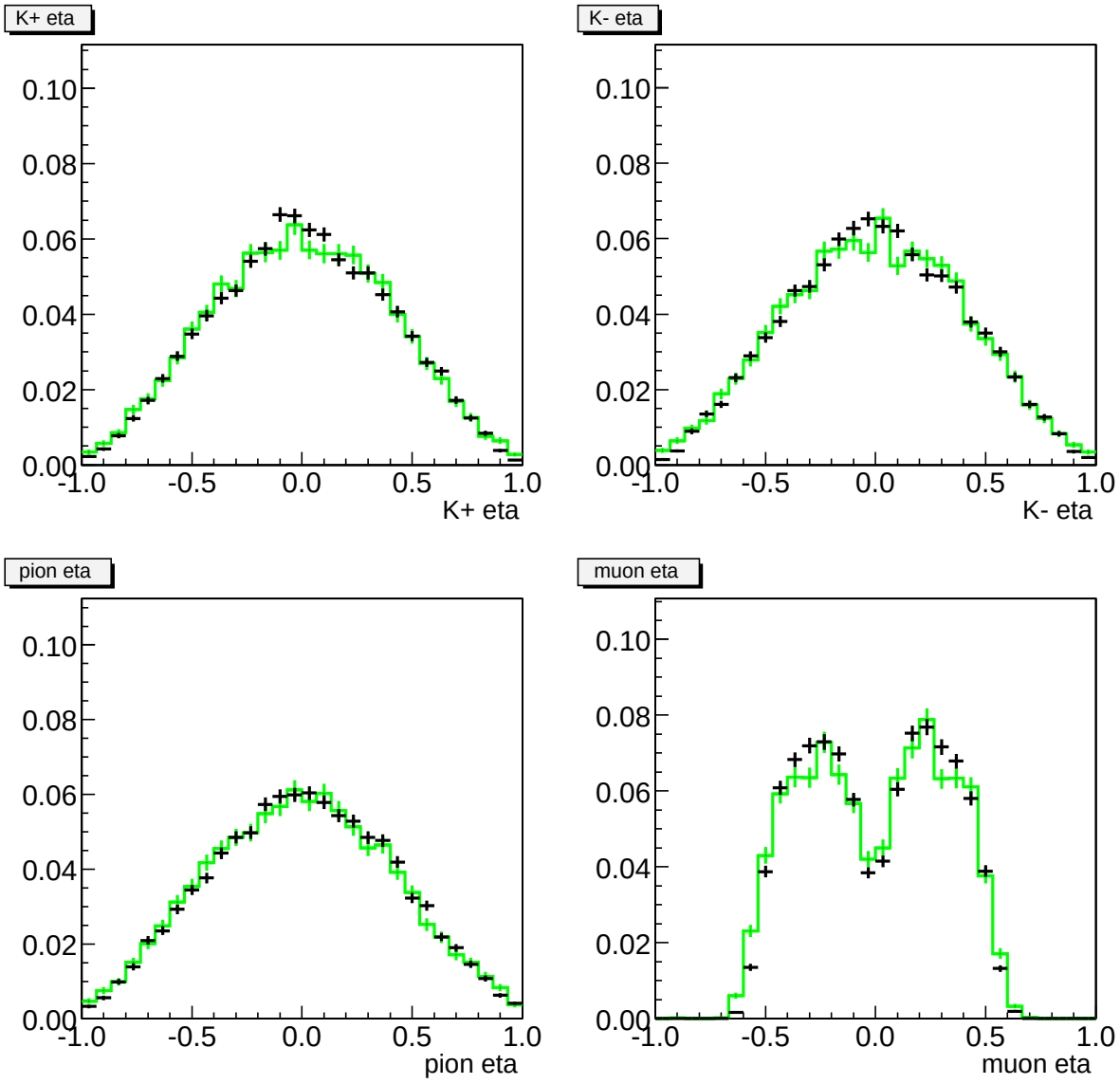

Figure 4.17: *Comparison of eta distributions in full Monte Carlo to parametric simulation. Parametric: black, Full: green*

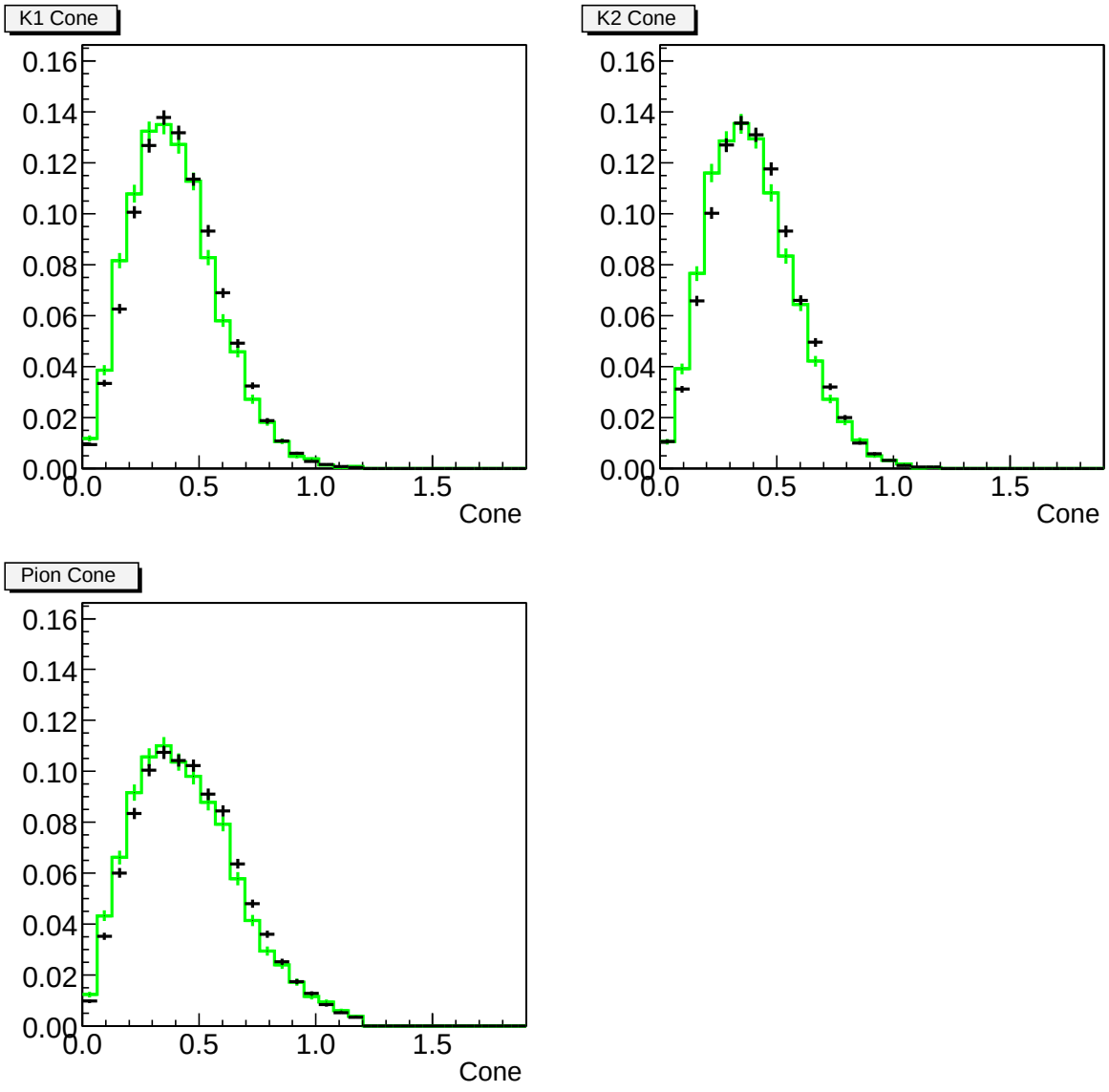

Figure 4.18: *Comparison of cone ($\Delta R = \sqrt{\phi^2 + \eta^2}$) distributions in full Monte Carlo to parametric simulation. Parametric: black, Full: green*

Chapter 5

Lifetime Fit Method

The methodology of the B_s^0 semileptonic, $B_s^0 \to \ell^+ \nu_\ell D_s^-$, lifetime measurement at CDF Run II is described here. An unbinned log-likelihood fit is made to the distribution of the pseudo-proper lifetime values of the B_s^0 candidates.

5.1 Methodology Overview

The proper lifetime of the B_s^0 meson is defined by

$$c\tau(B_s^0) = \frac{m(B_s^0) L_{xy}(B_s^0)}{p_T(B_s^0)} \tag{5.1}$$

The B_s^0 mass, $m(B_s^0)$, is known to great accuracy [1] from measurements in the fully reconstructed $B_s^0 \to J/\psi\phi$ channel [14]. The remaining two parameters, $p_T(B_s^0)$ and $L_{xy}(B_s^0)$, are inferred from experiment: $p_T(B_s^0)$ is the B_s^0 transverse momentum and $L_{xy}(B_s^0)$ is the B_s^0 transverse decay length.

The p_T of the B_s^0 is not fully measurable since the unobservable ν_ℓ carries away some momentum. Therefore the measurable p_T is $p_T(\ell^+ D_s^-)$ and this is corrected by a so-called K factor which is extracted from the simulation samples described in chapter 4. The K factor is discussed in section 5.2. The transverse B_s^0 decay length is the distance between the primary vertex and the B_s^0 decay vertex, projected into the transverse (x-y)

plane. The primary vertex is obtained from the beam position as described in section 3.4. To establish the secondary vertex location, the $D_s^- \to \phi\pi^-$ candidates are reconstructed in proximity to the trigger lepton as described in chapter 3. The B_s^0 candidate decay vertex is then determined by a vertex fit to the candidate D_s^- and ℓ^+ tracks. However, a further correction factor is necessary. The trigger is biased towards selecting longer lived B_s^0 mesons owing to the requirement that at least one track in the event should have an impact parameter of greater than 120μm. In addition, there is an upper cut on the impact parameter of 1mm which excludes very long-lived B_s^0 mesons. The bias is corrected for in the likelihood fit function, which is discussed in section 5.3, by folding in a correction obtained from simulated samples of B_s^0 decays with and without a trigger selection filter. In this way, the efficiency of the trigger to pass B_s^0 decays is binned in the true B_s^0 lifetime which is known in the simulation. These elements are folded together in a simultaneous fit to the lifetime distributions which are measured in defined signal and background regions. The background lifetime distribution is parameterised by fitting appropriate functions as described in section 5.5.4.

5.2 K Factor

As discussed above, the B_s^0 proper lifetime cannot be measured for the $B_s^0 \to \ell^+\nu_\ell D_s^-$ decay since the B_s^0 is only partially reconstructed, owing to the missing ν_ℓ. Therefore the proper lifetime is corrected by the K factor which is the ratio of the combined $\ell^+D_s^-$ to the B_s^0 transverse momenta:

$$c\tau^\star = \frac{m(B_s^0)L_{xy}(B_s^0)}{p_T(\ell^+D_s^-)}K, \qquad \text{with } K = \frac{p_T(\ell^+D_s^-)}{p_T(B_s^0)} \tag{5.2}$$

and $c\tau^\star$ is defined as the pseudo-proper decay length. This definition involves physically measurable quantities and takes account of the loss of the neutrino. In practice, the K factor distribution comes from simulation samples where the true p_T of the B_s^0 is known. The K factor is extracted from the simulation samples described in chapter 4. Histograms of the K factor distributions, H(K), measured in the parametric and full

simulation samples described in sections 4.3 and 4.4 are shown in figure 5.1 for the $B_s^0 \to \mu^+\nu_\mu D_s^-$ channel. The selection cuts defined in section 3.5 are also applied to the events used in this plot. The distribution peaks towards one, having a mean of 0.84 for the full simulation and the parametric simulation. Similar results hold for the electron sample which also has a K factor with a mean value of 0.84. The neutrino typically carries away little p_T and almost never more than 50% of the p_T of the B_s^0 meson. The small number of cases where the K factor has a value larger than one arise from events in which the ν_ℓ travels towards the beamline.

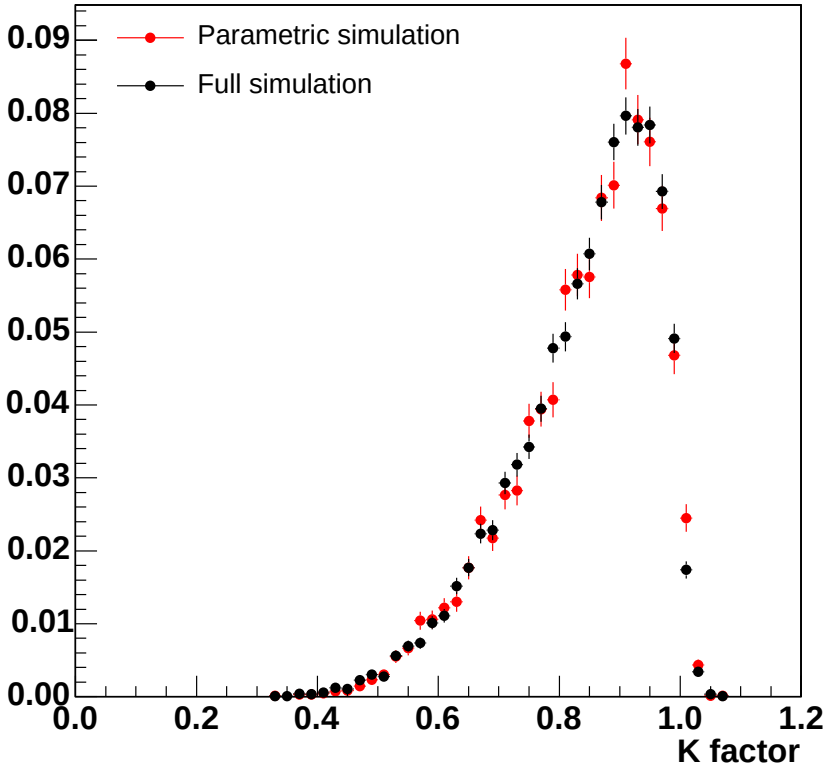

Figure 5.1: K *factor distribution,* $K = p_T(\ell\nu_\ell D_s^-)/p_T(B_s^0)$*, in the* $B_s^0 \to \mu^+\nu_\mu D_s^-$ *simulation sample.*

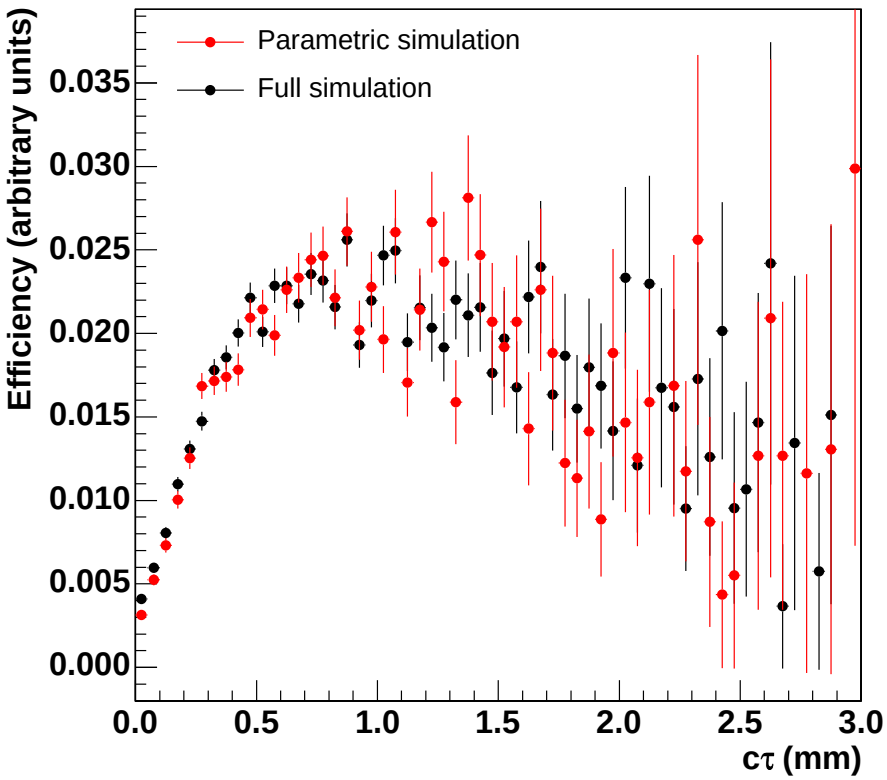

Figure 5.2: *Lifetime bias distribution in the* $B_s^0 \to \mu^+ \nu_\mu D_s^-$ *simulation sample. The efficiency is the ratio of the number of events in a simulation sample with the trigger simulation applied to the number of events in a sample where no trigger simulation is applied.*

5.3 Bias

The sample which is under study here comes from the lepton + displaced vertex trigger which requires a lepton with $p_T > 4$ GeV/c and a track with $p_T > 2$ GeV/c and $|d_0| > 0.12$mm and $|d_0| < 1.00$mm. While cutting on the impact parameter gives a much enriched sample of b hadrons, it also biases the lifetime. To account for this effect, the efficiency of the trigger as a function of $c\tau$ is measured in the simulation samples described in chapter

4. The efficiency is defined as the ratio of the generator (truth) level B_s^0 lifetime in a simulation sample with the trigger simulation switched on, to the same quantity in a sample which has no trigger simulation. This is the efficiency for the trigger to allow a B_s^0 of a particular lifetime to pass, ϵ. The selection cuts defined in section 3.5 are applied to the simulation sample. The resulting biases coming from parametric and full simulation samples are shown in figure 5.2. The shape follows the $|d_0|$ cuts: at low and high $c\tau$ the efficiency is reduced. The distribution is normalised. The units are not critical, but reflect the efficiency of the trigger $< \epsilon >$. The increasing errors reflect the $e^{-t/\tau}$ decay and so the statistics decrease for larger $c\tau$ values. The bias function, $\epsilon(x = c\tau)$, is parameterised over the range zero to three by the ratio of two polynomials:

$$\epsilon(x) = A(x+b)(\exp(-Cx) + D\exp(-Ex)) + F + G\exp\left(\frac{-x^2}{2H^2}\right) \tag{5.3}$$

This parameterisation is folded in to the likelihood function.

Applying the selection cuts to the simulation events should also take account of any bias caused by the cuts. There are four selection cuts which may bias the B_s^0 lifetime. Firstly, $L_{xy}(D_s^{PV})$ >400μm, where $L_{xy}(D_s^{PV})$ is the distance in the transverse plane between the primary vertex and the D_s^- meson decay vertex. For two B_s^0 decays with the same kinematics, $L_{xy}(D_s^{PV})$ is correlated to $L_{xy}(B_s^0)$. Removing this cut and refitting the lifetime yields a change of 0μm. Secondly, the requirement -100μm < $ct(D_s)$ <1mm, where $ct(D_s^-) = L_{xy}(D_s^-)m(D_s^-)/p_T(D_s^-)$, selects longer lived or lower $p_T D_s^-$ mesons. Removing this cut gives a change of +2μm. There is also a cut on the error of the $c\tau$ measurement of the B_s^0 : $\sigma(c\tau) < 400\mu$m. Removing this cut and refitting the lifetime yields a change of -1μm. Lastly, there is a cut on the significance of the decay distance from the primary vertex to the D_s^- vertex: $L_{xy}(D_s^{PV})/\sigma L_{xy}(D_s^{PV}) > 6$. Removing this cut gives a change of +5μm. This is considered an acceptable range and demonstrates that the bias caused by these cuts is modelled in the trigger bias function.

5.4 Definition of Signal and Sideband Regions

The B_s^0 lifetime is determined from a simultaneous, unbinned, maximum likelihood fit to the pseudo-proper decay length distributions in defined signal and background regions. For this purpose, signal and background subsamples are identified within the sample of D_s^- candidates, described in chapter 3. The signal region is defined by requiring the reconstructed D_s^- candidate mass to be within the D_s^- mass peak shown in figure 3.8. More precisely, this region is defined by a three sigma window (where σ is the width of a Gaussian distribution fit to the D_s^- mass) centred on the measured D_s^- mass, (M-3σ,M+3σ), where M and σ are the mean and width of a Gaussian distribution fit to the D_s^- mass peak.

$$\text{signal} : 1.941 < \mathrm{M}(\mathrm{D_s^-}) < 1.992 \text{ GeV/c}^2$$

In the sample of $D_s^- \to \phi\pi^-$, there are 1283 events in the signal region.

Sideband regions are used to model the contribution of the combinatorial background under the mass peak. The signal sample is fit simultaneously with defined sideband regions. These are three sigma windows to either side of the mass peak, separated from the signal region by one sigma:

$$\begin{aligned} \text{sidebands} : 1.908 &< M(\mathrm{D_s^-}) < 1.933\ GeV/c^2 \\ 2.000 &< M(\mathrm{D_s^-}) < 2.025\ GeV/c^2 \end{aligned}$$

In the sample of $D_s^- \to \phi\pi^-$, there are 370 events in the sideband region of figure 3.8. The choice of these regions assumes that the background can be fit with a single linear fit so that the extrapolated linear fit under the peak gives a measure of the amount of background under the peak, and hence the signal to background ratio.

5.5 Likelihood Fit Function

A simultaneous fit to the pseudo-proper decay length, $c\tau^{\star}$, in the signal and background regions establishes the background contribution to the signal, and the B_s^0 lifetime. As is true for any lifetime, the inherent distribution of the signal $c\tau^{\star}$ is an exponential decay. However, the observed function is smeared by detector and reconstruction effects and biased by the trigger's impact parameter requirement. In addition the K factor is also folded in. The background component is believed to be composed largely of other B hadron decays and some charm decays [99]. The background fit function does not seek to model these components individually but rather to parameterise the shape, using functions which are inspired by, but not derived from, physics processes. The signal and background fit functions will now be discussed in detail.

5.5.1 Signal

The signal probability distribution function, $\mathcal{F}_{sig}$, is composed of an exponential decay function which is convoluted with three components. The first component is a Gaussian resolution function, to account for the detector smearing. The second component is the K factor distribution, H(K), which corrects for the missing momentum carried by the neutrino. The third component is the multiplication by the trigger lifetime bias, $\epsilon(Kt)$, which is parameterised by equation 5.3. $\mathcal{F}_{sig}$ is then written

$$\mathcal{F}_{sig}(t) = N\frac{K}{c\tau}\exp\left(\frac{-Kt'}{c\tau}\right)\epsilon\left(Kt'\right) \otimes H(K) \otimes G(t-t', s\sigma_t) \tag{5.4}$$

Here σ_t is the error on the $\ell^+\nu_\ell D_s^-$ candidate's pseudo-proper decay length (t) which is returned from the vertex fit and s is an overall scale factor for the errors, the determination of which is described in 5.5.3. The overall normalisation, N, is given by the reciprocal of the total lifetime weighted bias. This ensures unit total probability. The trigger bias efficiency is applied only to the signal component and not to the background and so it is important to include this normalisation.

5.5.2 Convolution of Functions

The convolution, denoted $\otimes$, with the Gaussian function can be performed analytically resulting in an erfc function. The convolution with the K factor distribution is performed numerically as a finite sum.

The exponential component of the signal pseudo-proper lifetime distribution is:

$$E(x) = \Theta(x)\frac{1}{c\tau}e^{-x/c\tau} \quad \text{where } x = Kt' \tag{5.5}$$

and the Gaussian function is:

$$G(x) = \frac{1}{\sqrt{2\pi}\sigma}e^{-x^2/2\sigma^2} \tag{5.6}$$

The convolution of the exponential and Gaussian functions is given by:

$$E(x) \otimes G(x,\sigma) = \frac{1}{\sqrt{2\pi}\sigma c\tau}\int_{-\infty}^{x} e^{-(x-x')/c\tau}e^{-x'^2/2\sigma^2}dx' \tag{5.7}$$

$$= \frac{1}{\sqrt{2\pi}\sigma c\tau}\int_{-\infty}^{x} e^{-x/c\tau+\sigma^2/2(c\tau)^2-(x'-\sigma^2/c\tau)^2/2\sigma^2}dx' \tag{5.8}$$

Using the frequency function, defined by

$$\text{freq}(x) = \frac{1}{\sqrt{2\pi}}\int_{-\infty}^{x} e^{-\frac{t^2}{2}}dt \tag{5.9}$$

leads to

$$E(x) \otimes G(x,\sigma) = \frac{1}{c\tau}e^{\sigma^2/2(c\tau)^2-x/c\tau}\left[1 - \text{freq}\left(\frac{\sigma}{c\tau} - \frac{x}{\sigma}\right)\right] \tag{5.10}$$

The frequency function can be related to the error function, erf, and the complementary error function thus:

$$\text{freq}(x) = \begin{cases} \frac{1}{2} + \frac{1}{2}\text{erf}(x/\sqrt{2}) & (x \geq 0) \\ \frac{1}{2}\text{erfc}(|x|/\sqrt{2}) & (x < 0) \end{cases} \tag{5.11}$$

The error function can be calculated using a Chebyshev approximation [98] which simplifies the computations. The convolution of the exponential and Gaussian distributions is also used in the fit to the background component, which is discussed in section 5.5.4.

The convolution with the K factor cannot be evaluated analytically but instead is evaluated as a sum over the probabilities for each K factor value, $\sum_i H_i(K_i)$. Substituting this and equation 5.10 into $\mathcal{F}_{sig}$ (equation 5.4) results in

$$\mathcal{F}_{sig}(t) = N \sum_i H_i(K_i) \frac{K_i}{c\tau} \epsilon(K_i t) e^{\frac{(K_i s\sigma)^2}{2(c\tau)^2} - \frac{K_i t'}{c\tau}} \left[1 - \text{freq} \left(\frac{K_i s\sigma}{c\tau} - \frac{t'}{s\sigma} \right) \right] \tag{5.12}$$

with

$$N^{-1} = \int_0^\infty dx \frac{e^{-x/c\tau}}{c\tau} \epsilon(x) \tag{5.13}$$

This integral is calculated numerically.

5.5.3 Scale Factor Determination

The vertex fitting procedure which intersects the ℓ^+ with the D_s^- candidate determines the decay length of the B_s^0 meson, L_{xy}, and provides an error on this quantity, $\sigma(L_{xy})$. An overall scale factor, s, is included to compensate for a common over or under evaluation of this error. In most lifetime analyses, this scale factor would be determined by allowing the scale factor, s, to float in the fit. In this way, the prompt component of the background, which has $L_{xy} = 0$, contributes a Gaussian distribution centred on zero, to the L_{xy} distribution. However, in the lepton plus displaced vertex trigger the prompt component is mostly eliminated by the requirement of a track with large impact parameter. Therefore a separate sample which contains prompt physics is used to determine the scale factor [94]. A back-up electron sample which requires a Level 1 electron and has auto-accept for Levels 2 and 3 is used. The trigger path for this sample is ELECTRON_CENTRAL_L3PSnm_L1_CEM4_PT4. Here, nm denotes the prescale of the trigger and in this case two triggers are used, with prescales of 10 and 25. This means that only one in ten, or one in twenty five, events passing the trigger are recorded. The only electron identification requirement is that E_T >4 GeV and p_t >4 GeV/c and so most of the "electrons" are fake. Combinations of these fake electrons are made with three tracks which have similar kinematics to the signal D_s^- mesons. Thus a sample of fake electrons combined with fake D_s^- mesons is gathered. These events would appear in the

background to the lepton plus displaced vertex sample and would allow determination of s if there were no displaced track requirement. The scale factor is determined by the width of a Gaussian fit to the distribution of $L_{xy}/\sigma(L_{xy})$. This gives s=1.22±0.10.

5.5.4 Background

The background $c\tau^{\star}$ distribution is parameterised by two components: a delta function, to model a prompt component, and an exponential function, to model a long-lived component. Both have floating offsets from zero and are smeared by a Gaussian resolution function. The background probability distribution function is then

$$\mathcal{F}_{bkg}(t) = \left[(1-f_+)\delta(t'-\Delta_D) + \frac{f_+}{\lambda_+}\Theta(\Delta_E - t')\exp\left(\frac{t'-\Delta_E}{\lambda_+}\right)\right] \otimes G(t-t',\sigma_G) \quad (5.14)$$

where f_+ is the fraction of positive lifetime background, λ_+ is its lifetime, Δ_D is the offset of the zero lifetime component and Δ_E is the offset of the exponential component from zero. f_+, λ_+, Δ_D, Δ_G and σ_G are all floated in the fit to the background. The convolution with the Gaussian function is performed as described in section 5.5.3.

The signal and background distributions are weighted by the appropriate fractions and the resulting log likelihood function can then be written:

$$\mathcal{L} = \prod_i^{N_{sig}} \left[(1-f_{bkg})\,\mathcal{F}^i_{sig}(t_i) + f_{bkg}\mathcal{F}^i_{bkg}(t_i)\right] \cdot \prod_j^{N_{bkg}} \mathcal{F}^j_{bkg}(t_j) \quad (5.15)$$

where N_{sig} and N_{bkg} are the number of candidates in the signal and sideband regions respectively. Both $\mathcal{F}_{sig}$ and $\mathcal{F}_{bkg}$ are normalised to unit area. f_{bkg} is the fraction of background in the signal region. This fraction can be calculated using sideband subtraction in the data and is added as a constraint to the fit by including a χ^2 term to the likelihood:

$$\chi^2_{f_{bkg}} = \frac{\left(f_{bkg} - f^{sub}_{bkg}\right)^2}{\sigma^2_{f_{bkg}}} \quad (5.16)$$

where

$$f^{sub}_{bkg} = \frac{N_{bkg}}{N_{sig}-N_{bkg}} \quad \text{and} \quad \sigma^2_{bkg} = \frac{N_{sig}N_{bkg}(N_{sig}+N_{bkg})}{(N_{sig}-N_{bkg})^4} \quad (5.17)$$

The function minimised in practice is then

$$-2\ln\mathcal{L} + \chi^2_{f_{bkg}}$$

5.5.5 Fitter Validation

In order to have confidence in the fitter it should comply with two requirements. Firstly, the fitter is verified on a set of fake data samples which are generated by a toy Monte Carlo. The scaled residuals from the results are required to have zero mean, that is, to be unbiased. They should also have unit width in order to confirm that the error estimate is correct. Secondly, it should reproduce the input lifetime in the full simulation sample. These checks are now discussed.

Toy Monte Carlo

As a test of the fitter, 100 toy Monte Carlo samples were produced with 1000 signal events and 500 background events. The toy Monte Carlo is described in Appendix C. The sample sizes were chosen to be similar to the real data samples. The background is modelled using the fit values to the sideband regions in the data. The signal is modelled by $\mathcal{F}_{sig}$ using the K factor and bias from the parametric MC sample. Each sample is fitted and figure 5.3 shows the distribution of the scaled residuals or "pulls", defined by

$$p_j^{(i)} = \frac{f_j^{(i)} - f_{true}^{(i)}}{\sigma_j^{(i)}} \tag{5.18}$$

Here, i labels the parameter and j the dataset, so that $f_j^{(i)}$ and $\sigma_j^{(i)}$ are the fit result and error for the ith parameter in dataset j. An unbiased fitter gives pulls which are Gaussian distributions with a mean of 0 and a width of 1. The pull distributions are shown in figure 5.3 and the means and widths, given in table 5.1, are consistent with 0 and 1 respectively giving satisfactory evidence, in this test, of an unbiased fitter.

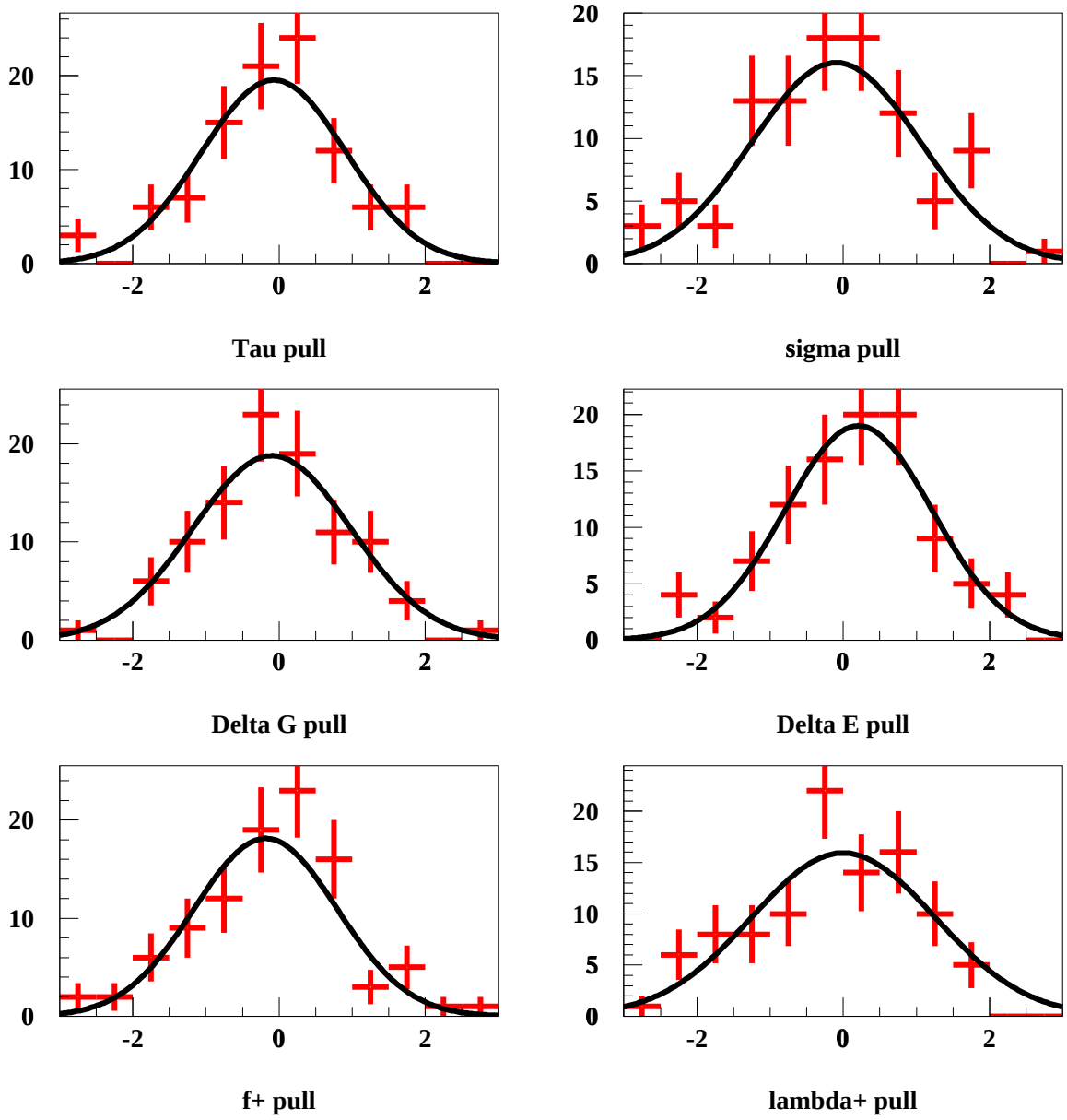

Figure 5.3: *Pull distributions for each of the fit parameters when fitting toy MC data sets with signal and background models. See the text for details. See table 5.1 for mean and sigma values.*

Fit Parameter	Mean	Sigma
$c\tau$	-0.07±0.11	0.99±0.17
σ_G	-0.10±0.13	1.15±0.16
Δ_D	-0.10±0.12	1.08±0.12
Δ_E	-0.21±0.11	1.01±0.11
f_+	-0.18±0.11	0.97±0.11
λ_+	-0.01±0.15	1.25±0.14

Table 5.1: *The mean value and width of the distribution of pulls measured using the fits to 100 samples, each of 1000 signal events and 500 background events.*

Parametric and Real Simulations

In addition to requiring that the fitter should have unbiased pulls, it should also reproduce the input lifetime value when fitting a full simulation sample. Figure 5.4 shows the fit to the full simulation, generated with $c\tau = 438\mu m$. For this fit, the K factor and bias extracted from the parametric sample are used. The fit result is $432 \pm 5\mu m$.

5.5.6 Inclusion of Irreducible Physics Backgrounds

The fitting method described in this chapter takes into account combinatorial backgrounds by the method of fitting simultaneously the signal and sideband regions, as defined in section 5.4. However, there are additional backgrounds which result in a real D_s^- meson and real lepton but which do not come from the semileptonic decay of the B_s^0 . Thus these backgrounds add to the signal sample, but not to the sideband sample and their contributions to the lifetime distribution must be determined and then incorporated in the fit. Simulation samples of these background processes allow the determination of their reconstruction efficiencies relative to that of the $B_s^0 \to \ell^+\nu_\ell D_s^-$ decays and their $c\tau$ distributions. The fractions of the backgrounds which are expected in the data are calcu-

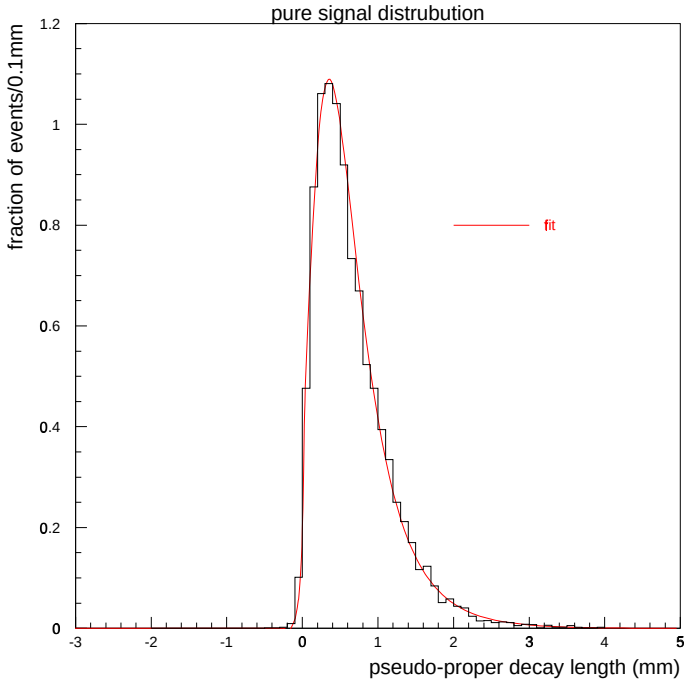

Figure 5.4: *Fit to full simulation using K factor and bias from parametric MC sample.*

lated using the branching ratios of the various decays. There are three such background components which are now discussed in turn. The quoted branching ratios are from the Particle Data Group [1] unless stated otherwise.

The first background contribution is from the B^- meson decays to $D_s^{(\star)-}D^{(\star)+/0}X$, with the $D^{(\star)+/0}$ decaying semileptonically. The $D_s^{\star-}$ meson always decays to a D_s^- meson. This background therefore results in a real D_s^- meson and a real lepton. Similarly, decays of the B_d^0 meson to $D_s^{(\star)-}D^{(\star)+/0}X$ with semileptonic $D^{(\star)+/0}$ decays result in the same signature. The efficiency for these decays to pass the trigger is expected to be lower than for the $B_s^0 \to \ell^+\nu_\ell D_s^-$ events since the momentum spectrum of the lepton in the $D^{(\star)+/0}$ decay is lower. Simulation samples of ten million events each of the B^- and B_d^0 decays were generated, allowing all decays which include a D_s^- meson. The events were generated using Bgenerator, decayed using EvtGen and were then passed through the parameteric

trigger simulation, GenTrig. These simulation packages are discussed in chapter 4. The $D_s^- \to \phi\pi^-$ and $\phi \to K^+K^-$ decays are forced, as in the $B_s^0 \to \ell^+\nu_\ell D_s^-$ sample. The events which pass the trigger simulation are then passed through the $B_s^0 \to \ell^+\nu_\ell D_s^-$ analysis chain described in section 3.5. The efficiency to reconstruct a $\ell^+ D_s^-$ in the B^- and B_d^0 events relative to the efficiency for reconstructing a $\ell^+ D_s^-$ in $B_s^0 \to \ell^+\nu_\ell D_s^-$ decays is

$$\epsilon^{\rm rel}_{D_sD} = \frac{\epsilon_{D_sD}(B \to D_s^{(\star)-} D^{(\star)+/0} X)}{\epsilon_{D_s\ell}(B_s^0 \to \ell^+\nu_\ell D_s^-)} = 0.1168 \pm 0.0035$$

Here an equal admixture of B^- and B_d^0 events is used. This means that they are added together with equal weight since they are produced in equal number ($f_u = f_d$). The fraction of false signal events which are expected from this irreducible background to true signal events is given by

$$f_{B\to D_sD} = \epsilon^{\rm rel}_{D_sD} \frac{f_u + f_d}{f_s} \frac{\mathrm{BR}(B \to D_s^- X) \times \mathrm{BR}(D \to \ell^+ X)}{\mathrm{BR}(B_s^0 \to \ell^+\nu_\ell D_s^-)} \tag{5.19}$$

where the f_u, f_d and f_s are the hadronisation fractions, discussed and quoted in section 1.4.2, which account for the relative production fractions of the B^- , B_d^0 and B_s^0 mesons. The world average measurement of $\mathrm{BR}(B \to D_s^- X)$ =10.5±0.8% is for the B_d^0 /B^- admixture and the branching ratio for $B_s^0 \to \ell^+\nu_\ell D_s^-$ is 7.9±2.4% [100]. The branching ratio of D meson semileptonic decays is a weighted average of the $\mathrm{BR}(D^+ \to \ell^+ X)$=17.2±1.9% and $\mathrm{BR}(D^0 \to \ell^+ X)$=6.5±0.8%. The weights are given by the relative number of reconstructed events in the simulation sample which have leptons from D^+ and D^0 . Thus

$$\mathrm{BR}(D \to \ell X) = 0.70 \times \mathrm{BR}(D^0 \to \ell^+ X) + 0.30 \times \mathrm{BR}(D^+ \to \ell^+ X) = 9.7 \pm 0.8\%$$

The resulting contributing fraction is

$$f_{B\to D_sD} = 0.0704 \pm 0.0213$$

The second background contribution is from the B_s^0 meson decays to $D_s^{(\star)-} D_s^{(\star)+} X$ where one D_s decays semileptonically and the other decays to $\phi\pi$. Similarly to the B^- /B_d^0 case, simulation samples of $B_s^0 \to D_sD_sX$ events are generated. The efficiency for

reconstructing D_s^- mesons in this sample relative to that in the $B_s^0 \to \ell^+\nu_\ell D_s^-$ sample is

$$\epsilon^{\rm rel}_{D_sD_s} = \frac{\epsilon_{D_sD_s}(B_s^0 \to D_s^{(\star)-}D_s^{(\star)+}X)}{\epsilon_{D_s\ell}(B_s^0 \to \ell^+\nu_\ell D_s^-)} = 0.2468 \pm 0.0073$$

The fraction of false signal events which are expected from this irreducible background to true signal events is given by

$$f_{D_sD_s} = \epsilon^{\rm rel}_{D_sD_s} \frac{\mathrm{BR}(B_s^0 \to D_s^{(\star)-}D_s^{(\star)+}X) \times \mathrm{BR}(D_s \to \ell X) \times 2}{\mathrm{BR}(B_s^0 \to \ell^+\nu_\ell D_s^-)} \tag{5.20}$$

where the factor of two accounts for the two possibilities $D_s^+D_s^- \to \ell^+\phi\pi^-(X), \phi\pi^+\ell^-(X)$. The world average measurement of the branching ratio for $B_s^0 \to D_s^{(\star)-}D_s^{(\star)+}X$ is quite inaccurately measured and so the EvtGen model prediction of 2.82% is used [91]. Similarly, the measured semileptonic branching ratio of $D_s^- \to \ell^- X$ is measured to be $8^{+6}_{-5}\%$. Therefore a prediction, of 6.32%, is made in EvtGen which is compatible with assuming that the partial widths of the D^0 and D^- to semileptonic final states are the same as for the D_s^- , as the spectator model predicts.

The branching ratio for $B_s^0 \to \ell^+\nu_\ell D_s^-$ is, as above, 7.9±2.4%. This results in a contribution to the sample of

$$f_{B_s \to D_sD_s} = 0.0151 \pm 0.0046$$

The third background contribution is also a decay of the B_s^0 meson, in this case $B_s^0 \to D_s^{(\star)-}D^{(\star)+/0}X$. Simulation samples are generated for this decay mode as for the previous cases. The relative number of reconstructed D_s^- mesons in this sample relative to that in the $B_s^0 \to \ell^+\nu_\ell D_s^-$ simulation sample is

$$\epsilon^{\rm rel}_{B_s \to D_sD} = \frac{\epsilon_{B_s \to D_sD}(B_s^0 \to D_s^{(\star)-}D^{(\star)+/0}X)}{\epsilon_{D_s\ell}(B_s^0 \to \ell^+\nu_\ell D_s^-)} = 0.0350 \pm 0.0025$$

The fraction of these events expected in the data sample is given by

$$f_{B_s \to D_sD} = \epsilon^{\rm rel}_{B_s \to D_sD} \frac{\mathrm{BR}(B_s^0 \to D_s^{(\star)-}D^{(\star)+/0}X) \times \mathrm{BR}(D \to \ell^+X)}{\mathrm{BR}(B_s^0 \to \ell^+\nu_\ell D_s^-)} \tag{5.21}$$

As before, the branching ratio of D meson semileptonic decays is a weighted average of the $\mathrm{BR}(D^+ \to \ell^+X)$ and $\mathrm{BR}(D^0 \to \ell^+X)$. The weights are given by the relative number

of reconstructed events in the simulation sample which have leptons from D^+ and D^0. Thus in this case

$$\mathrm{BR}(\mathrm{D} \to \ell\mathrm{X}) = 0.43 \times \mathrm{BR}(\mathrm{D}^+ \to \ell\mathrm{X}) + 0.57 \times \mathrm{BR}(\mathrm{D}^0 \to \ell\mathrm{X}) = 11.1 \pm 0.9\%$$

The resulting fraction is

$$f_{\mathrm{B_s} \to \mathrm{D_s D}} = 0.0081 \pm 0.0009$$

The contributions from these backgrounds are included in the B_s^0 lifetime fit by adding three extra terms to the signal region's likelihood function. These extra terms consist of a relative fraction, discussed above, and a lifetime shape for each irreducible background contribution. These are obtained from fits to the $c\tau$ distributions given by the simulation samples. The fit function consists of a delta function and an offset exponential distribution each convoluted with a Gaussian:

$$\begin{aligned} \mathcal{F}_i(t) = & \left[(1 - f_+)\delta(t' - \Delta_D) \right. \\ & + \left. \frac{f_{+i}}{\lambda_{+i}} \Theta(\Delta_{+i} - t') \exp\left(\frac{t' - \Delta_{+i}}{\lambda_{+i}} \right) \right] \otimes G(t - t', \sigma_G) \end{aligned} \tag{5.22}$$

The resulting fits are shown in figures 5.5 to 5.7. The fit parameters are given in table 5.2. The likelihood defined in equation 5.15 is modified by the inclusion of these three irreducible backgrounds:

$$\mathcal{F}_{sig}(t) \longrightarrow \frac{1}{1 + \sum_i f_i} \left[\mathcal{F}_{sig}(t) + \sum_i \mathcal{F}_i(t) \right] \tag{5.23}$$

and the summation index i runs over the three irreducible background contributions.

	$B \to D_s D$	$B_s \to D_s D_s$	$B_s \to D_s D$
σ (mm)	0.17±0.01	0.15±0.02	0.19±0.03
Δ_D (mm)	1.25±0.11	0.45±0.05	1.63±0.09
Δ_+ (mm)	0.21±0.01	0.22±0.04	0.25±0.03
f_+	0.97±0.01	0.85±0.05	0.96±0.02
λ_+ (mm)	0.67±0.02	0.66±0.05	0.65±0.04

Table 5.2: *Results of the unbinned log-likelihood fits to the lifetime templates obtained from the simulations of irreducible background components.*

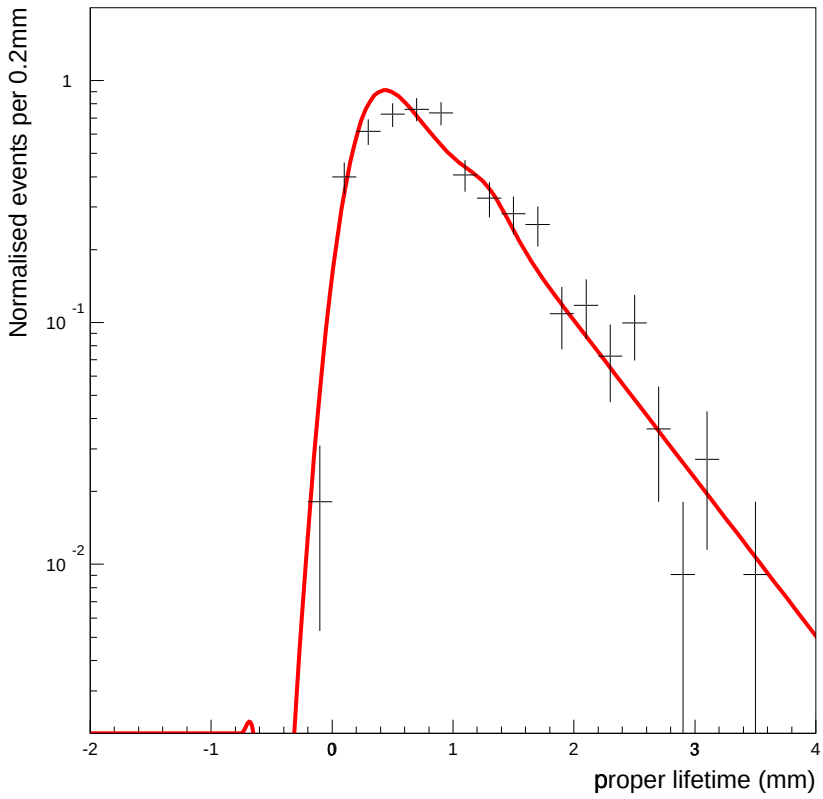

Figure 5.5: *Fit to the simulation lifetime template for the* $B_d^0 \to D_s^{(\star)-} D^{(\star)+/0} X$ *sample.*

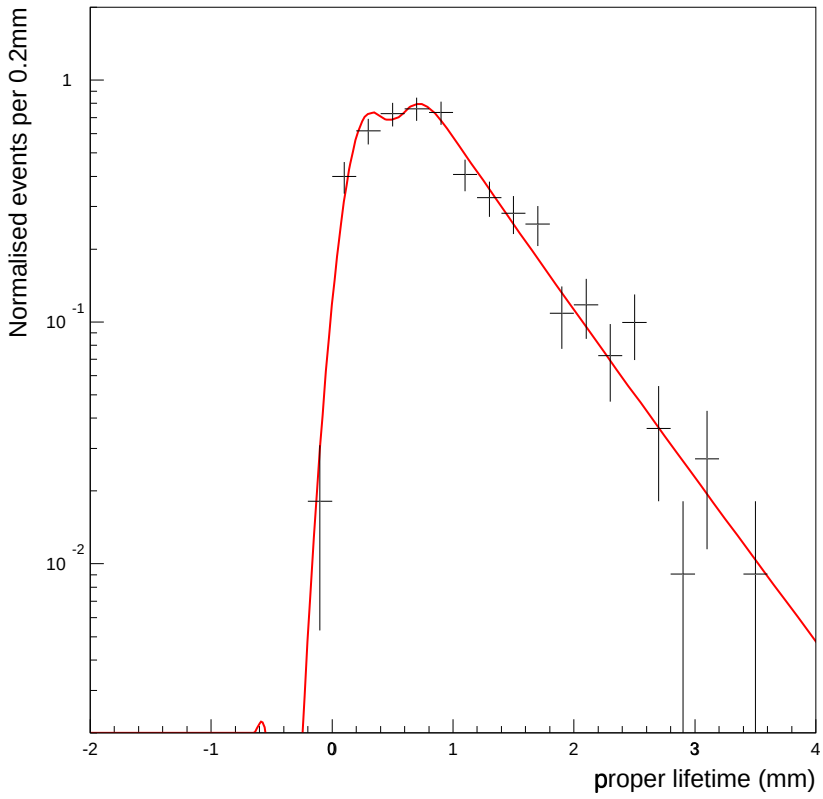

Figure 5.6: *Fit to the simulation lifetime template for the* $B_s^0 \to D_s^{(\star)-} D_s^{(\star)+} X$ *sample.*

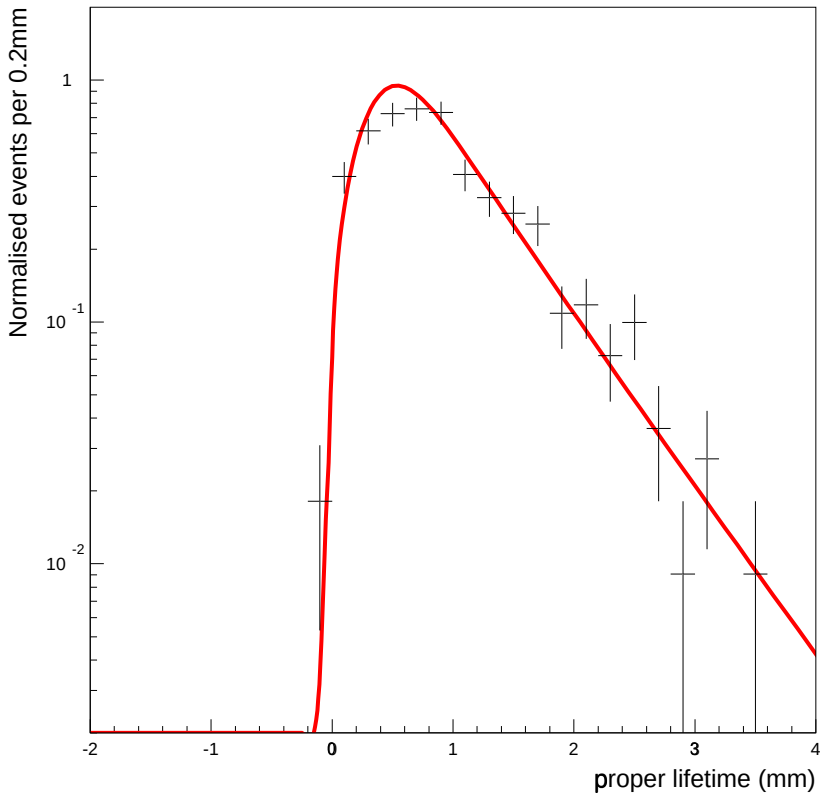

Figure 5.7: *Fit to the simulation lifetime template for the* $\mathrm{B_s^0} \to \mathrm{D_s}^{(\star)-}\mathrm{D}^{(\star)+/0}\mathrm{X}$ *sample.*

Chapter 6

Systematic Error Studies

The systematic uncertainty of the measurement of the B_s^0 lifetime is evaluated by examining the effect of the various ingredients on the fitted lifetime. The majority of the systematic effects considered are concerned with the details of the Monte Carlo simulation of events. Two types of simulation input parameters are varied: event generation parameters and trigger simulation parameters. The procedure for evaluating a systematic error from the simulation is discussed first. A discussion then follows of the remaining effects, which include the detector alignment and the $c\tau$ error scale factor. The individual systematic errors are added in quadrature to give the overall systematic error.

6.1 Systematic Errors from Monte Carlo Input Parameters

This analysis relies on Monte Carlo event samples to evaluate two important ingredients in the lifetime fit. These are the K factor, which corrects for the missing momentum due the the presence of a neutrino, and the lifetime bias which arises from having a displaced vertex trigger. As a result of this reliance, the lifetime fit is dependent on the input parameters used in the Monte Carlo generation. This dependence is scrutinised by varying each parameter individually. A systematic error is assigned according to the

change in the fitted lifetime. The procedure is as follows.

A toy MC simulation is used to generate large samples of signal- and background- like events using the fit functions described in chapter 5 with their parameters fixed to those fitted in data. This toy MC uses the K factor and bias from the parametric simulation described in chapter 4. The toy MC used was written by the author of this thesis and is described in appendix C. Many individual MC parameters in the parameteric simulation are then changed in turn according to the ranges, which will be discussed later to produce many new parametric simulation samples from which new K factors and biases are then extracted for each systematic effect. A lifetime fit is then made to the toy MC sample using the new K factor and bias. The largest difference between the $c\tau$ measured with the default settings and that measured with one parameter varied is taken as the systematic error for that parameter. This will be described in detail for each parameter.

6.1.1 Trigger Cuts on Impact Parameter

As described in section 3.2.1 the lepton plus displaced track trigger which collects the sample used in this analysis requires one track in the event to have an impact parameter, $|d_0|$, between 120μm and 1mm. The trigger used to enforce this cut is the Silicon Vertex Trigger which measures impact parameters at Level 2. To account for a systematic radial shift in the impact parameter, the $|d_0|$ range is varied by $\pm$10μm on the upper and lower cut values. The significance of this number is that the SVT measures the impact parameter in 10μm bins. The ranges which are measured are 110μm to 0.99mm and 130μm to 1.01mm. The differences between the fit for the default parameters and for these ranges are +9μm and +1μ respectively. The systematic error assigned is therefore +9μm.

6.1.2 Impact Parameter Resolution

The impact parameter resolution is measured in the data for both SVX and SVT measurements of the impact parameter. These resolutions are the Gaussian widths of the d_0 distribution measured by the SVX and SVT. They are used as inputs to the Monte Carlo simulation of the trigger. The resolutions measured in data are 47μm for the SVT and 40μm for the SVX. These are both varied by $\pm$ 10μm . The resulting systematic error is +8μm.

6.1.3 Peterson Epsilon Parameter

The Peterson epsilon parameter is explained in section 1.4.2. The Peterson function is a suggested form for the non-perturbative fragmentation function. Theory suggests that $\epsilon_{\rm Q} \sim \mathcal{O}(\Lambda/M_{\rm b})^2$. The default value for ϵ_b is 0.06 [102] and its value is varied by $\pm$0.02 to assign a systematic error. This is the range which was used for the CDF RunI B^+ cross-section analysis [103]. The differences between the fit for the default parameters and for the varied ϵ_b values are -4μm and +4μm.

6.1.4 $D/D^\star$ Fraction

The decay chains simulated in the Monte Carlo samples from which the K factor and trigger bias are extracted are

$$\begin{aligned} {\rm B_s^0} &\rightarrow \ell\nu{\rm D_s^-} \\ {\rm B_s^0} &\rightarrow \ell\nu{\rm D_s^{-\star}}, \quad {\rm D_s^{-\star}} \rightarrow {\rm D_s^-}\gamma/\pi^0 \end{aligned}$$

The proportion of events in which the D_s^- comes directly from the B_s^0 rather than from the $D_s^{-\star}$ is set, as a default, to the ratio of measured branching ratios measured in experiment [1]. A systematic error is assigned to this assumption by varying the ratio within the PDG errors on this number. This results in a change in lifetime of +2μm and -9μm. The systematic error assigned is therefore -9μm.

6.1.5 Trigger Simulation

As described in chapter 4, the lepton plus displaced vertex trigger is simulated in two ways. In the simpler case (GenTrig), a parametric simulation is used, in which the relevant detector components are described geometrically and the impact parameter and transverse momentum are smeared. In the alternative full simulation, a GEANT description of the detector material is utilised and the trigger is simulated at the bit level. This is expected to provide a more accurate trigger simulation, but is more computationally expensive. In section 4.5, both types of Monte Carlo were shown to agree with data. Therefore the parametric simulation is used for most of the Monte Carlo inputs and studies in this analysis. To account for simulation discrepancies, the difference in lifetime for the two approaches is included as a systematic uncertainty. The difference between the parametric and full simulations is 8μm which is assigned as the systematic error.

6.1.6 Lepton Momentum Threshold

The trigger requires a lepton with transverse momentum of greater than 4GeV/c. This cut is varied by the p_{T} resolution of $\sigma(p_T)/p_T^2 < 0.1\%/\mathrm{GeV/c}$. The lifetime is evaluated with p_{T} cuts of 3.984GeV/c and 4.016GeV/c. This change is found to have no effect on the lifetime and so no sytematic error is assigned.

6.2 Systematics from Detector or Data effects

6.2.1 Alignment

The positions of the COT and SVXII detectors and their individual components were measured very precisely before their installation in the CDF detector. However, alignments are made using track information to determine the positions more accurately, and to account for any shifts, twists or bows which have occurred since installation. The detector alignments for the COT and SVXII detectors affect the track parameters, most

significantly for this analysis on the impact parameter and transverse momentum of the tracks. The systematic error for the alignment is evaluated in the analysis of the B_s^0 lifetime in the decay $B_s^0 \to J/\psi\phi$ [101]. To evaluate the systematic error due to the alignment, the geometry of the detector is distorted in four ways, leading to four new alignment files. The distortions are: all ladders are shifted uniformly in the radial direction by 50μm inwards and outwards; all ladders are bowed, such that only the central two wafers of each silicon ladder (containing four wafers) are shifted by 50μm inwards and outwards. The lifetime is evaluated with each of these new alignments and the variation is found to be $\pm 1\mu$m which is taken as the alignment systematic error for this analysis.

6.2.2 Scale Factor

The error on the pseudo-proper decay length, L_{xy}, comes from the vertex fit to the B_s^0 decay products' tracks. An overall under or over estimate of this error is measured in a separate data sample, which has no impact parameter cuts and therefore no lifetime bias. This procedure is explained in section 5.5.1. The resulting measurement is 1.22 ± 0.1 which indicates that the errors were underestimated by 22%. A systematic error is assigned by refitting the lifetime for $\pm 3\sigma$ from the central value of 1.22. The resulting lifetime differences are $+2\mu$m for a scale factor of 1.12 and -4μm for a scale factor of 1.32. The systematic error assigned is $+4\mu$m.

6.3 Summary

The systematic errors are given in table 6.1. The errors are added in quadrature to give a total systematic error of $^{+15}_{-13}\,\mu$m.

Systematic Source	**Range**	**Systematic Error (μm)**
d0 range	110μm to 0.99mm to 130μm to 1.01mm	+9
SVT d0 resolution	25→50 μm	+8
Peterson epsilon	0.004→0.008	$\pm$4
D/D* fraction	1.94/5.3→2.34/5.76	$^{+2}_{-9}$
Trigger Sim	GenTrig/svtsim	$\pm$8
Lepton Momentum	3.84→4.16GeV/c	0
Alignment	See text	+1
Scale Factor	1.12→1.32	$^{+2}_{-4}$
	Total	$^{+15}_{-13}$

Table 6.1: *Systematic error assignments*

Chapter 7

Lifetime Results

The B_s^0 meson lifetime is fitted in the muon and electron samples described in chapter 3 using the fitting method described in chapter 5 with the bias and K factor taken from the full simulation sample described in chapter 4.

In the electron sample there are 526 events in the signal region and 151 events in the combined sideband regions. In the muon sample there are 757 events in the signal region and 219 events in the sideband regions. The B_s^0 lifetime is extracted from an unbinned log-likelihood fit which is applied simultaneously to the signal and sideband regions.

The distributions of observed lifetimes with the fit results overlaid are shown in figures 7.1 and 7.2 for electrons and muons respectively and the fit parameters are given in table 7.1. The results from the electron and muon samples are consistent. A combined fit to electron and muon samples is also performed and the result is shown in figure 7.3. The fit parameters are also given in table 7.1.

The lifetime results and the world average measurement [100] are given in picoseconds in table 7.2. The separate electron and muon measurments and the combined measurement are all consistent with the current world average [100] and current world best published measurement [15]. The statistical error of this analysis equals that of the world best measurement and the systematic error is smaller in this analysis.

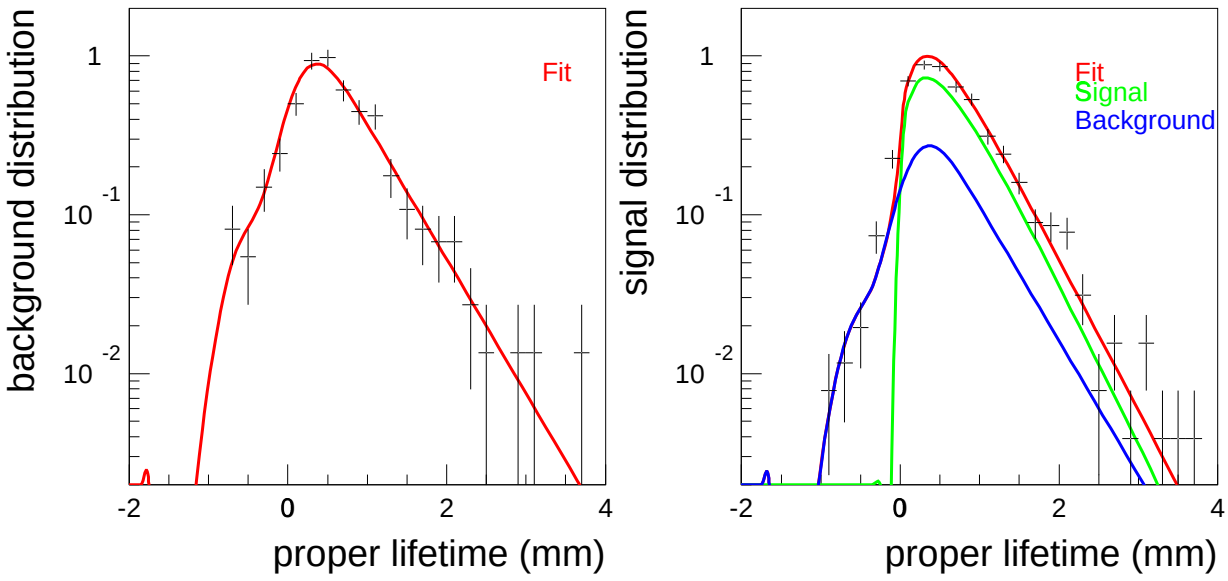

Figure 7.1: *Lifetime fits to signal and background regions in the muon sample.*

	Muon Fit	Electron Fit	Combined Fit
$c\tau$ (μm)	421±36	418±40	419±28
f_{bkg}	0.31±0.02	0.30±0.02	0.32±0.02
σ (mm)	0.25±0.03	0.24±0.05	0.25±0.03
Δ_D (mm)	−0.48±0.10	−0.28±0.12	−0.41±0.08
Δ_E (mm)	0.11±0.04	0.07±0.07	0.09±0.03
f_+	0.95±0.02	0.92±0.05	0.95±0.02
λ_+ (mm)	0.51±0.05	0.59±0.06	0.55±0.04

Table 7.1: *Results of the fits to data. The errors shown are statistical only.*

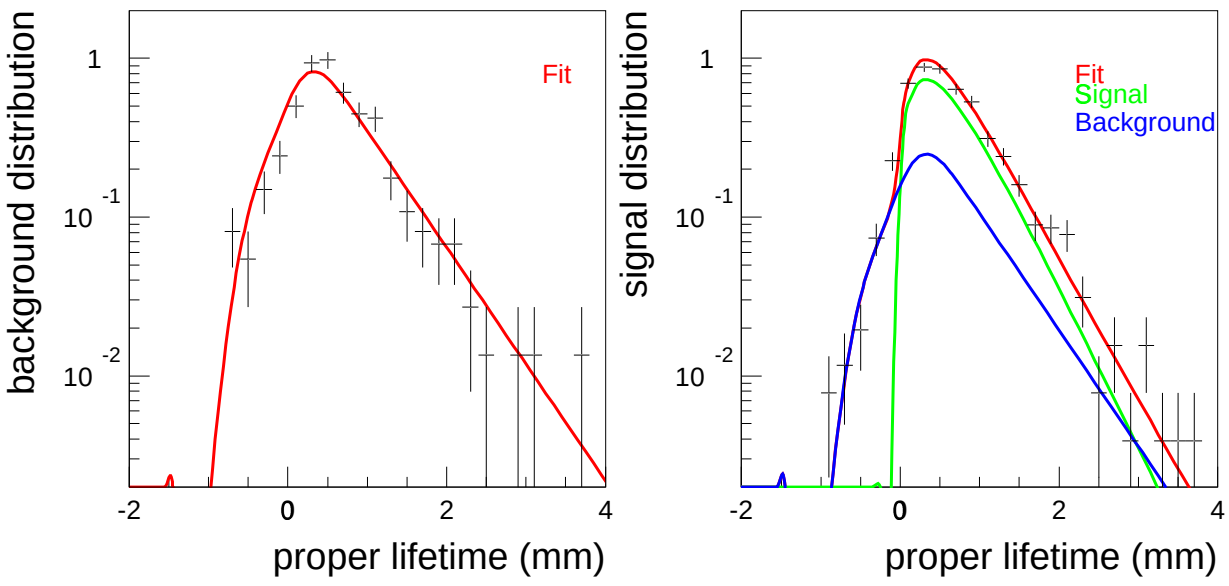

Figure 7.2: *Lifetime fits to signal and background regions in the electron sample.*

Muon Fit	1.404±0.120(stat.)
Electron Fit	1.394± 0.133(stat.)
Combined Fit	$1.398 \pm 0.093(\text{stat.})^{+0.050}_{-0.043}(\text{sys.})$
Combined Fit	$1.398^{+0.106}_{-0.102}(\text{stat.} \oplus \text{sys.})$
World Average	1.461±0.057
World Best	$1.36 \pm 0.09(\text{stat.})^{+0.06}_{-0.05}(\text{sys.})$

Table 7.2: *Lifetime results in picoseconds. The combined result also shows the systematic errors.*

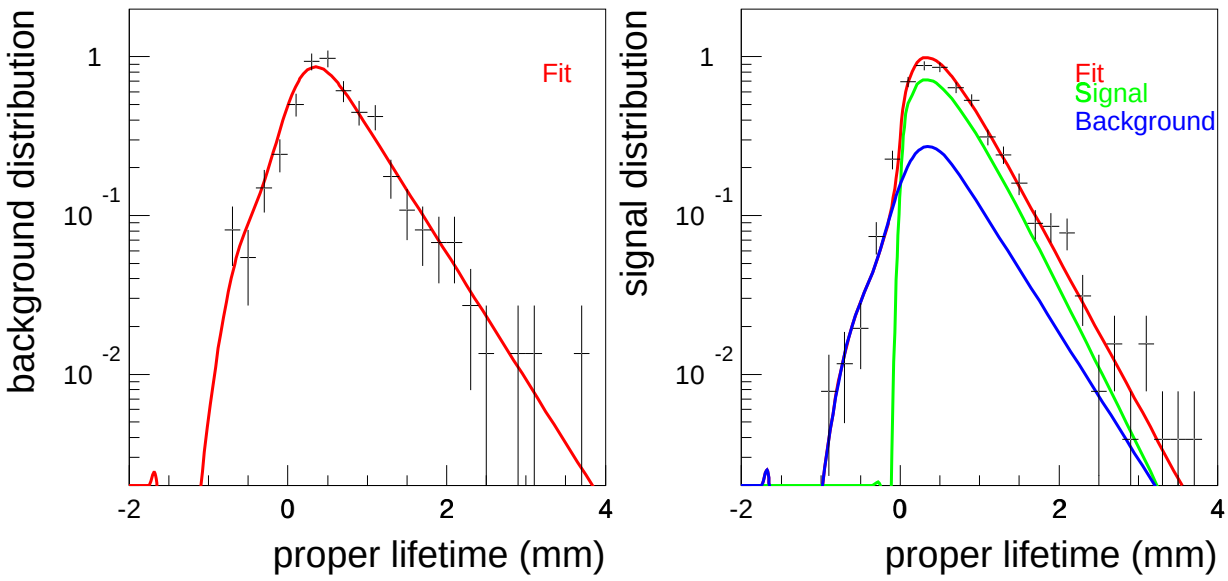

Figure 7.3: *Lifetime fits to signal and background regions in the combined electron and muon sample.*

Chapter 8

Control Sample Studies

The lepton plus displaced vertex trigger is used not only for the B_s^0 sample discussed in this thesis but also by other CDF collaborators to reconstruct a high statistics control sample of ℓ^+D^0 events, with $D^0 \to K^-\pi^+$, which can arise directly from the decay of a B^+ meson or from $B_d^0 \to \ell^+\nu_\ell D^0(\pi^-)$. The B^+ lifetime is $c\tau = 501.3 \pm 5.4\mu$m and the B_d^0 lifetime is $c\tau = 460.8 \pm 4.2\mu$m. In Monte Carlo simulation, the weighted average lifetime for the $\ell^+\nu_\ell D^0$ channels is $493\pm4\mu$m [104]. This lifetime has been measured in CDF Run II data by others, in a similar analysis to the B_s^0 analysis presented in this thesis, using the inclusive ℓ^+D^0 sample. The resulting lifetime is $434\pm9\mu$m which disagrees with the expected value by approximately five standard deviations [104]. Since this control sample lifetime measurement does not agree with the expected value by such a large amount, no b hadron lifetimes measured in semileptonic channels have been released to the public by the CDF Run II collaboration.

It should be noted that the B_s^0 semileptonic lifetime measurement described in this thesis shows no discrepancy with the PDG average value, but also that the statistics in this channel are lower by a factor of approximately eight than those of the $B^+/B_d^0 \to \ell^+\nu_\ell D^0$ channel. This chapter is written with the intention of documenting the many studies which have taken place in an effort to understand the origin of the discrepancy. In chapter 6, many systematic effects in the $B_s^0 \to \ell^+\nu_\ell D_s^-$ channel are examined and discussed and

these may also be considered to form part of the studies. The remaining studies which do not fall into the category of "systematic checks" are described here. This chapter is the only one containing work which is not solely that of the author. The work carried out by others is clearly referenced.

8.1 Verification of the Discrepancy

8.1.1 Crosscheck of the Lifetime Fitter

The pseudo-proper lifetime distributions of the $B^+/B^0_d \to \ell^+\nu_\ell D^0$ candidates identified in the CDF Run II studies [104] were fit with the lifetime fitting code implemented in this B^0_s analysis in order to rule out errors in the fitting code in [104]. The resulting lifetime agrees with that measured in the original analysis and has a value of $439\pm8\mu$m.

8.1.2 Candidate Selection Crosschecks

In addition, a further cross check analysis for the $B^+/B^0_d \to \ell^+\nu_\ell D^0$ sample was carried out by [108]. This study has independent reconstruction, simulation samples and fitting software. This analysis gives a measurement of $423\pm7\mu$m, in agreement with the result measured by [104] and confirmed by the crosscheck described in section 8.1.1.

8.2 Alternative Control Sample B^0_d / $B^+ \to \ell^+\nu_\ell D^-$

The $B^+/B^0_d \to \ell^+\nu_\ell D^0$ decays detailed above are partially reconstructed by identifying the decay of the D^0 into $K^-\pi^+$, a two-prong decay. As an alternative, it is interesting to study the lifetime in a decay of different topology and for this purpose the decay $B^0_d/B^+ \to \ell^+\nu_\ell D^-$ (BR$\sim$ 4%) with $D^- \to K^+\pi^-\pi^-$ (BR=9.2$\pm$0.6%) was reconstructed. This is similar to the D^-_s decay of interest in this thesis and this facilitates using a similar reconstruction method and cuts.

The difference in topology of the decays could be sensitive to alignment or trigger effects and so a control sample closer in topology to the D_s^- decay was chosen as a crosscheck. The decay of the D_s^- to $\phi\pi^-$ with ϕ to K^+K^- is a three-prong decay. For this purpose the $D^- \to K\pi\pi$ channel is chosen. This is again a mixture of B^+ and B_d^0 decays. The relative weights are given by the branching ratios of the decays $B_d^0 \to \ell^- \nu_\ell D^{-(\star(\star))}$ where some of the $D^{-\star(\star)}$ mesons decay into D^- mesons [91] and the decays of $B^+ \to \ell^+ \nu_\ell D^{0\star(\star)}$ where again some of the $D^{0\star(\star)}$ mesons decay into D^- mesons. The weighting is 87% B_d^0 and 13% B^+ so that the expected lifetime value is $466 \pm 4\mu$m.

8.2.1 B_d^0 / $B^+ \to \ell^+ D^-$ Selection Cuts

The selection cuts for the B_d^0 / $B^+ \to \ell^+ \nu_\ell D^-$ channel were chosen to be as close as possible to the $B_s^0 \to \ell^+ \nu_\ell D_s^-$ selection cuts given in section 3.5.1. The trigger, filter and track quality cuts are the same as in the B_s^0 analysis the details of which are discussed in chapter 3. The selection cuts for D^- candidates are as follows

- At least one of the three tracks, K^+, π^- or π^-, should be the SVT matched track.
- $p_T(K) > 0.8$ GeV/c
- $p_T(\pi) > 0.3$ GeV/c
- Q(ℓ)=Q(K) In a decay where the D^- and ℓ^+ come from the same B_d^0 , the K and ℓ must, by simple charge conservation, have the same charge.
- $\Delta R(\text{track}, \ell) \leq 1.2$ for each of the decay products of the D^- : K^+, π^-, π^-.
- $3.0 < m(\ell^+ D^-) < 5.0$ GeV/c^2 to exclude combinatorial background. The upper limit of 5 GeV/c^2 excludes unphysical combinatorial background since the mass of the B is not fully reconstructed.
- $L_{xy}(D^{PV}) > 400\mu$m, where $L_{xy}(D^{PV})$ is the distance between the D^- decay vertex and the primary vertex. Since D^- mesons are long-lived ($c\tau_{D^-} = 347 \pm 2\mu$m), this

cut reduces combinatoric background to the D^- .

- $\sigma(L_{xy}(B_d^0)) < 500\mu$m This cut removes events with large errors on the B_d^0 decay distance.

- $\text{Prob}(\chi^2_{r\phi}) > 10^{-5}$ for the B_d^0 vertex. The vertexing procedure of the D^- meson with the lepton returns a probability that a χ^2 function has a value greater than the actual χ^2 of the fit. Hence smaller χ^2 values give larger probabilities.

- $-150\mu\text{m} < c\tau(D^-) < 0.10$cm is required to eliminate combinatorial background since the D^- is long-lived.

Two cuts which were applied in the B_s^0 analysis cannot be applied here, namely the ϕ mass cut and $\cos\psi$ cut since the decay of the D^- does not proceed largely through a narrow, spin-1 meson such as the ϕ. The $D^- \to K^+\pi^-\pi^-$ decay proceeds through several channels, both resonant and non-resonant. The resulting mass peak has a signal to background ratio of S/B=0.3 compared with S/B=0.71 for the D_s^- . The mass distribution of D^- candidates found in the muon plus displaced vertex sample which satisfy the above criteria is shown in figure 8.1.

8.2.2 B_d^0 / B^+ Lifetime Results

The K factor correction, for the missing neutrino, and the bias function are extracted from Monte Carlo samples of B_d^0 / $B^+ \to \ell^+\nu_\ell D^-$ events in the same way as for the $B_s^0 \to \ell^+\nu_\ell D_s^-$ decays as described in sections 5.2 and 5.3. The distribution of the B_d^0 pseudo-proper lifetimes is then fitted using the technique described in chapter 5. The resulting lifetime is $441\pm15\mu$m. The expected number is $466\pm4\mu$m. The discrepancy between the measured and world average value is therefore 1.6 standard deviations.

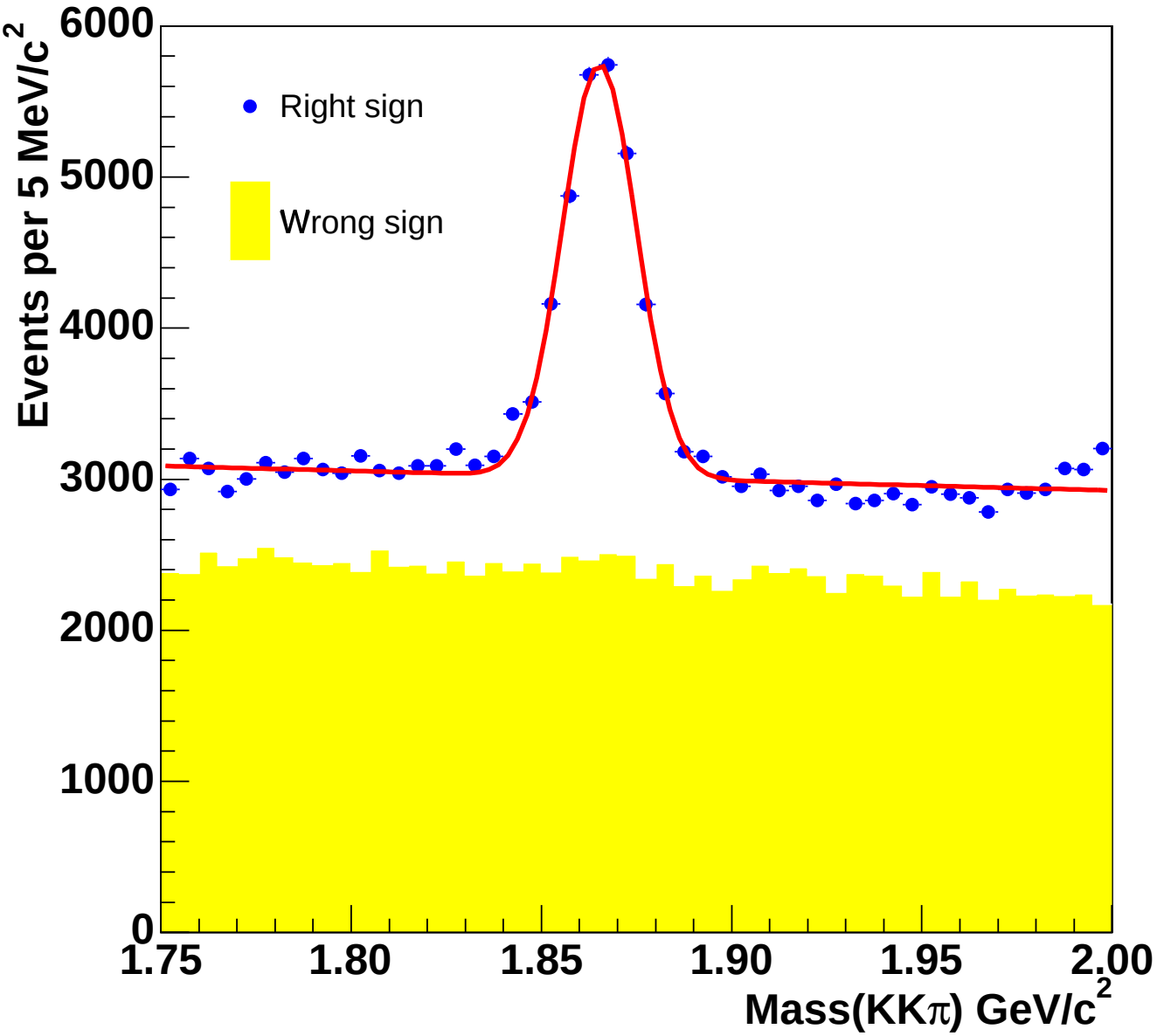

Figure 8.1: *D^- candidate mass from the muon sample. There are* 13291 ± 238 *signal events in the peak. The wrong sign events have the opposite charge correlation to that expected for a B semileptonic decay: $\ell^{\pm}K^{\mp}$ instead of $\ell^{\pm}K^{\pm}$.*

8.3 Studies in the B_d^0 /B^+ control sample

In this section, several studies are described which examine the possible effect on the lifetime of various detector and tracking parameters and also physics backgrounds. For this set of studies, the sample of B_d^0 /$B^+ \to \ell^+\nu_\ell D^-$ events was used, rather than the $B_s^0 \to \ell^+\nu_\ell D_s^-$ events. The B_s^0 sample is not used for such studies for two reasons. Firstly, the B_s^0 lifetime measurement is the more important for CDF and, although no longer a blind sample, it was decided that this sample should not be used for crosscheck studies. Secondly, the statistical error is larger than that in the B_d^0 / B^+ sample and so the level of sensitivity to effects will be lower. All of the work detailed in this section was carried out by the author of this thesis.

8.3.1 Alignment Effects

The positions of the COT and SVXII detectors and their individual components were measured very precisely before and during their installation in the CDF detector. However, runtime alignments are made using track information to determine the positions more accurately, and to account for any shifts, twists or bows which have occurred since installation. The detector alignments for the COT and SVXII detectors affect the track parameters, most significantly for this analysis the impact parameters and transverse momenta of the tracks. There are two approaches to obtaining a set of alignment parameters from the track information. The first approach is to minimise the sum of the χ^2 for each track between the fitted and measured track coordinates, with respect to the set of previously determined track parameters and the alignment parameters. This method is iterative and results in a series of track fits, which initially ignore refinements to the alignments. The assumption is made that the alignment corrections cancel on average. This is the default alignment procedure at CDF Run II. It was also used in Run I and is documented in [105]. An alternative approach makes only one very large simultaneous fit for all tracks and alignments [106]. In this case there is a very large error matrix

which describes the relationship between the track and alignment parameters. While this is a difficult fit, the procedure benefits from requiring only one fit instead of many. To invert the very large error matrix, Blobel's method [107] is used to divide the problem into smaller required inversions. The difference between these two alignment techniques is assessed by analysing B_d^0 /B^+ semileptonic decays using the standard method and the Blobel method. The alignment determined using Blobel's method was found to differ by $+10\mu$m, which is within the statistical error.

Dependence on ϕ

In the case of a gross misalignment, the lifetime could be expected to depend on the azimuthal angle, ϕ around the beampipe. The B_d^0 /B^+ lifetime was evaluated in bins of the ϕ of the lepton direction and the dependency, shown in figure 8.2, was examined and determined to be flat, within the available statistics. Fitting a straight line to the points gives a fit with χ^2 per degree of freedom of 0.98.

8.3.2 Definition of Primary Vertex

The determination of the primary vertex in the semileptonic decays of the B_s^0 and the control samples is discussed in section 3.4. The default method is to evaluate the beam equation to give the x and y coordinates of the beam at the average z position of the B_s^0 candidate decay tracks. As a cross check, an alternative prescription for determining the primary vertex is used. In the alternative method, the vertices are determined in each event by the algorithm described in section 3.4 and the closest vertex to the average z coordinate of the B decay product tracks is chosen as the primary vertex. The lifetime evaluated with this primary vertex definition differs by 7μm.

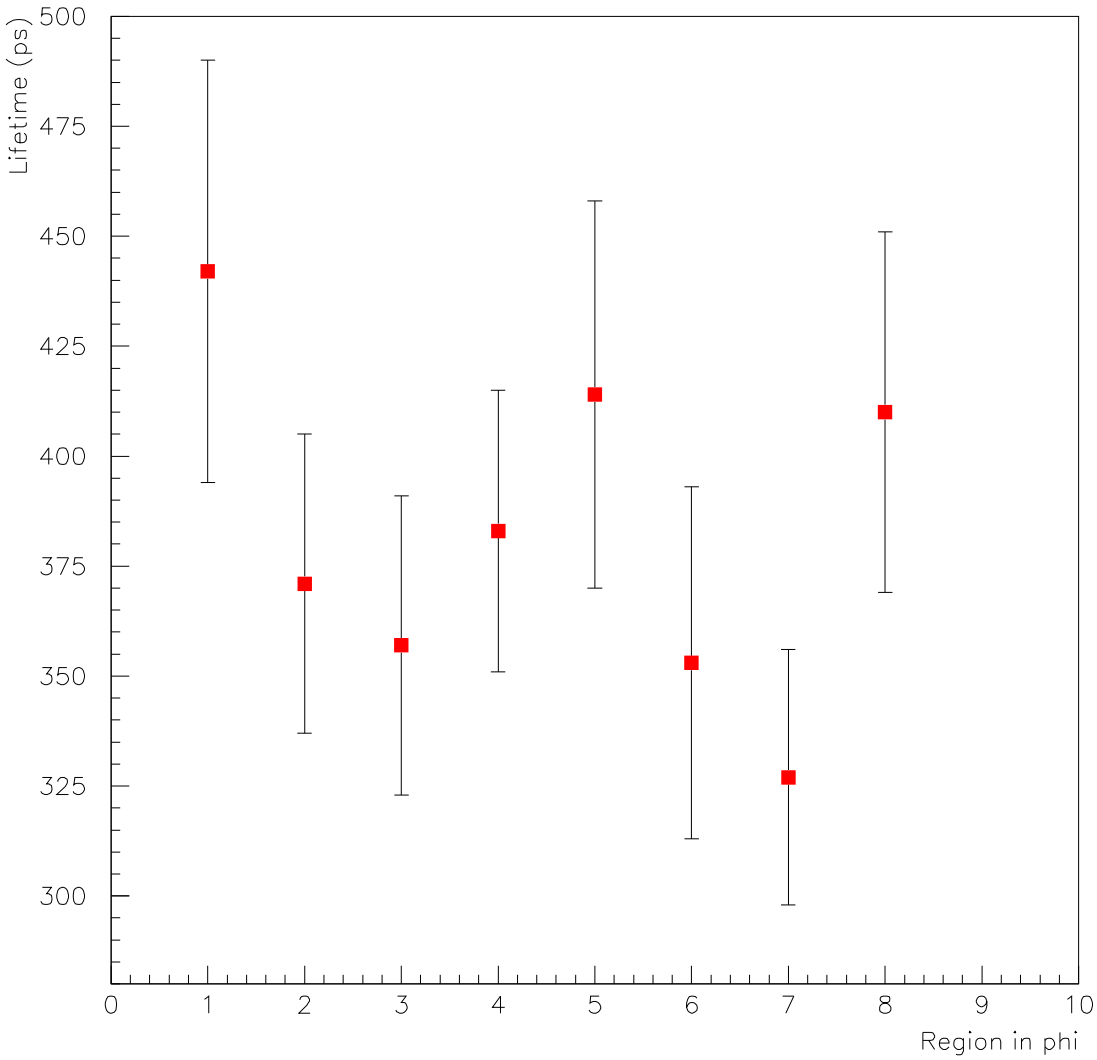

Figure 8.2: B_d^0 *lifetime as a function of the* ϕ *angle of the lepton.*

8.3.3 Tracking Algorithm

There are at least two variants of the algorithms used to form tracks from hits in the COT. The so-called histogram linking algorithm constrains tracks to originate from the primary vertex. This was found to give a considerable bias to lifetimes measured in

channels which included the reconstruction of long lived Λ or K_s^0 hadrons. Such hadrons travel some distance, of order 1m, before decaying, making it likely that they decay in the COT rather than within the Silicon detectors. Therefore, the assumption that the decay products of these hadrons originate at the primary vertex is false, by a considerable margin. The semileptonic B decays discussed do not include Λ or K_s^0 particles and so an effect on the lifetime due to this algorithm was not expected to be seen. However, a comparison was made for completeness and to test the hypothesis that the longlived hadrons were the only tracks affected. To do this, the tracking algorithms were run without the histogram linking algorithm and used the remaining standard algorithms. There was found to be no difference in lifetime, as expected.

8.3.4 Background Studies

The fitting method described in chapter 5 involves defining signal and sideband regions to which lifetime fits are made simulataneously. This method takes the sideband regions, which are combinatorial background consisting of fake D mesons, as representative of the background in the signal region. However, this does not account for the possibility of a background component consisting of a real D meson which makes a B meson candidate with either a real or fake lepton. The possibility of fake leptons being a significant source of background is negligible. The muon fake rate from decay in flight or punch through is 0.3 per mille and so the contribution of fake events is small. This is discussed in section 3.2.1. The fake rate can also be seen to be low by examining the wrong sign (ℓ^+D^+ or ℓ^-D^-) invariant mass distribution in figure 8.1. If there were a large fake rate then this should be apparent as a signal in the wrong sign distribution since the charge of the fake lepton would be uncorrelated to the charge of the D^- . No signal is perceptible in the wrong sign distribution.

This leaves only the possibility of a background from a real D meson which is vertexed with a genuine lepton from another source. One possible source of such a background is the gluon splitting to $c\overline{c}$ and the subsequent production of two charm hadrons, one of

which decays in the channel of interest, $D^- \to K^+\pi^-\pi^-$, and the other of which decays semileptonically thus producing a lepton. In order to test this hypothesis, a sample of all two-to-two QCD hard process events was generated using the Pythia Monte Carlo . Only events containing charm quarks which do not originate from b quarks are retained. The parametric trigger simulation is applied to the sample. The number of events which pass the trigger and reconstruction requirements is then counted. In order to establish the correct number of these events which are to be expected in the data, the simulation is normalised to the cross section for the production of D^+ mesons which has been measured in CDF Run II [109]. The resulting expectation is that 2-3% of the events identified in data as signal originate from $g \to c\overline{c}$ splittings. A template of the lifetime of the $g \to c\overline{c}$ events was folded into the likelihood but found not to make a signficant change to the lifetime when evaluated for a fixed fraction of 2-3% of expected events.

8.4 Studies by the Lifetimes Task Force

The discrepancy between B meson lifetimes measured in semileptonic channels and the world average values was investigated by a dedicated task force, the members of which are listed in [110]. All of the work in this section was carried out by other members of the lifetimes task force.

8.4.1 Evaluation in an 8 GeV/c Lepton Trigger

In addition to the triggers described in section 3.2, which utilise the Silicon Vertex Trigger to select events with displaced vertices, there is a control trigger for measuring semileptonic lifetimes. This is the same as the CDF Run I trigger, requiring a lepton (electron or muon) with a transverse momentum greater than 8GeV/c. The purity of this sample for b hadron events is lower than the triggers which use the SVT, since there is no cut on the impact parameter of a track in the event. The studies in this sample were performed by [104]. B^+ / $B^0_d \to \ell^+\nu_\ell D^0$ candidates were reconstructed using the same cuts as in the

lepton plus displaced vertex triggers. The appropriate K factor was extracted from Monte Carlo samples to which the trigger requirements were applied. In this sample the lifetime is not biased by the trigger and so the lifetime fitter was modified to remove the bias correction. The resulting lifetime is $432\pm10\mu$m, compared with $429\pm8\mu$m in the lepton plus displaced vertex sample. The agreement between these measurements demonstrates that the bias introduced by the SVT is not the cause of the discrepancy between the measured lifetimes and the PDG world average lifetimes [1].

8.4.2 The D^0 Meson Lifetime

To partially reconstruct the semileptonic decay of a B meson, such as $B^+/B^0_d \to \ell^+\nu_\ell D^0$, a D^0 meson is fully reconstructed. The sample of D^0 mesons collected in this way is used to determine the D^0 meson lifetime [104]. D mesons have appreciable lifetimes: $c\tau(D^0) = 123.1\pm4.5\mu$m [1]. A fit to the $c\tau$ distribution of D^0 candidates does not require a K factor, since the mesons are fully reconstructed, but still requires a bias function. This bias function is different from that used for the B mesons since the D lifetime is affected differently by the trigger. This is extracted from Monte Carlo and the fitting function is adjusted to remove the K factor. The measurement of the D^0 lifetime is a further check of internal silicon alignment and the bias function. The measured lifetime is $128.0\pm2.5\mu$m, in agreement with the world average value [1].

8.4.3 Vertex Algorithm

In case of errors in the vertex algorithm, the lifetime was also measured by using fixed track parameters to establish the intersection point of the D^+ decay tracks and the lepton without using the vertexing algorithm described in 3.5.1 [104]. The results were the same and an error in the vertex algorithm is ruled out.

8.5 Conclusion of Control Sample Studies

The measurements of B meson lifetimes in high statistics control samples disagree with the expected values by several standard deviations. Many possible explanations for this discrepancy have been examined and are described in this chapter.

The discrepancy in the $B^+/B_d^0 \to \ell^+\nu_\ell D^0$, ($D^0 \to K\pi$) sample which was measured by [104] has been verified by the author of this thesis and by an additional collaborator independently. Furthermore, a lifetime measurement in the $B^0/B^+ \to \ell^+\nu_\ell D^-$, ($D^- \to K\pi\pi$) sample also shows a small disagreement with the expected value by 1.6 standard deviations. With this channel, several detector, tracking and physics background effects were studied. These demonstrated that reasonable variations of the alignment, primary vertex definition and tracking algorithm do not rectify the discrepancy. In addition, the contribution from a background of $g \to c\overline{c}$ was quantified and shown to be small.

The work of the Lifetimes Taskforce included measuring the lifetime in a sample of $B^+/B_d^0 \to \ell^+\nu_\ell D^0$ in a sample for which the trigger does not require a displaced track and demonstrated that the discrepancy also exists in this sample. This shows that the new displaced track trigger and the handling of the consequent bias is not the reason for the discrepancy. The taskforce also measured the D^0 meson lifetime and obtained a result which agrees with the world average value. This further proves that the handling of the bias is correct and that tracking or alignment effects are not the cause of the discrepancy.

Chapter 9

Conclusions

This thesis details a measurement of the B_s^0 meson lifetime in semileptonic decays at CDF Run II. Samples of B_s^0 mesons are partially reconstructed in a trigger which requires a lepton (μ or e) and a track with large impact parameter. The B_s^0 is identified by its semileptonic decay to $\ell^+\nu_\ell D_s^-$ where the D_s^- meson decays to $\phi\pi^-$ and the ϕ meson decays to K^+K^-. This yields a total sample of 905 ± 42 $\ell^+D_s^-$ candidates in a data sample of 140pb^{-1}. The pseudo-proper lifetime distribution of these candidates is fitted with an unbinned maximum likelihood fit and yields the result for the B_s^0 lifetime

$$\begin{aligned} c\tau(B_s^0) &= 419 \pm 28^{+16}_{-13}\ \mu\text{m} \\ \tau(B_s^0) &= 1.397 \pm 0.093^{+0.053}_{-0.043}\ \text{ps} \end{aligned}$$

where the first error is statistical and the second is systematic.

The statistical errors are the same as those for the CDF Run I analysis which is currently the world's best published measurement [15]. The systematic errors have been assessed conservatively and are smaller than those of the world's best measurement.

Appendix A

Silicon Monitoring

SiliMon [111] is an online program which produces histograms of silicon data using the root graphics program. These histograms are used to monitor and evaluate the performance of the silicon detectors. Histograms of raw silicon information are provided as well as preliminary reconstructed track information and clusters of silicon hits (groupings of nearby hits passing a threshold) for all events which pass the highest level (3) trigger.

My involvement with SiliMon has been to study the many (3139 in total) plots to identify problems in the silicon detectors and the SiliMon code. The vast number of plots makes it desirable to automate the monitoring process and so I have written root macros, in the C++ programming language, which flag problem channels by a number of means.

By visual inspection of the plots, problems were first identified and categorised and then tests were devised and tuned to flag the problematic components. These tests were then run weekly and the results presented weekly at the silicon detector group's meeting. The tests are:

Ratio of sides In this test the number of clusters associated with tracks on one side of a silicon ladder divided by the number on the other side is plotted. Firstly, this easily identifies ladders with one dead side. Secondly, this is a useful test of the tracking since we should expect both sides to be similar and the ratio should be close to one. Typical results are shown in figure A.1.

Kolmogorov Smirnov tests These were applied to several distributions. First a "good" ladder was identified by eye to act as a comparator for all other ladders. Then the Kolmogorov distance to the ladder under test was computed. This is a measure of the similarity between two plots which works by taking the maximum of modulo the difference of the cumulative distribution functions of the two plots. This was particularly useful in signalling, for example, a ladder with a stuck bit, that is where one of the digital readouts was stuck on all of the time. This has a distinctive distribution shown in figure A.2. The KS test was applied not only on a ladder-by-ladder basis but also chip-by-chip. There are 1584 chips and so clearly this is a task which requires automation. The KS distance cut value was tuned to flag as many bad ladders as possible, while not flagging an absurd number of borderline cases. In general, running all tests together flags all bad ladders, although individual tests do not do so. The tuning of the KS distance is shown in figure A.3 which shows the distance for bad and good chips and the efficiency and purity as a function of the KS distance cut.

Ratio of number of clusters to number of clusters on track This test probes both the tracking and the level of noise in the silicon detector.

Ratio of number of clusters on a chip to the number for the ladder This quantity was normalised by the number of chips on a ladder, which is different for each layer. This flags individual chips which are performing badly.

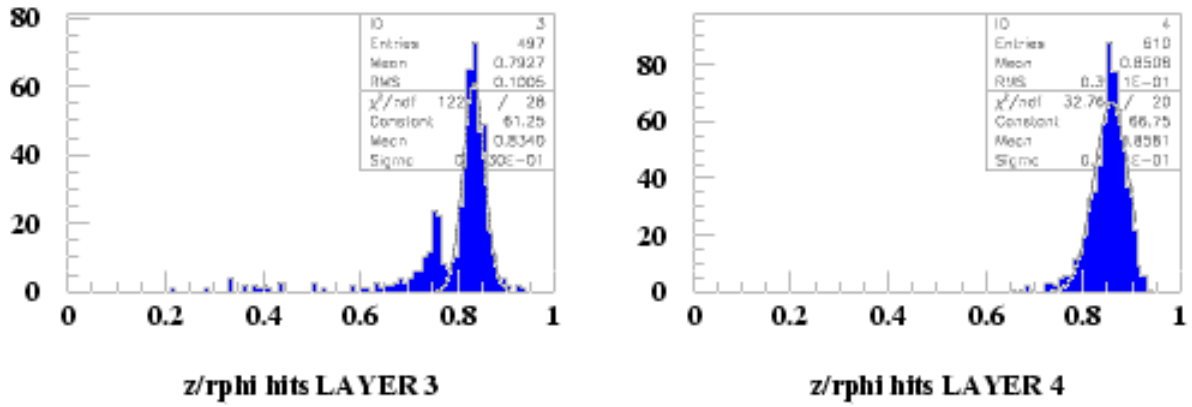

Figure A.1: *Number of clusters associated with tracks on one side of the silicon divided by the number on the other side for SVXII layers three and four of the central barrel. The secondary, lower, peak in the layer 3 plot is due to ladders which have a lower efficiency since the ladder in the next radial layer is switched off.*

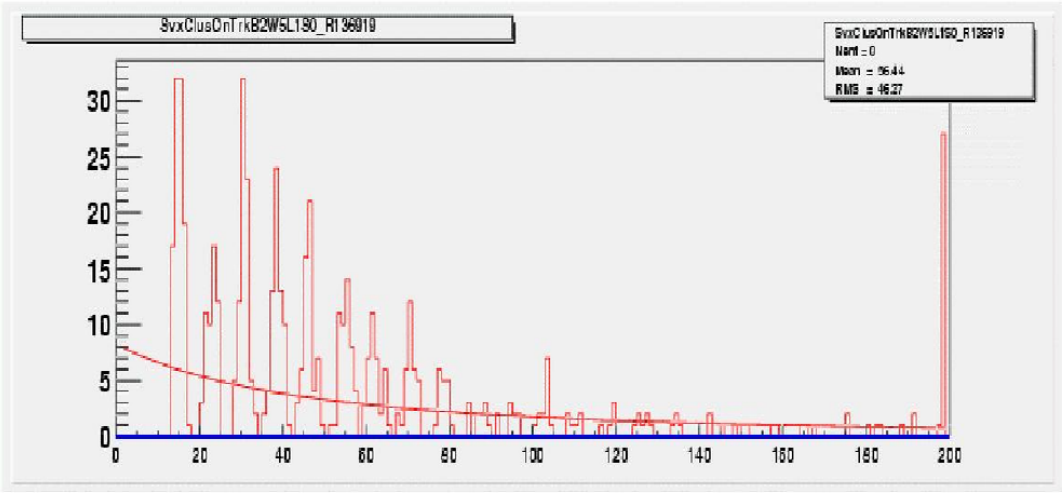

Figure A.2: *Cluster on track distribution for a ladder with a stuck bit. This distribution should be a Landau but when a bit is stuck, the distribution has this periodic structure since only certain values are then allowed.*

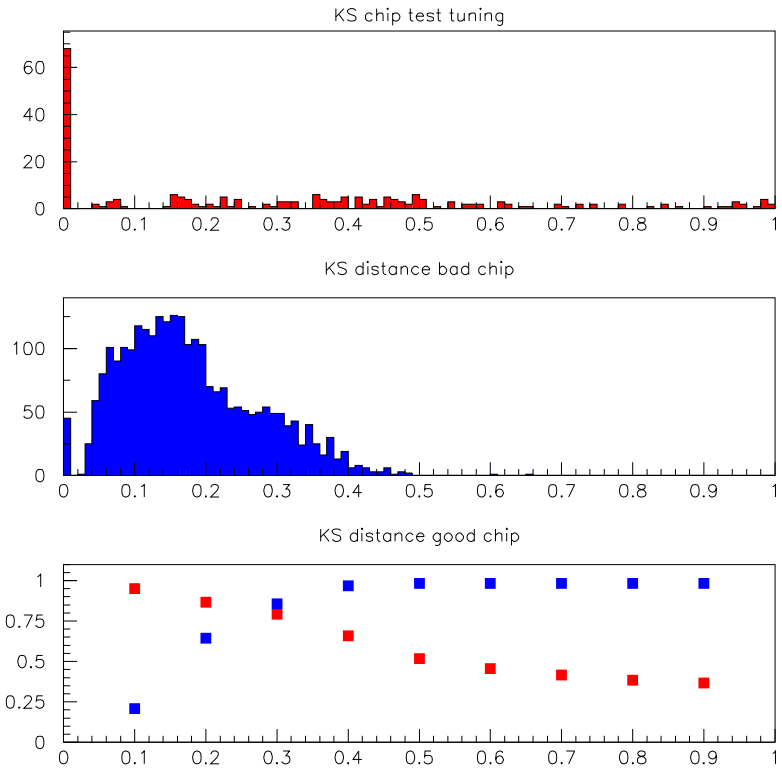

Figure A.3: *KS distance for bad chips (top), good chips (middle) and in the bottom plot are the efficiency (red) and purity (blue). In practice chips with a KS distance above 0.4 are flagged as bad.*

Appendix B

Trigger Paths

The trigger path names in CDF software are:

- muon+SVT trigger:

  L1_CMUP6_PT4

  L2_TRK2_D120_L1_CMUP6_PT4

  L3_B_SEMI_CMUP4_TRACK2_D120

- electron+SVT trigger:

  L1_CEM4_PT4

  L2_TRK2_D120_L1_CEM4_PT4

  L3_B_SEMI_CEM4_TRACK2_D120.

Appendix C

Toy Monte Carlo

A toy Monte Carlo simulation is used to produce large samples of signal and background -like events for the purposes of validating the lifetime fitting code as discussed in chapter 5 and for systematics studies as discussed in chapter 6. This simulation tool was written for this thesis and is described here.

The toy Monte Carlo simulation generates event lifetimes according to the probability distributions defined in chapter 5 for signal and background events:

$$\mathcal{F}_{sig}(t) = N \quad \frac{K}{\tau}\exp\left(\frac{-Kt'}{\tau}\right)\epsilon\left(Kt'\right) \otimes H(K) \otimes G(t-t',\sigma_G) \tag{C.1}$$

$$\mathcal{F}_{bkg}(t) = \left[\quad (1-f_+)\delta(t'-\Delta_D) + \frac{f_+}{\tau_+}\Theta(\Delta_E - t')\exp\left(\frac{t'-\Delta_E}{\tau_+}\right)\right] \otimes \quad G(t-t',\sigma_G) \tag{C.2}$$

In order to generate these distributions, it is necessary to be able to generate the component exponential and Gaussian distributions.

C.1 Exponentially Distributed Random Numbers

The normalised exponential distribution is defined by

$$\frac{1}{\tau}e^{-t/\tau}$$

Given a (pseudo) random number, $R_{\#}$, uniformly distributed between 0 and 1, it is possible to generate an exponentially distributed number, t, by solving the implicit equation

$$R_{\#} \int_0^{\infty} ds \frac{e^{-s/\tau}}{\tau} = \int_0^{t} ds \frac{e^{-s/\tau}}{\tau} \tag{C.3}$$

This integral can be calculated analytically to give

$$R_{\#} = 1 - e^{-t/\tau} \tag{C.4}$$

The resulting equation can be inverted. An exponentially distributed number, t, is then given by

$$t = -\tau \ln R'_{\#} \tag{C.5}$$

C.2 Gaussian Distributed Random Numbers

The normalised Gaussian distribution is given by

$$\frac{e^{-x^2/2\sigma^2}}{\sqrt{2\pi\sigma^2}} \tag{C.6}$$

The procedure described above to generate an exponentially distributed random number cannot be used in this instance since the Gaussian function is not analytically integrable. However, it is possible to use the procedure to generate two Gaussian distributed numbers by first transforming to polar coordinates:

$$dx \frac{e^{-x^2/2\sigma^2}}{\sqrt{2\pi\sigma^2}} \times dy \frac{e^{-y^2/2\sigma^2}}{\sqrt{2\pi\sigma^2}} = d\phi \frac{1}{2\pi} \times dr\, r \frac{1}{\sigma^2} e^{-r^2/2\sigma^2} \tag{C.7}$$

Thus, given a ϕ uniformly distributed between 0 and 2π and an r between 0 and ∞ distributed according to $\frac{1}{\sigma^2} r e^{-r^2/2\sigma^2}$ the Gaussian distributed numbers x and y are given by

$$x = r\cos\phi \tag{C.8}$$

$$y = r\sin\phi \tag{C.9}$$

To generate values of r, it is necessary to solve

$$\begin{aligned} R_{\#} &= \int_0^r ds \frac{e^{-s^2/2\sigma^2}}{\sigma^2} \\ &= 1 - e^{-r^2/2\sigma^2} \end{aligned} \tag{C.10}$$

and so r is given by

$$r = \sigma\sqrt{-2\ln R'_{\#}} \tag{C.11}$$

C.3 Generation of Background Event Lifetime Distribution

In order to generate lifetime values for background events, the form given in equation C.2 is used. The procedure is as follows:

- A random number, $R_{\#1}$, between 0 and 1 is generated.
- If $R_{\#1}$ is less than f_+ then the background τ is from an exponential distribution and so $t_1 = \Delta_E - \tau_+ \ln R_{\#2}$.
- If $R_{\#1}$ is greater than f_+ then the background is in the delta function and so $t_1 = \Delta_D$.
- The convolution with the Gaussian is then added:

  $$t - t_1 = \sigma_G\sqrt{-2\ln R_{\#3}}\cos(R_{\#4}.2\pi) \tag{C.12}$$

  and so $t = t_1 + (t - t_1)$.

C.4 Generation of Signal Event Lifetime Distribution

In order to generate lifetime values for signal events, the form given in equation C.1 is used. The procedure is as follows:

- To generate the K factor value, a random number, $R_{\#1}$, is generated. The cumulative distribution of the binned K factor is normalised such that $\sum_{i=1}^{N} f_i = 1$ where f_i is the probability of selecting the value K_i. The selected K factor is found by solving

$$\sum_{i=1}^{n-1} < R_{\#1} \leq \sum_{i=1}^{n} f_i \quad \text{and} \quad R_{\#1} > \sum_{i=1}^{n-1} f_i \tag{C.13}$$

  for the nth bin.

- The exponentially distributed lifetime value, t', is then be generated according to $t_1 = -\frac{\tau}{K} \ln R_{\#2}$.

- Events are then accepted or rejected depending on the bias function, $\epsilon(Kt')$, by comparing a uniformly distributed random number with the value of ϵ at the given K and t' values described in the steps above. If $R_{\#3} \times \epsilon_{max}$ is greater than $\epsilon(Kt_1)$ then the event is rejected; if it is less then the event is accepted.

- The Gaussian convolution is included as described before

$$t - t_1 = \sigma_G \sqrt{-2 \ln R_{\#4}} \cos(R_{\#5}.2\pi) \tag{C.14}$$

Bibliography

[1] K. Hagiwara et al. Phys. Rev. **D66** (2002) 010001 (updated web edition)

[2] I. Dunietz Phys. Lett. **B369** (1996) 144

[3] K.Anikeev, C.Paus *Using Transversity Variable to Disentangle (C)P Eigenstates in* $B_s^0 \to J/\psi\phi$ *and* $B_d^0 \to J/\psi K^{*0}$ CDF Internal Note 6551 (2004)

[4] K. Anikeev et al. *Time-Dependent Angular Analysis of* $B_s^0 \to J/\psi\phi$ *and* $B_d^0 \to J/\psi K^{*0}$ *Decays* CDF Internal Note 7044 (2004)

[5] D. Buskulic et al. Phys. Lett. **B294** (1992) 145

[6] P. Abreu et al. Phys. Lett. **B289** (1992) 199

[7] P.D. Acton et al. Phys. Lett. **295** (1992) 357

[8] P.D. Acton et al. Phys. Lett. **B312** (1993) 501

[9] D. Buskulic et al. Phys. Lett. **B322** (1994) 275

[10] P. Abreu et al. Z. Phys **C61** (1994) 407

[11] D. Buskulic et al. Phys. Lett **B311** (1993) 425

[12] P. Abreu et al. Phys. Lett. **B324** (1994) 500

[13] R. Akers et al. Phys. Lett. **337** (1994) 196

[14] F. Abe et al. Phys. Rev. **D53** (1996) 3496

[15] F. Abe et al. Phys. Rev. **D59** (1999) 032004

[16] R.K. Ellis, W.J. Stirling, B.R. Webber *QCD and Collider Physics* Cambridge University Press, 1996

[17] G. Dissertori, I.G. Knowles, M. Schmelling *Quantum Chromodynamics: High Energy Experiments and Theory* Oxford University Press, 2003

[18] C. Avila et al. Phys. Lett. **B445** (1998) 419

[19] F. Abe et al. Phys. Rev. **D50** (1994) 5550

[20] N. Amos et al. Phys. Rev. Lett. **68** (1991) 2433

[21] F. Abe et al. Phys. Rev. **D50** (1993) 5518

[22] Amos et al. Phys. Lett. **B243** (1991) 15

[23] F. Abe et al. Phys. Rev. **D50** (1994) 5535

[24] K. Anikeev et al. *B Physics at the Tevatron: Run II and Beyond* hep-ph/0201071 (2001)

[25] S. Abachi et. al. Phys. Rev. Lett. **74** (1995) 3548

[26] Y.L. Dokshitzer, Sov. Phys. JETP **46** (1977) 641, V.N. Gribov and L.N. Lipatov, Yad. Fiz. **15** (1972) 781, G. Altarelli and G. Parisi, Nucl. Phys. **B126** (1977) 298

[27] M Hirai, S.Kumano, M. Miyama Phys. Rev. **D64** (2001) 034003

[28] M.L. Mangano, *Two Lectures on Heavy Quark Production in Hadronic Collisions*, hep-ph/9711337 (1997)

[29] R.D. Field, Phys. Rev. **D65** (2002) 094006

[30] T. Affolder et al. Phys. Rev. Lett. **84** (2000) 1663

[31] C. Peterson et al. Phys. Ref. **D27** (1983) 105

[32] T. Sjöstrand et al. Comp. Phys. Comm. **135** (2001) 238

[33] G. Corcella et al. JHEP **0101** (2001) 010, hep-ph/0210213

[34] D.E. Groom et al., European Physical Journal **C15** (2000) 1

[35] M. Neubert, Phys. Rep. **245** (1994) 259

[36] N. Isgur, B. Grinstein, D. Scora, M. Wise Phys. Rev. **D39** (1989) 799

[37] N. Isgur, D. Scora Phys. Rev. **D52** (1995) 2783

[38] V.F. Weisskopf, E.P. Wigner, Zeit. fur Physik **63** (1930) 54

[39] I. Dunietz, Phys. Rev. **D52** (1995) 3048

[40] I.I. Bigi, A.I. Sanda, *CP Violation* (2000) Cambridge University Press

[41] J.P. Silva, L. Lavoura, G. Branco *CP Violation* (1999) Oxford University Press

[42] T. Affolder et al. Phys. Rev. **D60** (1999) 112004

[43] M. Chemarin, Nucl. Phys.**B85** (2000) 67

[44] A. F. Falk, M. Neubert *Second Order Power Corrections in the Heavy Quark Effective Theory* hep-ph/9209268 (1992)

[45] M. Neubert, *Heavy-Quark Effective Theory and Weak Matrix Elements* hep-ph/9801269 (1998)

[46] A. S. Kronfeld, *Heavy Quarks and Lattice QCD* hep-lat/0310063

[47] M.B. Voloshin *Inclusive weak decay rate of heavy hadrons* hep-ph/0004257

[48] G. Altarelli, S. Petrarca Phys. Lett. **B261** (1991) (303)

[49] A.J. Buras et al. Nucl. Phys. **B347** (1990) 491

[50] M. Beneke, G. Buchalla, I. Dunietz Phys. Rev. **D54** (1996) 4419

[51] P.Abreu et al. Phys. Lett. **B439** (1998) 209
R.Barate et al. Phys. Lett. **B465** (1999) 349

[52] F.Abe et al. Phys. Rev. Lett. **74** (1995) 2626

[53] J.Alexander et al.
http://www.slac.stanford.edu/xorg/hfag/index.html

[54] *The Fermilab Main Injector Technical Design Handbook*
http://www-fmi.fnal.gov/fmiinternal/MI_Technical_Design/index.html

[55] MINOS experiment
http://www-numi.fnal.gov

[56] S. Lai et al. *An Updated Measurement of the Beam Width at CDF* CDF Internal Note 6492 (2003)

[57] Comments Nucl.Part.Phys.**2** (2002) A323

[58] R. Blair et al. The CDF II Detector: Technical Design Report, FERMILAB-Pub-96/390-E (1996)

[59] T.K. Nelson, Nucl. Inst. Meth. **A485** (2002) 1

[60] P. Singh et al. DPF Conf. (1994) 1825, FERMILAB-CONF-94-352-E

[61] The CDF Collaboration *A Time of Flight System for CDF* CDF Internal Note 2573 (1994)

[62] L. Balka et al. *The CDF Central Electromagnetic Calorimeter*, FERMILAB-Pub-87/172-E (1987), Nucl. Instr. Meth. **A267** (1988) 272

[63] G. Apollinari et al. *The CDF Central and Endwall Hadron Calorimeter*, FERMILAB-Pub-87/174-E (1987)

[64] R. Oishi Nucl. Inst. Meth. **A453** (2000) 227

[65] G. Ascoli et al. *CDF Central Muon Detector* FERMILAB-Pub-87/179-E (1987)

[66] T. Dorigo, Nucl. Inst. Meth. **A461** (2001) 560

[67] M. Paulini, B. Wicklund *Summary of Proposals for B Physics Triggers in CDF Run II* CDF Internal Note 5483 (2000)

[68] CDF Collaboration (W. Ashmanskas et al.), Nucl. Inst. Meth. **A447**, (2000) 218

[69] M. Kirk, J. Lewis, M. Tanaka *Run II Semileptonic Trigger Study* CDF Internal Note 5324 (2000)

[70] B. Wagner *Electron Identification for Run II: Algorithms* CDF Internal Note 5456 (2003)

[71] B. Wagner Private Communication 16th March 2004

[72] M. Tanaka Private Communication 10th June 2004

[73] F. Ukegawa et al. *Measurement of charged and neutral B meson lifetimes using electron-charm events* CDF Internal Note 2598 (1994)

[74] B. Wagner *Electron Identification for Run II: Understanding and Using* L_{shr} CDF Internal Note 6249 (2003)

[75] J. Proudfoot *Electron Identificiation in the CDF Central Calorimeter* CDF Internal Note 935

[76] J.N. Bellinger et al. *A Guide to Muon Reconstruction and Software for Run 2* CDF Internal Note 5870 (2002)

[77] G. Pope et al. Study of $B_c^- \to J/\psi\mu^-$ in Run II Data CDF Internal Note 6956 (2004)

[78] R. Brun, F. Carminati, *GEANT Detector Description and Simulation Tool*, CERN Program Library Long Write-up W5013;
http://consult.cern.ch/writeup/geant

[79] M. Bishai et al. *COT and SVXII Tracking Performance* CDF Internal Note 5931 (2002)

[80] K. Anikeev et al. *Measurement of the B Meson Masses in the Exclusive J/ψ Channels* CDF Internal Note 5958 (2002)

[81] G. Bauer, A. Korn, C. Paus *Update on Calibration of Energy Loss and Magnetic Field using J/ψ Events in Run II* CDF Internal Note 6355 (2003)

[82] A. Cerri et al. *SemiLeptonicB/LeptonSvtSel– An offline filter module for lepton-SVT data* CDF Internal Note 6326 (2003)

[83] E. Halkiadakis et al. *A Conversion Removal Algorithm for the 2003 Winter Conferences* CDF Internal Note 6250 (2003)

[84] H. Stadie et al. *The Beam Position in Run II* CDF Internal Note 6327 (2003)

[85] G. Bauer et al. *Selection of Semileptonic B decays optimised for B Mixing Measurements* CDF Internal Note 6780 (2003)

[86] VertexFit package, CDF software
http://cdfkits.fnal.gov/CdfCode/source/VertexAlg

[87] K. Anikeev, P. Murat and C. Paus *Description of Bgenerator II* CDF Internal Note 5092 (1999), P. Sphicas *A $b\bar{b}$ Monte Carlo Generator* CDF Internal Note 2655 (1994)

[88] P. Nason, S. Dawson and R.K. Ellis, Nucl. Phys. **B303** (1988) 607

[89] M. Mangano, P. Nason and G. Ridolfi, Nucl. Phys. **B373** (1992) 295

[90] QQ - The CLEO Event Generator
http://www.lns.cornell.edu/public/CLEO/soft/QQ (unpublished)

[91] D. J. Lange, Nucl. Inst. Meth. **A462** (2001) 152

[92] I.K. Furic, C. Paus, J. Seely CDF Internal Note 5348 (2000)

[93] K. Anikeev,A. Korn, C. Paus CDF Internal Note 5686 (2001)

[94] M. Tanaka, B Semileptonic Meeting, 18th February 2003

[95] I. Kravchenko, Private Communication 28th February 2003

[96] TRGSim++ package, CDF software,
http://cdfkits.fnal.gov/CdfCode/source/TriggerMods

[97] svtfilter package CDF software,
http://cdfkits.fnal.gov/CdfCode/source/SemiLeptonicB

[98] W.H. Press et al., *Numerical Recipes in Fortran 77*, Cambridge University Press, 1992

[99] M. Jones, D. Usynin, J. Kroll, B. Wicklund CDF Internal Note 6480 (2003)

[100] S. Eidelman et al., Phys. Lett., **B592** (2004) 1

[101] K. Anikeev, C. Paus, CDF Internal Note 6551 (2004)

[102] J. Chrin, Z. Phys **C36** (1987) 163

[103] D. Acosta et al., Phys. Rev. **D65** (2002) 052005

[104] Studies by Satoru Uozumi detailed in
http://fcdfhome.fnal.gov/usr/satoru/lifetime/index.html

[105] C.H. Wang et al., CDF Internal Note 3002 (1995)

[106] R. McNulty, T. Shears, S. Tourneur CDF Internal Note 5700 (2001)

[107] V. Blobel, C. Kleinwort hep-ex/0208021 (2002)

[108] Studies by Ilya Kravchenko detailed in
http://mit.fnal.gov/ ikrav/work/lifetimes/lifetimes.html

[109] D. Acosta et al. Phys. Rev. Lett., **91** (2003) 241804

[110] B Lifetimes Taskforce: Alessandro Cerri, Sinead Farrington, Andrew Foland, Ilya Kravchenko, Manfred Paulini, Christoph Paus, Marjorie Shapiro, Masa Tanaka, Fumi Ukewaga, Satoru Uozumi, Barry Wicklund, Kai Yi

[111] R. McNulty, T. Shears, S. Tourneur CDF Internal Note 5701 (2001)